Alexander Braun

Addressing Single Yb^+ Ions

A new scheme for quantum computing in linear ion traps

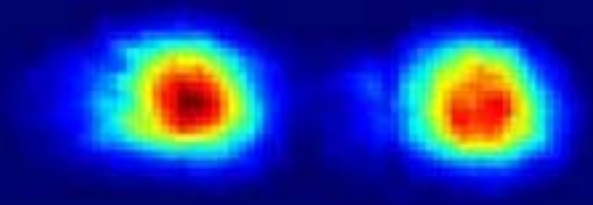

Cuvillier Verlag Göttingen

Alexander Braun

Addressing Single Yb^+ Ions

A new scheme for quantum computing in linear ion traps

Addressing Single Yb^+ Ions

A new scheme for quantum computing in linear ion traps

Dissertation

zur Erlangung des Doktorgrades

des Fachbereichs Physik

der Universität Siegen

vorgelegt von

Alexander Braun

aus Haselünne

Experimente durchgeführt am

Institut für Laser-Physik

der Universität Hamburg

Siegen

2007

Bibliografische Information Der Deutschen Bibliothek
Die Deutsche Bibliothek verzeichnet diese Publikation in der Deutschen Nationalbibliografie; detaillierte bibliografische Daten sind im Internet über http://dnb.ddb.de abrufbar.
1. Aufl. - Göttingen : Cuvillier, 2007
Zugl.: Hamburg, Univ., Diss., 2007

978-3-86727-276-6

Gutachter der Dissertation	Prof. Dr. Christof Wunderlich
	Prof. Dr. Werner Neuhauser
Gutachter der Disputation	Prof. Dr. Christof Wunderlich
	Prof. Dr. Werner Neuhauser
	Prof. Dr. Wolfgang Kilian
Datum der Disputation	14. Mai 2007

© CUVILLIER VERLAG, Göttingen 2007
Nonnenstieg 8, 37075 Göttingen
Telefon: 0551-54724-0
Telefax: 0551-54724-21
www.cuvillier.de

Alle Rechte vorbehalten. Ohne ausdrückliche Genehmigung des Verlages ist es nicht gestattet, das Buch oder Teile daraus auf fotomechanischem Weg (Fotokopie, Mikrokopie) zu vervielfältigen.
1. Auflage, 2007
Gedruckt auf säurefreiem Papier

978-3-86727-276-6

Abstract

This work reports on the individual addressing of single ytterbium ions confined in a linear Paul trap. The addressing procedure is one step in a new scheme for quantum computing in linear ion traps. This thesis presents the first experimental implementation of this scheme. $^{172}Yb^{+}$ ions are laser cooled to the Doppler limit and form a linear ion crystal. Such a string of ions can be used for quantum computing, where each ion represents a qubit. A quantum algorithm necessarily contains a sequence of coherent manipulations of the state of the ions. A prerequisite for these manipulations is the ability to address the qubits independently. The degeneracy of the different qubits is lifted by applying a static magnetic field gradient. The spatially inhomogeneous magnetic field induces a Zeeman-splitting that is dependent on the position of the ions. The ions can thus be addressed by changing the frequency of the interacting electro-magnetic field.

The four-level Doppler-cooling cycle involves two laser transitions near 369 nm, driving the ground-state transition from the $^2S_{1/2}$ ($4f^{14}6s$) to the $^2P_{1/2}$ ($4f^{14}6p$) level, and close to 935 nm, coupling the $^2D_{3/2}$ ($4f^{14}5d$) level to the $^2[3/2]_{1/2}$ ($4f^{13}5d6s$) level. The $D_{3/2}$ state has four Zeeman-sublevels that are used here to demonstrate individual addressing of single ions. A radio-frequency optical double-resonance spectroscopy was set up to probe the state of the four sub-levels of the $D_{3/2}$ level. The levels are coherently coupled by rf-radiation at the Larmor-frequency of the Zeeman-splitting. The spectroscopy itself was investigated in detail, as it forms the basis for the actual addressing measurements. These were subsequently performed successfully and demonstrate the feasibility of the gradient scheme. Measurements for the addressing of two, three, five and sixteen ions are presented. The maximal magnetic field gradient attained was 0.51(2) T/m.

During the course of this thesis a linear trap was put to operation. This is the first time a linear Paul trap has been employed to experiment with cold Yb-ion crystals. The rf-spectroscopy allowed for the measurement of the g_j factor of the $D_{3/2}$ state. The measurement represents the first experimental verification of a historical footnote [Fawcett & Wilson, 1991] pertaining to the measurement of the g_j value by Meggers in 1967, and confirms LS-coupling. As an important step to simplify the trapping procedure itself photo-ionization - with many advantages over electron impact ionization - of ytterbium atoms has been realized. This is the first time for ion trap purposes that ytterbium ions have been produced by photo-ionization. Last but not least a new design for the trap drives creating the trapping potential has been implemented that proved to be experimentally robust with regard to amplitude and frequency stability.

Zusammenfassung

In dieser Arbeit wird über die individuelle Adressierung von einzelnen, in einer linearen Paul-Falle gespeicherten Ytterbium-Ionen berichtet. Diese Adressierungs-Vorschrift ist Teil eines neuen Schemas, um Quanten-Computer in linearen Ionenfallen zu realisieren. Diese Arbeit präsentiert zum ersten Mal die experimentelle Umsetzung dieses Schemas. Die ^{172}Yb Ionen werden durch Laser-Kühlung bis zur Doppler-Grenze zu Ionen-Kristallen eingefroren. Solch ein Ionen-Kristall kann als Quanten-Computer verwendet werden, bei dem jedes Ion ein Qubit darstellt. Ein Quantenalgorithmus benötigt eine Serie von kohärenten Wechselwirkungen mit den Zuständen der Ionen. Eine Voraussetzung für diese Manipulationen ist die Möglichkeit, die Ionen unabhängig voneinander anzusprechen. Die Entartung der verschiedenen Qubits wird durch einen Magnetfeldgradienten aufgehoben, indem das räumlich inhomogene Magnetfeld die Zeeman-Aufspaltung von der Position der Ionen abhängig macht. Die Ionen können dann über die Frequenz der wechselwirkenden elektro-magnetischen Strahlung adressiert werden.

Der Vier-Niveau Kühl-Zyklus besteht aus zwei Übergängen, die durch Laserlicht getrieben werden: dem Haupt-Übergang nahe 369 nm, welcher das $^2S_{1/2}$ ($4f^{14}6s$) Level mit dem $^2P_{1/2}$ ($4f^{14}6p$) Level verbindet, und bei 935 nm, durch den das $^2D_{3/2}$ ($4f^{14}5d$) Level und das $^2[3/2]_{1/2}$ ($4f^{13}5d6s$) Level gekoppelt werden. Das $D_{3/2}$ Niveau besteht aus vier Zeeman-Unterniveaus, welche hier für die Adressierung der einzelnen Ionen eingesetzt werden. Um den Zustand der vier Zeeman Unterzustände zu bestimmen wurde eine radiowellen-optische Doppel-Resonanz-Spektroskopie aufgebaut. Die Niveaus werden durch RF-Strahlung mit der Larmor-Frequenz der Zeeman-Aufspaltung kohärent gekoppelt. Die spektroskopische Methode wurde gründlich untersucht, da sie die Basis für die Adressierungs-Messungen darstellt. Diese wurden im folgenden erfolgreich durchgeführt, und demonstrieren den Erfolg des Gradienten-Schemas. In den Messungen wurden zwei, drei, fünf und sechzehn Ionen adressiert. Der maximale Gradient wurde zu 0.51(2) T/m bestimmt.

Im Rahmen dieser Arbeit wurde eine neue lineare Ionenfalle in Betrieb genommen. Dies ist das erste Mal, dass das Speichern von kalten Yb-Ionen Kristallen in einer lineare Paul-Falle demonstriert wurde. Die RF-Spektroskopie ermöglichte die Messung des g_j-Faktors des $D_{3/2}$ Niveaus. Diese Messung stellt erstmalig die Verifikation einer publizierten Fußnote [Fawcett & Wilson, 1991] dar, in Bezug auf die Messung des g_j-Faktors von Meggers 1967, und bestätigt LS-Kopplung. Photoionisation von Ytterbium-Atomen zum Speichern in Ionenfallen - mit vielen Vorteilen gegenüber Elektronenstoß-Ionisation - wurde entwickelt. Dies erstmalig in Ionenfallen eingesetzte Verfahren ist ein wichtiger Schritt um den Speicherprozess zu vereinfachen. Zu guter Letzt gab es einen neuen Entwurf für den Fallen-Antrieb, der das Speicherpotential erzeugt. Dieses stellte sich im Experiment als sehr robust gegenüber Amplituden- und Frequenzschwankungen heraus.

Contents

1 Introduction **1**
1.1 A brief history of Quantum Computing 1
1.2 Ion trap quantum computing 4
1.3 Magnetic field gradient proposal 6

2 Interaction of ions with em-fields **11**
2.1 Interaction with the RF trapping potential 12
2.1.1 Potential and stability diagram 12
2.1.2 Secular and micro-motion 15
2.1.3 Ion crystals 17
2.2 Interaction with laser light 19
2.2.1 Laser cooling 19
2.2.2 Optical pumping 25
2.3 RF radiation: incoherent measurements and coherent interaction 28
2.3.1 Possible qubits 28
2.3.2 Four-level dynamics: Bloch equations 32
2.3.3 Incoherent spectra: Lorentz profiles 35
2.4 Interaction with the magnetic gradient field 38
2.4.1 Ion addressing 38
2.4.2 Coupling internal and external dynamics 41

3 Trapping single Yb^+ ions **47**
3.1 The linear trap 48
3.1.1 Design 48
3.1.2 Ovens 50
3.1.3 Trap drives 53
3.1.4 Secular frequencies 56
3.1.5 Micro-motion 60
3.2 Lasers and optics 63
3.2.1 Diode lasers 63

3.2.2 Laser system at 369 nm . . . 66
3.2.3 Intensity level control and light field switching . . . 67
3.2.4 Laser optics . . . 69
3.3 Detection systems . . . 71
3.3.1 Photo-multiplier . . . 71
3.3.2 Intensified CCD-camera . . . 73
3.4 Static and dynamic magnetic fields . . . 78
3.4.1 Static magnetic field coils . . . 78
3.4.2 RF-excitation coil . . . 81
3.5 Experiment control . . . 83

4 Photo-Ionization **87**
4.1 Ionization processes . . . 89
4.2 Atomic excitation spectra . . . 92
4.3 Deterministic number loading of ions . . . 99

5 Addressing single Yb^+ ions **101**
5.1 RF-optical double-resonance spectroscopy of a Yb^+ ion . . . 102
5.1.1 Line-width . . . 103
5.1.2 Amplitude . . . 108
5.2 Static magnetic fields . . . 109
5.3 Dynamic magnetic fields . . . 116
5.3.1 Simulation . . . 120
5.3.2 Rabi oscillations . . . 122
5.4 Magnetic gradient field . . . 131
5.4.1 Simulation . . . 131
5.4.2 Gradient alignment . . . 133
5.4.3 Ion addressing . . . 135

6 Conclusion **147**

A Solution of the four level Bloch-equations **153**

B Fluorescence rate: a simple rate equation model **157**

C Ytterbium **161**

Bibliography **165**

Danksagung **175**

Nach der klassischen Logik kann dann das Atom entweder in der linken oder in der rechten Hälfte des Kastens sein. Es gibt keine dritte Möglichkeit; ' tertium non datur'.

Werner Heisenberg [Heisenberg, 1990]

1 Introduction

1.1 A brief history of Quantum Computing

Werner Heisenberg early on noted the dilemma of quantum mechanics illustrated in the quotation above[1]. The ≪tertium non datur≫ of classical logic was apparently in stark contradiction to the superposition principle of quantum mechanics. His former student Carl-Friedrich von Weizsäcker postulated - in the sense of Bohr-complementarity - that classical logic was the classical limit and the a-priori preliminary of some yet-to-be-definded quantum logic [von Weizsäcker, 1990]. In an article ≪Komplementarität und Logik ≫- dedicated to Niels Bohr on the occasion of Bohrs 70th birthday in 1955 - von Weizsäcker breaks with two-valued logic, and he anticipates the idea of a qubit-based quantum logic by applying the Kopenhagen interpretation of quantum mechanics not to measurements, but to logical statements:

> Für jede einfache *Aussage* bezüglich einer Alternative [...] wird eine komplexe Zahl als ein Maß für ihren 'Wahrheitswert' eingeführt. [...] Das Absolut-Quadrat der komplexen Zahl gibt die Wahrscheinlichkeit dafür an, daß die *Aussage* richtig ist [2].

[1] "Following classical logic the atom can then either be in the left or the right half of the box. There is no third possibility; 'tertium non datur'."

[2] "For every simple *statement* with regard to an alternative a complex number is introduced as a measure

The «simple statement with regard to an alternative» means a two-valued alternative 'true - false' as known from classical information theory, albeit now with the expanded possibilities stemming from the super-position principle. von Weizsäcker tried to formalize this idea further by breaking down the whole quantum mechanical theory into these elementary decisions - or *Ur* as he called it - represented by a 2-dimensional Hilbert-space. In that sense he also anticipated the universality claim of the quantum computer - the development of which will be described in the following.

Interestingly enough todays quantum information theory was arrived at a good 25 years later via quite a different reasoning: the question of simulating physics. The philosophically motivated ansatz of von Weizsäcker seems to have been too 'heavy-weighted' to gain acknowledgment and popularity as fast as the pragmatic approach of how to efficiently compute physical phenomena. The starting point is usually attributed to a keynote given by *Feynman* at a conference 'Simulating physics with computers' in 1982 where he addresses the incomputability of certain problems, specifically the impossibility to efficiently simulate entanglement of a two-partite system by classical numerical computation. But he proposes an alternative approach [Feynman, 1982]:

> Now it turns out, as far as I can tell, that you can simulate this [quantum effect] with a quantum system, with quantum computer elements. [...] It has been found that there is a kind of (classical) universal computer that can do anything, and it doesn't make much difference specifically how it's designed. The same way we should try to find out what kinds of quantum mechanical systems are mutually intersimulatable, and try to find a specific class, or a character of that class which will simulate everything. [...] I believe it's rather simple to answer that question and to find the class, but I just haven't done it.

David Deutsch took to the call. His paper "Quantum theory, the Church-Turing principle and the universal quantum computer" [Deutsch, 1985] can be considered the starting point of a formalized quantum information theory. He shows how 'every finitely realizable physical system' - including quantum system - can be efficiently simulated by a finite-element *quantum computer*, the quantum mechanical analog of a (classical) universal *Turing*-machine, and delivers a proof of the quantum mechanical Church-Turing hypothesis. Just as the Turing-machine calculates any computable function by a series of operations on one or two bits - and hence the name universal - Deutsch constructs a universal quantum computer that simulates any unitary evolution of a finite quantum system by a series

for its 'truth value'. The absolute square of the complex number states the probability for the truthfulness of the *statement*."

of operations on one or two quantum bits, or *qubits*. Like its classical counter-part the qubit comprises two distinguishable states, $|0\rangle$ and $|1\rangle$. In contrast to the classical bit though, the general state of the qubit is a super-position of its basis states (also called the computational basis):

$$|\psi\rangle = \alpha|0\rangle + \beta|1\rangle, \tag{1.1}$$

with $|\alpha|^2 + |\beta|^2 = 1$. Eq. 1.1 also nicely illustrates the coup against the "tertium non datur".

So now the 'class which will simulate everything' has been found, and quantum mechanical phenomena including entanglement can be efficiently calculated. This in itself is an exciting field of research for basal quantum mechanical questions, but David Deutsch went one step further and showed a surprising property of the new device: the quantum computer can efficiently calculate certain classical functions that are *not* efficiently computable on a classical Turing machine. By exploiting the super-position capability of the qubit the quantum computer can calculate a function of all possible input states in parallel. Cunning unitary evolutions applied to the whole super-position state then use this massive 'quantum parallelism' to obtain an exponential speed-up for the calculation of certain problems. This quantum parallelism will be briefly sketched in the following.

Let an input register with N qubits be described by the basis states

$$|n\rangle = |b_1\rangle \otimes |b_2\rangle \otimes \cdots \otimes |b_N\rangle = |b_1 b_2 \dots b_N\rangle, \tag{1.2}$$

where $b_k \in \{0, 1\}, k = 1 \dots N$ and thus $n = 0 \dots 2^N - 1$. A classical register would hold one of the values n, whereas the quantum register can hold all values n as a super-position (ignoring normalization factors):

$$|\Psi\rangle = \sum_{n=0}^{2^N-1} |n\rangle. \tag{1.3}$$

Consequently, if we were to calculate the function $f(|n\rangle)$ of an input state - represented by a unitary transformation U_f - the linearity of quantum mechanics ensures that this can be done in parallel by applying U_f to the super-position $|\Psi\rangle$:

$$U_\mathrm{f}(|\Psi\rangle) = U_\mathrm{f}\left(\sum_{n=0}^{2^N-1} |n\rangle\right) = \sum_{n=0}^{2^N-1} U_\mathrm{f}(|n\rangle). \tag{1.4}$$

In one time step the quantum computer has evaluated all possible results of f. Of course, the result is in form of a super-position, which is not a usable (classical) result. If we were

to measure $U_{\mathrm{f}}(|\Psi\rangle)$ the wave-function would collapse, not only giving only one solution $U_{\mathrm{f}}(|n\rangle)$, but this value would furthermore be a random choice between the N different input states $|n\rangle$. The real ingenuity is the realization that this massive parallelism can be accessed by subsequently performing interference experiments on $U_{\mathrm{f}}(|\Psi\rangle)$ that enhance the measurement probability of the desired result state. To accurately describe this process for a real quantum algorithm is beyond the scope of this introduction.

The first true quantum algorithm that exhibits a computational speed-up is the *Deutsch-Jozsa* algorithm that determines if a given function f is even or odd [Deutsch & Jozsa, 1992]. As it operates on just two qubits it is also is the first algorithm that was experimentally implemented [Jones & Mosca, 1998], and it still is used as a demonstration for new experimental systems [Gulde et al., 2003]. Then a discovery by *Peter Shor* incited an interest that went far beyond that of quantum physicists: a quantum algorithm for prime factorization of large numbers with an exponential speed-up over its classical pendant [Shor, 1994]. The large interest stems from the fact that current classical encryption schemes - like the wide-spread RSA [Rivest et al., 1978] - rely on the 'hardness' of the problem of prime factorization. Shor's algorithm thus jeopardizes (at least theoretically) a large part of todays encryption industry. The basis for Shor's algorithm is the quantum Fourier transformation (QFT) that operates exponentially faster then the fastest classical Fourier transform (FFT): $\mathcal{O}(n^2)$ to $\mathcal{O}(n \cdot 2^n)$ [Chuang, 2003].

Quantum computing is now just one field of many different and interesting applications of quantum information theory. Quantum cryptography, quantum teleportation and dense coding are just a sample. Many different experimental implementations have been proposed for a quantum computer. Liquid-state nuclear magnetic resonance (NMR) [Jones & Mosca, 1998], ion traps or super-conducting flux qubits (Josephson junctions) [Devoret & Martinis, 2003] are but an excerpt of the proposal list currently being tested for the 'transistor of the future'. This thesis is an experimental work that researches a new approach to quantum computing with trapped ions. In the following, 'traditional' ion trap quantum computing is presented first in Sec. 1.2. In Sec. 1.3 the new proposal for ion trap quantum computing with a magnetic gradient field will be introduced.

1.2 Ion trap quantum computing

The first proposal to use a linear ion trap as 'a realistic physical system to implement a quantum computer' appeared in 1995 by *Ignacio Cirac* and *Peter Zoller* [Cirac & Zoller, 1995]. The authors suggest to compose a qubit of two internal energy levels of an ion. The com-

munication between the ions is mediated by the Coulomb repulsion, which together with the confining trap potential forms a set of common (harmonic) oscillator modes of the ion string. By using one particular oscillation mode as a 'bus-qubit' conditional quantum dynamics between two ions is possible. For this purpose the state of one qubit is copied into the bus-qubit by coupling the internal dynamics of the ion with the external dynamics of the oscillation mode. In the article a quantum controlled-not operation (the 'c-not' gate) is explicitly constructed from a series of laser pulses acting on the ions. It had been shown before that 'there exists a 2-bit quantum gate that is sufficient to build any quantum logic network' [Sleator & Weinfurter, 1995]: the aforementioned c-not gate. This is not an exclusive universality. The c-not is just one possible realization of an universal conditional 2-qubit gate. It seems worth to stress the universality of that claim [Deutsch, 1985]: the c-not gate together with a set of one-qubit operations allows to simulate *every* finite physical system! The same year the c-not gate was experimentally implemented between an ion and an oscillation mode by the group of Dave Wineland [Monroe et al., 1995], and later the full Cirac-Zoller c-not gate between two ions was experimentally realized by the group of Rainer Blatt [Schmidt-Kaler et al., 2003b].

Since then the last decade has seen considerable progress of quantum information science in linear ion traps. Enhanced rotation angle estimation [Meyer et al., 2001] and robust geometric phase gates [Leibfried et al., 2003], Bell-inequality measurements [Rowe et al., 2001], self-learning estimation of quantum states [Hannemann et al., 2002], the realization of quantum error correction [Chiaverini et al., 2004] and the implementation of the full Deutsch-Josza-algorithm [Gulde et al., 2003] show the potential of quantum information science and quantum computing with only a single or two ions. As of late the spectacular quantum teleportation of atomic qubits [Riebe et al., 2004, Barrett et al., 2004] or the demonstration of the first Qubyte with eight ions [Haffner et al., 2005] have pushed the limits. On the theoretical side, an article by Soerensen and Molmer [Sorensen & Molmer, 2000] proposed a similar c-not gate relying on two-photon transitions that is distinctly less stringent in its demand on the state of the bus-qubit, i.e. the Sorensen-Molmer gate does not require ground-state cooling of the coupling oscillator mode. Cirac and Zoller eliminated the direct dependence of the oscillation mode with a proposal involving short laser pulses, allowing arbitrarily fast gate times [Garca-Ripoll et al., 2003]. The new Cirac-Zoller gate has until now not been experimentally realized.

Notwithstanding these successes several problems remain that prohibit scaling to a larger number of qubits. The coherence time of optical qubits (i.e. qubits where the energy difference between the two states is on the order of an optical transition) is limited by the life-time of the upper level. For $^{40}Ca^{+}$ used in Innsbruck [Schmidt-Kaler et al., 2003a] and

Oxford [Lucas et al., 2003] the $D_{5/2}$ state has a life-time of approximately 1 s, ultimately limiting the length of a quantum algorithm. The demands on the laser stability both in frequency and amplitude control require state-of-the-art equipment. In comparison to coherent manipulation of qubits in the radio-frequency domain this is a substantial experimental disadvantage. The addressing of the ions is the direct and exclusive illumination of only one ion by a tightly focused laser beam. For larger ion strings with a small inter-ion distance this addressing becomes increasingly difficult. A rest illumination of neighboring ions is unavoidable, inducing unwanted residual transitions.

To counter theses problems a different trap design has been envisaged. The new type of trap is micro-fabricated by standard lithographic techniques, and comprises many different trapping zones [Kielpinski et al., 2002]. Only two ions at a time interact in special interaction zones. This avoids the addressing problems arising for longer ion strings. After interaction, the ions are shuttled to cooling zones, where they are sympathetically cooled. The short maximal coherence time for optical transitions is avoided using hyper-fine states instead. This reduces the coherence requirement of the driving laser from the optical to the micro-wave regime, implemented in form of a Raman-laser setup.

A large effort in the community is underway to realize this new type of trap. In the meantime, we propose a modification of the existing form of the linear trap QC that simplifies both the addressing and the coherent manipulation of the qubits even more. As such, we hope to fill the gap between the few-qubit QC already demonstrated and the large-scale (hundreds of qubits) architecture described above. Furthermore, no fundamental reason prohibits the combination of the micro-array trap design with the gradient scheme presented in this work. Therefore, the gradient scheme may offer advantages for all ion trap quantum computers.

1.3 Magnetic field gradient proposal

The scheme to use ion traps with a static, magnetic gradient field for quantum computation [Mintert & Wunderlich, 2001, Wunderlich, 2001, Wunderlich et al., 2005] aims at both increasing the scalability of the system and at opening up new possibilities for it. The scalability is mainly increased by simplifying the experimental complexity. A solution for the problems inherent to the addressing and the coherent manipulation discussed above is presented. All methods requiring so far optical radiation - e.g. side-band cooling, c-not gate - will become feasible with MW- or RF-radiation alone. In the end the goal is to combine the present advantages of the ion trap with those of a NMR quantum computer.

The first part of the gradient scheme is the addressing of the ions. In the presence of a magnetic gradient field the Zeeman-splitting of the energy levels now depends on the position of the ions. If we assume for simplicity a magnetic field that is linearly increasing in the z-direction (parallel to the trap axis) the Larmor-frequency of the Zeeman-splitting for a (linear) string of ions increases linearly as well. Using rf-radiation the addressing of the qubits then is straight-forward by changing the rf-frequency to the resonance frequency of the desired ion. But a larger obstacle remains: to be able to use rf-radiation (or micro-wave radiation, for that matter) for the addressing in the first place we need to be able to perform conditional quantum logic gates with rf-radiation as well. This forms the second part of the gradient scheme.

The ultimate reason why so far coherent manipulation of qubits in ion traps is performed with laser sources is the necessity to couple the internal dynamics of the ion (driven by the laser source) with the external dynamics, the oscillatory movement of the ion in the trap potential. The Circac-Zoller-proposal uses the common oscillation mode of the ions as a bus-mode that mediates the communication between the ions. The measure for the strength of the coupling between the internal and the external dynamics is given by the so-called Lamb-Dicke-parameter (LDP):

$$\eta = k \cdot \Delta X = \frac{\hbar k}{2\Delta P}. \tag{1.5}$$

k is the wave-vector of the exciting electro-magnetic radiation and $\Delta X = \sqrt{\frac{\hbar}{2m\omega}}$ and $\Delta P = \sqrt{\frac{1}{2}m\hbar\omega}$ are the spread of the position and momentum operator, respectively, of the ground-state wave-function of the quantum harmonic oscillator. In other words, the LDP is measure of how much the amplitude of the electro-magnetic wave varies over the spatial extent of the ion, or how much momentum the wave carries with respect to the momentum of the ion. Inserting the numbers for a typical secular trap frequency of $\omega = 2\pi \cdot 1\,\mathrm{MHz}$ it becomes clear that only for optical radiation does η take on a appreciable value $> 10^{-3}$, and a relevant coupling between the internal and external dynamics of the ion arises. Following this logic, micro-wave or even radio-frequency radiation never was a choice for ion trap quantum computing. This explains why even for the hyper-fine qubit with a transition frequency in the micro-wave regime a laser source is required (in form of a Raman-laser setup), instead of using the experimentally much less demanding direct irradiation with micro-waves.

Central to the second step of the gradient scheme is the emergence of a new, effective Lamb-Dicke-parameter η_{eff} due to the interaction of the ions with the magnetic gradient field. Quite generally, for a conservative potential ϕ a force stems from the gradient of

that potential, i.e. $F = -\nabla\phi$. The magnetic dipole moment $\vec{\mu} = g_j m_j \vec{\mu_B}$ of the ion in an external magnetic field $\vec{B}$ has the potential energy $\phi = -\vec{\mu} \cdot \vec{B}$. For the case of our magnetic gradient field this implies a state-dependent force:

$$F = \mu \cdot \nabla B. \tag{1.6}$$

Graphically speaking, the ion is displaced to a new equilibrium position by this force, with the sign of the displacement - with respect to the original equilibrium position - depending on the internal state m_j of the ion. Accordingly, changing the internal state of the ion (e.g. by a π-pulse using rf-radiation) pushes it to the other equilibrium position. The Coulomb repulsion between the ions now lets the other ions of the whole string 'feel' this displacement. In effect, there is a chance that the state of the oscillation mode of the ion string is excited. But this is just the same as saying that the effective LDP η_{eff} has an appreciable value. This admittedly rather illustrative description of η_{eff} will be motivated (and calculated) more thoroughly in Sec. 2.4.2.

The implications of the new, effective LDP are important for ion trap quantum computing. Using η_{eff}, side-band cooling with micro-waves becomes feasible as side-bands in the rf- or mw-spectrum emerge. But the coupling between internal and external dynamics further allows for coherent interaction on side-band transitions, basic ingredient of the Cirac-Zoller c-not gate. In conclusion, η_{eff} eliminates the need for extremely stable laser-sources, as the coherent manipulation of the qubit states can now be performed with mw- or rf-radiation directly.

The theory pertaining to this concept has been developed in detail in the references given above. This thesis is the first experimental step to implement the gradient scheme. During the course of this work a new linear trap has been put in operation with alternative radio-frequency trap drives, photo-ionization of ytterbium for ion trap purposes has been implemented for the first time, and a magnetic gradient field has been setup with permanent magnets. The method of rf-optical double-resonance spectroscopy has been adapted for ion trap purposes to have an experimental probe that is magnetically sensitive. The measurements characterizing the magnetic field gradient by rf-spectroscopy form the central aspect of this work.

The long-term goal is to perform measurements with the ^{171}Yb isotope of ytterbium. It has a nuclear spin of $I = 1/2$ with a convenient hyper-fine structure for quantum information processing. Nonetheless, it is experimentally more challenging than its 'sibling', the ^{172}Yb isotope, as the fluorescence rate and hence the cooling rates are lower [Balzer, 2003], making it more difficult to cool and localize. Therefore, the Zeeman sub-levels of the ^{172}Yb isotope are employed instead, in a first step to demonstrate the addressing ability of the

gradient scheme. The rf-optical double resonance spectroscopy is an adequate tool to probe this magnetic four-level sub-structure, both incoherently and coherently.

After this introduction Chapter 2 presents the theory relevant for this work. It is grouped in 'interactions': the interaction of the ions with the trapping potential (2.1), with laser light (2.2), with the exciting rf-radiation used for the double-resonance spectroscopy (2.3), and finally with the magnetic gradient field (2.4). Next, following the theory, Chapter 3 describes the experimental issues pertaining to trapping single ytterbium ions. Its sections are formed by functionality: the linear trap itself (3.1), lasers and optics (3.2), the detection systems (3.3), magnetic fields (3.4) and experimental control (3.5). The experimental results are split into two chapters. First, the photo-ionization experiments are discussed in Chapter 4. Using an oven with natural abundance isotope distribution the isotope shift of the atomic $^1S_0 \rightarrow {}^1P_1$ transition is determined from atomic excitation spectra in (4.2). Photo-ionization furthermore allows for the deterministic loading of a desired number of ions, shown in (4.3). Finally, Chapter 5 comprises the main experimental results of this work. First, the double-resonance spectroscopy itself is established (5.1). With it, the static magnetic fields creating a well-defined quantization axis for the following measurements are characterized (5.2). Qubits are manipulated by coherent interactions. That the double-resonance spectroscopy allows for these types of measurements is shown in (5.3), where coherent Rabi-oscillations are presented. And last but not least, the permanent magnets are put in place to create the magnetic gradient field (5.4). This section contains the actual measurements showing the individual addressing of single ytterbium ions in a linear ion crystal. The main body of this thesis closes with the conclusion and outlook in Chapter 6.

2

Interaction of ions with em-fields

This chapter comprises the theoretical body of this thesis. All relevant interactions are electro-magnetic in nature, differing in regime and application. First, the ions are trapped in the radio-frequency potential of a Paul-trap. The resulting effective potential as well as the interplay between confining trap potential and repulsive Coulomb interaction between the ions is described in Sec. 2.1. The ions are then laser cooled to temperatures ranging in the mili-Kelvin regime for good localization and detection. Sec. 2.2 describes the interaction of ions with laser light. That section is kept semi-classical. Both the incoherent measurements with and the coherent interaction of radio-frequency radiation with the ions are presented in Sec. 2.3. After a discussion of the possible qubits the Bloch-equations are expanded to four energy levels. Closing this chapter is Sec. 2.4, where the influence of the magnetic field gradient is calculated. Both the addressing of single ions - together with an error estimate of residual excitation of other ions - and the emergence of an effective Lamb-Dicke-parameter from the interaction with the field gradient are discussed. Note that a more detailed description of the energy levels and optical transitions of $^{172}Yb^{+}$ are to be found in Appendix C.

2.1 Interaction with the RF trapping potential

Of the different interaction forms presented in this chapter the trapping potential is probably the most basic. All other interactions make the ions visible or manipulate them for quantum information processing, but the trapping potential keeps the ion confined to a small volume in the first place. The original idea for the localization of small, charged particles came from *Wolfgang Paul* in 1958 [Paul et al., 1958]. After trapping single electrons in 1973 [Wineland et al., 1973] the proposals for laser cooling [Hänsch & Schawlow, 1975, Wineland & Dehmelt, 1975] paved the road for trapping and detecting small clouds of atoms [Neuhauser et al., 1978,Wineland et al., 1978], culminating in the deterministic detection of a single trapped ion for the first time [Neuhauser et al., 1980]. An active ion trapping community today researches subjects ranging from parity nonconservation [Koerber, 2003] to atomic clocks [Taylor et al., 1998,Oskay et al., 2006,Schneider et al., 2005] to quantum computing [Monroe et al., 1995,Nägerl et al., 1998,Balzer & Wunderlich, 2003]. Positively charged molecules are trapped in linear traps and sympathetically cooled to the Doppler limit by laser cooled ions [Fröhlich et al., 2004], and in plasma physics and chemistry the potential of the linear trap (without endcaps) has become a valuable tool as the quadrupole mass filter.

This section explains the basic features of a linear ion trap. The potential itself and the resulting equations of motion for a single charged particle are presented in Sec. 2.1.1. Next, the resulting oscillatory movements of the ion in the trap are discussed in Sec. 2.1.2. The number of ions is increased in Sec. 2.1.3 where some characteristics of ion crystals conclude this section.

2.1.1 Potential and stability diagram

There are many different designs and experimental realizations of the original idea of *Paul* to trap charged particles. The starting point for all is known as *Earnshaws* Theorem: no static potential alone is able to confine a charged particle. This theorem is derived from the *Laplace* equation

$$\Delta\Phi = (\partial_{\mathrm{x}}^2 + \partial_{\mathrm{y}}^2 + \partial_{\mathrm{z}}^2)\Phi = 0. \tag{2.1}$$

For any given static potential that has a resulting confining force, e.g., in the x-direction, a balancing repelling force results to satisfy *Laplace* (moreover: his law), such that the sum of second derivatives add to zero. In other words, no static electric potential has an absolute minimum in vacuum.

Consequently, dynamical fields are necessary for trapping purposes. Inverting the polarity of a given potential with the mentioned properties will reverse the role of the attractive and the repulsive force, and if this switch is performed fast enough a charged particle proves to be too inert to escape. Before it is able to leave the trap in the direction of the repulsive force the potential is already inverted, and the ion is pushed back into the center. As a time-average an effective potential arises from the dynamic potential that is confining in all spatial dimensions, the so-called pseudo-potential.

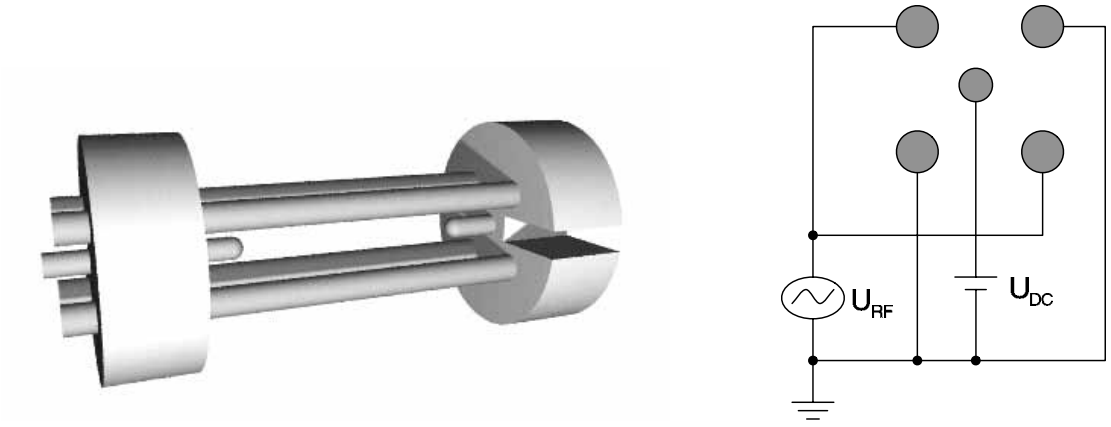

(a) Linear trap

(b) Schematic electrode configuration

Figure 2.1: Schematic drawing of the linear trap (a) and its electrical setup (b).

Figure 2.1 shows the linear trap employed in this work in a schematic drawing (see also Sec. 3.1.1). Four straight, parallel rod electrodes are grouped diagonally in pairs. One pair is kept on electrical ground, while the other is connected to the so-called trap drive, a radio-frequency (RF) signal of high voltage amplitude. Additionally, static potentials can be added to the RF fields. Two endcap electrodes create a static potential along the z-axis.

Applying thus a voltage of the form $U(t) = U_0 + V_0 \cos(\Omega t)$ to the rod electrodes the potential in the radial (x-y) plane is given to second-order by

$$\Phi(x, y, t) = [U_0 - V_0 \cos(\Omega t)] \frac{x^2 - y^2}{2R^2}, \tag{2.2}$$

where R is the distance from the z-axis to the surface of the rod electrodes, and the origin is chosen on the z-axis at the center of the trap. A perfect quadrupole potential is generated by hyperbolic electrode surfaces, not circular as assumed here [Paul et al., 1958]. As the

spread of the ions wavefunction is very small compared to the trap size (on the order of nm) the potential is very well approximated with the second order. An ion of mass m and charge Q experiences a force $\vec{F} = -Q\vec{\nabla}\Phi$ such that the equations of motion of the ion become

$$m\ddot{x} = -[U_0 - V_0\cos(\Omega t)]\frac{Q}{R^2}x, \tag{2.3}$$

$$m\ddot{y} = [U_0 - V_0\cos(\Omega t)]\frac{Q}{R^2}y. \tag{2.4}$$

With the following substitutions

$$q = \frac{2QV_0}{mR^2\Omega^2}, \quad a = \frac{4QU_0}{mR^2\Omega^2} \quad \text{and} \quad 2\tau = \Omega t \tag{2.5}$$

we then retrieve the *Mathieu* equations for the motion of the ions:

$$\frac{\partial^2 x}{\partial\tau^2} + [a - 2q\cos 2\tau]\,x = 0, \tag{2.6}$$

$$\frac{\partial^2 y}{\partial\tau^2} + [-a + 2q\cos 2\tau]\,y = 0. \tag{2.7}$$

The *Mathieu* equations are well-established differential equations, whose analytical solutions are described in the frame of the *Floquet* theory as a Fourier-series [Ghosh, 1995]:

$$\zeta(\tau) = Ae^{\pm i\beta\tau}\sum_{n=-\infty}^{+\infty} C_{2n}e^{i2n\tau} + Be^{\mp i\beta\tau}\sum_{n=-\infty}^{+\infty} C_{2n}e^{-i2n\tau}. \tag{2.8}$$

The initial conditions determine the coefficients A and B. The Floquet exponent $\beta = \beta(a,q)$ and the coefficients $C_{2n} = C_{2n}(a,q,\Omega)$ of this series depend solely on the a and q parameters defined in Eq. 2.5, and on the frequency of the trap drive. Regarding the exponentials in front of the sums of Eq. 2.8 it is obvious that the solution diverges for coefficients β that contain an imaginary part. This is equivalent to an unstable orbit, i.e. the ion is not trapped. The restraint to real numbers of β allows for the graphical representation of the sets of parameters (a,q) for which stable trapping can be achieved. Figure 2.2 depicts such a representation, it is called the a-q- or stability diagram. The shaded areas indicate the stability regions where bounded solutions of the Mathieu equations exist. As q describes the RF signal a change of sign is simply a phase change for that oscillation. Therefore, the graph is symmetric with respect to the a-axis.

Apparently, the stability diagram has to be fulfilled independently for every spatial direction, in our case for the x- and y-direction. As the sign of a changes in Eq. 2.6 and Eq. 2.7 the stability diagrams for x and y are mirror-images by rotation along the q axis. Consequently, the trapping region is found where these two diagrams overlap. Here it is indicated by the hatched areas.

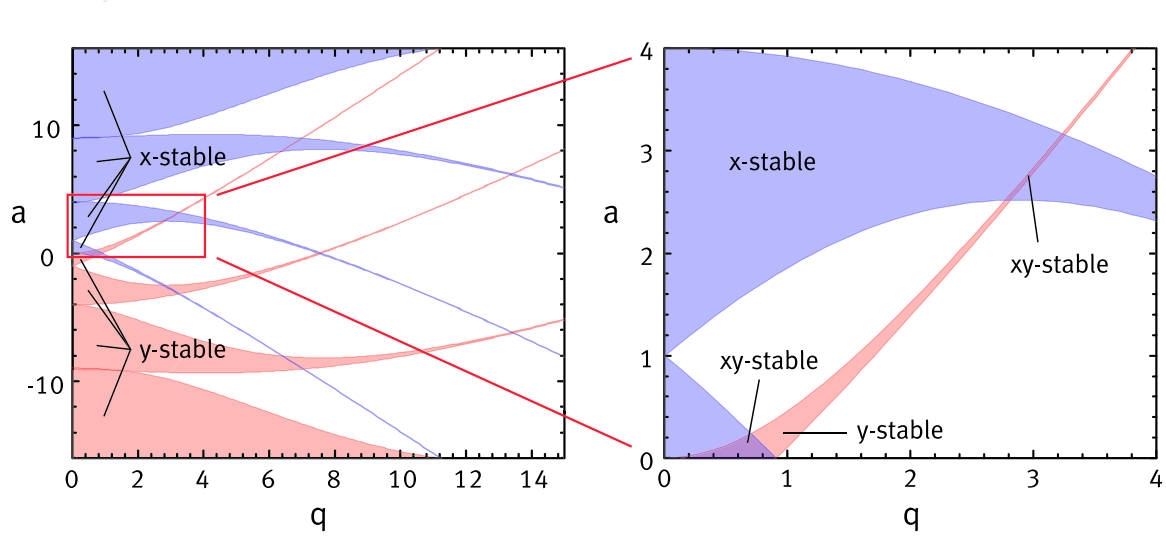

Figure 2.2: a-q-diagram or stability diagram for the solutions to the Mathieu equations in x- and y-direction.

2.1.2 Secular and micro-motion

In principle, infinitely many regions in the a-q-diagram exist where a combination of a and q parameter allow stable solutions (i.e. stable trapping) of the Mathieu equations. As a and q are related proportionally to the DC- and RF-potential, respectively (see Eq. 2.5), for practical purposes only the lowest region of stability plays a role experimentally. This is the region where the necessary potentials are readily accessible in the laboratory. Furthermore, linear traps are usually operated with $U_0 = 0$, i.e. $a = 0$. In that case the solutions are stable within a parameter range of $0 < q < 0.908$ [Ghosh, 1995]. As will be shown in Sec. 3.1.4 the value for q in this work was always even below 0.25. In that case (i.e. $|a|, q^2 \ll 1$), the solutions for the oscillations in the radial direction are well approximated to first order by

$$x(t) = x_0 \cos(\omega_x t + \phi_x) \left(1 + \frac{q_x}{2} \cos(\Omega t)\right), \tag{2.9}$$

$$y(t) = y_0 \cos(\omega_y t + \phi_y) \left(1 + \frac{q_y}{2} \cos(\Omega t)\right), \tag{2.10}$$

with

$$\omega_x = \frac{\Omega}{2}\sqrt{\frac{q^2}{2} + a}, \tag{2.11}$$

$$\omega_y = \frac{\Omega}{2}\sqrt{\frac{q^2}{2} - a}. \tag{2.12}$$

x_0, y_0, ϕ_x and ϕ_y are determined by the initial position and velocity of the ion. The solution are oscillations at frequencies ω_i ($i \in \{x, y\}$), whose amplitude is modulated at the trap drive frequency Ω. The fact that $q^2 \ll 1$ holds (and $a = 0$ for all practical purposes) implies firstly that the so-called 'secular frequency' ω_i is slow in comparison to Ω, and secondly that the modulation of the amplitude at Ω is small. Furthermore, for $a = 0$ the radial frequencies are the same: $\omega_x = \omega_y \equiv \omega_r$.

Based on this analysis the motion of the ion is thus separated into two terms: the slow 'secular' oscillation at ω_r onto which a fast oscillation is superimposed that is called the 'micro-motion'. As the amplitude of the micro-motion is dependent upon the displacement of the ion from the origin (in radial direction) this implies that it can be reduced to zero by moving the ions perfectly into the center of the trap. The reduction of the micro-motion is an important experimental aspect, and is dealt with in detail in Sec. 3.1.5.

So far the axial confinement has been neglected, which shall be remedied in the following. Adding a constant and equal voltage to both endcap electrodes that can be seen in Figure 2.1 gives rise to a harmonic potential at the trap center:

$$\Phi_{\text{end}}(x, y, z) = \kappa U_{\text{end}} \left[z^2 - \frac{1}{2}(x^2 + y^2) \right]. \tag{2.13}$$

κ is a empirical geometrical factor that is different for every trap design. To fulfill Laplaces' equation the field extends also in the x- and the y-direction. For the z-axis it follows immediately that the movement of the ion is harmonic with a frequency

$$\omega_z = \sqrt{\frac{2Q\kappa U_{\text{end}}}{m}}. \tag{2.14}$$

Clearly the terms in radial direction in Eq. 2.13 have a defocusing effect on the original radial potential Φ. Applying the additional term to Φ in a straight-forward manner a new set of Mathieu equations emerges:

$$\frac{\partial^2 x}{\partial \tau^2} + [a + a_z - 2q\cos 2\tau]\, x = 0, \tag{2.15}$$

$$\frac{\partial^2 y}{\partial \tau^2} - [a - a_z - 2q\cos 2\tau]\, y = 0. \tag{2.16}$$

with

$$a_z = -2\left(\frac{\omega_z}{\Omega}\right)^2. \tag{2.17}$$

Accordingly, the radial secular frequencies change as well:

$$\omega_x = \frac{\Omega}{2}\sqrt{\frac{q^2}{2} + a + a_z}, \tag{2.18}$$

$$\omega_y = \frac{\Omega}{2}\sqrt{\frac{q^2}{2} - a + a_z}. \tag{2.19}$$

It is interesting to note that the axial secular frequency does not depend on the amplitude of the trap drive, but that the endcap voltage has a decided influence on the radial secular frequencies.

2.1.3 Ion crystals

The Coulomb force in form of the trapping potential is responsible for keeping the ions localized to a small volume, but thus far the Coulomb force between the ions themselves has been neglected. Apparently, an equilibrium is reached between the repelling forces of the ion interaction and the attractive forces of the trapping potential. If the laser cooling (see Sec. 2.2.1) is effective enough to reduce the kinetic energy of the ions below a certain energy the ions are frozen into a crystalline formation. In this regime the average kinetic energy is lower than the energy needed for two ions to change place in the trap potential. An (linear) ion string results when the radial confinement is stronger than the axial confinement, i.e. if $\omega_z < \omega_r$. Figure 2.3 displays one such string of 23 ions.

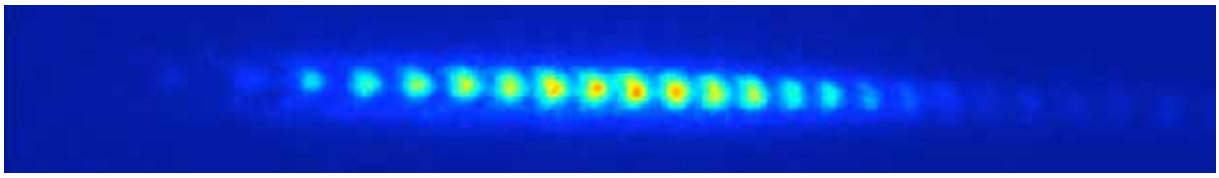

Figure 2.3: A string of $^{172}Yb^+$ 23 ions cooled to crystal formation. Only the center part is well illuminated by the cooling lasers.

In this case, the potential energy of the ions is given by two terms representing the trap and the interaction potential:

$$V = \sum_{n=1}^{N} \frac{1}{2} M \omega_z^2 x_n^2 + \sum_{n,m=1,\, m\neq n}^{N} \frac{Q^2}{8\pi\epsilon_0} \frac{1}{|x_n - x_m|}. \tag{2.20}$$

Here, x_i denotes the position of ion i, and ω_z is the axial trap frequency. The assumption is made that the confinement in radial direction is so strong that the movement of the ions in this direction can be neglected. Furthermore, if the ions do not change place the position x can linearized about its equilibrium position:

$$x_n(t) = x_n^{(0)} + q_n(t). \tag{2.21}$$

The equilibrium position can then be calculated by finding the minima of the potential V, i.e. where

$$\left[\frac{\partial V}{\partial x_n}\right]_{x_n^{(0)}} \stackrel{!}{=} 0. \tag{2.22}$$

This equation has been solved for the case of up to ten ions by James [James, 1998], analytically for two and three ions, numerically otherwise. Figure 2.4 displays the ion positions as determined in [James, 1998] for a string of one to ten ions. There, the equilibrium

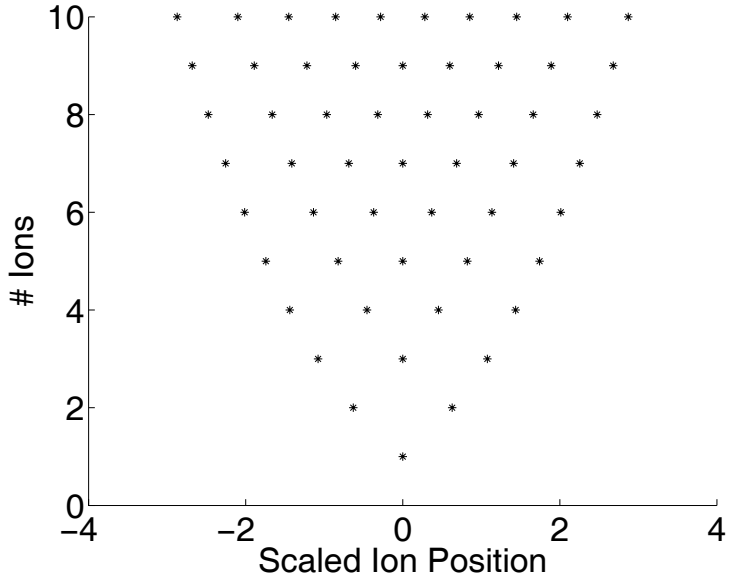

Figure 2.4: Scaled ion position in units of ℓ (see Eq. 2.23) for strings of ions of length 1 - 10.

positions are expressed in units of an appropriate length scale ℓ

$$\ell^3 = \frac{Q^2}{4\pi\epsilon_0 M\omega_z^2}. \tag{2.23}$$

An important aspect of relation (2.23) is that it calibrates the imaging scale of the CCD detection system, if the axial trap frequency ω_z is known. As ω_z is an readily attainable experimental parameter (see Sec. 3.1.4) this method proves to be quite practicable. A comparison of two different calibration procedures is given in Sec. 3.3.

Of further interest for the characterization of strings of ions in a linear trap are the different oscillation modes resulting from the Coulomb interaction between the ions. There are as many different modes of oscillation as there are ions (again neglecting radial modes), each with its own frequency. As in the case for the equilibrium positions this problem is analytically solvable for two and three ions [James, 1998, Rohde, 2001]:

$$N = 2: \quad \omega_{\text{com}} = \omega_z, \quad \omega_{\text{breath}} = \sqrt{3}\omega_z, \tag{2.24}$$

$$N = 3: \quad \omega_{\text{com}} = \omega_z, \quad \omega_{\text{breath}} = \sqrt{3}\omega_z, \quad \omega_3 = \sqrt{\frac{29}{5}}\omega_z. \tag{2.25}$$

The first mode is always the center-of-mass mode, where all ions oscillate with the same amplitude in the same direction. The second mode is usually called the breathing mode, where the ions movements have opposite signs and increasing amplitude depending on their relative position to the origin. In this work, only the lowest oscillation mode - the center-of-mass mode - plays a role experimentally.

2.2 Interaction with laser light

Fundamentally, the interaction of atoms or ions with light and with RF radiation is the same, they differ only in the energy scale involved. Nonetheless, whereas it is straightforward to implement a coherent phase relation between a rf radiation field and an atom, for optical transitions to retain the coherence between light field and atom constitutes an experimental feat. This is why one main goal of the gradient scheme pursued in this work is to reduce the experimental overhead necessary for quantum computing. With coherent interaction between electro-magnetic fields and atoms at its core, the possibility to perform conditional quantum logic operations between two qubits with RF radiation alone would therefore imply a distinct experimental advantage.

Following this, all sections in this chapter of laser-light interactions are semi-classical in nature. After trapping, the ions need to be laser cooled, which is described in Sec. 2.2.1. The rf-optical double resonance spectroscopy employed in this thesis uses optical pumping as an initialization step (Sec. 2.2.2). A description of the energy levels and relevant optical transitions of $^{172}Yb^{+}$ can be found in Appendix C.

2.2.1 Laser cooling

The first proposals to use laser light to cool matter date from 1975. *Hänsch* and *Schawlow* [Hänsch & Schawlow, 1975] and alternatively *Wineland* and *Dehmelt* [Wineland & Dehmelt, 1975] had the idea to exploit the Doppler effect to couple internal and external degrees of freedom of an atomic system, i.e. to couple the interaction dynamics of the laser-atom system with the movement of the particle. This coupling then allows for the dissipation of kinetic energy of the particle by the scattered photons, hence laser cooling [Neuhauser et al., 1978]. The central aspect of this scheme is the Doppler-shift of the laser frequency as seen by an atom that is moving relative to the direction of propagation of the laser beam. The Doppler-shifted laser frequency is

$$\nu = \nu_0 \left(1 \pm \frac{v}{c}\right), \tag{2.26}$$

where ν_0 is the frequency of the laser in its own inertial system, and v is the velocity of the atom in direction of the laser beam. The frequency is decreased when the atom is moving away in the direction of the laser beam, and vice versa. Moreover, this implies that the momentum $\hbar k = h\nu/c$ the atom receives during the absorption process of a photon can be increased or decreased.

There are many ways to exploit this fact to dissipate kinetic energy of an atomic system. The field of laser cooling today is an active and differentiated field of research. Its importance and variety is underlined by the Nobel prizes in Physics in 1989 for trapping and rendering visible of a single ion, in 1997 for laser cooling itself and in 2001 for the creation of a Bose-Einstein-condensate. Laser cooling is applicable to both neutral atoms [Hansen, 2006] and ions, and molecules are sympathetically cooled by other laser cooled particles [Fröhlich et al., 2004]. We are here concerned with trapped ions, and concentrate on Doppler-cooling of trapped ions in the remainder of this section.

Two regimes for laser cooling of trapped ions will be considered here. When the frequency of the secular motion of the ion in the trap ω_z is lower than the line-width of the cooling transition Γ the absorption spectrum basically remains unchanged and is Lorentzian-shaped. This is called 'weak-trapping'. Doppler-cooling as it is understood today takes place in this regime. On the other hand, when $\omega_z \gg \Gamma$ the absorption spectrum develops sidebands at ω_z, which is called 'strong-trapping'. This permits another cooling scheme called 'sideband-cooling'. The different aspects of these regimes are treated in the following paragraphs.

A note concerning the terminology seems in order when talking about 'cooling' a single atom. Temperature is a well-defined term in statistical physics for a large ensemble of particles in thermodynamic equilibrium. This definition certainly does not apply to a single atom, and hence the 'cooling' of a single atom - i.e. reducing its temperature - seems paradoxical. Considering that the term temperature in statistical physics is related to the unordered movement of atoms (their external degrees of freedom) the inappropriate use nonetheless is retained. One simply has to bear in mind that equating the kinetic energy of a single atom with $k_{\mathrm{B}}T$ is a crutch to relate the abstract quantum mechanics to the daily experience of statistical physics.

Doppler cooling

The absorption of a single photon by an atom is accompanied by the transfer of the momentum $\hbar\vec{k}$ from the photon to the atom, where $\vec{k}$ is the wave vector of the exciting light field. When the atom then emits a photon by spontaneous emission, it looses the same

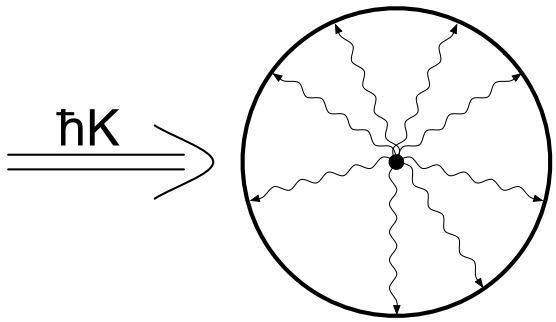

Figure 2.5: Momentum transfer from the laser light field to the atomic system.

amount of momentum as recoil, but in a random direction (assuming isotrope distribution of the density of electro-magnetic field modes). For many absorption and emission cycles the change of momentum for the atom is given by

$$\Delta\vec{p} = \hbar \sum \left(\vec{k}_{\text{abs}} + \vec{k}_{\text{em}} \right). \tag{2.27}$$

As the direction of the emitted photons is random the net recoil momentum is zero

$$\left\langle \sum \vec{k}_{\text{em}} \right\rangle_t = 0, \tag{2.28}$$

and the time-averaged momentum imparted on the atom becomes

$$\langle \vec{p} \rangle_t = \hbar \sum \vec{k}_{\text{abs}}. \tag{2.29}$$

This situation is depicted in Figure 2.5. Now all that has to be done is to create a situation in which the ion absorbs photons only when it is counter-propagating the light field. The momentum transfer is then always directed against the momentum of the ion, and accordingly slows it down.

For a trapped particle that is oscillating in a (harmonic) potential with a frequency ω_z and the line-width of the light field $\Gamma \gg \omega_z$ the frequency of the light field is modulated by the movement of the particle (assuming $\vec{k} \cdot \vec{v} \neq 0$). By choosing a detuning of the laser frequency that is lower than the unmodified atomic resonance frequency the atom and the light field come closer to resonance when the atom is moving towards the laser beam, i.e. anti-parallel to $\vec{k}$. Therefore, when the ion is moving towards the laser beam the chance to absorb photons is enhanced, and it is slowed down. When it moves away the resonance condition is not fulfilled and the chance to absorb a photon is reduced. This detuning is called 'red' detuning of the laser frequency, as red light has a lower frequency than blue light. Accordingly, when the laser frequency is set above resonance that setting is called

'blue' detuning. In terms of energy for red detuning the laser photon does not have enough energy $h\nu$ to excite the ion, but the energy difference is supplied by the kinetic energy of the ion. The ion emits on average the photons at its full energy, and thus dissipates kinetic energy into the surroundings.

The lowest temperature that can be reached via Doppler cooling is limited by the randomness of the spontaneous emission process. The ion does a random walk in momentum space, and for many emission cycles the mean momentum transfer is zero. But on the scale of a single absorption and emission process the momentum of the ion is indetermined to within $2\hbar\vec{k}$, in other words, the ion has a fluctuating rest kinetic energy. This can be seen as a heating process concurring with the cooling process, and the final temperature reached is the equilibrium between the two. This temperature limit - called the Doppler-limit or Doppler-temperature - is determined by a single parameter, the line-width of the cooling transition:

$$E_{\mathrm{Doppler}} = \frac{\hbar\Gamma}{2} \quad \left(\stackrel{!}{=} k_{\mathrm{B}} T_{\mathrm{Doppler}}\right). \tag{2.30}$$

This Doppler limit is reached for a detuning of the laser frequency of [Balzer, 2003]

$$\Delta = -\frac{\Gamma}{\sqrt{3}}. \tag{2.31}$$

For the case of $^{172}\mathrm{Yb}^{+}$ with $\Gamma/2\pi = 19.8\,\mathrm{MHz}$ this results in a temperature of $T_{\mathrm{Doppler}} \approx 1\,\mathrm{mK}$.

Absorption spectrum

We now turn to the second regime of laser cooling where $\Gamma \ll \omega_z$. This case is called 'strong trapping'. When the oscillation frequency is higher than the transition line-width sidebands in the absorption spectrum become resolvable. An example is a weak optical quadrupole transition [Appasamy, 1997]. In this regime, the internal dynamics are comparatively slow and hence the spatial position of the ion changes an appreciable amount during the absorption of a photon. Consequently, the frequency of the laser light field as seen by the ion is modulated.

A prerequisite is the Doppler cooling of the ion, such that the oscillatory movement of the ion can be developed around its equilibrium position: $\zeta(t) = \zeta_0 \sin\omega_z t$. The kinetic energy of the ion is

$$E_{\mathrm{kin}} = \frac{1}{2} m |\vec{v}|^2 = \frac{1}{2} m \omega_z^2 \zeta_0^2, \tag{2.32}$$

and the Doppler-shift becomes $\vec{v} \cdot \vec{k}$, where $\vec{k}$ is the wave-vector of the laser light field. Assuming a monochromatic sinusoidal light field with frequency ω_{L} and amplitude E_0 the

modulated electric component of the field takes the form [Appasamy, 1997]

$$E(t) = E_0 \exp\left(i\omega_{\mathrm{L}} t + k\zeta_0 \sin\left(\omega_z t\right)\right). \tag{2.33}$$

This term is expressible in form of Bessel functions [Appasamy, 1997]:

$$E(t) = E_0 \sum_{n=-\infty}^{+\infty} J_n(k\zeta_0) e^{i(\omega_{\mathrm{L}} + nk\zeta_0)t}. \tag{2.34}$$

This expression is a superposition of infinitely many monochromatic waves forming a frequency comb with constant frequency difference $k\zeta_0$, whose relative amplitudes are weighted by the Bessel function. The excitation spectrum of the ion irradiated by this frequency comb thus is a sum of weighted Lorentzian profiles, one for each frequency component. In practice the modulation index $k\zeta_0$ is small and it suffices to take into account the sidebands to order $N > k\zeta_0$. The excitation spectrum thus becomes [Balzer, 2003]

$$I(\delta_{\mathrm{L}}) = \sum_{n=-N}^{N} |J_n(\eta)|^2 \frac{1}{\pi} \frac{\Gamma'/4}{(\delta_{\mathrm{L}} - n\omega_z)^2 + (\Gamma'/2)^2}. \tag{2.35}$$

δ_{L} denotes the detuning of the laser frequency from the Bohr frequency of the optical transition, and $\Gamma'^2 = \Gamma^2 + 2\Omega_{\mathrm{R}}^2$ is the power broadened line-width of the transition, with Ω_{R} the Rabi-frequency of the light field. The modulation index η is just the Lamb-Dicke-parameter introduced in Eq. 1.5, used here as a classical parameter.

Figure 2.6 depicts a spectrum for the case of three different values of η. The graph illustrates an experimentally relevant case of micro-motion, where the oscillation frequency is not a secular trap frequency, but rather an oscillation at the much higher trap drive frequency of $\Omega = 21\,\mathrm{MHz}$. Thus, Ω takes on the role of ω_z in the examples before. The calculation simulates the fluorescence spectrum received by a scan of the repump laser at 935 nm, as actually performed in Sec. 3.1.5. The line-width of the repump transition is $\Gamma = 2.7\,\mathrm{MHz}$. Therefore, $\Gamma \ll \omega$ holds and the side-bands can be resolved. In the image, the amplitude is normalized to yield a value of 1 for $\eta = 0$. The parameters are a trap-drive frequency of 21 MHz, $\Omega = 2\pi \cdot 0.5\,\mathrm{MHz}$ and $\Gamma = 2\pi \cdot 2.7\,\mathrm{MHz}$. For the case $\eta = 0$ the spectrum remains unmodulated, a simple Lorentzian line-shape results. The higher values of η illustrate how complicated the spectrum can become, and that the width of the spectrum can increase to many times the natural line-width of the transition. Furthermore, the amplitude decreases significantly with rising η, which is important for the reduction of the micro-motion of the ions and the resulting maximum fluorescence amplitude (see Sec. 2.1.2 and Sec. 3.1.5).

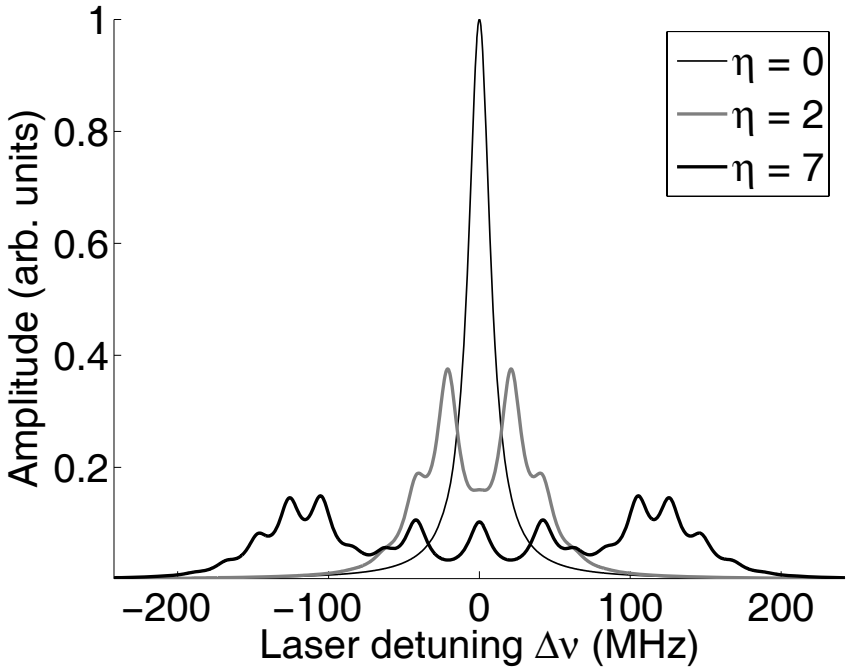

Figure 2.6: Simulated fluorescence spectrum for three different values (0.0, 2.0 and 7.0) of the modulation index (Lamb-Dicke-parameter) η, gained by scanning the repump laser at 935 nm through resonance. The transition rate is modulated by the movement of the ion in the strong trapping regime. The side-bands of the trap drive at 21 MHz are clearly resolved. Parameters: optical Rabi-frequency $\Omega = 0.5\,\mathrm{MHz}$, natural line-width $\Gamma = 2.7\,\mathrm{MHz}$.

Side-band cooling

As mentioned before another cooling scheme exist in the strong trapping regime that relies on the resolution of the sidebands. The main idea is straight-forward: inducing a transition on the side-band both changes the internal state of the ion as well as its external state in the harmonic oscillator. Tuning the laser to the side-band with lower energy reduces the kinetic energy of the ion by one phonon, i.e. one excitation step in the ladder of the quantum harmonic oscillator. When the ion decays back to the former state by spontaneous emission the chances for a carrier transition are distinctly higher than for a spontaneous side-band transition, which does not change the external state. This process can be seen analogous to an anti-Stokes Raman transition. The ion has the same internal state as before, with the harmonic oscillator energy reduced.

Relevant for practical purposes is the cooling rate attainable with side-band cooling. As the line-width of the electro-magnetic transition needs to be smaller than the oscillation frequency of the ion in the trapping potential its inverse - the life-time of the upper

state - often is high. Accordingly, it takes a while for the spontaneous emission to occur. The natural line-width of the transition therefore is a measure for the maximum rate at which phonons can be annihilated. A way to increase the cooling rate is to couple the upper state to another level that rapidly decays back to the ground state (more accurately: back to the starting level, which usually is the same) [Roos, 2000]. The attainable temperature basically has no lower bound except the zero-point energy $1/2\hbar\omega_z$ of the harmonic oscillator. Temperatures were experimentally realized with a ground-state population $> 99.9\%$ [Roos et al., 1999, Rohde et al., 2001]. Using the effective LDP induced by a magnetic gradient field as proposed in Sec. 2.4.2 a side-band cooling scheme for RF- or MW-radiation seems feasible [Wunderlich et al., 2005].

2.2.2 Optical pumping

The initialization of the qubits is one preliminary for quantum information experiments. All quantum information algorithms start from a well-defined state of the participating qubits. Although an obvious demand, it is nonetheless experimentally not apparent that it is always met. For NMR experiments, e.g., it is not possible at all to prepare a pure state, rather a statistically mixed ρ with an abundance of the desired initial state is prepared. Also for the experiments performed in our lab with the ^{171}Yb isotope - where pure states are the rule - the initial state preparation currently has an error of approximately 5%. A solution allowing for a 100% pure initial state has been proposed and is currently being implemented [Balzer et al., 2006].

For qubits in ion traps the initialization relies on an process called optical pumping. A Zeeman sub-level of a given state is selectively populated by choosing an appropriate polarization of the laser light that is driving an optical transition. Figure 2.7 illustrates the process for the case of the $D_{3/2}$ level used throughout this thesis. Every transition between different (non-degenerate) energy levels induced by electro-magnetic radiation is characterized by the angular momenta involved, those of the two energy levels of the atomic system, and that of the laser light field. A transition without a change of angular momentum (Δm_j or $\Delta m_F = 0$) is called a π-polarized or linearly polarized transition. A transition with Δm_j or $\Delta m_F = +1$ (i.e. when the atomic angular momentum is increased) is called σ^+ or right circular, if the atomic angular momentum is decreased (Δm_j or $\Delta m_F = -1$) it is called σ^- or left-circular.

Experimentally, the type of transition is determined by the relative angle between the external magnetic field causing the Zeeman splitting and the polarization of the light field. For linearly polarized light that is parallel to the magnetic field ($\vec{E} \parallel \vec{B}$) the π-polarized

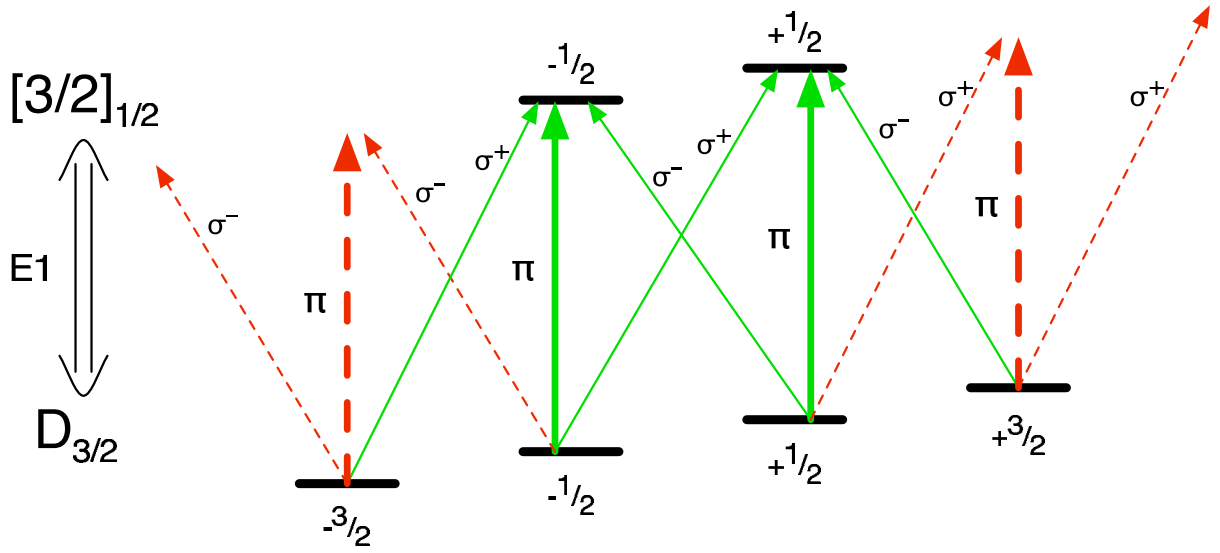

Figure 2.7: Illustration of optical pumping of the $m_j = \pm 3/2$ sub-levels of the $D_{3/2}$ state of $^{172}Yb^+$.

transitions are driven. For right- (left-) circular polarized light the σ^+ (σ^-) transitions are selected. A special case is linearly polarized light perpendicular to the external magnetic field ($\vec{E} \perp \vec{B}$). In this case the linearly polarized light can be viewed as a superposition of both left- and right-circular polarized light, and thus both σ^+ and σ^- transition are driven at the same time.

m_j	-3/2	-1/2	+1/2	+3/2
-1/2	1	$\sqrt{2/3}$	$\sqrt{1/3}$	-
+1/2	-	$\sqrt{1/3}$	$\sqrt{2/3}$	1

Table 2.1: Numerical values for the Clebsch-Gordon coefficients of the $P_{1/2} \rightarrow D_{3/2}$ transitions.

For the case of the $D_{3/2}$ level that is coupled by a laser light field to the jK-coupled $[3/2]_{1/2}$ level all three different polarizations lead to optical pumping, but each pumps different levels. For clarity we concentrate on just the case of π-polarized light. The Zeeman sub-levels of the $D_{3/2}$ are populated by a decay from the $P_{1/2}$ level (see Figure 2.8). The relative strength of population is given by the Clebsch-Gordan-coefficients for the $P_{1/2} \rightarrow D_{3/2}$ transition, listed in Table 2.1. If the ion decays into the $m_j = \pm 1/2$ states a π-photon at 935 nm transfers the ion into the $[3/2]_{1/2}$ state, from where it rapidly and with a high probability decays back into the $S_{1/2}$ ground-state. But if the ion decays into the $m_j = \pm 3/2$ states a photon with σ polarization would be needed to bring the ion into

the $[3/2]_{1/2}$ level. As the laser polarization is selected not to contain σ-polarized light, the $m_j = \pm 3/2$ levels are left uncoupled, and the ion thus remains in its state. It is this process that is called optical pumping of the $|D_{3/2}, m_j = \pm 3/2\rangle$ states. After several cooling cycles through the $D_{3/2}$ branch the $|D_{3/2}, m_j = \pm 3/2\rangle$ states have been populated with almost certainty. This is the qubit initialization used in this work. The exact value of the pumping time will be estimated in the experimental part in Sec. 5.3.

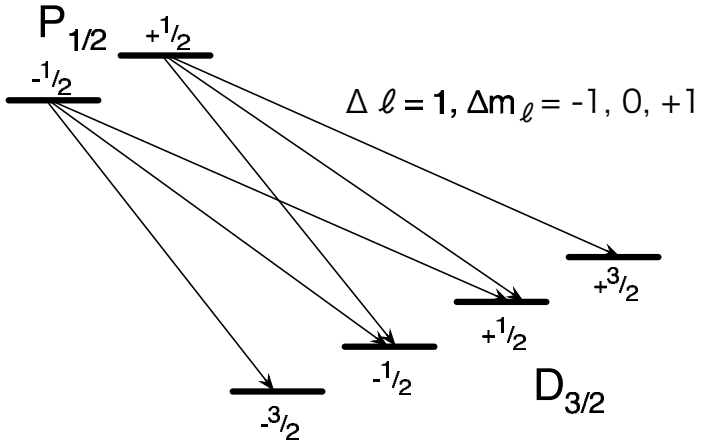

Figure 2.8: Visualization of the Clebsch-Gordon-coefficients for the $P_{1/2} \rightarrow D_{3/2}$ transition that determine the relative population of the different Zeeman sub-levels of the $D_{3/2}$ level. The photon carries an angular momentum $\ell = 1$ which can be oriented along the quantization axis as $m_\ell = 0, \pm 1$.

As a consequence of the optical pumping, the cooling cycle is interrupted and the resonance fluorescence of the $S_{1/2} \rightarrow P_{1/2}$ transition vanishes. If the polarization of the laser light field is not perfectly linearly polarized a rest probability for the excitation of the σ transitions remains, which is visible as a fluorescence signal. This fact will be used later on to optimize the optical pumping and hence the qubit initialization for the experiments. Furthermore, when the optical pumping is optimized $\vec{E} \parallel \vec{B}$. A measurement of the polarization of $\vec{E}$ thus allows for the spatial characterization of $\vec{B}$, a fact that will be extensively used in Sec. 5.2.

2.3 RF radiation: incoherent measurements and coherent interaction

When describing the interaction of electro-magnetic radiation with an atom the distinction between the coherent or incoherent form is quite important. The difference between the two is the time-scale of decoherence destroying the phase relation between the levels. Ignoring in a first step scattering events with background gas atoms, the main source of decoherence is spontaneous emission. For an optical dipole transition the spontaneous emission rate is on the order of tens of megahertz, resulting in very short coherence times. For a Zeeman-splitting in the radio-frequency domain though the rates for spontaneous transitions are negligible, and hence the decoherence induced by this channel is negligible as well. This is one important reason why hyperfine-structure levels in the micro-wave domain and Zeeman sub-levels are held to be the future qubit in ion trap quantum computing. The coherence between the electro-magnetic field in that regime and the atomic state today poses no experimental challenge.

One aim with the gradient scheme is to replace the optical methods required so far for quantum computing with MW- or RF-equivalents. In order to be able to work with the experimentally more accessible ^{172}Yb isotope we examine the Zeeman sub-levels of the $S_{1/2}$ and $D_{3/2}$ state of the $^{172}Yb^{+}$ isotope as possible qubit candidates in Sec. 2.3.1. In this thesis both coherent and incoherent spectroscopy of the Zeeman sub-levels are performed to demonstrate the possibilities of the gradient scheme. Sec. 2.3.2 present the theory for the coherent interaction between only one RF-radiation field and the ion. This form of spectroscopy is used to characterize the dynamical magnetic fields. With the incoherent spectroscopy, a optical dipole transition is used as a spontaneous process to intentionally destroy the phase relation between the different energy levels. This is described in Sec. 2.3.3. This type of spectroscopy allows for the characterization of the static magnetic fields used throughout this work, and specifically for the magnetic field gradient.

2.3.1 Possible qubits

One way to implement a qubit in ytterbium-ions is the hyperfine-structure of the ^{171}Yb isoptope. The odd number of constituents of the nucleus leads to a nuclear spin $I = 1/2$ and a resulting hyperfine splitting of 12.6 GHz between the levels $|S_{1/2}, F = 0\rangle$ and $|S_{1/2}, F = 1\rangle$. As this splitting is much larger than the line-width of the energy levels or of the cooling laser transition only one level is resonantly coupled to the Doppler-cooling cycle. The other level is thus optically pumped by off-resonant excitation, breaking the cooling

cycle and interrupting the detected fluorescence. In order to depopulate the $|S_{1/2}, F = 0\rangle$ level microwave radiation at 12.6 GHz is coupled into the trap and resonantly closes the cooling cycle. Such a setup is called a double-resonance spectroscopy. The hyperfine-qubit has excellent characteristics as it exhibits almost no spontaneous emission and therefore a negligible decoherence rate. It basically doesn't couple to the environment, resulting in an unmatched coherence stability for a qubit [Hannemann, 2002].

Nonetheless, all these advantages come at a price. The ^{171}Yb isotope is experimentally very challenging, as the line-width of the ground state of 1.8 MHz is very small [Balzer, 2003]. Accordingly, the cooling rate is low, making it difficult to effectively cool the ion to the Doppler limit, a preliminary for quantum information experiments. We therefore decided to use a different type of double-resonance spectroscopy that allowed us to work with the ^{172}Yb isotope, as a first step to demonstrate the ability to address ions individually in a string of ions. Here, the Zeeman sub-levels of the $D_{3/2}$ state in the ^{172}Yb isotope split up in an external magnetic field. An appropriate RF-field can then be used to spectroscopically investigate the resulting transition between different m_j-levels [Koerber, 2003].

In the following the possibilities offered by the $S_{1/2}$ and $D_{3/2}$ levels of the ^{172}Yb isotope to act as a magnetically sensitive are considered. First, the two energy diagrams for the two levels are presented. We discuss how to selectively populate certain states by optical pumping and give a rough estimate for the expected fluorescence scattering rate as an important parameter for the cooling and detection of the ions.

Qubit in the $S_{1/2}$ state

The relevant energy levels are the $S_{1/2}$ and the $P_{1/2}$ as shown in Figure 2.9. As the even isotope has no nuclear spin ($I = 0$) and a hydrogen-like electron structure (closed Xe configuration plus one extra electron with ground state $S_{1/2}$) the total angular momentum of the ion is defined by the single outer electron. Accordingly, the $S_{1/2}$ and the $P_{1/2}$ both have $j = l + s = 1/2$, with $l = 0$ and $s = 1/2$ for the $S_{1/2}$, and $l = 1$ and $s = -1/2$ for the $P_{1/2}$. The magnetic moment of the ion is orientated in an external magnetic field and splits into two components corresponding to $m_j \pm 1/2$. The energy difference between the two m_j states is given by

$$\Delta E = g_j \mu_B B. \tag{2.36}$$

For the $S_{1/2}$ level $g_j = 2$, and with $\mu_B = 9.274 \cdot 10^{-24}\mathrm{Am}^2$ the splitting expressed in units of the Larmor-frequency is $\Delta E/h = 2.8\,\mathrm{MHz/G}$. The main idea now is to use σ-polarized light at 369 nm to achieve optical pumping into either $m_j = +1/2$ or $m_j = -1/2$, depending on

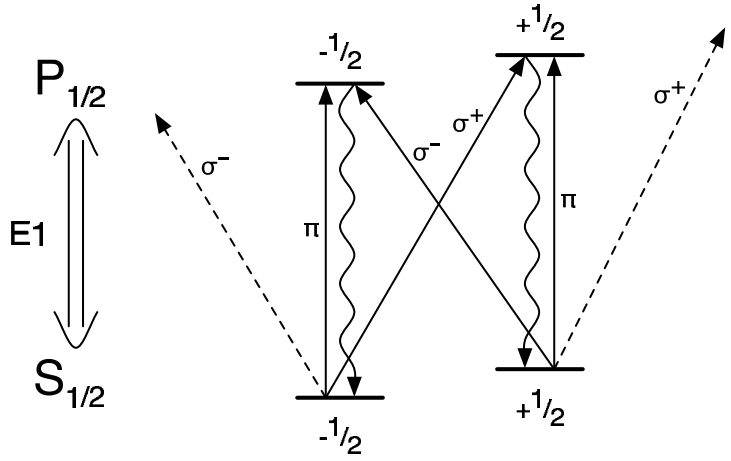

Figure 2.9: Zeeman-splitting and laser transitions of the ^{172}Yb isotope in an external magnetic field.

the orientation of the polarization. This optical pumping is in analogy to the population of the $S_{1/2}, F = 0\rangle$level in the ^{171}Yb isotope by off-resonant excitation.

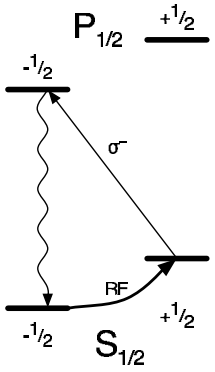

Figure 2.10: Main branch of the cooling cycle for the RF-spectroscopy of the $S_{1/2}$ level

The optical pumping breaks the Doppler-cooling cycle and thus interrupts the detected fluorescence. This cycle can be closed again by inducing transitions between the two Zeeman sub-levels of the $S_{1/2}$ state with a RF-field at exactly the Larmor frequency (Figure 2.10. The ion is transferred from the $m_j = -1/2$ to the $m_j = +1/2$ state, and another cooling cycle begins. The Clebsch-Gordan coefficients for the decay into either $m_j = \pm 1/2$ from the excited $P_{1/2}$ state are just 1/2, and therefore need not be taken into account for the fluorescence rate. This also means that it takes only 3 photons on the average to optically pump the ion into a dark state. The resulting fluorescence rate is thus limited by the speed of the RF-transition, as for every third photon at 369 nm this transition needs to

be driven. The Rabi-frequency is the appropriate measure for this transition rate. As will be shown in Sec. 3.4.2 the expected Rabi-frequency is on the order of several tens of kHz. Even with a factor of two this compares most unfavorable with the usual fluorescence rate of 60 MHz. Accordingly, this transition is not pursued further for our purposes.

Zeeman sub-levels of the $D_{3/2}$ state

Alternatively, the Zeeman sub-levels of the $D_{3/2}$ can be used as well for our purposes of demonstrating the addressing of individual ions. The relevant energy levels for this system have already been presented as Figure 2.7 in Sec. 2.2.2. In order to simulate a two-level qubit we subsume the outer levels with $m_j = \pm 3/2$ as the qubit $|0\rangle$ state, and the inner levels with $m_j = \pm 1/2$ as the qubit $|1\rangle$ state.

Using π-polarized light only the $m_j = \pm 1/2$ levels are coupled back to the cooling cycle by the laser near 935 nm via the $[3/2]_{1/2}$ state (cf. Sec. 2.2.2). As before the optical pumping of the $m_j = \pm 3/2$ levels interrupts the fluorescence cycle, and the resonance fluorescence stops. Inducing rf-transitions between the $m_j = \pm 3/2$ and the $m_j = \pm 1/2$ levels couples the levels back to the cooling cycle, and resonance fluorescence resumes. The absolute value of m_j can thus be detected by the presence or absence of resonance fluorescence.

To completely calculate the resulting fluorescence rate for a closed cooling cycle is not as straight-forward as before. As a start though, the branching ratio of the $P_{1/2}$ level into the $D_{3/2}$ level together with the expected Rabi frequency of the RF-transition gives a first estimate. The branching ratio of the $P_{1/2}$ level is $Q_{P\to D} = 0.00483$ [Yu & Maleki, 2000], which means that after $1/0.00483 \approx 207$ photons at 369 nm a RF-transition needs to occur to close the cooling cycle. Assuming a) a Rabi frequency and hence a RF transition rate of 50 kHz and b) an immediate decay back into the $S_{1/2}$ level we arrive at a fluorescence rate on the order of $207 \cdot 50$ kHz, or 10.4 MHz. Even though a factor of six less than the normal fluorescence rate of 60 MHz (see Appendix B) this is still encouraging, as a signal should be detectable. Usually from a single ^{172}Yb ion about 30 kHz of photons are collected, yielding for the case of RF-spectroscopy a detected fluorescence rate of 5 kHz per ion. As will be shown the realized fluorescence rate with RF-spectroscopy on these levels is even higher.

In conclusion, the $D_{3/2}$ state is a promising candidate for the addressing measurements. It allows to use the ^{172}Yb isotope for the first steps of the gradient scheme instead of the experimentally more cumbersome ^{171}Yb isotope. In the following, the basic characteristics of incoherent and coherent spectroscopy on this level structure are examined.

2.3.2 Four-level dynamics: Bloch equations

In order to calculate the dynamics of the ion during the interaction with a radio-frequency radiation field it is necessary to take into account all four Zeeman sub-levels of the $D_{3/2}$ state. In textbooks the formalism restricts itself to two energy levels to obtain the optical Bloch equations (OBE), which are then solved, yielding the time-evolution of the system. We therefore need to modify the formalism to include all four levels. This modification of the OBE orients itself at the textbook approach and will be presented in the following. First, the atomic Hamiltonian and the Hamiltonian describing the interaction between the ion and the radiation field are presented. The rotating-wave approximation (RWA) is applied. Using an unitary transformation into the reference frame co-rotating with the radiation frequency the time-dependence of the Hamiltonian is eliminated. The resulting Bloch equations are then numerically solvable. The value of the Rabi-frequencies and their role in the illustrative picture of Rabi-oscillations conclude this section. The literature used for this calculation are [Cohen-Tannoudji et al., 1999a, Cohen-Tannoudji et al., 1999b] and [Cohen-Tannoudji et al., 1998] as textbooks, and the Ph.D. theses of Timo Körber [Koerber, 2003] and Christoph Balzer [Balzer, 2003].

Bloch-equations for $j = 3/2$

The interaction between the ion and the radio-frequency field will be treated in a semi-classical manner. The degeneracy of the Zeeman sub-levels of the $D_{3/2}$ state is lifted by an external static magnetic field, chosen to be along the z-axis. The ion with its discrete energy levels $|m\rangle$ is then described by its density matrix

$$\rho = \sum_{m,m'} \rho_{mm'} |m\rangle\langle m'|. \tag{2.37}$$

The ion is irradiated by a classical radio-frequency field, whose magnetic component is perpendicular to the static magnetic field:

$$\vec{B} = \begin{pmatrix} B_x \\ B_y \\ B_z \end{pmatrix} = B_{\mathrm{rf}} \begin{pmatrix} \cos \omega_{\mathrm{rf}} t \\ 0 \\ 0 \end{pmatrix}. \tag{2.38}$$

A note is in order concerning the spatial variation of $\vec{B}$, which has already been neglected in Eq. 2.38. Usually, a electro-magnetic wave would be described as $\vec{B}(\vec{x}, t) = \vec{B}_0 \cos(\vec{k} \cdot \vec{x} + \omega t + \varphi)$, where $\vec{k}$ is the wave-vector defining the spatial direction of the wave, and φ is the phase of the field. The spatial spread of the Doppler-cooled ion and

hence $\vec{x}$ is small in comparison to the wave-length of the used RF-radiation, such that the value of $B(\vec{x}, t)$ can be considered constant over the spatial extension of the ion. The term $\vec{k} \cdot \vec{x}$ thus becomes a constant phase factor, which - together with φ - can be neglected in the physical discussion. Doing so is called the dipole approximation, which will be assumed for the rest of this section. For the gradient scheme this term will become relevant, and Sec. 2.4.2 shows the calculation when this dipole approximation is not applied.

The whole system is then described by a Hamiltonian comprising two parts, one for the atomic energy and one for the interaction:

$$H = H_0 + H_{\text{int}}. \tag{2.39}$$

The time-evolution of the system follows the von Neumann equation:

$$i\hbar\dot{\rho} = [H, \rho]. \tag{2.40}$$

In order to solve Eq. 2.40 the Hamiltonians H_0 and H_{int} are now calculated and transformed into the rotating frame to eliminate the time-dependence of H.

H_0 is simply given by

$$H_0 = \hbar \sum_{m=-3/2}^{+3/2} \omega_m |m\rangle\langle m|. \tag{2.41}$$

m denotes the m_j of the different Zeeman sub-levels of the $D_{3/2}$ state. From here on the index j is dropped, as we only treat the $j = 3/2$ case of the $D_{3/2}$ level. The exact values for the ω_m depend on the selection of the zero point of energy.

For the optical Bloch-equations the interaction is given by the electric dipole moment of the ion, i.e. $\vec{d} \cdot \vec{E}$. Here, the interaction is described by the energy of the magnetic dipole moment of the ion, which looks formally the same:

$$H_{\text{int}} = \sum_{m,m'} \langle m' | \, \vec{\mu} \cdot \vec{B} \, | m \rangle. \tag{2.42}$$

The dipole moment μ is proportional to the angular momentum J of the ion, connected by the Landé-factor g (or the gyro-magnetic ratio γ, as $\hbar\gamma = g\mu_{\text{B}}$ [Haken & Wolf, 2004]). Remembering Eq. 2.38 the dipole moment is rotating around the x-axis, and

$$\vec{\mu} \cdot \vec{B} = \mu_x \cdot B_{\text{rf}} \cos\omega_{\text{rf}} t = \langle m' | g\mu_{\text{B}} J_x | m \rangle \cdot B_{\text{rf}} \frac{1}{2} \left(e^{i\omega_{\text{rf}} t} + e^{-i\omega_{\text{rf}} t} \right). \tag{2.43}$$

The dipole moment μ_x depends on the exact values of m and m'. The values of the dipole moments will be calculated below. J_x is the x-component of the angular momentum operator, which can be expressed as a combination of the lowering and raising operators:

$$J_x = \frac{1}{2}(J_+ + J_-). \tag{2.44}$$

Inserting Eq. 2.44 into Eq. 2.43 a sum of four terms results. The rotating-wave approximation (RWA) now eliminates two of these terms. In a mathematical view the two terms will be eliminated after the transformation of Eq. 2.43 into the rotating frame. Terms of the form $\exp\{i(\omega_m \pm \omega_{\mathrm{rf}})t\}$ appear, that on resonance become either static, or rapidly oscillate at double the frequency, $2\omega_m$. The oscillations are faster than the relevant time-scale and on the average become very small, such that they can be ignored. A more physically motivated view of the RWA is the association of $e^{+i\omega_{\mathrm{rf}}t}$ with the emission of a photon, and of $e^{-i\omega_{\mathrm{rf}}t}$ with the absorption of a photon ([Cohen-Tannoudji et al., 1998], p. 358). Then the term $J_- e^{-i\omega_{\mathrm{rf}}t}$ describes the situation where a photon is absorbed while at the same time the ion is lowered. This situation has a negligible chance of occuring and is consequently ignored. The same holds for the inverse situation $J_+ e^{+i\omega_{\mathrm{rf}}t}$. Regardless of the view, the interaction Hamiltonian in rotating-wave approximation explicitly becomes

$$H_{\mathrm{int}} = \frac{\hbar}{2} \begin{pmatrix} 0 & \Omega_{12} e^{i\omega_{\mathrm{rf}}t} & 0 & 0 \\ \Omega_{21} e^{-i\omega_{\mathrm{rf}}t} & 0 & \Omega_{23} e^{i\omega_{\mathrm{rf}}t} & 0 \\ 0 & \Omega_{32} e^{-i\omega_{\mathrm{rf}}t} & 0 & \Omega_{34} e^{i\omega_{\mathrm{rf}}t} \\ 0 & 0 & \Omega_{43} e^{-i\omega_{\mathrm{rf}}t} & 0 \end{pmatrix}, \tag{2.45}$$

where the Rabi-frequency Ω_{ij} has been introduced as a measure for the strength of the coupling between the electro-magnetic field and the atomic (magnetic) dipole. For clarity the indices m and m' were relabeled, with $-3/2 \to 1, \ldots, +3/2 \to 4$. In the two-level system there is just one Rabi-frequency, which at the same time is the frequency of the so-called Rabi-oscillations. In the four-level case (in fact for arbitrary $j \neq \frac{1}{2}$) the Rabi-frequencies for the different transitions ($1 \to 2, 2 \to 3$, etc.) may differ (see Eq. 2.43). Their exact values as well as the modification of the Rabi-oscillations are discussed below.

The problem is now solved in a reference frame co-rotating with the radio-frequency field. The explicit calculation of the unitary transformation is performed in Appendix A. Here we only state the final Hamiltonian in the interaction picture:

$$\hat{H} = \hat{H}_0 + \hat{H}_{\mathrm{int}} = \frac{\hbar}{2} \begin{pmatrix} -3\delta & \Omega_{12} & 0 & 0 \\ \Omega_{21} & -\delta & \Omega_{23} & 0 \\ 0 & \Omega_{32} & +\delta & \Omega_{34} \\ 0 & 0 & \Omega_{43} & +3\delta \end{pmatrix}. \tag{2.46}$$

Unsurprising, this Hamiltonian looks very similar to the two-level case, except that here the Rabi-frequencies may differ. Inserting this Hamiltonian in Eq. 2.40 yields a set of sixteen coupled linear differential equations as a solution. This set is also explicitly given in Appendix A, which can then be numerically solved.

Different Rabi-frequencies

For the two level case, the frequency at which the dipole is turning is equal to the Rabi-frequency defining the coupling strength. Hence, there is only one Rabi-frequency. As is clear from Eq. 2.43 the Rabi-frequencies $\Omega_{m,m'}$ of the four level case depend on the type of transition, i.e. on m and m', and it is not apparent which frequency is *the* Rabi-frequency. We follow the illustrative approach presented in [Koerber, 2003] and define *the* Rabi-frequency Ω (without index) as the frequency at which the magnetic dipole is turning, and then to relate the different Rabi-frequencies $\Omega_{mm'}$ to it.

The frequency Ω at which the dipole is turning is directly given by

$$\hbar\Omega = \frac{1}{2} g \mu_{\mathrm{B}} B_{\mathrm{rf}}. \tag{2.47}$$

The Rabi-frequencies $\Omega_{mm'}$ are derived from Eq. 2.43 by finding J_x. For $j = 3/2$ the operator is determined to ([Cohen-Tannoudji et al., 1999a], p. 631):

$$J_x = \frac{\hbar}{2} \begin{pmatrix} 0 & \sqrt{3} & 0 & 0 \\ \sqrt{3} & 0 & 2 & 0 \\ 0 & 2 & 0 & \sqrt{3} \\ 0 & 0 & \sqrt{3} & 0 \end{pmatrix}. \tag{2.48}$$

We therefore find for the Rabi-frequencies

$$-3/2 \rightarrow -1/2: \quad \Omega_{12} = \Omega_{21} = \sqrt{3} \cdot \Omega \tag{2.49}$$

$$-1/2 \rightarrow +1/2: \quad \Omega_{23} = \Omega_{32} = 2 \cdot \Omega \tag{2.50}$$

$$+1/2 \rightarrow 3/2: \quad \Omega_{34} = \Omega_{43} = \sqrt{3} \cdot \Omega \tag{2.51}$$

The Hamiltonian in the interaction picture can thus be rewritten as

$$\hat{H} = \frac{\hbar}{2} \begin{pmatrix} -3\delta & \sqrt{3}\Omega & 0 & 0 \\ \sqrt{3}\Omega & -\delta & 2\Omega & 0 \\ 0 & 2\Omega & +\delta & \sqrt{3}\Omega \\ 0 & 0 & \sqrt{3}\Omega & +3\delta \end{pmatrix}. \tag{2.52}$$

2.3.3 Incoherent spectra: Lorentz profiles

As the coherent interaction is more difficult to realize experimentally, the first type of spectroscopy performed with the RF-radiation field and the ion is the simple scan of the frequency of the radiation. The cooling laser at 369 nm is set slightly below resonance,

to cool the ion and to achieve a high resonance fluorescence rate. The repump laser at 935 nm is set on resonance with π-polarization to decouple the $m_j = \pm 3/2$ sub-levels of the $D_{3/2}$ state from the cooling cycle. Figure 2.7 on p.26 depicts the relevant energy levels. The frequency of the RF-radiation is swept through the resonance defined by the Larmor frequency

$$\hbar\omega_{\mathrm{L}} = g_j \mu_{\mathrm{B}} |B|. \tag{2.53}$$

The method is called a rf optical double-resonance spectroscopy [Haken & Wolf, 2004], as both the RF-field and the light field need to be on resonance to achieve a measurable signal.

The resulting line-shape of the observed spectrum is given by a Lorentzian profile

$$I(\omega) = \frac{c}{(\omega - \omega_{\mathrm{L}})^2 + (\Lambda/2)^2}, \tag{2.54}$$

where ω is the frequency of the RF-radiation (in 2π Hz), and Λ determines the overall line-width. The value of the constant c used as an amplitude normalization in Eq. 2.54 is not apparent for the given system, as the observed signal is the resonance fluorescence from the cooling transition at 369 nm. The dependence of this fluorescence from the RF-transitions in the $D_{3/2}$ state has been modeled in a simple rate equation system in Appendix B to estimate the amplitude. Eq. 2.54 is illustrated in Figure 2.11.

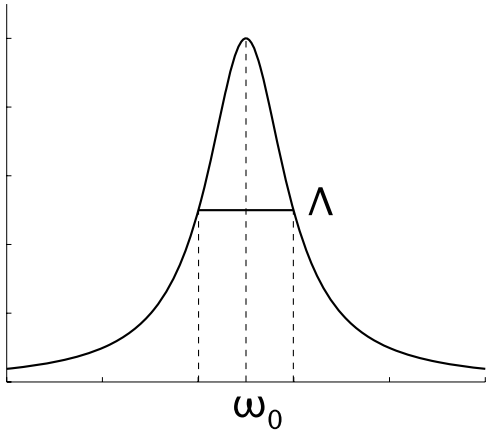

Figure 2.11: Spectrum of the cooling fluorescence with rf-optical double-resonance spectroscopy. The Lorentzian line-shape has a line-width given by $\Lambda = 2\sqrt{\Gamma_{\mathrm{rf}}^2 + \Gamma_{935}^2}$.

The line-width comprises several contributions given by

$$\Lambda = 2\sqrt{\Gamma_{\mathrm{rf}}^2 + \Gamma_{935}^2 + (2\pi/\tau)^2}. \tag{2.55}$$

The life-time of the $D_{3/2}$ level is $\tau = 52.2\,\mathrm{ms}$ [Balzer, 2003], and the resulting contribution to the line-width of 3 Hz will be neglected from here on. Thus the line-width of the Lorentzian profile is governed by the transition rates Γ_{rf} and Γ_{935}. The former denotes the rate of depopulation of the $m_j = \pm 1/2$ levels, induced by the rf-radiation. The latter describes the depopulation of the $m_j = \pm 1/2$ levels by the repump laser at 935 nm. For two-level systems, these rates are equal to the respective Rabi-frequencies of the magnetic or electric dipole. The repump laser with π-polarization couples only two levels, but does this twice: the $m_j = -1/2$ levels of the $D_{3/2}$ and the jK states form one electric dipole, the $m_j = +1/2$ levels the other. It is therefore expected that indeed $\Gamma_{935} = \Omega_{935}$, where Ω_{935} is the optical Rabi-frequency characterizing the coupling strength of the repump laser.

The derivation of the line-width due to the interaction with the rf-radiation field is not as straight-forward because $\Gamma_{\mathrm{rf}} \neq \Omega_{\mathrm{rf}}$. As the discussion about the Rabi-frequencies in Sec. 2.3.2 showed the actual coupling strengths between the different Zeeman sub-levels deviate from the Rabi-frequency describing the rotating magnetic dipole. A mathematically thorough solution would include finding the analytical expression for the population evolution of each sub-level with different m_j. For the simple two-level case, in [Cohen-Tannoudji et al., 1999a] this analytical expression is then integrated together with an exponential decay to find the steady-state solution for different excitation frequencies of the radiation field. A result is the exact expression for the line-width of the Lorentzian profile. This calculation is left to be desired for future work though.

Here, a physically motivated heuristic ansatz shall suffice. Regarding the $m_j = -1/2$ sub-level of the $D_{3/2}$ state, it is de-populated by rf-induced transitions into both the $m_j = -3/2$ and the $m_j = +1/2$ levels. The first assumption now made is that these two rates add like other independent transition rates, such that

$$\Gamma_{\mathrm{rf}} = \sqrt{(\Gamma_{-1/2\to-3/2})^2 + (\Gamma_{-1/2\to+1/2})^2}. \tag{2.56}$$

The second assumption is the association of the transition rates with the specific Rabi-frequencies Eq. 2.49 - Eq. 2.51 calculated in Sec. 2.3.2, such that

$$\begin{aligned} \Gamma_{\mathrm{rf}} &= \sqrt{(\sqrt{3}\Omega_{\mathrm{rf}})^2 + (2\Omega_{\mathrm{rf}})^2} && (2.57)\\ &= \sqrt{7}\Omega_{\mathrm{rf}}. && (2.58) \end{aligned}$$

It is therefore expected that the resulting line-width caused by the rf-interaction with a four-level system is a factor of $\sqrt{7} \approx 2.65$ larger than for a two-level system, and the resulting line-width becomes

$$\Lambda = 2\sqrt{7\Omega_{\mathrm{rf}}^2 + \Omega_{935}^2}. \tag{2.59}$$

2.4 Interaction with the magnetic gradient field

The static magnetic gradient field is the central element of this thesis. The experimental scheme presented in the following paragraphs offers advantages to distinctly reduce the experimental complexity of quantum computing experiments in linear ion traps. Two aspects are examined. First, the ions can be addressed by simply changing the frequency of the exciting radiation, instead of focusing a laser beam onto the ions. The exact procedure as well as a discussion of the error induced in other ions is detailed in Sec. 2.4.1. The interaction of the ions with the magnetic gradient field furthermore leads to a coupling of the internal and external dynamics of the ions. The calculations and implications of a new, effective Lamb-Dicke-parameter are outlined in Sec. 2.4.2.

2.4.1 Ion addressing

The spatially varying Zeeman-splitting of the energy levels leads to a spatial dependence of the RF resonance frequency. Figure 2.12 illustrates this idea for the $S_{1/2}$ level, assuming a static linear magnetic gradient in the z-direction.

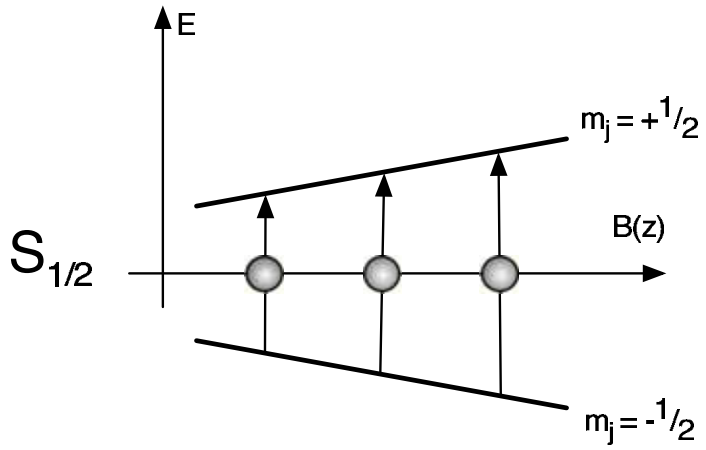

Figure 2.12: Addressing the ions with a magnetic gradient $B(z)$.

The Larmor-frequency is proportional to the absolute value of $B(z)$:

$$\omega(z) = \Delta E/\hbar = \frac{\Delta m_j g_j \mu_B |B(z)|}{\hbar}. \tag{2.60}$$

For a linear magnetic gradient of $\partial_z B = 1\,\mathrm{T/m}$ and with $g_j = 2$ for the $S_{1/2}$ level this leads to a spatial variation of the Larmor-frequency of

$$\partial_z \omega = 2\pi \cdot 28\,\mathrm{kHz/\mu m} \tag{2.61}$$

Accordingly, for the $D_{3/2}$ state with $g_j = 4/5$ the frequency gradient is

$$\partial_z \omega = 2\pi \cdot 11.2\,\mathrm{kHz/\mu m}. \tag{2.62}$$

The value for the gradient of 1 T/m is appropriate for the experiments of this work (see also Sec. 5.4). Assuming a small inter-ion distance of 5 µm even on the $D_{3/2}$ level the resulting frequency shift of approximately 56 kHz is ample to individually address the ions with a RF-field on the carrier transition. Figure 2.13 exemplary shows the resulting fluorescence spectrum for incoherent excitation calculated for realistic experimental parameters.

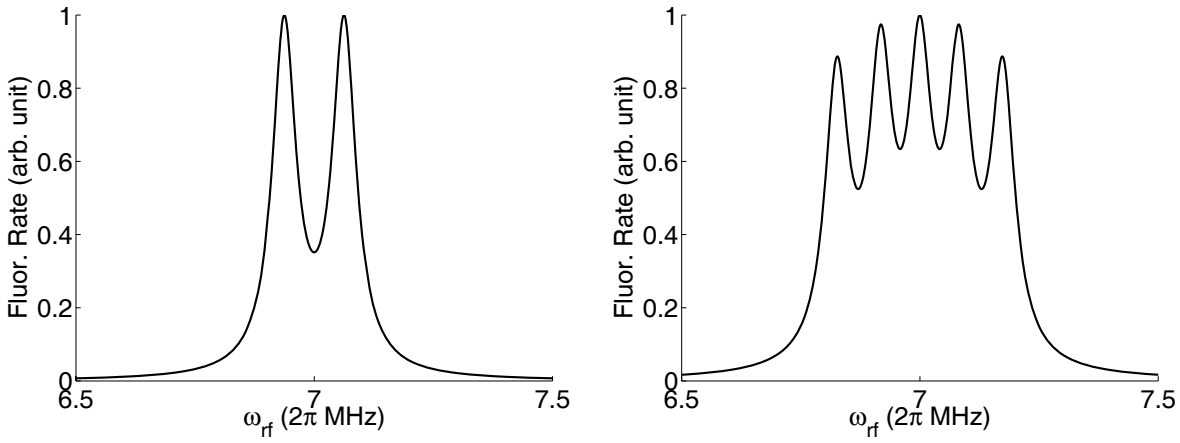

(a) Two ions

(b) Five ions

Figure 2.13: Calculated fluorescence spectra (for incoherent excitation) for two (a) and five (b) ions in a magnetic gradient field of 0.5 T/m. The inter-ion distance is evaluated from the axial secular frequency $\omega_z = 2\pi \cdot 60$ kHz. The line-width of each single profile is assumed to be 60 kHz. The static magnetic field is calculated from a given center frequency of the whole spectrum of 7 MHz.

An important question arising is the residual off-resonant excitation of ions other than the one being currently addressed. Ideally, the state of one and only one ion is manipulated by a rf-pulse. Experimentally, due to the Lorentz-profile of excitation (Sec. 2.3.3) there always exist a rest probability of excitation for all ions. This is not a drawback of the gradient addressing scheme alone, the optical addressing by a tight laser focus deals with similar problems. In the gradient scheme, ions next to the ion currently being addressed interact with the same field amplitude due to the long wave-length of the radiation, but with a large detuning in frequency space. For optical addressing the situation is reversed: the ions interact on resonance, but with a distinctly smaller field amplitude.

In order to quantify the error a quality factor has been defined for the optical addressing scheme that is the ratio of the two Rabi-frequencies resulting for the addressed and the neighboring ion [Gulde, 2003]. This magnitude is inconvenient for the gradient addressing scheme, as the effective (or generalized) Rabi-frequency $\Omega_{\text{eff}} = \sqrt{\Omega^2 + \Delta^2}$ is dependent upon the detuning Δ, and hence a ratio $\Omega_{\text{neighbour}}/\Omega_{\text{resonance}}$ is not a sensible criterion. We therefore define the maximum off-resonant excitation probability of a two-level system

$$\epsilon_{\text{err}} = \frac{\Omega_{\text{res}}^2}{\Omega_{\text{res}}^2 + \Delta^2} \tag{2.63}$$

as the error criterion for the gradient addressing scheme. Ω_{res} is the Rabi-frequency on resonance valid for the addressing ion, and Δ is the detuning from resonance of the neighboring ion due to the magnetic field gradient.

Usually, Eq. 2.63 would be used to quantify the error for a given set of experimental settings, like strength of the magnetic field gradient and the Rabi-frequency on resonance. The value of the gradient defines the frequency splitting of the resonances, and the Rabi-frequency the line-width of the transition. On the other hand, the Rabi-frequency is proportional to the square-root of the intensity of the rf-radiation, and thus an easily adjustable experimental parameter. The demand for an upper bound of ϵ_{err} is therefore equal to an upper bound for the Rabi-frequency of the addressing ion given by

$$\Omega_{\text{res}} \leq \frac{\Delta}{\sqrt{1/\epsilon_{\text{err}} - 1}}. \tag{2.64}$$

If, for example, the error should be no larger than 1% ($\epsilon_{\text{err}} < 10^{-2}$) then $\Omega_{\text{res}} \leq \Delta/\sqrt{99} \approx 0.1\Delta$.

It is informative to insert the values for different settings. In this work the maximum gradient achieved is approximately 0.5 T/m. For the $D_{3/2}$ state and an inter-ion distance of 25 µm this yields a splitting of 130 kHz, limiting the Rabi-frequency to 13 kHz for an error below 1%. Assuming the calculated maximum gradient achievable with the current experimental setup of 2 T/m this value is quadrupled to 52 kHz. In the long run the aim is to use the $S_{1/2}$ level of the ^{171}Yb isotope. With a gradient of 2 T/m this increases the maximum Rabi-frequency by a factor of $g_{\text{S}}^{171}/g_{\text{D}}^{172} = 5/2$ to 130 kHz. Decreasing the inter-ion distance for the odd isotope to 10 µm then reduces this number again to 52 kHz, and accordingly to 26 kHz for 5 µm. It should be noted that currently the maximum Rabi-frequency for the $^{171}Yb^+$ ion is on the order of 10 kHz. The next-generation gradient design will allow for gradients of 100 T/m. From the values above it becomes clear that the Rabi-frequency will then - for all practical purposes - not be limited by the finite frequency difference between the ions.

Another point worth mentioning is the development of pulse shaping techniques in the NMR community to counter exactly the given problem of erroneous excitation. In liquid-state NMR quantum computing the frequency resolution to address single spins of the molecule can be on the order of several tens of Hz (!). This is realized by so-called 'soft' or 'shaped' pulses (see [Vandersypen, 2001] and references therein), where an amplitude envelope ramps the amplitude of the exciting rf-field up and down, e.g., in a Gaussian profile. Briefly, by Fourier reasoning the pulse length is given by the inverse of the frequency resolution. For small separations of the resonance frequencies (like 20 Hz) the pulse length will be inconveniently long for quantum computation. With a detuning, though, of several tens of kHz for two arbitrary ions this remains a feasible approach to decrease the residual excitation in our gradient scheme of ion trap quantum computing.

We have developed in our group a versatile frequency generator (described in Sec. 3.5) that allows for very fast phase and amplitude switching and ramping, which can be used for such pulse shaping experiments. The implementation is out of the scope of this work though, but first steps are already being taken at the ring-trap experiment present in our lab. Taking together the values expected for the Rabi-frequencies and the possibility to almost completely avoid erroneous excitation by pulse shaping techniques, the conclusion can be drawn that the scheme presented in this section permits easy and error-free (to arbitrary precision) addressing of ions for quantum computation in linear ion traps.

2.4.2 Coupling internal and external dynamics

The section presents the calculations for the new, effective Lamb-Dicke-parameter (LDP) η_{eff} that is induced by the interaction of the ions with the static magnetic gradient field. The unmodified LDP is defined as the ratio of the spatial spread Δz of the ground-state wave-function of the ion to the wave-length λ of the exciting radiation:

$$\eta = \frac{2\pi}{\lambda}\Delta z = k\Delta z. \tag{2.65}$$

Here, $(\Delta z)^2 = (\Delta X)^2 = \hbar/2m\omega_z$ is the spread of the ground-state wave-function of a quantum harmonic oscillator with oscillation frequency ω_z, and m the mass of the ion [Cohen-Tannoudji et al., 1999a]. Another - for our purposes more illustrative - picture is the momentum view. The LDP η is the relative strength of the momentum of a electromagnetic photon $\hbar k$ in comparison to the momentum of the quantum harmonic oscillator, i.e.

$$\eta = \frac{\hbar k}{2\Delta P}, \tag{2.66}$$

where $(\Delta P)^2 = \frac{1}{2}m\hbar\omega_z$ is the spread of the ground-state wave-function in momentum space. Graphically speaking, the LDP gives an estimate for the chance that the momentum of the electro-magnetic photon is enough to both excite the internal dynamics (i.e. the absorption of the photon by the ion) and at the same time change the state of the quantum harmonic oscillator. This is the same as saying that an absorption of a photon on a motional sideband occurs. These sideband transitions are of special importance for quantum information processing in linear ion traps, as the basal c-Not gate by *Cirac* and *Zoller* [Cirac & Zoller, 1995, Monroe et al., 1995] is based on just such a sideband transition to entangle the two ions.

Inserting the appropriate values for micro-wave or radio-frequency radiation in Eq. 2.66 shows that $\eta < 10^{-7}$, and hence side-band transitions are not possible. This is an important reason why so far the proposals for conditional quantum information processing (i.e. involving two qubits) in ion traps were restrained to optical methods. One main aspect of the gradient scheme discussed and implemented in this work is the emergence of an effective new LDP that is distinctly higher than without the magnetic gradient. With it, all optical methods available for quantum information processing in ion traps become feasible with RF- or MW-radiation, which considerably simplifies the experimental aufwand for coherent manipulation of the qubits.

The Hamilton operator for this situation reads very similar to Eq. 2.39:

$$H = H_0 + H_{\text{osc}} + H_{\text{int}}, \tag{2.67}$$

where H_0 denotes the internal energy of the ion, and H_{int} the interaction energy of the exciting radiation. The apparent difference to Eq. 2.39 is H_{osc}, the energy in the external oscillator potential. But the terms H_0 and H_{int} themselves contain differences. The internal energy H_0 is now dependent on the position of the ion (cf. Eq. 2.41):

$$H_0 = \hbar \sum_{m=-3/2}^{+3/2} \omega_m(z)|m\rangle\langle m| = \hbar\omega(z)J_z. \tag{2.68}$$

The Larmor-frequency $\omega(z)$ is given by Eq. 2.60. The position operator X can be replaced by $X = \Delta z(a^\dagger + a)$, such that

$$z = \zeta X = \zeta\Delta z(a^\dagger + a). \tag{2.69}$$

ζ is the expansion coefficient of the displacement of the ion in terms of the normal mode coordinate, i.e. a factor of how much the ion participates in a given oscillation mode (see

also Sec. 2.1.3, Eq. 2.24). Then $\omega(z)$ is expanded to first order in z around the equilibrium position $z = 0$:

$$\omega(z) = \omega_0 + \zeta \Delta z (a^\dagger + a) \cdot \frac{g_j \mu_\mathrm{B}}{\hbar} \partial_z |B|. \tag{2.70}$$

Inserting Eq. 2.70 into Eq. 2.68 yields

$$H_0 = \hbar\omega_0 J_z + \zeta \Delta z (a^\dagger + a) g_j \mu_\mathrm{B} \partial_z |B| J_z \tag{2.71}$$

Using the energy of the harmonic oscillator in its standard form $H_\mathrm{osc} = \hbar\omega_z a^\dagger a$ the first two terms of Eq. 2.67 become

$$H_0 + H_\mathrm{osc} = \hbar\omega_0 J_z + \hbar\omega_z a^\dagger a + \hbar\omega_z \kappa (a^\dagger + a) J_z, \tag{2.72}$$

where

$$\kappa = (\zeta \Delta z g_j \mu_\mathrm{B} \partial_z |B|) \frac{1}{\hbar\omega_z} \tag{2.73}$$

has been introduced as a convenient definition. The last term of Eq. 2.72 is a coupling energy between the internal state J_z and the external dynamics described by $(a^\dagger + a)$ that will give rise to the new, effective LDP. It is useful to eliminate this explicit coupling of the external and the internal dynamics from Eq. 2.72 by transforming into the basis shifted by $S = \frac{1}{2}\kappa(a^\dagger - a)J_z$. Applying the unitary transformation $\tilde{H} = e^S H e^{-S}$ and dropping constant terms we find

$$\tilde{H}_1 = \hbar\omega_0 \tilde{J}_z + \hbar\omega_z \tilde{a}^\dagger \tilde{a}, \tag{2.74}$$

where the transformed operators are given by

$$\tilde{a} = a - \frac{1}{2}\kappa J_z, \tag{2.75}$$

$$\tilde{a}^\dagger = a^\dagger - \frac{1}{2}\kappa J_z, \tag{2.76}$$

$$\tilde{J}_+ = J_+ e^{\kappa(a^\dagger - a)}, \tag{2.77}$$

$$\tilde{J}_- = J_- e^{-\kappa(a^\dagger - a)}. \tag{2.78}$$

Turning to the interaction energy H_int, it is basically the same as Eq. 2.43, except that now the dipole approximation (see remark below Eq. 2.38) is not applied to retain the spatial information of $\vec{B}$. Remembering Eq. 2.65, $\vec{k}\cdot\vec{x}$ can be expressed as $\vec{k}\cdot\vec{x} = \eta(a^\dagger + a)$, and

$$H_\mathrm{int} = \frac{1}{2} g \mu_\mathrm{B} (J_+ + J_-) \cdot B_\mathrm{rf} \left[e^{i(\eta(a^\dagger + a) - \omega_\mathrm{rf} t)} + e^{-i(\eta(a^\dagger + a) - \omega_\mathrm{rf} t)} \right]. \tag{2.79}$$

This Hamiltonian is now first transformed into the 'gradient' reference frame $e^S H_\mathrm{int} e^{-S}$. Replacing the operators in Eq. 2.79 with Eq. 2.75 - Eq. 2.78 yields

$$\tilde{H}_\mathrm{int} = \frac{1}{2}\hbar\Omega \left(J_+ e^{\kappa(a^\dagger - a)} + J_- e^{-\kappa(a^\dagger - a)} \right) \cdot \left[e^{i(\eta(a^\dagger + a - \kappa J_z) - \omega_\mathrm{rf} t)} + e^{-i(\eta(a^\dagger + a - \kappa J_z) - \omega_\mathrm{rf} t)} \right]. \tag{2.80}$$

Ω is the Rabi-frequency defining the magnetic interaction strength. In the next step the time dependence is eliminated from Eq. 2.80 by the usual transformation into the interaction picture, while terms oscillating at $\pm(\omega_{\mathrm{rf}}+\omega_0)$ are neglected (rotating-wave approximation). The terms are rearranged in a longish calculation, remembering that $X = (a^\dagger + a)$ and $P = (a^\dagger - a)$, and using $e^X \cdot e^P = e^{1/2[X,P]} \cdot e^{X+P}$. Terms of the form

$$e^{i[(\eta+i\kappa)a+(\eta-i\kappa)a^\dagger]} \tag{2.81}$$

appear, that already show the new, effective LDP. $\eta' = \eta+i\kappa$ is a complex number, that can be decomposed in its absolute value and a phase. We define, therefore, the new, effective Lamb-Dicke parameter as

$$\eta_{\mathrm{eff}} = \sqrt{\eta^2 + \kappa^2}. \tag{2.82}$$

The phase can be incorporated - together with the other remaining constant phases - into the initial conditions for J_+. The result is the usual interaction Hamiltonian, where the LDP η has been replaced by the new, effective LDP:

$$\tilde{H}_{\mathrm{int}} = \frac{1}{2}\hbar\Omega\left(J_+ e^{-i\eta_{\mathrm{eff}}(a^\dagger+a)} e^{-i\delta t} + \mathrm{H.c.}\right), \tag{2.83}$$

where $\delta = \omega_{\mathrm{rf}} - \omega_0$ is the detuning of the radiation frequency from the atomic resonance.

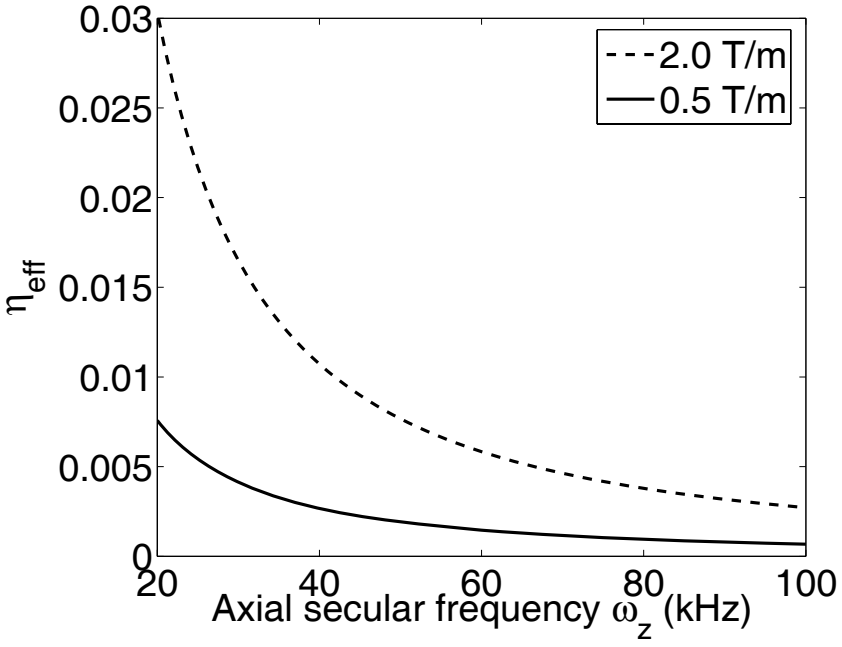

Figure 2.14: Effective Lamb-Dicke-parameter under variation of the axial secular frequency ω_z.

Figure 2.14 shows the calculation of $\eta_{\mathrm{eff}} = \sqrt{\eta^2 + \kappa^2} \approx \kappa$, with κ given by Eq. 2.73. η_{eff} is plotted against the axial secular frequency ω_z. Two graphs for different values of the

magnetic field gradient are shown. These values are experimentally realistic. The graphs show the current need to work at low ω_z in order to achieve an appreciable η_{eff}, due to the experimentally limited value of the gradient. At lower ω_z though, a value of $1.5 - 2 \cdot 10^{-2}$ is within experimental reach.

This new term η_{eff} has far-reaching implications. As stated above, the value of η (as defined in Eq. 2.66) is negligible, which is the reason why so far MW- or RF-radiation could not be used for quantum computing experiments in ion traps. Applying a magnetic gradient field κ (as defined in Eq. 2.73) takes on an appreciable value, coupling the internal and the external dynamics of the ion. Side-bands in the spectrum appear, and coherent side-band transitions are possible. This allows for side-band cooling with micro-waves and entanglement of two ions. In other words, all operations that required optical radiation thus far can now be replaced by MW- or RF-radiation. This is experimentally a distinct advantage, as it simplifies the experimental complexity, and renders ion trap quantum computing more scalable.

. . . we are not experimenting with single particles, any more than we can raise Ichthyosauria in the zoo.

Erwin Schrödinger

3

Trapping single Yb^+ ions

In the 1950-ies the idea of isolating a single atom for study seemed to quite firmly belong to the realm of gedanken experiments. In less then 25 years though this fiction was brought into reality by the deterministic trapping and detection of a single Barium atom by Neuhauser et al. [Neuhauser et al., 1980]. Since then another 25 years have passed, and the trapping of single ions has become standard - which should not be misinterpreted for easy - for many fields of research. The following chapter is devoted to the experimental issues raised in trapping and detecting a single or a few ytterbium ions, as well as to the apparatus used for the manipulation of the ions to perform quantum logic operations. The design and operation of a ion trap heads this chaper (Sec. 3.1), followed by the description of the lasers and optics involved for photo-ionization and laser cooling (Sec. 3.2). The detection systems are detailed in Sec. 3.3, closing the ion trapping part. Zeeman sub-levels are utilized for quantum logic operations, and Sec. 3.4 illustrates the generation of the static and dynamic magnetic fields necessary for the manipulation of these energy levels. Concluding this chapter Sec. 3.5 portrays the experimental control by real-time digital signal processing (DSP) and computer interfaces.

3.1 The linear trap

The operation and characterization of the linear trap formed a significant part of the experimental work of this thesis. This section details many of the steps taken during this time and characterizes the trap with its most important parameters.

3.1.1 Design

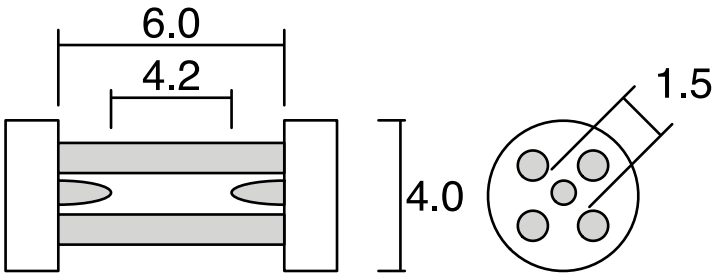

Figure 3.1: Schematic drawing of the linear trap with dimensions in milimeters. The end-caps have a diameter of 0.4 mm, and the rods a diameter of 0.5 mm (omitted in the figure for clarity).

The linear trap used throughout this thesis was designed and built by Dr. Christoph Balzer. Figure 3.2 depicts the trap before final assembly into the vacuum chamber. Two ceramic plates made of vacuum-compatible Macor mechanically guide the trap electrodes for rigidity and stability. Four longer rod electrodes in quadrupole configuration form the linear trap, radially confining the ions on the symmetry axis. Two endcap electrodes with suitably chosen voltages provide axial confinement. The two Macor plates have a diameter of 4 mm, a width of 2 mm, and are spaced 6 mm apart. The rod electrodes are pieces of Molybdenum wire with a diameter of 0.5 mm. The endcaps are also made from Molybdenum wire, but with a diameter of 0.4 mm. Here, the end segments were rounded off by filing them under a microscope to obtain a cap-like shape. The radial distance R from the middle of the trap to the surface of the rod electrodes is 0.75 mm, influencing the trapping parameter q as shown in Eq. 2.5. The distance between the two endcaps at first was approximately 2.5 mm, which was increased to 4.1(2) mm during the first rebuild. A different experimental aim at the time of the trap design is responsible for the initial small interval between the cap electrodes.

Further elements of the construction are a correction electrode outside the trap volume, an electron gun consisting of a field-emitting needle together with a stainless steel focusing aperture, and the atomic ovens. The latter are described in detail in Sec. 3.1.2. The field-

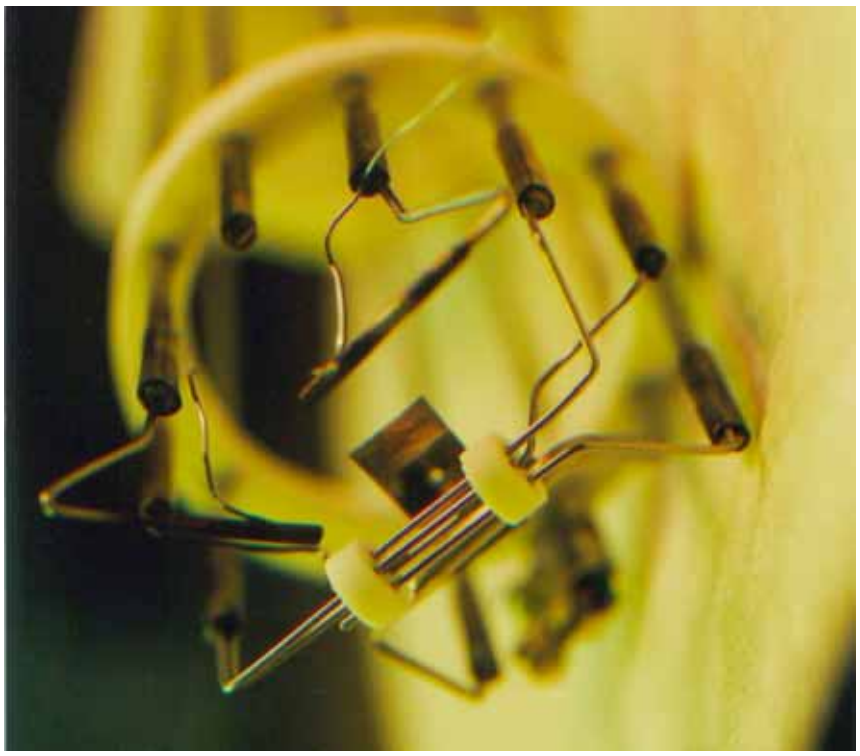

Figure 3.2: Photo of the linear trap before final assembly into the vacuum apparatus. The ovens are not aligned yet.

emitter - being the only means for ionization at that time - was unfortunately never used to trap ions, as the stray potential induced by its operation prohibited stable trapping of ions. Understandably this effect became apparent only after photo-ionization had been introduced to the experiment. The correction electrode seen in Figure 3.2 is a stainless steel electrode 1.6 mm in diameter, spaced 1 mm apart from the nearest rod electrode.

Different electrical setups for the RF trap voltage are possible and have been shown to work [Prestage et al., 1989,Raizen et al., 1992,Nägerl et al., 1998,Molhave, 2000,Lucas et al., 2003]. We chose to supply only two diagonally opposite rods with the high-voltage RF-trapping potential to reduce the number of vacuum feed-throughs necessary. Thus, only one is needed for the trapping potential. Of the two remaining rod electrodes one is grounded inside the vacuum chamber, while the other is connected to a vacuum feed-through and can be used as a second correction voltage. The a-parameter (cf. Eq. 2.5) can be controlled by simultaneously applying a DC-field in addition to the RF trap drive; this was never used though, the a-parameter was kept at zero value for all experiments. Both endcaps are connected to the same vacuum feed-through to ensure the same potential on both. The correction electrode outside the trap volume is connected to its own feed-through. Fur-

thermore, if need be the ovens could be used as correction electrodes as well by applying a suitably chosen voltage (of course without closing the circuit).

To give an estimate of the expected resulting secular frequencies and the q parameter the values above are inserted into Eq. 2.5. Assuming a trap drive frequency of 21 MHz and a RF amplitude of 1 kV a value of $q = 0.114$ is found, which accords to a radial secular frequency of $\omega_r = 2\pi \cdot 850\,\text{kHz}$. For a RF voltage amplitude of 500 V these values decrease to $q = 0.057$ and $\omega_r = 2\pi \cdot 425\,\text{kHz}$. Inserting alternatively a trap drive frequency of 10.25 MHz for 1 kV amplitude $q = 0.48$ and $\omega_r = 1.74\,\text{MHz}$, and for 500 V amplitude $q = 0.24$ and $\omega_r = 870\,\text{kHz}$. The secular frequencies are examined in detail in Sec. 3.1.4.

3.1.2 Ovens

The atom ovens are quite apparently an important part of every ion trap experiment. The ideal oven emits only a minimal number of atoms to avoid spoiling the vacuum, or worse, silvering the glass windows with a metallic layer. Other groups also report such strong coating of the trap electrodes that the trap had to be cleansed. Wanted criteria are therefore a tight atomic beam focused into the ionization volume and an easily controllable flux rate. The formed is usually implemented using extra apertures and small diameter of the oven [Rotter, 2003]. The latter is normally achieved by controlling the temperature of the oven, and hence the vapor pressure of the ytterbium.

Two new techniques were employed that allow for a good characterization of the ovens. This turned out to be especially helpful during the construction of the new ovens. First, the new ionization laser at 398 nm allows for the characterization of the fluorescence from the atomic beam. The wave-length is in resonance with the atomic $^1S_1 \rightarrow {}^1P_1$ transition, and the resulting fluorescence can simply be observed with the normal detection setup. By scanning the laser frequency an excitation spectrum is obtained. The data pertaining to these measurements is presented in Chap. 4.

Second, due to the fact that the vacuum-recipient of this trap is all-glass the ovens are directly observable, which has proven to be another valuable resource of information. Usually the ovens are built into a flange of the steel recipient, where they can't be seen. In our experiment an IR-sensitive CCD-camera (sensitive up to a wave-length of 2 µm) monitors the heating of the ovens by detecting its Planck-spectrum. This additional technique is very helpful in controlling the oven temperature, even if no absolute scale is used. It is especially important for ytterbium where the melting (824 °C) and boiling point (1194 °C) are close together. When the temperature rises a little too high the experimenter risks the sudden evaporation of all remaining metal, thus silvering the trap apparatus. The direct

heat imaging greatly reduces this risk. Last but not least the exact spatial distribution of heat can be determined, revealing critical oven sections.

The ovens were characterized more thouroughly than the simple use to trap ions warranted due to the fact that several basic problems occured, necesciting in the end the opening of the recipient and the rebuilding of the ovens. Therefore both techniques - atomic excitation spectrum and heat imaging - were extensively used before and during the rebuilding process. In this section only the most important results are presented.

The principle of operation of these ovens is direct ohmic heating. Typically a few to several amperes (1-6 A) of current are needed to appreciatively heat the oven, depending on the cross-section of the cylinder and the resistance of the other segments. When the temperature of the oven increases the solid ytterbium starts to melt. The vapour pressure inside the cylinder increases and atomic ytterbium diffuses out through the top opening.

The goals for the new ovens were a small aperture for good beam collimation, thinner tube walls for higher ohmic impedance of the tube itself and a 'cooling' mass connection. If the mass connection is massive enough to rapidly transport the heat from the oven the opening of the tube is cooled, or more accurately, is not heated in the first place. This increases the collimation of the beam as atoms hitting the wall close to the opening will condense on the wall, and only those atoms that travel close to the axis of the cylinder will leave the oven. Furthermore, the mass connection of the old ovens was glowing so brightly that it was creating considerable stray light levels in the detection systems. This would be avoided with cool (or cooler) mass connection as well. The whole setup is similar to the one described in [Rotter, 2003]. Figure 3.3 depicts the new ovens, as a schematic drawing (a), and as a real image (b) taken from the direction of the image-intensified CCD-camera. The wall thickness of the molybdenum tube was reduced to 0.2 mm, with an inner diameter of 0.78 mm, the length of the tube is 12.5 mm. The original mass connection of a small wire (diamter 0.25 mm) was replaced by a piece of tantalum foil ($d = 0.2$ mm) approximately $2 \times 4\,\mathrm{mm}^2$ in size. A molybdenum wire (diameter 2 mm) is spot-welded to the mass connection. The ovens for ^{171}Yb and ^{172}Yb share a common mass connection, their mass wires are spot-welded together.

Figure 3.4 displays the false-color coded IR-images for all three ovens, taken when the ovens were tested for the first time. The ovens are operated at maximum current (7.0 A for (a), 7.5 A for (b) and (c)), which is higher than the current used for trapping ions (approx. 4.8 - 5.5 A). The images are normalized to the maximum intensity. The insets show the main section of each image with the same intensity scale for each (maximum is 2^{15}). Apparently, the ohmic resistance of the natural abundance oven (a) is higher, as it exhibits the hottest temperature at the lowest current. The cool spots on the mass foil of

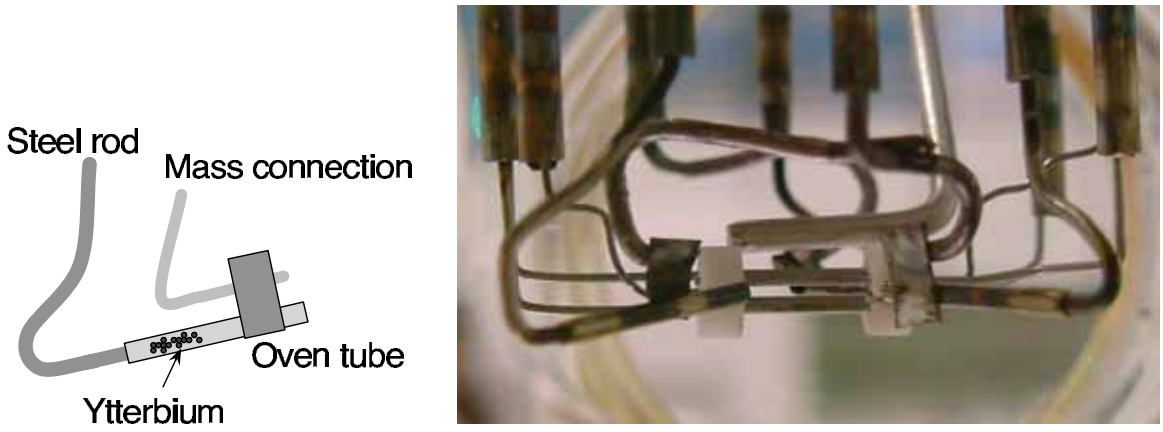

(a) Schematic drawing (b) Picture

Figure 3.3: (a) Schematic drawing of the new ovens for ^{172}Yb and ^{171}Yb. (b) Direct image of the ^{172}Yb oven (left) and the ^{171}Yb oven(right). The third oven with natural abundance ytterbium is visible on the far side of the trap, its opening half hidden by the upper rod electrode.

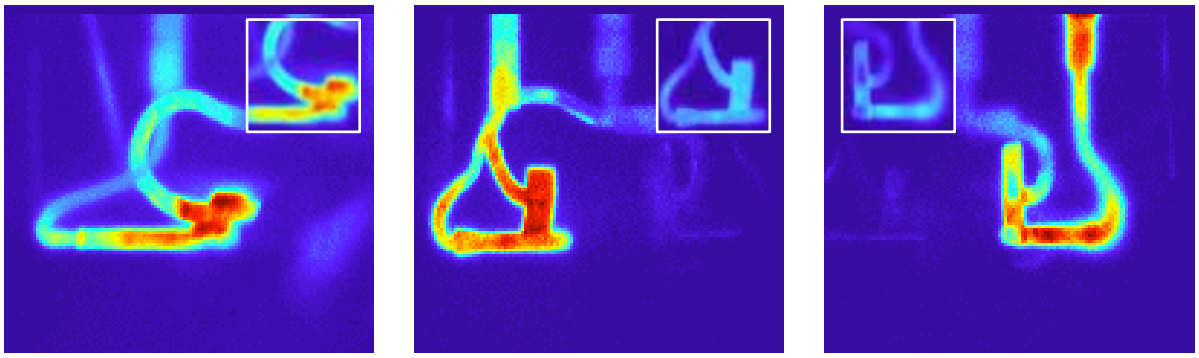

(a) Natural Yb (b) ^{172}Yb (c) ^{171}Yb

Figure 3.4: IR-images of the hot ovens. The images are false-color coded, normalized to maximum intensity. The insets excerpt the ovens main section, all three normalized to 15 bit resolution for direct comparison of the heat. Interestingly, the hottest oven (natural Yb) runs at the lowest current of 7.0 A. The other images were taken at 7.5 A.

the ^{171}Yb oven (c) reveal the welding-spots, which in (a) and (b) are on the far side of the foil. The images reveal that the mass connections have not been designed large enough to be an actual cool part that enhances the collimation of the atom beam. The images underline the usefulness of this technique, which will be employed in the construction process of the next-generation ovens.

3.1.3 Trap drives

Although it is an important technical element of every ion trapping experiment oddly enough no really robust design has emerged for the generation of the high-voltage RF signal that creates the trapping potential. Since the beginning of trapping small clouds and single ions the standard setup employed is a so-called helical resonator that is essentially a *LC*-circuit. The inductance is a solid metal helix which is enclosed by an optionally closed metal cylinder, thus forming the capacitance. While these resonators in principle readily do what they are supposed to (i.e., provide high voltage at radio frequencies), the actual implementation still labors with many problems of mostly indeterministic nature[1]. Time-consuming trial-and-error construction to find the right frequency [Gulde, 2003], sensitive quality factor leading to amplitude fluctuations and degradation of the quality factor over time [Stacey, 2003] are but an excerpt of the available problem list. Several publications present stable and reproducible designs for alternatives to the standard helical resonator, but are limited to approximately 500-600 V [Jones et al., 1997, Jones & Anderson, 2000, Cermaka, 2005].

New resonator design

The following section presents yet another design of a slightly modified helical resonator that has proven itself during the course of this thesis to be experimentally undemanding and stable, while delivering up to 2.0 kV voltage amplitude. The main idea and the construction of several resonators is the work of *Dr. Ivo Polak* of Prague University, whose proficiency in RF-circuitry has been a very valuable resource. The design is so robust that the resonator for 10 MHz was independently constructed in Prague, shipped to Hamburg and immediately worked as specified by simply soldering it to the vacuum-feedthrough connected to the trap electrodes [2].

[1] A fact that often prompted Prof. Neuhauser to exclaim 'Black magic!' every time the resonator did - or did not - work.

[2] The setup in Hamburg took less than 10 minutes, due mainly looking for cable connections and heating the soldering iron to temperature.

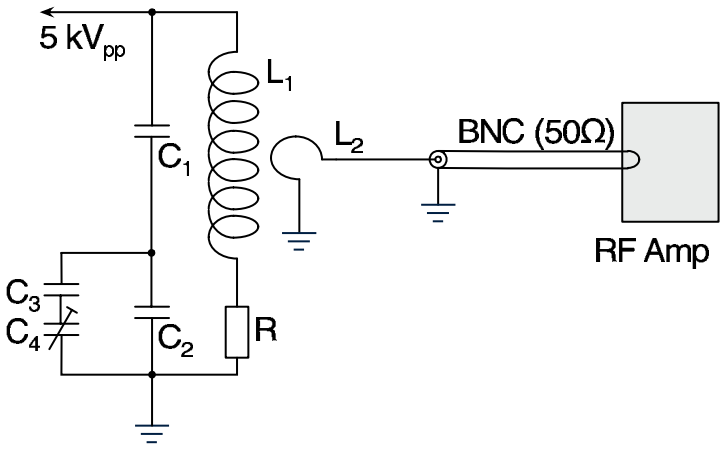

Figure 3.5: Schematic wiring diagram of the new helical resonator ('trap drive'). The ohmic resistance R stabilizes the resonance circuit.

Figure 3.5 depicts the schematic diagram of the resonator. A helical coil with approximately 15 windings (L_1) is situated within a solid copper tube, just as with a standard helical resonator. The input signal is connected inductively to the resonator by a small single-winded coil (L_2). The input coil is mechanically movable to match the impedance of the circuit to 50 Ω. The signal of a frequency generator (SRS 345) is amplified by a standard RF-amplifier (Calmus 110C) and provides up to 10 W of input power. The output circuit further has a variable capacitor to match the impedance of the circuit to the trap load. A resistor of low resistance ($\approx 1\,\Omega$) connects in series to the coil. It is the reason for the claimed stability of this design, and will be elaborated in the following.

Usually, the construction of such a resonance circuit aims at a high quality factor Q to achieve high voltage amplification. For that purpose all real resistances are reduced to a minimum, and especially an explicit resistor as indicated in Figure 3.5 is avoided. The reason for this is simple: first, the resistor strongly decreases the quality factor, necessitating much higher RF-power to reach the same voltage amplitude as without it. Secondly, this RF-power is mostly dissipated by the resistor, which then needs to be actively cooled for the power levels employed in this situation. But the discussion often restrains itself to the possibility of no resistor, or a resistance of 50 Ω [Stacey, 2003].

The main idea for our new design now is to use a low ohmic resistor with just one or a few ohms. The increase in power level as well as the heat-dissipation remains manageable. As an added advantage the lower Q-value decreases the sensitivity of the resonator to frequency fluctuations. But the main advantage is a well-defined impedance of the circuit on resonance. For a perfect LC-circuit the impedance vanishes on resonance, but in

practice line resistance and other stray impedances form a small and often indeterministic impedance, both real and imaginary. We attribute this situation to be - to a large part - the source of the aforementioned problems. On the other hand, when the explicit ohmic resistance is larger than the random impedance fluctuations then the circuit on resonance is largely determined by that resistance, and hence well-defined.

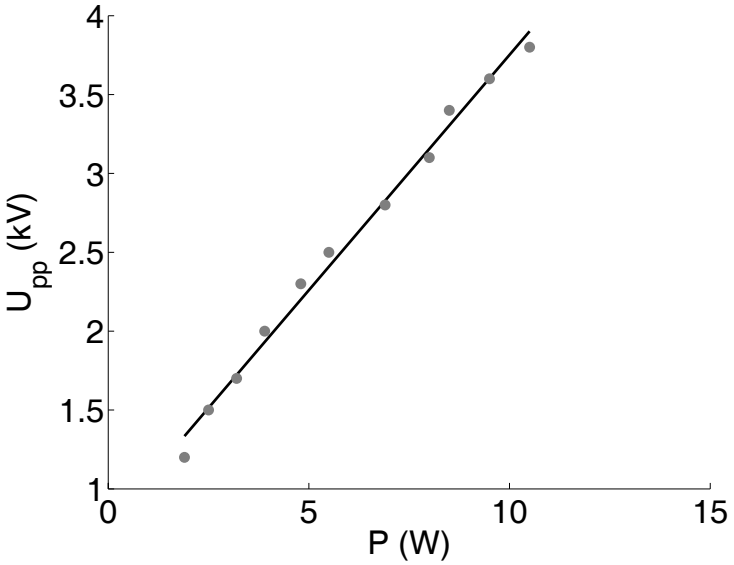

Figure 3.6: Calibration data of the new helical resonator. A maximum voltage of $3.8\,\mathrm{kV_{pp}}$ was attained at 10.5 W.

Both one 'traditional' as well as two resonators of the new design have been in operation for the experiments. The existing resonator has a resonance frequency between 20.5 MHz and 22.5 MHz, slightly adjustable by mechanically stretching or compressing the spring-like helix. This resonator has been described by Ingo Weissgerber [Weisgerber, 2003]. The maximum quality factor measured was 282, with a typical working value of 170. The first resonator of the new design was constructed to allow for the comparison of the two resonators, with a resonance frequency of 22.3 MHz. As the helix resides inaccessibly within the copper cylinder the resonance frequency remained fixed. With the stabilizing ohmic resistance in series the quality factor for this resonator is per definition low and was in fact not measured. Instead, a calibration of the voltage amplitude was performed in Prague by Dr. Polak. A voltage divider (1:100, not shown in Figure 3.5) directs a small portion of the high voltage signal to a scale. The scale was calibrated by Dr. Polak. Using this scale, the resonator was again tested in Hamburg. The data is presented in Figure 3.6. A maximum voltage amplitude of $1.9\,\mathrm{kV} = 3.8\,\mathrm{kV_{pp}}$ was attained at 10.5 W input power. Using Eq. 2.5 and Eq. 2.11 this evaluates to $q = 0.45$ and $\omega_r = 2\pi \cdot 1.52\,\mathrm{MHz}$.

Unfortunately, due to a instability of the trap impedance the highest power levels could not be utilized. It turned out that the trap had an non-negligible ohmic resistance that heated considerably at higher power levels. Consequently, as the voltage could not be increased a second resonator of the new design was constructed for a lower resonance frequency to achieve a tighter confinement of the ions. Both the trap parameter q and hence the radial secular frequencies ω_r depend on the trap drive frequency, with $q \sim 1/\Omega^2$ (see Eq. 2.5 and Eq. 2.11 in Sec. 2.1, pp. 14). The resonator was constructed to work at a approximately half the old value, at 10.25 MHz. Apart from the different size owing to the different resonance frequency the resonator is technically the same as the first resonator of the new design. At full amplitude of 1.9 kV measured above the resulting secular frequencies would be at the stability limit of the a-q-diagram: $q = 0.91$ and $\omega_r = 3.3$ MHz.

3.1.4 Secular frequencies

The secular frequencies of an ion trap are an important experimental characteristic for every ion trap. Not only does the knowledge of these frequencies allow for the determination of the exact RF voltage amplitude reaching the trap electrodes, the frequencies themselves often are important parameters for quantum information processing. The lowest common mode of the ions axial oscillation is used as a 'quantum bus' in the Cirac-Zoller-scheme for the c-not gate. In the gradient scheme presented in this work the effective Lamb-Dicke-parameter arising from the interaction of the ions with a magnetic field gradient is inversely proportional to the axial secular frequency. Last but not least, knowing the axial secular frequency calibrates the image scale (see Sec. 3.3).

Determining secular frequencies

The ions movement in the trap is resonantly excited using a RF-signal at the oscillation frequency. The RF-signal can be produced by a simple antenna (piece of wire, wire loop) or directly applied to the existing trap electrodes. In our case a simple home-made bias-tee mixed the RF-signal with the DC-voltage for the end cap electrodes. The resonance frequency is found by observing either the scalar photo-multiplier signal, or directly the image of the ions with the intensified CCD-camera. Due to the excitation the ions heat up, and the oscillation amplitude becomes so large that the laser cooling is relatively ineffective. This effect is visible as a sharp decline of the resonance fluorescence signal. Alternatively, the large spatial spread is directly visible on the CCD-image. Figure 3.7 exemplary shows the excitation of the axial (a) and radial (b) secular oscillation mode. An advantage of the

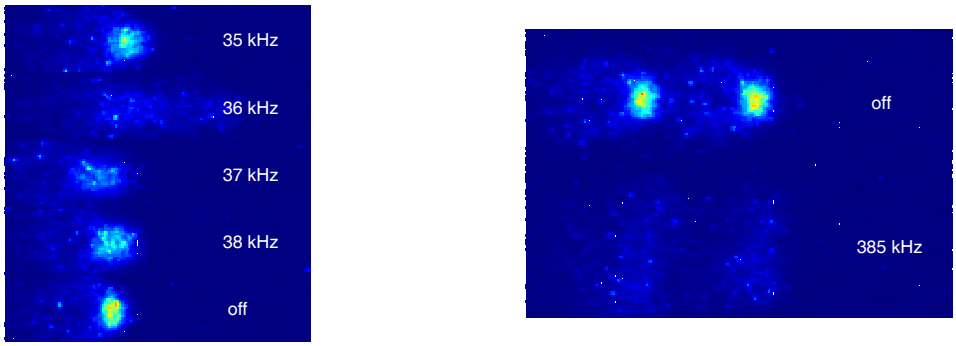

(a) Axial excitation (b) Radial excitation

Figure 3.7: Excitation of the axial (a) and the radial (b) secular frequency.

imaging method is that the direction of oscillation (radial or axial) is directly observable, as is clearly visible in the figure. The frequency of the RF-signal is given directly in the images, indicating a frequency resolution of 1 kHz. Peter Staanum developed a full-fledged formalism for the amplitude of the oscillation and derived sub-kilohertz accuracy from a series of images [Staanum, 2004]. This was not aimed for in this work.

Axial secular frequency

Following Eq. 2.14 the axial secular frequency shows a square-root dependence from the voltage applied to the endcap electrodes, and it is independent of the trap drive amplitude. The independence of the trap depth was verified in several different runs. Figure 3.8 displays the data taken for different endcap voltages U_{Endcap}. The square-root dependence shown in the figure by the solid line appears not unreasonable. Theoretically, this graph should be extensible to lower trap frequencies still, but could not be realized experimentally. It is not understood why no stable trapping regime was found for the lowest axial secular frequencies, but mechanical imperfections of the trap itself are presumed to be the main cause.

Higher axial secular frequencies were not aimed for for two reasons. The lower the axial secular frequency, the larger the spatial separation between two ions. For the addressing scheme implemented with the magnetic gradient field this implies a higher frequency splitting of the ions. In the long run a higher ω_z is desirable for faster gate operation, but for the first experiments with the gradient the low ω_z proved to be advantageous. Secondly,

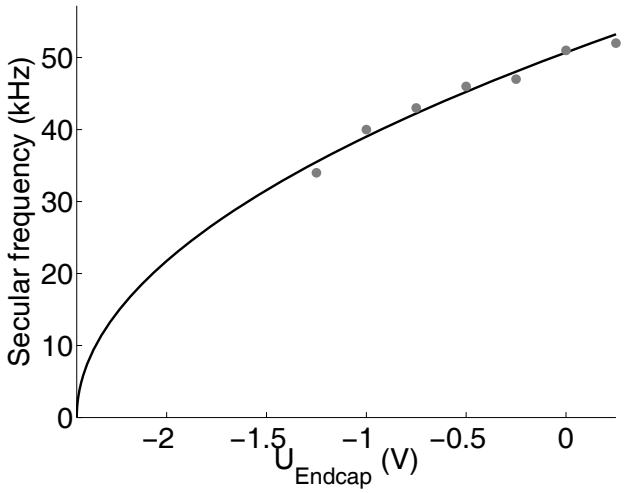

Figure 3.8: Variation of the axial secular frequency in dependence of the end cap electrode voltage. The data (gray dots) is fitted to a square-root dependence (solid line).

the coupling η_{eff} between internal and external dynamics of the ions arising from interaction with the magnetic gradient field (see Sec. 2.4.2) is inversely proportional to ω_z, i.e. the lower ω_z the higher the coupling.

The negativity of the endcap voltages remains unexplained, though. At first, unknown stray potentials were blamed for this unexpected behavior. This effect has been observed in other groups as well [Steane, pc]. On the other hand, numerical simulations performed in our group indicate the principal possibility of trapping ions with negative endcap voltages. For these simulations, the trap potential was evaluated with finite-element methods (FEM), and the equations of motion for a charged particle in this potential were numerically solved. The result shows that negative endcap voltages are just as viable as positive endcap voltages for trapping purposes. The adequate incorporation of these results in a modified set of Mathieu-equations could not be performed in the frame of this thesis though, and is left to be desired for future work.

Radial secular frequency

Assuming an a-parameter of zero the radial secular frequencies ω_x and ω_y are degenerate (see Eq. 2.11), which is denoted by subsuming them as ω_r. In that case the relation between ω_r and the q-parameter is given by

$$\omega_r = \frac{\Omega}{2}\sqrt{\frac{q^2}{2} + a_z}. \tag{3.1}$$

As we are interested in q as a characteristic parameter of the operating trap it is expressed in dependence of ω_r and ω_z:

$$q = \sqrt{8\left(\frac{\omega_r}{\Omega}\right)^2 - 2a_z} \tag{3.2}$$

$$= \frac{2}{\Omega}\sqrt{2\omega_r^2 + \omega_z^2}, \tag{3.3}$$

where the relation $a_z = -2(\omega_z/\Omega)^2$ has been used.

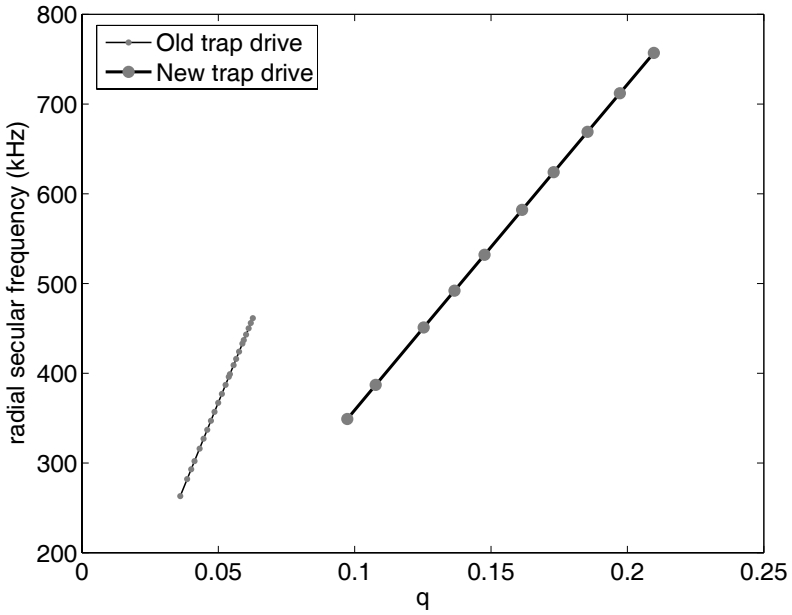

Figure 3.9: Comparison of the measured q values for the old and the new trap drive running at 21 MHz and 10 MHz, respectively. The q values are derived from the measured radial secular frequencies. The data series are connected by straight lines to guide the eye.

Two different trap drives operating at 21 MHz and 10.2 MHz were employed during the course of this work. Both trap drives were characterized by measuring the radial secular frequency under variation of the trap drive amplitude V_0. The maximum voltage amplitude was limited to approximately 500 V due to unexpected trap impedance instabilities. A bend in the wire carrying the RF-signal poses an ohmic impedance that heats up for power levels that are too high. Figure 3.9 illustrates the data by plotting the measured secular frequencies against the value of q as determined by Eq. 3.3. The axial secular frequency ω_z was found to be 64 kHz for both measurement series. The graph clearly shows the need for the lower trap drive frequency of 10.2 MHz to achieve a tighter trapping, when the voltage amplitude is as limited as it is.

3.1.5 Micro-motion

As shown in Sec. 2.1.2 the movement of the ion in the trap potential is a superposition of two oscillations at different frequencies: the oscillation at the frequency of the RF trap drive called micro-motion, and the movement in the so-called pseudo-potential, the secular oscillation. The RF quadrupole potential has a minimum where the electric field vanishes. In case of a Paul trap of ring symmetry this minimum is a single point in space, for a linear trap as employed in this work the minimum is along a straight line. If the ions mean position coincides spatially with this minimum the interaction between the electric field component and the ion vanishes.

For a perfectly symmetric trap the minimum of the quadrupole potential and the position of the ions should always overlap, but construction inaccuracies and residual stray electric fields that are always present in such a trap push the ions away from the center, which increases the amplitude of the micro-motion. These stray potentials arise, e.g., from chemical potentials of different touching metals, like metallic ytterbium deposited from the atomic beams on the molybdenum electrodes. Accordingly, correction potentials are necessary to compensate this effect and to reduce the unwanted micro-motion of the ions. In our linear trap two compensation electrodes are connected explicitly for this purpose (see Sec. 3.1.1) and have proven to be sufficient.

The are several schemes of different and decreasing coarseness (or increasing sensitivity) for the reduction of micro-motion:

1. Position of the ions at different trap depths
2. Sidebands in the laser spectrum
3. RF-correlation spectroscopy

All three methods are used in our lab, though the RF-correlation spectroscopy was employed only at the ring trap, and not at the linear trap. The first method observes the position of the ion under variation of the trap depth. If the ion is perfectly on the symmetry axis of the trap potential, then the position of the ion does not change. On the other hand, if residual static electric fields push the ion away from the center the position of the ion will change with decreasing trap amplitude in the direction of the electric field. This method is a quick way to start on the compensation of micro-motion, and then to proceed with a more accurate method.

The second method relies on the influence the movement of the ion has on the lineshape of the laser resonances. In most experiments the line-width of the cooling laser is too large

to actually resolve single sidebands at the trap drive frequency, which for these traps is on the order of 10-30 MHz. Instead, the lineshape is broadened to a non-Lorentzian form, which in the following can be reduced by observing its change with different compensation potentials [Webster, 2005]. This method is a somewhat rough estimate, though.

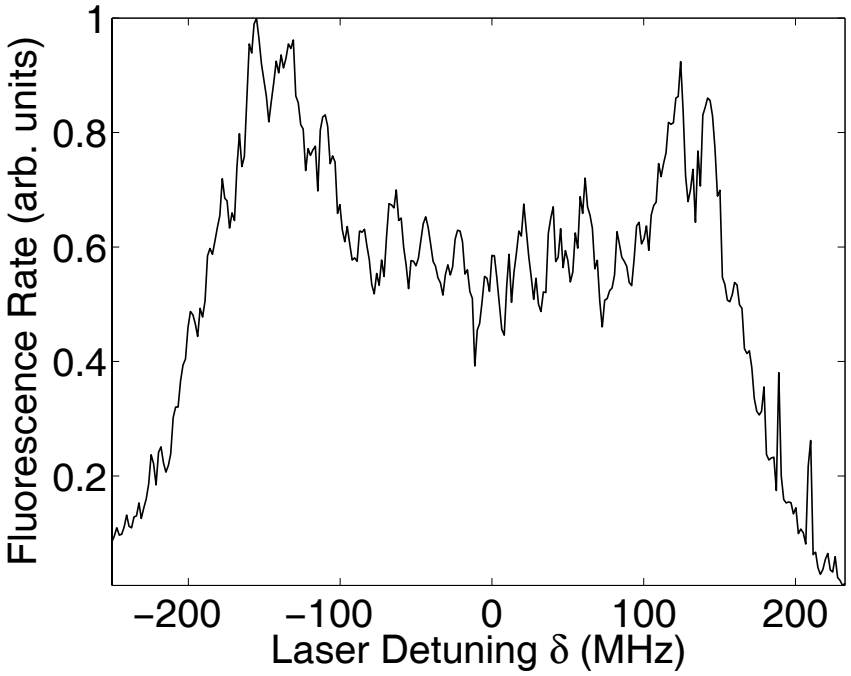

Figure 3.10: Resonance scan of the repump laser at 935 nm to demonstrate excessive micro-motion of the ion.

The ytterbium ion offers the nice advantage that the line-width of the repumping laser at 935 nm is $\Gamma_{935} = 2.7$ MHz, which is clearly below the lowest trap drive frequency employed, at 10.25 MHz. The energy levels and transitions involved are found in Appendix C. When scanning the laser at 935 nm over the resonance the repumping process into the cooling cycle will be more or less efficient, thus increasing or decreasing the fluorescence that is detected at the cooling wave-length of 369 nm. Therefore, the sidebands induced by the micro-motion can be resolved by scanning the repump laser over resonance. Figure 3.10 shows such a scan before any compensation voltages are applied, i.e. with full micro-motion that is present when the ions are trapped for the first time. The power of the 935 nm laser is strongly reduced in the scan to avoid power broadening of the resonance (this is performed empirically until the peaks are resolved acceptably, without measuring the exact power). A plethora of resonances indicate the strong modulation of the ions movement caused by the micro-motion. The modulation index for this spectrum has been estimated by comparison

with calculated spectra to approximately $\eta = 7.5(5)$.

The initial compensation with the first method reduces this 'picket-fence' of resonances to a countable number. Figure 3.11 (a) shows the situation at that point, where the center frequency of the resonance can clearly be inferred, and two sidebands are visible to the left and the right of the resonance. The scans were taken in the linear trap with a trap drive frequency of 20.855 MHz. In sequence the voltage applied to the correction electrode is varied. The main peak of the resonance fluorescence increases continuously while at the same time the sidebands vanish, indicating the reduction of the amplitude of micro-motion. Finally, the lineshape is Lorentzian to a good approximation. The modulation index η is indicated in the images. For the linear trap, this was the best method employed for the compensation of micro-motion.

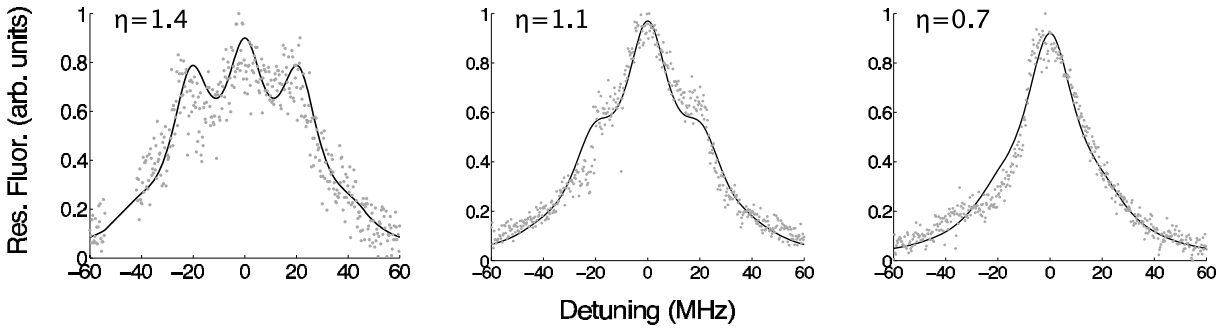

Figure 3.11: Compensation of micro-motion by reduction of motional sidebands in the resonance spectrum of the 935 nm laser. The short breaks in the ions fluorescence in (a) and (b) are quantum jumps into a dark state and back.

Last but not least, the third method for the compensation of micro-motion is the most sensitive. Here, the arrival time of the photons on the photo-multiplier is recorded by a time-to-digital converter (TDC) and compared to the phase of the RF trap drive voltage. If the ions movement is influenced by micro-motion the absorption and emission process of photons by the ion will be modulated at that frequency due to the Doppler effect, i.e. the arrival time of the photons will be correlated to the phase of the RF field. Graphically speaking, the ion will absorb (and hence emit) photons better at the turning point of its oscillation where the velocity is low, and vice versa. Gradually, then, the micro-motion can be reduced by eliminating the correlation peaks in the TDC-spectrum with the appropriate compensation voltages.

This approach has the added advantage that it is slightly more quantitative, as the TDC-spectrum of a perfectly uncorrelated ion is known: it is purely Poissonian. Accord-

ingly, the mean square root of the histogram of the spectrum should equal $\sqrt{N}$, where N is the number of counted photons. Any deviation from the Poissonian distribution will reveal itself by a higher mean square root. It is easy to implement a comparison in the experiment software that compares the calculated mean square root with just $\sqrt{N}$:

$$\sqrt{N} \stackrel{!}{=} \Delta_{\mathrm{msr}} = \sqrt{\sum_{i=1}^{N}(n_i - \bar{n})^2}. \tag{3.4}$$

Here, n_i is the number of photons arriving in time bin t_i, and $\bar{n}$ is the average number of photons per time bin. This analysis allows for a very fine-grained control of the compensation voltages to reduce the micro-motion of the ion.

3.2 Lasers and optics

This section describes the different lasers that have been used in the course of the experiments, as well as several optical components pertaining to the overlay and the shaping of the different laser beams. Three of the four laser systems employed are extended-cavity diode lasers (ECDL), a diode laser at 398.9 nm for photo-ionization, and two repump lasers at 935 nm and 638 nm. The 'main' cooling laser light at 369 nm is generated by frequency doubling the output of a solid-state pumped Ti:Sa laser. Appendix C details the relevant energy level diagram. These systems were first introduced to the experiment by Christoph Balzer, and are described in detail in his PhD thesis. The description here will therefore restrict itself to recapitulating the main characteristics of the laser systems in Sec. 3.2.1 and Sec. 3.2.2. The light fields of the cooling laser and the repump laser at 935 nm pass through an acousto-optical modulator (AOM) for switching on and off, and for setting the power level of the light fields. These components are described in Sec. 3.2.3. Finally, two optical components for the manipulation of the laser beams that have been set up are detailed in Sec. 3.2.4.

3.2.1 Diode lasers

398 nm

The light from the laser at 398 nm photo-ionizes the atoms. It is a commercial ECDL system by Toptica that includes temperature, current and grating voltage controls. The diode has a free-running wave-length of 398.8 nm and can consequently be operated at room-temperature (20 °C). Even though a frequency control module is present the laser

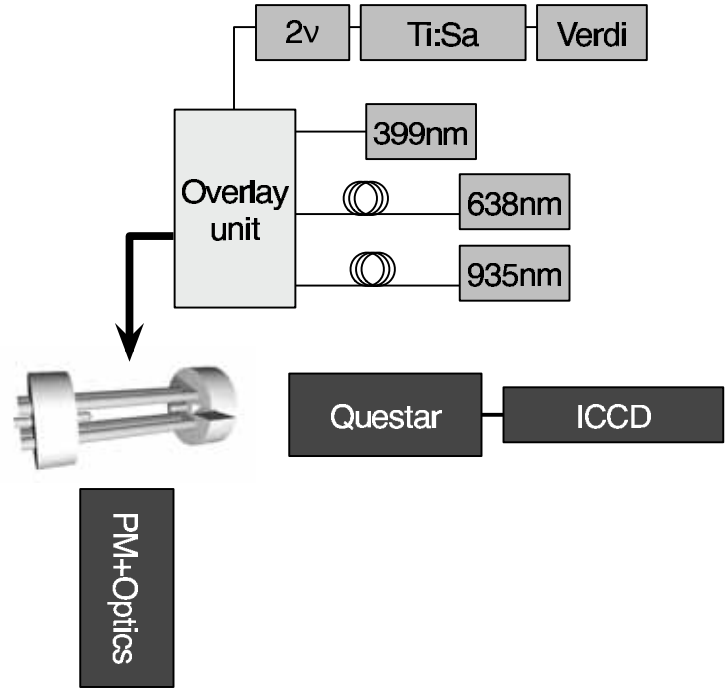

Figure 3.12: Overview of the laser and optics setup. The four laser light fields are combined in the overlay unit. Two separate detection paths are present, one equipped with a photo-multiplier, the other with an intensified CCD-camera.

runs uncontrolled due to the low demand on the frequency stability. A control signal from an atomic ytterbium beam has been envisaged and should be implementable in a straightforward manner, but this is left for future work. The frequency is controlled with the lambda-meter to an accuracy of below 100 MHz, which is sufficient for ionization. Even for the Doppler-free excitation spectrum of the natural abundance oven (see Sec. 4.2) with line-widths below 100 MHz the loading rate is still ample even if the laser is not perfectly on resonance. The laser is focused through a pin-hole with a 25 µm diameter to retrieve a Gaussian-like beam profile. Approximately 1 mW of usable laser light reach the trap. This is more than enough for ionization purposes, and the light can be attenuated by neutral density filters for stray light reduction.

935 nm and 638 nm

The repump lasers at 935 nm and 638 nm are home-made ECDLs with side-of-fringe frequency stabilization. As before the diode temperature, diode current and the grating voltage are controlled. The free-running wave-length of the 935 nm diode is 940 nm, necessitating an operating temperature of 8 °C. As this temperature is below the condensation

point usually present in the lab the casing is permanently flooded with dried air. The diode at 638 nm is operated at 25 °C without further measures. Both laser light fields pass through optical fibers (see Sec. 3.2.4) to obtain a Gaussian beam profile.

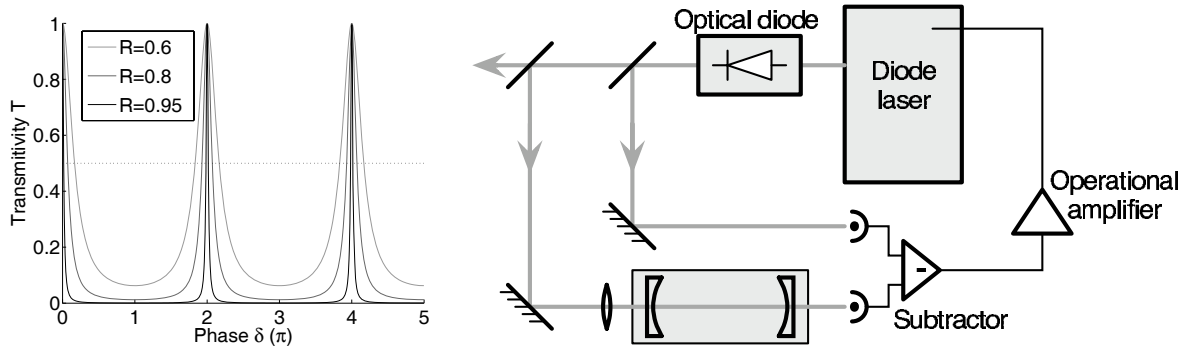

(a) Airy transmission function of the resonator

(b) Frequency control scheme

Figure 3.13: Side-of-fringe frequency stabilization for the diode lasers at 935 nm and 638 nm. (a) Airy-function for different reflectivities of the cavity mirrors. (b) Scheme of the control loop.

Figure 3.13 illustrates the side-of-fringe frequency stabilization. A small part of the laser light is reflected from a glass plate towards a photo-diode (PD2) as a reference to eliminate intensity fluctuations of the laser light from the control loop. A second glass plate reflects another part of the light towards the reference cavity. A lens adapts the beam profile to the cavity. Both cavities are low-reflectivity with $Q \approx 100$ for the laser at 935 nm and $Q \approx 10$ for the 638 nm laser. The latter was deliberately chosen with such a low Q-factor to render the signal passing through the cavity insensitive to spatial beam deviations. This way, an optional AOM right before the cavity allows for a fine-grained frequency control of the laser at 638 nm.

The length of the cavity is adjustable with a piezo-ceramic that controls the position of the first mirror. The light passing through the cavity is reflected onto the second photo-diode (PD1). The difference of the two photo-diode signals is the error signal for the control loop. A variable light attenuator selects the intensity of the reference beam. The intensity is set to half the transmission maximum of the cavity. Now, the length of the cavity and hence its eigenfrequency is adjusted such that the transmitted intensity is equal to the reference intensity, and the difference signal is zero. When the laser frequency fluctuates, the signal transmitted through the cavity will move up or down, indicating the sign of the frequency drift. This is the working point of the control loop, and the frequency of

the laser is held half-way up on the fringe of the transmission Airy-function of the cavity. When the control loop is active the frequency of the laser diode is controlled by changing the cavity length with an offset voltage to the piezo-ceramic. Both laser are tunable in a range of 1 GHz. More details for both lasers are to be found in the PhD thesis of Christoph Balzer [Balzer, 2003].

3.2.2 Laser system at 369 nm

The only light field in the experiment that is not generated by a diode laser is the 'main' cooling light field for the $S_{1/2} \rightarrow P_{1/2}$ transition at 369.4 nm. Instead, the light emitted from a commercial Ti:Sa laser is frequency doubled. Figure 3.14 presents the setup. A

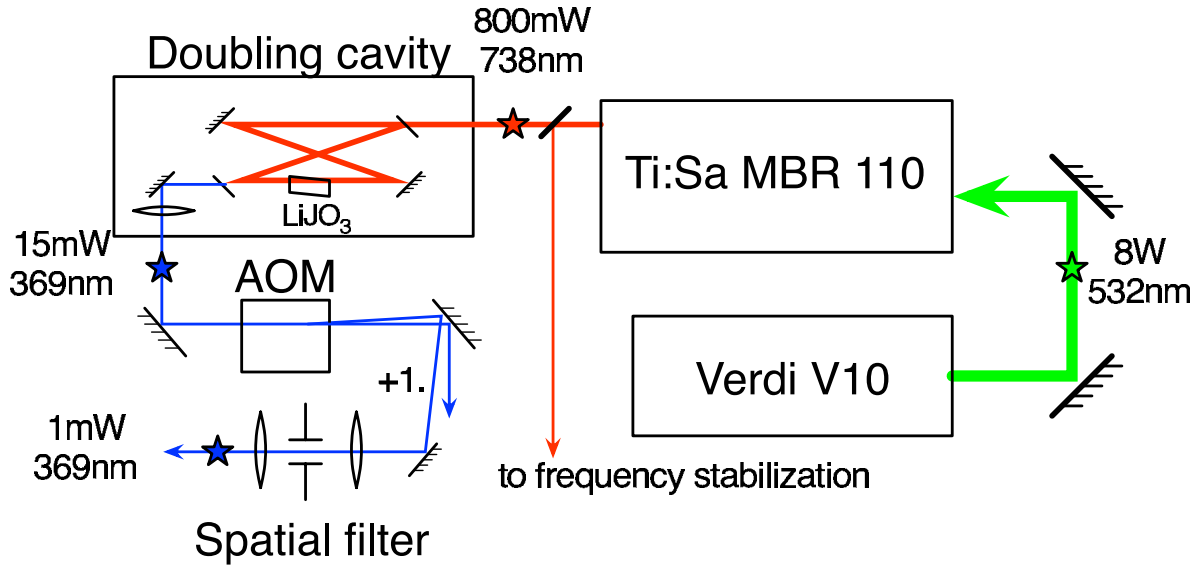

Figure 3.14: Schematic setup for the generation of laser light at 369 nm

commercial pump laser (Verdi V10, diode-pumped solid-state laser, Nd:YAG @ 532 nm) with a maximum output of 10 W optically pumps a Ti:Sa laser (Coherent MBR 110). The pump laser is usually operated at 8 W to enhance the life-time of the pump diodes. Due to the comparatively low gain profile of the Ti:Sa crystal at 738 nm, and because the Ti:Sa laser is running in unidirectional mode the output is typically only 800 mW. The light at 738 nm enters a doubling cavity in bow-tie configuration to resonantly enhance the intensity of the incoming light field and thus increase the non-linear doubling effect of the lithium-iodate crystal ($LiJO_3$). The doubling cavity is controlled to stay resonant with the incoming light field by a Hänsch-Couillaud setup. The active element is a piezo-actuator behind a mirror adjusting the length of the cavity, and hence its eigenfrequency. Due to

a strong walk-off of the crystal for this wave-length the doubling efficiency nonetheless is rather low. An output mirror of the doubling cavity is highly transmissive for 369 nm, and on the order of 15 mW of laser light at 369 nm exit the cavity.

A lens with a long focal length (500 mm) focuses the light into an acousto-optical modulator (AOM) at 200 MHz for fast switching of the light field intensity. The large spot size and Rayleigh-length of the focus afford a high efficiency, such that a maximum of 80% of the light is found in the first order of diffraction. Unfortunately, the spatial profile of the beam exiting the doubling cavity is highly non-Gaussian, requiring further beam 'cleansing' by a spatial filter. The filter is a standard setup comprising an aperture situated in the focal plane of an lens. The higher spatial frequencies of the light field are not focused and hence do not pass the aperture. A lens of small focal length ($f = 50$ mm) creates a (Gaussian) spot size of approximately 5 µm. The diameter of the aperture is selected accordingly with 20 µm to strike a compromise between filtering and losses. Behind the aperture a second lens collimates the beam. Only 1 mW of filtered light remains for the experiment though. Fortunately 10 µW (measured in front of the traps input window) are enough to saturate the cooling transition, implying ample power for the experiment.

The Ti:Sa laser has an internal reference cavity made from Invar for both line-width reduction and frequency stabilization. Even though the internal cavity is temperature-controlled the frequency stability of the laser is not adequate for single ion spectroscopy. The frequency drift was determined to 20 MHz/min. With the aid of a glass plate a part of the Ti:Sa light is therefore reflected to another home-made frequency stabilization, as indicated in Figure 3.14. This control is again a side-of-fringe setup, just as described above (see Figure 3.13), with a passively temperature-controlled low-q cavity made from quartz-glass. The active element here is length of the internal Invar cavity, that can be adjusted by an external control voltage. The frequency drift is thus reduced to less than 5 MHz/h.

3.2.3 Intensity level control and light field switching

The ideal situation for coherent RF-spectroscopy is when only the RF-radiation is interacting with the ion(s), and all other electro-magnetic fields are turned off or shuttered. In the simple case, the additional electric field induces a level shift (light shift or AC-Stark effect). In the worst case, the light field leads to decoherence of the RF-interaction, prohibiting coherent measurements like Rabi-flopping. This is the case for the light field of the repump laser at 935 nm, which directly couples to the qubit levels (see Sec. 2.3.1 and Sec. 5.1). Therefore, the light fields of both the cooling laser at 369 nm and the repump

laser can be switched on and off by means of an acousto-optical modulator (AOM). Turning off the RF-power driving the AOM turns off the light field intensity in the diffracted orders. Combining the first order of diffraction of the AOM with a subsequent spatial filtering element (pinhole for the cooling laser, optical fiber for the repump laser) suppresses the laser intensity between the states on and off by a factor > 50 dB for the cooling laser. For the repump laser a rest intensity could not be measured (suppression > 60 dB). The rest intensity is therefore not limited by the dynamics of the switch, which is specified with a suppression of 100 dB.

An experimentally important parameter is the time scale of the switch. This is dominated by the AOM and the time it takes for the sound-wave in the crystal to decay. Using fast photo-diodes (band-width 10 MHz) the fall-time (to $1/e$ value) for the light fields was determined to 300 ns for the repump laser, and an upper bound of 100 ns for the cooling laser, limited by the band-with of the photo-diode. For the repump laser the switching time was furthermore examined by coherent spectroscopy (see Sec. 5.3). The repump laser would induce decoherence in the coherent interaction between the radiation-field and the ion, reducing the contrast of the observed fringes. For a waiting time of 1 µs after turning of the light field the spectra were not influenced by the repump laser.

As an added advantage it proved to be experimentally convenient to access the laser intensity as a parameter from the PC. This is realized for both laser light fields with a variable attenuator. The variable attenuator changes the RF-power driving the AOM, which influences the efficiency of diffraction and hence the intensity of the diffracted light field. For the cooling laser the AOM setup is described in [Ettler, 2004]. The setup for AOM of the repump laser at 935 nm will be briefly recapitulated in the following.

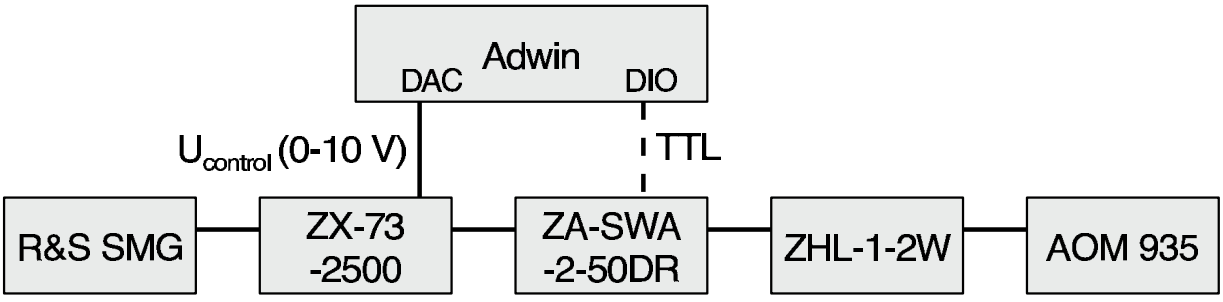

Figure 3.15: Electronic chain driving the AOM for the repump laser at 935 nm.

Figure 3.15 depicts the setup. The signal of a Rhode&Schwarz frequency generator (SMG) passes the variable attenuator and the switch before a RF-amplifier (gain: +32 dB) generates the necessary 2.5 W (approx. +34 dBm) RF-power to drive the AOM (Crystal

Technology, 3110-125). A control voltage from the DAC-port of the DSP system in the range of 0-10 V sets the attenuation value within a measured range of 60 dB (specified: 55 dB). This allows for the same attenuation of the light field power. The switch is also controlled from the DSP by means of a TTL-type signal generated by a digital output port. Sometimes the switch was controlled by the DIO of the VFG-150 (see Sec. 3.5).

Two problems remain using the AOM that stem from the same source: the temperature change induced in the AOM crystal due to the different RF-power levels applied. First, the crystal of the AOM is birefringent and changes the polarization of the light field depending on the RF-power level. Second, the efficiency of diffraction also varies with the temperature. In equilibrium this poses no problem. For the fast switching sequence of a real experiment though this leads to temperature drifts during the experiment with according unwanted effects. The polarization change can be countered to a good degree with a $\lambda/2$ retardation plate, by turning the polarization of the linearly polarized light field onto the optical axis of the crystal. This was tested using a polarizing beam splitter and two photo-diodes right behind the AOM. The amplitude of modulation clearly visible on the signal of the photo-diodes could be reduced by a factor of five.

The intensity fluctuation arising from the changing diffraction efficiency remains a problem for now. A best-practice known is to permanently switch the laser on and off such that the mean RF-power level is constant for both experimental sequences and steady operation. This has not been implemented yet.

3.2.4 Laser optics

Two aspects of the experiments optics were improved in the course of this thesis. Optical fibers were introduced into the experimental setup, and a new unit to overlay and parallelize the different laser beams was designed and implemented. This section describes these changes.

Fibers

Optical fibers offer distinct advantages to many experiments. Most prominently for our purposes is the decoupling of the experimental alignment at the site of the ion trap from the laser alignment. Now the laser itself can be completely realigned during maintenance without affecting the alignment at the ion trap. For ion trap experiments where the beams need to be aligned at the position of a single ion with a µm accuracy after several meters of optical path over the experimental table this is an important advantage. In addition the fiber acts as a spatial filter removing any non-Gaussian $\vec{k}$-components in the laser beams

spatial spectrum. For diode lasers with an often strongly non-Gaussian beam profile this usually means large loss of intensity (in our case approximately 50%), but with saturation power levels in the low µW regime when working with single ions this loss of intensity is not problematic. A clean beam profile is an advantage that allows for a deterministic handling and focusing of the laser beam, and it creates less stray light.

For extremely narrow-band or high-precision spectroscopy experiments an optical fiber poses the problem of noise in the acoustic regime. Phase fluctuations occur due to acoustical vibrations of the fiber, broadening the frequency spectrum of the laser beam. As the repump laser is neither narrow-band nor is it used for high-precision spectroscopy this effect has not been visible in any experiment. Fibers were used for the laser systems at 638 nm and 935 nm. For the UV lasers system at 369 nm optical fibers are difficult to obtain. One try with a fiber with a cut-off wave-length of 380 nm yielded no positive result, but further research into this direction is being pursued.

Overlay unit

So far the different laser beams were added with the aid of a prism, each beam entering the prism at a different angle and leaving it in parallel due to its dispersion. Allowing for any wave-length and basically any number of lasers to be aligned this way, still two problems remained. In order to achieve an appreciable spatial separation of the laser beams on the input side - to allow for mirror positioning and aligning - the distance between the prism and the first mirror (looking in reverse) had to be quite long. This was not only taking up much space on the optical table but furthermore made the aligning more error-prone, due to the long optical lever. E.g., temperature drifts in the laboratory lead to a higher change of the laser beam positions. Furthermore, the prism had transmission losses for the UV laser systems that were unnecessarily high.

For these reasons and in order to take advantage of the new possibilities the optical fibers offered a new overlay unit was designed with stability, compact design and the possibility to integrate a polarization control in mind. The decision was made for a micro-bench system by *Linos*. Figure 3.16 shows a schematic drawing of the current solution. The order of the beam splitters was selected such that the attenuation for the cooling laser light at 369 nm is the least, and that overall loss is minimized. Both fiber couplers are held fast by an adapter ring in the micro-bench system. The beams exiting the couplers then pass through a $\lambda/2$-plate and a polarizing beam splitter (PBS) to ensure a defined polarization of the beams. The PBS defines the polarization used for the experiment while the retardation-plate turns the polarization of the beam exiting the fiber coupler such that

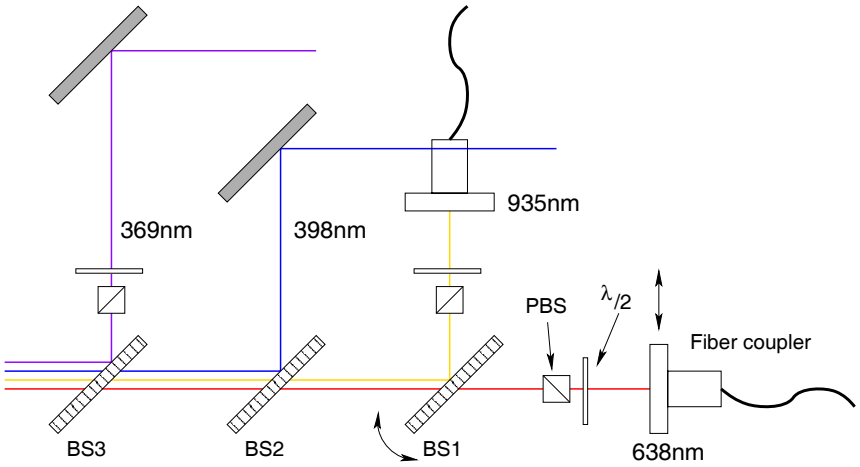

Figure 3.16: Schematic drawing of the overlay unit.

maximum transmission through the PBS is achieved.

All four beams are joined by tailor-made beam-splitters that transmit one wave-length and let the other wave-lengths pass. BS1 is mounted on a stage to change the relative angle between the red and the infra-red laser beams. The fiber coupler of the red laser is situated on a translation stage to move the parallel light beams on top of each other. The two blue laser beams are made co-linear to the red and the infra-red laser beams by two external mirrors each (only one shown).

3.3 Detection systems

This section details the two detection systems that were used in the course of the experiments for this thesis. Both a photo-multiplier yielding an integrated fluorescence signal, and a spatially resolving image-intensified CCD-camera were employed.

3.3.1 Photo-multiplier

Figure 3.17 displays the detection path for the photo-multiplier (PM) setup in a side view. An optimized condenser (*Melles Grillot* 01-CMP-191, two element air-spaced condenser) nearly collimates the fluorescence from the ions. Its focal length as well as its diameter is 50 mm, resulting theoretically in a f-number of 1, equivalent to a numerical aperture NA ≈ 0.7. Practically, as the condenser is designed to work optimally when slightly focusing the distance between it and the ions is between 58-60 mm. A simple lens ($f = 100$ mm) then focuses the light into an aperture to minimize the stray light arriving at the photo-

sensitive cathode. Furthermore, without this additional lens the optical path would become so large as to be experimentally cumbersome. The distance from the aperture to the PM is selected such that the photo cathode is evenly illuminated.

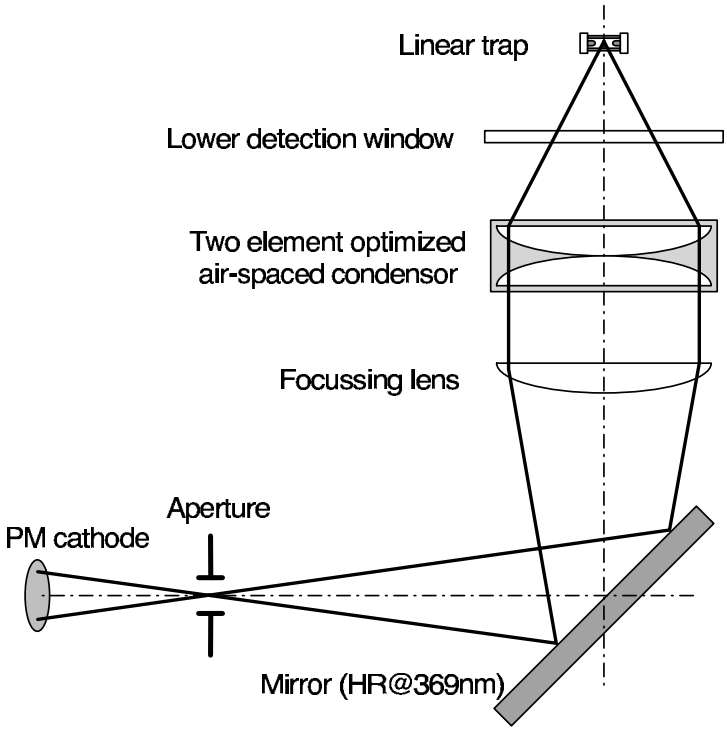

Figure 3.17: Detection path for the PM system (side view), not on scale.

The PM tube is a *Hamamatsu* R5600P housed in a home-made casing of copper and plastic. The cathode has a high quantum efficiency at 369 nm of 20%. The operational voltage range is up to 1000 V. It features a low dark-count rate of 80 cps, which can furthermore be decreased by a cooling stage in the housing. Fortunately, the mentioned dark count of the tube is so low that this was not needed. Optical access to the photo-multiplier tube is controlled via a mechanical shutter screwed to the housing. The current burst for a single event is discriminated and translated into a voltage TTL pulse by a photon counting unit (Hamamatsu C6465) that can drive a 50 Ω line. The TTL pulses are collected and counted by the digital signal processor (DSP) system (see Sec. 3.5). The counter of the DSP system serves as a photon-counting gate with a time resolution of 25 ns.

The highest photon count rate achieved with this setup was approximately 27 kHz, which is in fair agreement with the ring trap operated in our laboratory (35 kHz) as well as rates reported from other groups [Roberts et al., 1999]. Taking into account the rest modulation of the ions movement by micro-motion (remaining modulation index $\eta = 0.7$,

Sec. 3.1.5) the actual detection rate is 10% higher at 30 kHz. The overall detection efficiency of this system is estimated with the rate equation model presented in Appendix B. The rate equation model calculates the absolute photon scattering rate to be 60.3 MHz, including the $D_{3/2}$ level branch, but excluding the double-resonance scheme used in this work. The overall detection efficiency thus becomes 30 kHz /60.3 MHz = 0.05 %. Unfortunately, the stray light level is extremely high, ranging between 2-4 kHz, due to a combination of the optical accessibility and the trap design. In brief, with the optical access available we cannot avoid a rest illumination of the endcap electrodes. This problem will be dealt with in the next generation of traps by using an optical glass cuvette as vacuum recipient, giving basically unlimited optical access to the trap.

3.3.2 Intensified CCD-camera

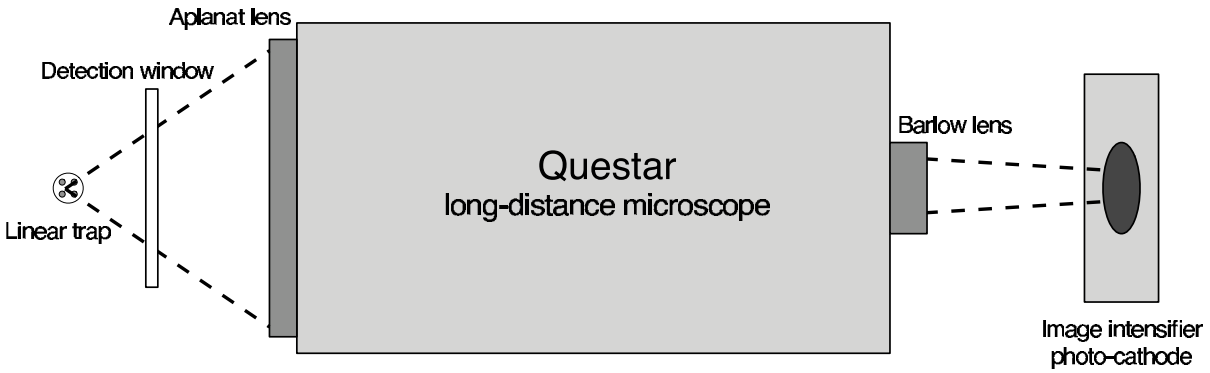

Figure 3.18: Detection path for the CCD-camera (side view, not on scale).

As before for the PM setup a schematic drawing of the detection path for the CCD camera is shown, in Figure 3.18. Here, the main optical component is a *Questar* QM100, a long-distance microscope. Our model is additionally equipped with both an aplanat lens at the entrance port to increase the resolution as well as a 3x-Barlow lens at the exit port of the instrument, increasing the magnification. Both lenses are AR-coated for 369 nm. At maximum magnification - which is the usual working point in the experiments - the resolution is specified to be sub-micrometer with a field-of-vision of 280 µm on a 2/3" chip [www.questarcorp.com]. The NA for this combination is given as 0.185 at a distance of 10 cm from the object. The microscope is mounted onto a *xyz*-translation stage. During the experiment, the magnification of the Questar - adjustable via a focus rod at the rear - is left at maximum, while the focus is adjusted by moving the whole microscope back and forth using the translation stage.

The microscope images the ions fluorescence onto the photo-cathode of the image-intensifier. The photo-electrons are accelerated through the micro-channel plate (MCP) and illuminate a phosphor screen situated at the rear exit of the MCP. With two camera lenses the phosphor screen is imaged onto the CCD-chip. The system is constructed to yield a 1:1 image of the photo-cathode of the intensifier on the CCD-chip. The image intensifier, the lenses and the CCD-camera are rigidly assembled and need no adjustment.

The camera is equipped with a $512 \times 512\,\mathrm{px}^2$ CCD array (TE/CCD512TKB), cooled to -40 °C with a double Peltier cooling stage and air circulation to reduce dark current. The square pixels have a size of 24 µm, equivalent to a chip size of 12.3 mm. The analog-digital converter (ADC) has a resolution of 16 bit with an effective resolution of the whole system of approximately 14 bit, limited by the capacity of the electron well. The maximum ADC speed is 1 MHz, with a full frame readout time specified at 0.5 s. The repetition frame rate was experimentally determined to be slightly higher at 2.85 Hz (350 ms) for full frame readout, and 4.55 Hz (220 ms) for a typical image size of 130x40 pixel. Here, the repetition rate is limited by the overhead of the camera controller, which turned out to be on the order of 220 ms.

Exposure time

The exposure time is completely controlled by the image intensifier, which acts as a shutter to the CCD-camera. Only when the high-voltage of the MCP is applied does the CCD-camera receive any light from the phosphorescent screen at the rear port of the intensifier. For longer exposure times the intensifier controller allows for the direct gating of the high-voltage. Due to the low light levels involved in photographing a single ion a typical value for the exposure time is on the order of 100 ms.

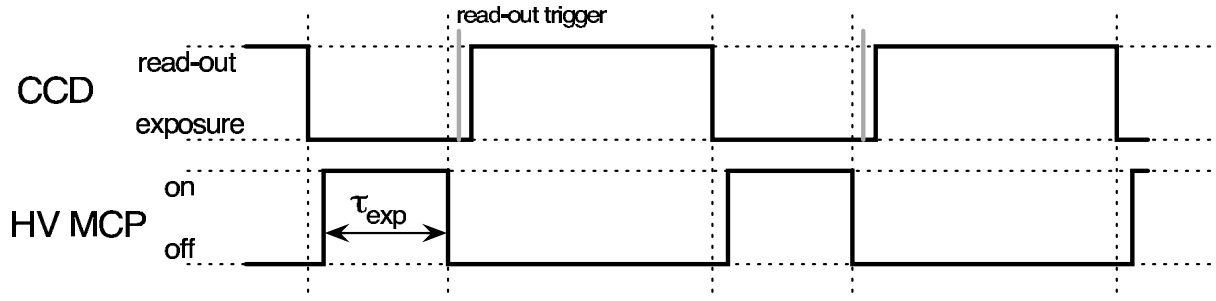

Figure 3.19: Exposure timing for the imaging cycle

An exemplary timing cycle is demonstrated in Figure 3.19. All trigger pulses are sup-

plied by the DSP system (Sec. 3.5). The controller of the CCD-camera is programmed to immediately begin read-out when the according trigger pulse arrives. The read-out trigger is indicated in gray in the upper branch. After the trigger the read-out begins and the chip remains inactive. As soon as the read-out is finished the CCD-camera immediately begins accumulating charge in the pixels from the dark current. A brief delay after the CCD-controller is finished reading-out ensures that the action time of the image intensifier is completely within the accumulation time of the CCD-chip. The high-voltage is applied to the MCP for the duration τ_{exp}, the exposure time. Immediately following this pulse the camera is triggered for read-out again, and the cycle starts anew. The fact that the CCD-chip is active for a longer time than τ_{exp} is quantitatively irrelevant, as the overall timing is stable to below 1 ms. The dark count accumulated during this time is a constant and easily subtracted by taking a calibration image with the same timing without intensifier.

Imaging scale

Another important aspect of the direct imaging of the ions is the scale of the image. In order to evaluate the strength of the magnetic field gradient examined in Sec. 5.4 the distance between two ions is relevant. The measured magnitude is the shift of the Larmor-frequency of the Zeeman-splitting for different ions, sitting at different positions. In order to translate the frequency shift into a spatial gradient the distance between the ions needs to be known. Two methods to determine the imaging scale are presented in the following.

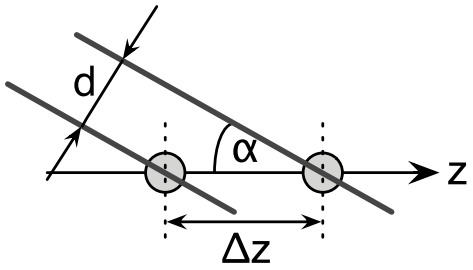

Figure 3.20: Schematic drawing of the image scale calibration by ion movement. The ions are moved by a distance Δz by applying voltages to the correction electrodes. The movement of the laser focus is to first order linear in the displacement d of the focusing lens, mounted on a translation stage with micrometer-screw.

The first method relies on the fact that the focusing lens for the laser beams is attached to a xyz-translation stage with micrometer screws. The position of the laser beams is easy to set on a string of ions by moving the focusing lens back and forth and observing how the

ions are illuminated. The attained accuracy is within ±5 µm. Applying a constant voltage to the correction electrodes moves the ions to a different position. When the laser beams are always set to the center of the ion string the offset in the ions position - as recorded in the image - can then be correlated to the micrometer-screw position of the focusing lens, thus calibrating the imaging scale. Figure 3.20 displays the principle. Moving the ions by a distance of Δz the micrometer screw has to be adjusted by a distance d, and

$$\Delta z = \frac{d}{\sin \alpha}. \tag{3.5}$$

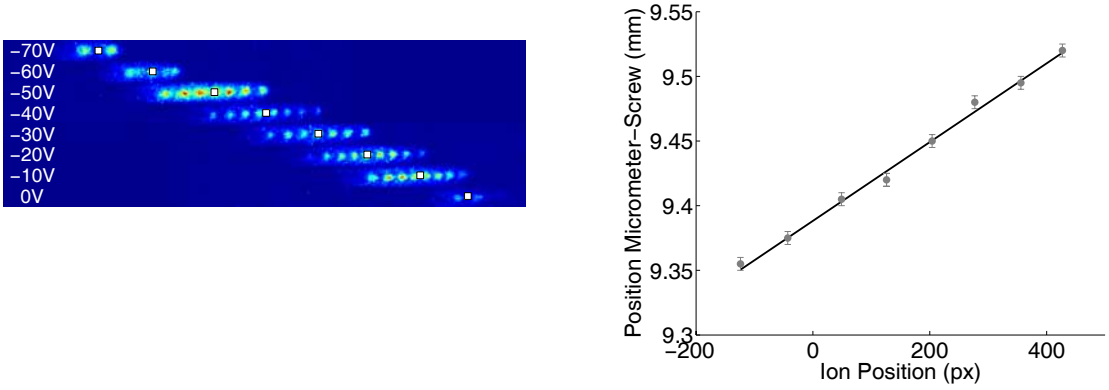

(a) Ion positions

(b) Calibration graph

Figure 3.21: Calibration data. (a) Sequence of images for different correction voltages, with the center position indicated by white squares. (b) Calibration graph.

The position of the ions in the image can be determined by eye with an accuracy of ±1 px. Furthermore, for longer ion strings the center position is confirmed by comparison with the middle between corresponding outer ions (i.e. 1 and 7, 2 and 6, 3 and 5 for $N = 7$). Figure 3.21 (a) shows the calibration data, where the center of an ion string is indicated by white squares. The figure comprises eight individual images that have been assembled to illustrate the ions movement. A slight vertical movement present in the original images is neglected both in the assembly and the evaluation. At U_{corr} = -40 V two images were taken while the position of the microscope was shifted horizontally to accommodate further movement. The offset of 266 px is directly incorporated into Figure 3.21 (a) and explains the negative positions in (b).

The slope of graph (b) in Figure 3.21 needs only to be corrected for by the factor $1/\sin\alpha$ as indicated in Eq. 3.5 to yield the scale of the image in µm/px. With $\alpha = (30 \pm 2)°$ the scale is 0.61(4) µm/px, corresponding to a FOV of 312 µm. A second calibration from another day yielded 0.68(4) µm/px (FOV 348 µm). The angle α was not determined to a better accuracy due to limited access to the components on the optical table.

When the imaging scale is known the distance between the ions is equivalent to axial secular frequency ω_z as determined by the length scale ℓ (Eq. 2.23) and the ion position (Figure 2.4). Accordingly, the measurement of ω_z is also a measurement of the image scale. Figure 3.22 (a) shows an image of two ions that was taken as a calibration image directly before the axial secular frequency was measured (compare also to Sec. 3.1.4). Figure 3.22 (b) shows the same data, with all rows summed to yield a scalar signal per position x. Two Gaussian distributions are fitted numerically to the data to determine the center of the two ions, and hence the exact distance.

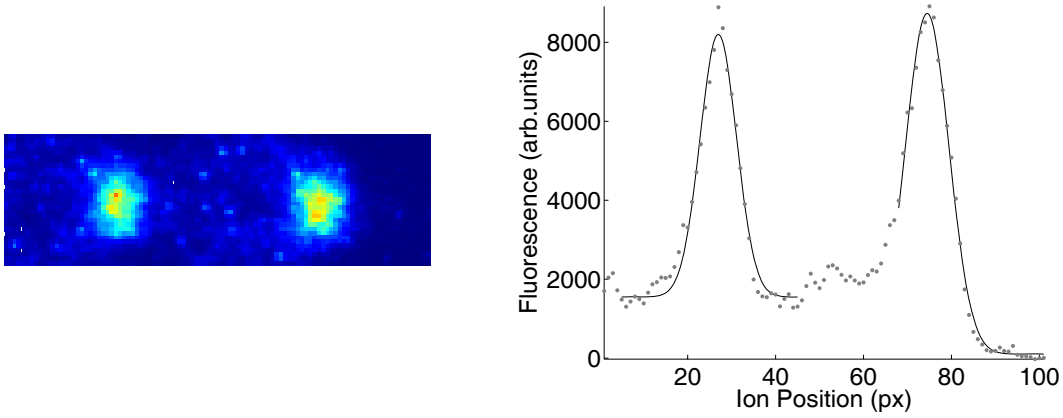

(a) Direct image (b) Fitted ion positions

Figure 3.22: Determining the imaging scale by measurement of the secular frequency. (a) The calibration image from which the data was taken. The axial secular frequency is $\omega_z = 36.5$ kHz. (b) Fit of two independent Gaussian profiles after summing over the rows of the image. The distance between the ions is $\Delta x = 47.3$ px.

The distance in units of pixel is $\Delta x = 47.3(4)$, the axial secular frequency was determined to $\omega_z = 36.5(5)$ kHz. The error ranges are derived from the numerical fit, and from Sec. 3.1.4, respectively. The distance between two ions is given by [James, 1998]

$$\Delta\xi = 2\sqrt[3]{(1/2)^2}, \tag{3.6}$$

which is approximately 1.260 in units of ℓ. Recalling Eq. 2.23 we find

$$\Delta x = \ell \Delta\xi = \frac{Q^2}{4\pi\epsilon_0 M\omega_z^2}\Delta\xi = 31.2(5)\,\mu\text{m}. \tag{3.7}$$

Thus the scale is determined to be $31.2/47.3 = 0.66(5)$ µm/px, according to a FOV of 338 µm. In the following the mean of the three values derived in this section 0.65 µm/px is taken as the image scale where needed.

3.4 Static and dynamic magnetic fields

The Zeeman sub-levels of the $D_{3/2}$ level of Yb^+ are the energy states that form the basis for the quantum logic operations performed in this thesis. The degeneracy of the levels is lifted by a constant external magnetic field, separating the $D_{3/2}$ into four states with $m_j = -3/2 \cdots + 3/2$. A dynamic magnetic (RF-) field with its frequency tuned to the Larmor frequency of the level splitting couples the sub-levels.

3.4.1 Static magnetic field coils

This section describes how the static magnetic fields are created and controlled at the site of the ions. The existing setup had to be replaced as eddy currents in the brass formers prohibited the goal of RF-spectroscopy. The new magnetic fields coils are calibrated with an external measurement and compared to numerical simulations.

Design and construction

A set of three pairs of coils were present at the experiment. The old coils were wound on brass formers. This is unfortunate for two situations which both occured during the setup of the RF-spectroscopy:

1. Fast switching of the magnetic field ($\approx 1\,\mu$s) is rendered impossible.

2. RF-signals are completely damped inside the coil-'cage'.

Both points originate from eddy currents induced in the formers, which prohibits a fast decrease of the current through the coils - and hence a fast decrease of the magnetic field - for the former case. For the latter case it completely changes the impedance of the antenna used for radiating RF-signals into the trap volume: the power is reflected back into the amplifier, i.e. no RF-signal reaches the ions.

(a) Field coils with plastic combiners

(b) Complete assembly with stray-light shielding

Figure 3.23: Three magnetic field coils for xyz (a) and stray-light shielding (b). Everything except for the copper wire is made from plastic.

This situation necessitated a complete rebuild of the magnetic field coils with plastic formers. The aluminum stray-light shielding was rebuild in the same material as well. The selected material is Polyoxymethylene (POM), which has the advantage over PVC (Polyvinylchloride) of a higher maximum operating temperature of 100 °C, as opposed to 65 °C. POM starts to soften at 165 °C, which will limit the operating current to several amperes. But as the gradient is created using permanent magnets these coils do not need to support very high currents. An informal test revealed that the coils do no significantly warm up at 3 A for several minutes. Figure 3.23 depicts the new design, with half the coil-'cage' shown in (a), and the whole setup including stray-light shielding in (b). The holders that link the coils and the screws are made from plastic as well, as seen in (a). Each coil carries a hundred windings of insulated copper wire with a diameter of 1 mm, wound in ten layers. The diameters of the coils were slightly increased for better optical accessibility. The inner radii are now 45.5 mm for the horizontal coils and 52.0 mm for the larger vertical pair. The distance from the trap center to the surface of the former is 57.5 mm for all formers, resulting in a distance of 63.5 mm for the first winding (i.e., 64 mm for the center of the first winding). Even though the radius is not equal to the distance between the coils this Helmholtz-like configuration nonetheless is expected to ensure spatial homogeneity to a good degree. Numerical simulations show a deviation of the absolute value of the magnetic field below 1% for an offset of ±4 mm from the center of the coil-cage.

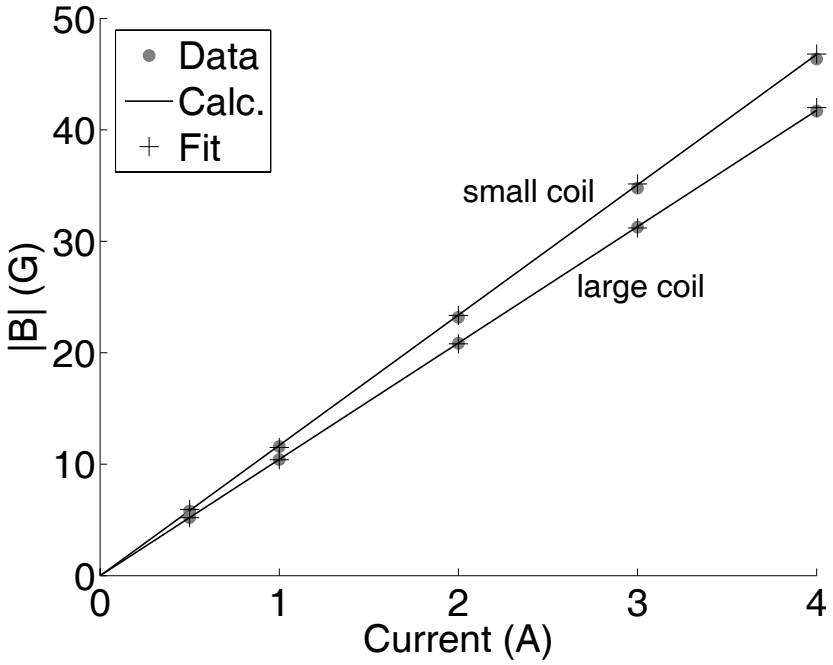

Figure 3.24: Calibration measurement of the magnetic field coils. Also shown are the linear fit to the data and the results from the numerical simulation.

Figure 3.24 depicts the calibration measurement. The plot shows the absolute value of the field, a linear fit to the data and a simulation. The field was measured for different currents with a Hall probe, situated on the symmetry axis and 6.5 mm from the center of the first winding of the coil. The B-field of a single winding of wire on its symmetry axis is given by

$$B(z) = \frac{\mu_0}{4\pi} \frac{2\pi R^2}{(z^2 + R^2)^{3/2}} I, \tag{3.8}$$

in units of Tesla. A matlab-script calculated this magnitude for all of the 100 windings of the coil, taking into account the different z and R values for each winding of the different layers. The 6.5 mm distance between the Hall probe and the first winding derives from the width of the former, as the outer rim of the former served as a reference point for the probe. The width of the former (6 mm) plus half the width of the first winding (0.5 mm) add to the used value. The simulation and the data are in excellent agreement, with less than 1% deviation. This is to be expected, as the distances involved are known to construction accuracy (0.1 mm), and the on-axis magnetic field of a coil is given analytically. The calibration factors finally used for the actual measurements are $c_{\mathrm{calib}}/c_{\mathrm{simul}} = 11.6905/11.5898 = 1.0087$ for the small coils, and $10.4381/10.4229 = 1.0015$ for the large coils. Here, the c_{x} are the factors of proportionality between B and I.

It is desirable for some experiments that the magnetic field can be quickly and programmatically turned on and off. A power switch was developed by the electronics workshop that allows to gate the current flowing through a pair of coils with a TTL pulse. The switch is inserted into the lines connecting the power supply with the field coils. The load is switched between the coils and a dissipative component, to keep the work-load constant for the power supply. Measuring the voltage over the coil indicates a time-scale of 1 ms for the current to stop. Even though longer than expected, this is short enough for the experiments performed with it.

3.4.2 RF-excitation coil

In order to gauge the fluorescence rate that can be obtained with a double-resonance spectroscopy a simple rate equation model has been developed in Appendix B. There, the Rabi frequency of the RF transition between different sub-levels of the $D_{3/2}$ state is the central parameter that determines the fluorescence rate. Before the decision was made to try the RF-spectroscopy experiments the Rabi frequency had to be estimated. This paragraph shows some calculated characteristics of the coil used to produce the RF-magnetic field that induces the transition between Zeeman sub-levels. The coil is assumed to be a circular coil of two windings with a given diameter and a given distance to the trap center. The maximum current attainable as well as an estimate of resulting the Rabi-frequency is given.

Coil characteristics

Basically two simple setups present themselves as alternatives for the excitation coil, either with a low or a high tuning bandwidth. If the Larmor-frequency is well known and does not change, an LC-circuit resonant to that frequency allows for high currents at low power due to low ohmic impedance. This ensures high Rabi frequencies, but the bandwidth scales anti-proportionally with the quality factor. Initially, when searching for the RF-transition in an unknown magnetic field the Larmor-frequency is not determined yet. The bandwidth of the setup should therefore be as large as possible. This is achieved by using a high-power ohmic resistor of $50\,\Omega$ which is completely independent of the frequency, thus not limiting the bandwidth at all.

Figure 3.25 depicts the setup. The current flowing through the winding is produced by a standard RF-amplifier amplifying a sine input from a frequency generator at a frequency of several MHz. For impedance matching a high-power resistor with $R = 50\,\Omega$ is connected in series to the coil. The resistor is screwed to a heat-spread with an attached fan to

dissipate the waste heat, as practically all RF-power is dissipated in the resistor. The windings are made of copper wire with a diameter of 1.5 mm, wound on a plastic former for mechanical rigidity. For the calculations the ohmic and inductive impedance of the two windings is neglected, and the circuit is assumed to have an strictly ohmic impedance of 50 Ω. The amplifier is limited to 25 W. At 50 Ω and with $P = RI^2$ the resulting current

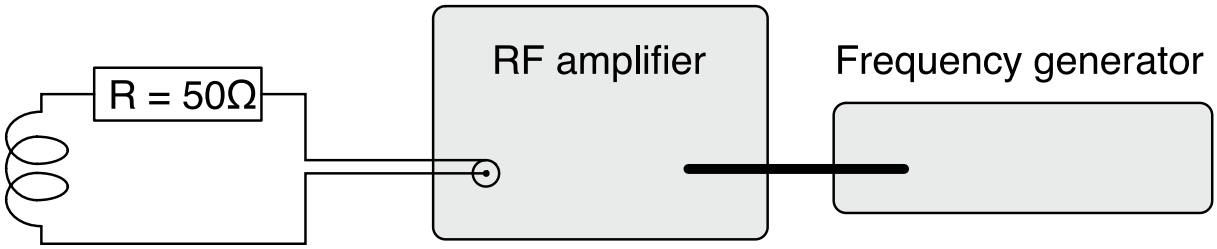

Figure 3.25: Diagram of the rf-circuit producing the dynamic magnetic dipole field, used for the rf-optical double-resonance spectroscopy.

is $I_{\max} = \sqrt{P/R} \approx 0.7$A. This current is the upper limit for the calculation of the Rabi-frequency. A second amplifier also in use with 10 W can drive up to 0.45 A.

The magnetic field on the center axis of a single winding coil is given by Eq. 3.8. The minimum on-axis distance between the trap and the coil is 30 mm, limited by the glass recipient. In order to maximize the magnetic field amplitude and thus the Rabi-frequency the magnetic field of a single winding is calculated for different diameters, as shown in Figure 3.26. Eq. 3.8 is used with $I = 0.7$ A and $z = 30$ mm. The maximum amplitude of the magnetic field is attained with a radius of 42 mm and has a value of 56.4 mG. The diameter finally selected is slightly lower at 78 mm, yielding 56.2 mG. This way, the excitation coil together with its former can be inserted into the experimental setup without removing one or more of the magnetic field coils, whose inner diameter is 91 mm.

Rabi-frequency

The Rabi-frequency for a magnetic dipole is given by

$$\Omega = \frac{\vec{\mu} \cdot \vec{B}}{\hbar}. \tag{3.9}$$

In rotating wave approximation this reduces to

$$\Omega = \frac{1}{2} g_j \frac{\mu_B \cdot B}{\hbar}, \tag{3.10}$$

with g_j the Land factor for the level, μ_B the Bohr magneton, and $\hbar$ Plancks constant. For the amplifier with 25 W that supports a maximum current of 0.7 A and for two windings

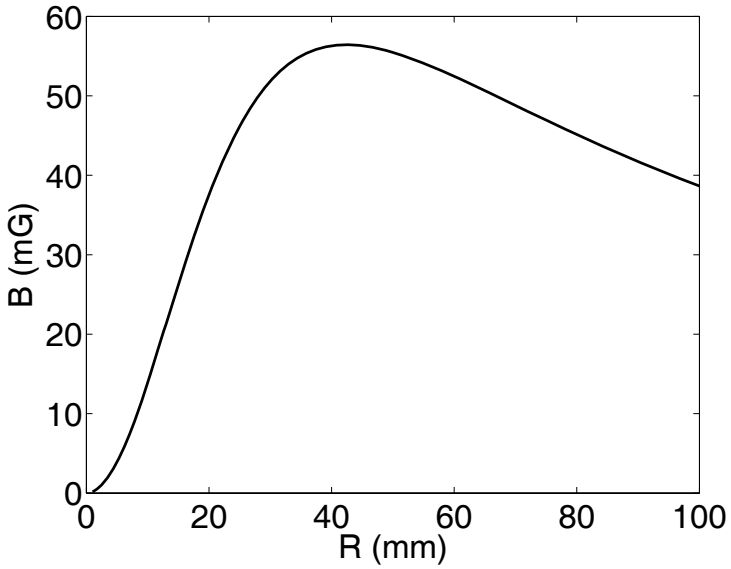

Figure 3.26: Magnetic field of a single-winding coil with varying diameter D

on the RF-coil this evaluates to (using $g_j = 4/5$) $\Omega_{\max} = 2\pi \cdot 63\,\mathrm{kHz}$. For the amplifier with 10 W (which was finally used for the measurements) and a maximum current of 0.45 A the result is

$$\Omega_{\max} = 2\pi \cdot 40.6\,\mathrm{kHz}. \tag{3.11}$$

3.5 Experiment control

This section describes the different systems used to control the timing of the experimental runs. A typical sequence of an experiment for quantum information processing involves many repetitions of short pulses, be it optical, MW- or RF-radiation. The Rabi-frequency of the interaction offers an estimate for the time resolution required, which is on the order of µs for the experiments presented in this work. Several special systems are employed to gain that control.

Figure 3.27 gives an overview of the components involved. Both a real-time digital-signal processor (DSP) *Adwin* as well as the versatile frequency generator (VFG) ensure the temporal control of the experimental sequence. The VFG has been developed in this group by Thilo Hannemann. The Adwin system is a commercial real-time DSP with a specified time-resolution of 1 µs. The VFG and the DSP connect via USB to the main PC. The main PC serves as central user interface that instructs the VFG and the DSP. Here all experimental parameters and the exact sequence of events are programmed. The sequence

is transferred via USB to the time-critical components VFG and DSP, which then execute the experimental sequence independently from the PC. If data is acquired by the input ports of the DSP this data is read-out and displayed by the PC with low priority (i.e. with no timing relevance). The data is subsequently stored in simple text files.

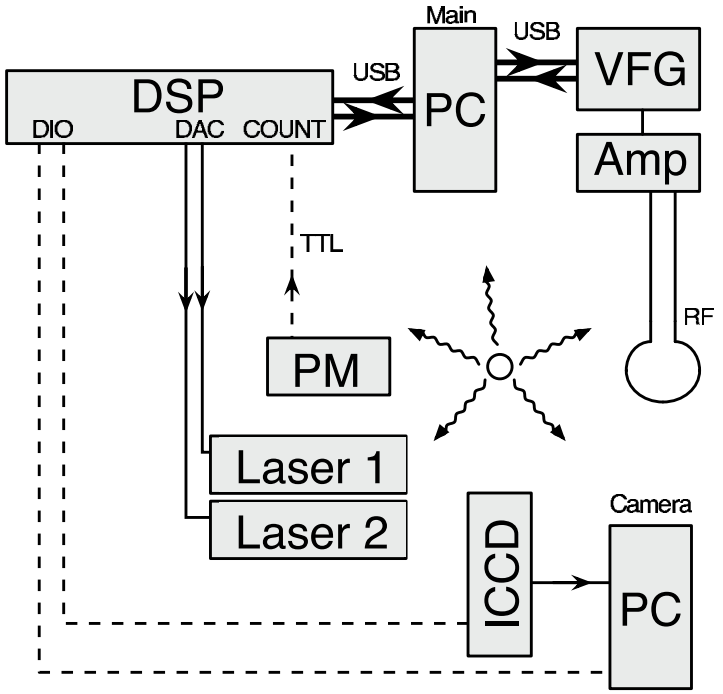

Figure 3.27: Principle setup of the experiment from a control point of view. Solid lines indicate analog signals, dashed lines digital (TTL) signals.

In the setup presented in Figure 3.27 the analog voltage signals from the DAC output ports of the DSP are used to control laser parameters. The signals can be used for different purposes, but the standard configuration is that DAC 1 controls the intensity of the cooling laser at 369 nm, and DAC 2 controls the frequency of the repump laser at 935 nm. Alternatively, DAC 2 also controls the intensity of the repump laser. The intensity control is realized with a variable attenuator changing the input RF power for the AOM. The attenuation is controllable by an external voltage, which in this case is supplied by the DSP system. This component is explained in more detail in Sec. 3.2.3. The frequency of the repump laser is changed by amplifying the signal from DAC 2 and directly applying it to the piezo ceramic controlling the angle of the optical grating. If the image-intensified camera (ICCD) is used the exposure time and read-out start are also controlled by the DSP system via the DIOs (see Sec. 3.3.2).

Real-time DSP

The DSP system (Keithley ADwin-Pro, ADSP 21062 processor) is equipped with 32 digital ports that can be used both for input and for output (DIO) of TTL-type signals. Four digital-analog converters (DAC) with 16 bit resolution, four fast and eight slow (12 bit) analog-digital converters (ADC) are present. Furthermore a counter module with eight dedicated counters allows for the time-resolved counting of a discriminated (TTL) signal. Depending on the type of experiment only a small subset of the possible ports is used. The DSP is programmed in ADbasic, a proprietary Basic-like programming language supplied with the hardware, together with an integrated development environment (IDE). A home-made 'operating system' running as main thread on the system forms an application programming interface (API) that facilitates the easy creation of experimental sequences, avoiding the need to develop a full program for every experiment [Hannemann, 2002]. The sequence is then passed from the PC to the system as a data array, where each entry in the array represents one action. A maximum of two input arguments for every action can be passed as well. Data can also be passed from the DSP to the PC, which is used solely for the results of photo-counting. All communication between the DSP and the PC is based on an asynchronous FIFO (first-in first-out) memory to ensure data integrity.

Versatile RF-generator

The versatile frequency generator 'VFG-150' used for many experiments in this work is a home-made development by Thilo Hannemann, a former member of our group. It is based on a field programmable gate array chip (FPGA) and features two main characteristics not found in other commercial frequency generators:

1. Very fast (5 ns) switching of all parameters
2. Phase-coherent switching between frequencies

The first point permits the almost arbitrarily fast switching of RF pulses, at least compared to the usual time scale of 1 µs relevant for quantum information processing in ion traps. Every 5 ns every parameter of the VFG - notably amplitude, frequency and phase - can be changed to any value. Using the VFG it is now possible to test proposals for quantum gates based on sequences made up of virtually thousands of very short RF-pulses [Kobzar et al., 2003]. Furthermore, it is straight-forward to implement not only pulse sequences but also pulse shaping by, e.g., amplitude modulation in form of an amplitude envelope. This method has been demonstrated by measuring a sequence of STIRAP pulses in Innsbruck [Wunderlich et al., 2006].

The second point is relevant for multi-qubit quantum computers. When for example the gradient scheme presented in this work permits the individual addressing and manipulation of single qubits in frequency space the experimentor needs to switch between different frequencies while retaining the phase information for each frequency. One way would be to use one frequency generator for every qubit. Here though, the frequency generator itself remembers the phase for every frequency and switching between different presets automagically is phase-coherent.

Apart from these special features the VFG-150 has a maximum output frequency of 150 MHz and a maximum amplitude of 0 dBm. The dynamic range is 60 dB. It has four digital (TTL) output ports that allow a fast control of other experiment components. A TTL sync port permits the synchronization to a TTL trigger, which is used to synchronize the VFG to the DSP system. As the frequency stability of the VFG is not high enough for quantum information processing it can be locked to an external stable frequency source. Similar to the DSP the VFG is controlled from the PC by passing a data array of commands via USB.

Computer control and interface

The user interface on the PC is programmed in *LabView*, a proprietary graphical programming language. Its large instrumentation library and the wide acceptance in the industry allows for the easy communication between the PC and almost any component in the lab. Many instruments (frequency generator, spectrum analyzer, multi-meter) are connected to the PC via the GPIB bus, and the vendors supply LabView drivers for this scenario. The drivers for the USB-connected VFG are home-made.

Every experiment is represented by one LabView program. Parameters - like the duration of a RF-pulse - are accessible via the GUI. The exact timing-sequence is different for every experiment, and hence it is hard-wired into the program code. The LabView program constructs the data arrays that contain the commandos for the DSP and the VFG, sends the data to the components, reads the data coming from the DSP and displays it on the screen in near real-time. For complex sequences the PC is fully occupied by the construction of the commando arrays and the communication with the components. In that case the display of the data can be distinctly out of sync with the experiments actual progress. The data is then stored in simple text files which permits general use.

4 Photo-Ionization

Photo-Ionization has been known for a long time. Its predecessor, the photo-electric effect, was experimentally observed in 1888 [Hallwachs, 1888] and theoretically explained in 1905 by Einstein [Einstein, 1905], introducing the photon as one quantum of the light field. Nonetheless, only in recent years has the ion trap community begun to change the ionization method from the established electron bombardment to photo-ionization. The advent of cheap UV laser sources made this step possible. At first though, Kjaergard et al. introduced the photo-ionization of calcium and magnesium using a frequency-doubled dye-laser [Kjrgaard et al., 2000]. They proved photo-ionization to be a viable and advantageous ionization method for ion trapping purposes. A second scheme for calcium eliminated the need for the dye-lasers and relied on two diode lasers alone [Gulde et al., 2001]. This chapter presents a photo-ionization method for ytterbium based on just a single diode laser near 399 nm.

Photo-Ionization has several advantages for ion trap purposes. First, it is highly efficient in comparison with electron impact ionization, yielding loading rates at several orders of magnitude higher. This allows to reduce the atom flux considerably, avoiding trap contamination by deposition of the metallic atoms on trap electrodes or other, isolating trap components. Second, the electron bombardment introduces excess charges into the trap volume, leading to unwanted patch potentials that disturb the trapping potential.

These are avoided with photo-ionization. And third, being a resonantly enhanced process, it is isotope selective. Not only does it allow for the selective trapping of a certain isotope which is impossible with the indiscriminating electron impact method. But it furthermore eliminates the need for isotope-enriched ovens, normally a preliminary for experiments with isotope-pure ionic crystals. All isotopes can now be loaded from a single oven with natural abundance. As a smaller advantage, for electron impact ionization the electrons usually have a kinetic energy on the order of 1 keV. This leads to an enhanced cross-section for double and triple ionization. Depending on the trap parameters the higher charged ions may be trapped as well. This is completely avoided with the resonant photo-ionization process. Last but not least, one aspect shall be mentioned that is only of practical importance, but in application is a significant advantage. When building a new trap the fact that the atoms are visible by their fluorescence means they are *there*. This excludes an important amount of error-sources and has proven itself very helpful during the three rebuilds of the ovens (see Sec. 3.1.2).

The first proposals of photo-ionization processes for ytterbium required experimentally cumbersome solid-state lasers to generate three light fields between 555 nm and 583 nm [Choet et al., 1995,Tkachev & Yakovlenko, 1996,Borisov et al., 1998]. Another process proposed by *Sankari* and *Suryanarayana* [Sankari & Suryanarayana, 1998] uses the ground state transition $^1S_0 \rightarrow {}^1P_1$ (398.9 nm) as a first resonant excitation step. From the $^1P_1$ level a second light field with a wave-length lower than 394 nm is required to ionize the ytterbium atom. Conveniently, this second light field is already present at our experiment with the cooling laser at 369 nm for Yb^+. This process was implemented in our group using only a single diode laser near 399 nm. It is to the best of our knowledge the first working instance of photo-ionization of ytterbium for ion trap purposes. Interestingly, it turns out that a second light field lower than 394 nm is not necessary in ion traps. The Stark effect of the trapping potential lowers the ionization threshold such that a second photon at 398.9 nm is enough to ionize the atom. This process is explained in detail in Sec. 4.1.

This chapter presents the experimental results gained at the linear trap that is used throughout this thesis. After the initial success of the photo-ionization itself a new oven was built with natural abundance isotope distribution to further test the scheme. Thus three ovens are present in the vacuum chamber of the linear trap: two isotope pure ovens for ^{171}Yb and ^{172}Yb, and one oven with natural ytterbium. The atomic excitation spectra from the three ovens are given in Sec. 4.2, with special attention on the resolution of the isotope shift. If the isotope shift is spectroscopically resolvable than the isotope selective photo-ionization should be feasible. The second section 4.3 demonstrates deterministic

loading of a desired number of ions, another advantage of photo-ionization for work with a linear trap.

4.1 Ionization processes

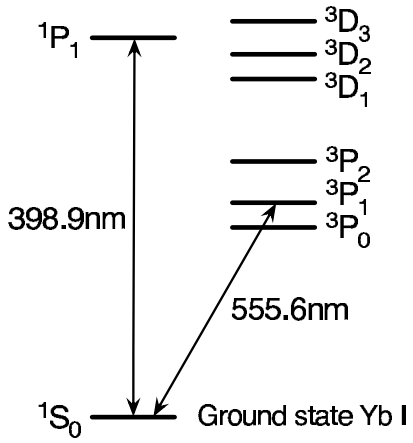

Figure 4.1: Level scheme in Yb I relevant for photo-ionization.

The photo-ionization process used in the experiment was implemented as a diploma thesis by Christian Paape [Paape, 2004] during the course of this PhD work. It is to our knowledge the first working instance of photo-ionization of ytterbium for ion trap purposes. Several experiments pertaining to the characterization of the process were conducted at the linear trap, including a newly built oven with natural abundance isotope distribution. These results - that extend the work of the aforementioned diploma thesis - are presented in this thesis. First, in this section the theoretical features of the ionization process are discussed. Later, Chap. 4 details the experimental advantages and results.

Fig. 4.1 depicts the relevant lower energy levels in Yb I. Starting from the $^1S_0$ state several energy levels may serve as a first excitation level from which the actual ionization process occurs. The inter-combination line near 555.6 nm has been extensively studied by Borisov [Borisov et al., 1998] and Tkachev [Tkachev & Yakovlenko, 1996] as starting point for a photo-ionization process. Unfortunately, this wave-length is only accessible with a dye-laser, which is experimentally cumbersome in comparison to a diode laser. We therefore concentrate on the transition to the $^1P_1$ level near 398.9 nm, as a laser diode is readily available at this wave-length.

The ionization energy for Yb I is 6.25 eV, equivalent to 50443.2 cm^{-1}. Fig. 4.2 shows that a second light-field with a wave-length below 394 nm is required to reach the contin-

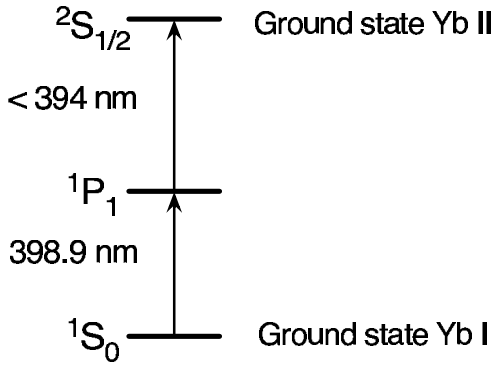

Figure 4.2: Ionization scheme. After excitation of the $^1P_1$ state a second photon with a wavelength smaller than 394 nm is required to ionize the atom.

uum. This process has already been proposed by Sankari et al. [Sankari & Suryanarayana, 1998]. Fortunately, the second light-field is easily supplied by the cooling laser for the Yb II ion near 369 nm which is already present at the experiment. This makes this scheme very practical indeed, as only one other diode laser needs to be set up. In the following this process is termed 'two-color' ionization.

This is in contrast to the scheme presented in the remainder of this section, which we call 'one-color' ionization. It turns out that the second light-field near 369 nm is not necessary to ionize the ions in an ion trap, but that only the laser at 398.9 nm is enough. We developed several explanations for this observation, which shall briefly be sketched in the following.

First, the possibility of resonantly exciting a Rydberg state with a second photon at 398.9 nm was investigated. From there, a third photon at the same wave-length could excite the atom into the ionic state, or else through field ionization by the electrical field of the trapping potential. Starting from the $^1P_1$ level the dipole-selection rules allow only transitions into either S- or D-Rydberg states, as $\Delta\ell = \pm 1$. Investigations of the energy levels of the S- and D-Rydberg series show that no level exists at $50136.444\,\mathrm{cm}^{-1}$, the energy corresponding to two photons at 398.9 nm [Xu et al., 1994, Camus et al., 1980]. The nearest singulett states are the $6s23s^1S_0$ at $50130.98\,\mathrm{cm}^{-1}$ and the $6s22d^1D_2$ at $50148.59\,\mathrm{cm}^{-1}$, with an energy difference of $5.464\,\mathrm{cm}^{-1}$ and $12.146\,\mathrm{cm}^{-1}$, respectively. As a rough estimate, the dipole moment scales with n^2, and will be on the order of 400-500 times larger than the ground-state dipole moment, implying a line-width of approximately 40 GHz or $1\,\mathrm{cm}^{-1}$. This dipole moment is distributed over the different possible ℓ states, which number $\sum_\ell^{n=22}(2\ell+1) \approx 500$. Taken together the transition line-width is estimated to be on the order of the ground-state transition, i.e. approximately 100 MHz or $3 \cdot 10^{-3}\,\mathrm{cm}^{-1}$. This

is much smaller than the detuning calculated above, and we therefore exclude this channel as a likely candidate for the observed photo-ionization by a single light-field.

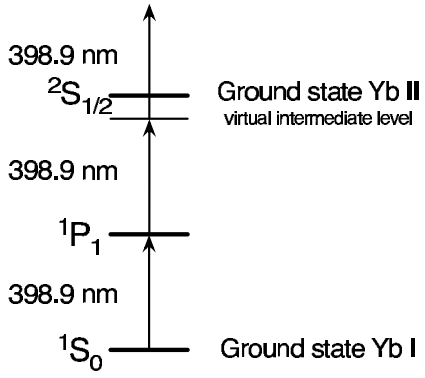

Figure 4.3: Photo-Ionization by two-photon excitation with an intermediate virtual energy level.

A second explanation is a two-photon absorption process following resonant excitation of the $^1P_1$ state. Fig. 4.3 shows the relevant energy terms. Starting from the $^1P_1$ state after resonant excitation from the ground state a two-photon absorption process occurs that lifts the electron into the continuum. As both photons and the first resonant excitation photon stem from the same source the probability for this transition should depend on the cube of the intensity of the light field. This dependence was experimentally refuted in our lab [Paape, 2004], and the excitation of a virtual level is excluded as explanation for the photo-ionization process.

Fig. 4.4 (a) shows another possibility. The influence of the trapping potential lowers the ionization threshold such that a second photon at 398.9 nm directly reaches the continuum. The Stark effect of the trapping potential changes the energy levels of the atom, and the binding Coulomb potential is directly altered as depicted in part (b) of the same figure. Assuming a linear dependence of the external electric potential an asymmetric binding potential with a saddle point results [Demtröder, 2003]:

$$V = -\frac{e}{4\pi\epsilon_0}\frac{1}{r} - |\vec{E}|r. \tag{4.1}$$

The saddle point is found at

$$r = \sqrt{\frac{e}{4\pi\epsilon_0|\vec{E}|}}, \tag{4.2}$$

which leads to a lowering of the threshold by

$$\Delta E = \sqrt{\frac{e^3|\vec{E}|}{\pi\epsilon_0}}. \tag{4.3}$$

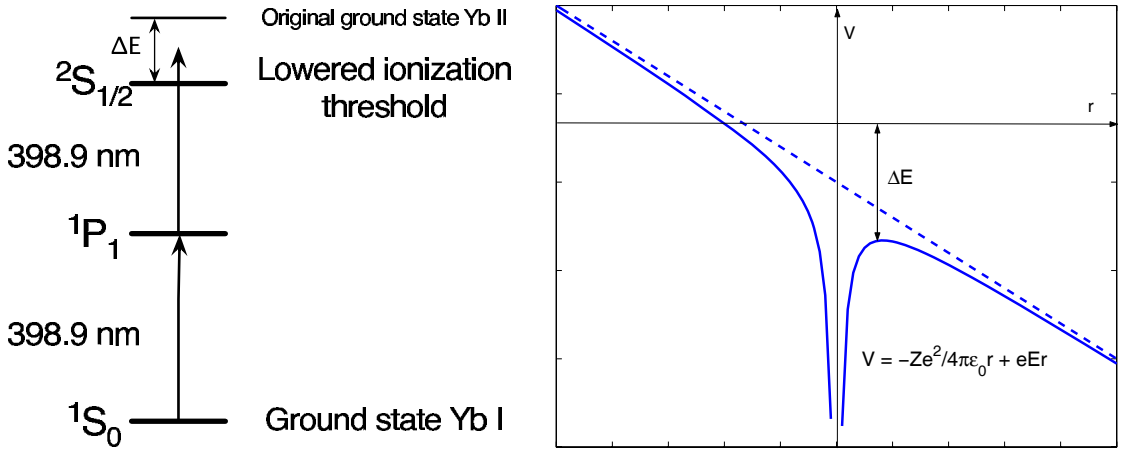

(a) Field ionization scheme

(b) Lowering of the ionization threshold

Figure 4.4: Photo-Ionization by field ionization. The ionization threshold is lowered due to the electric field of the trapping potential (a). This is explained by an alteration of the binding Coulomb potential as shown in (b).

Inserting $|\vec{E}| = 7 \cdot 10^5$ V/m - a typical value for the ion traps employed - yields a lowering of $\Delta E = 511.5$ cm^{-1} to 49931.7 cm^{-1}. This is lower than the energy of two photons at 398.9 nm (50136.4 cm^{-1}), and accordingly this is a reasonable explanation for the observed photo-ionization by the laser at 398.9 nm alone.

4.2 Atomic excitation spectra

An important parameter for the atomic excitation spectra is the angle formed by the $\vec{k}$ vector of the laser light and the velocity vector $\vec{v}$ of the atoms. The Doppler effect shifts the measured atomic resonance by an amount v/c, such that

$$\nu = \nu_0(1 \pm \frac{v}{c}). \tag{4.4}$$

Here, ν is the Doppler shifted resonance frequency and ν_0 is the undisturbed resonance frequency of the atomic transition. The resonance frequency is lowered for atoms flying away from the observer, and vice versa. The Doppler-broadening of the spectra due to the Boltzmann velocity distribution of the atoms becomes the dominating factor for the measured line-width when an appreciable part of $\vec{v}$ points in the direction of $\vec{k}$. On the other hand, the Doppler broadening vanishes for $\vec{k} \perp \vec{v}$. Therefore, the ovens were inserted into

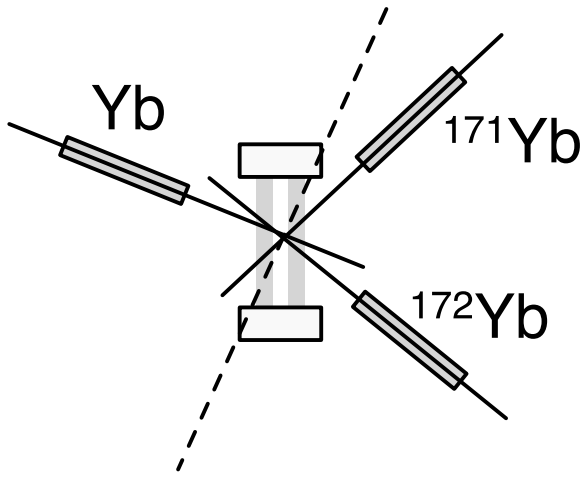

Figure 4.5: Approximate position and direction of the three atomic ovens. The dashed line indicates laser beam direction. Neither positions nor directions are to scale.

the vacuum recipient as depicted in Figure 4.5. With the goal of isotope-selective photo-ionization the isotope shifts of the atomic resonances need to be resolved. To avoid Doppler broadening, care was taken to insert the natural abundance oven ('Yb' in Figure 4.5) at an angle of approximately 90° to the expected laser beam direction. For the other ovens the reduction of the line-width was not necessary nor desirable, as the broader resonances are less sensitive to frequency drifts of the uncontrolled ionization laser. Due to the mechanical constraints of the trap design the ^{172}Yb oven was still very close to 90°, whereas the ^{171}Yb oven is quite oblique as indicated in the figure. The angles were not measured.

Excitation spectra for ^{171}Yb and ^{172}Yb

Figure 4.6 shows the atomic excitation spectra for the isotope pure ^{171}Yb and ^{172}Yb ovens. For each scan the ovens are pre-heated for several tens of minutes to reach thermal equilibrium. Only the photo-ionization laser at 398.9 nm is directed into the trap to avoid stray light from the other lasers. The trapping potential is turned off. Thus a larger ion cloud in the center of the trap and more importantly in the center of the detection volume does not influence the atomic beam. The fluorescence rate collected from the atoms by the photo-multiplier is plotted against the scan detuning in MHz. The detection path is optimized to yield maximum fluorescence signal. This mainly implies variation of the condenser position (cf. Sec. 3.3.1), as the atomic beams cross the trap center at slightly different positions. The range of the scan is determined by measuring the wave-length of the laser at the beginning and the end of the scan.

The signal in (a) is clearly Doppler-broadened and of Gaussian lineshape, as expected from the position of the oven. The numerical fit of a Gaussian profile to the data yields a line-width (FWHM) of $\sigma = 634$ MHz. A non-linearity of the scan distinctly deviates the measured data from a perfect Gaussian shape. It is assumed that the wave-length of the laser does not linearly follow the voltage applied to the optical grating. This has not been examined in detail. The background stray-light from the laser is increasing during the scan, an effect that is reproducible and supposed to stem from the spatial beam variation by the turning grating of the diode laser.

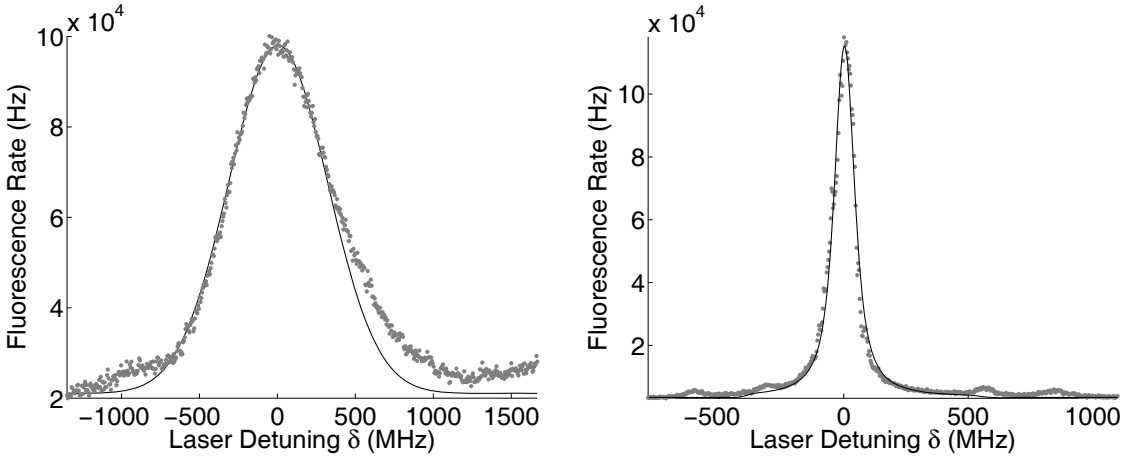

(a) ^{171}Yb (b) ^{172}Yb

Figure 4.6: Atomic excitation spectra near 398.91 nm for the ^{171}Yb and ^{172}Yb oven. The signal from the ^{171}Yb oven is clearly Doppler broadened, with a line-width of $\sigma = 634$ MHz. The ^{172}Yb oven forms an angle close to 90° with the incoming laser light. The signal from the ^{172}Yb oven is almost Doppler free: a fit with a Voigt profile yielded $\sigma = 41$ MHz and $\Gamma = 2\pi \cdot 145$ MHz.

In (b) of Figure 4.6 the same scan for the ^{172}Yb oven is shown. The line-width of this atomic resonance is distinctly smaller, and the shape clearly more Lorentzian than Gaussian. A numerical fit of a Voigt profile to the measured data yields a Gaussian line-width of $\sigma = 41$ MHz and a Lorentzian width of $\Gamma = 2\pi \cdot 145$ MHz. Apparently the Doppler broadening is mostly eliminated by the angle between the laser and the atomic beam close to 90°. The high value of Γ in comparison to the natural line-width of 28 MHz is power broadening. Furthermore, some atoms from the slightly diverging atomic beam will always have a rest velocity in the direction of the laser beam, and hence experience a Doppler shift. Thus even for lowest excitation light levels the line-width does not decrease

below approximately 60 MHz. Nonetheless, these line-width values are all below the isotope shift of the different isotopes of ytterbium. Thus, the rest abundance of other isotopes is visible by the small excitation peaks to the left and right of the main resonance. The rest abundance is below 5% for all isotopes, measured as the peak amplitudes in relation to the maximum amplitude from the ^{172}Yb signal. This demonstrates a good enrichment of the material employed. The identification and the exact spectral position of the other isotopes will be determined in the next section.

Excitation spectra for natural abundance ytterbium

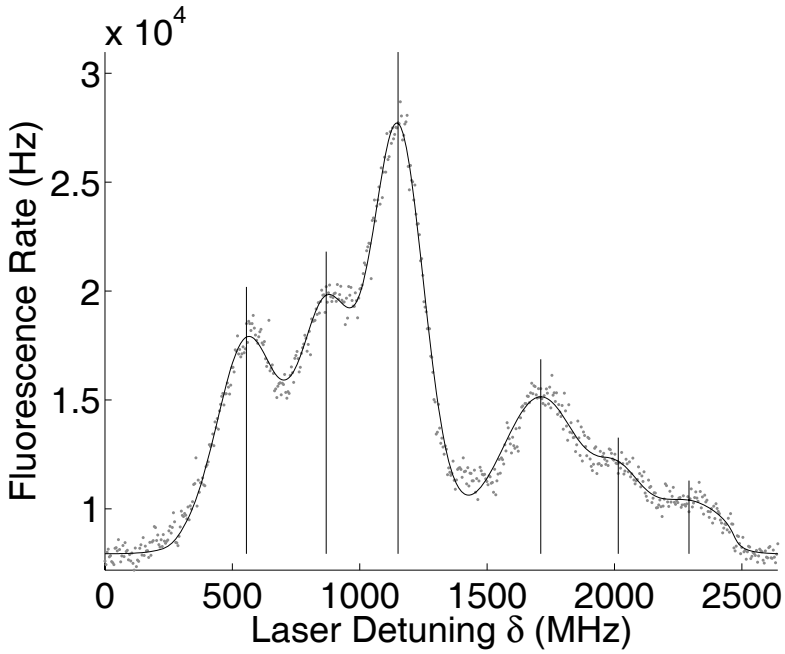

Figure 4.7: Doppler-broadened atomic excitation spectrum from the oven with natural abundance isotope distribution. The data (grey dots) is numerically fitted to a sum of six Voigt-profiles (black line).

Figure 4.7 and Figure 4.8 show the atomic excitation spectra for the newly build oven with natural ytterbium. To demonstrate the dependence of the line-width from the angle between the laser and the atomic beam both a Doppler-broadened and an almost Doppler-free spectrum are shown. The direction of the laser beam was variable in a range of approximately 30°, limited by the input window of the recipient and the necessity to direct the laser through the trap itself. The scans were taken several weeks apart. The scan method is the same as described in the section before.

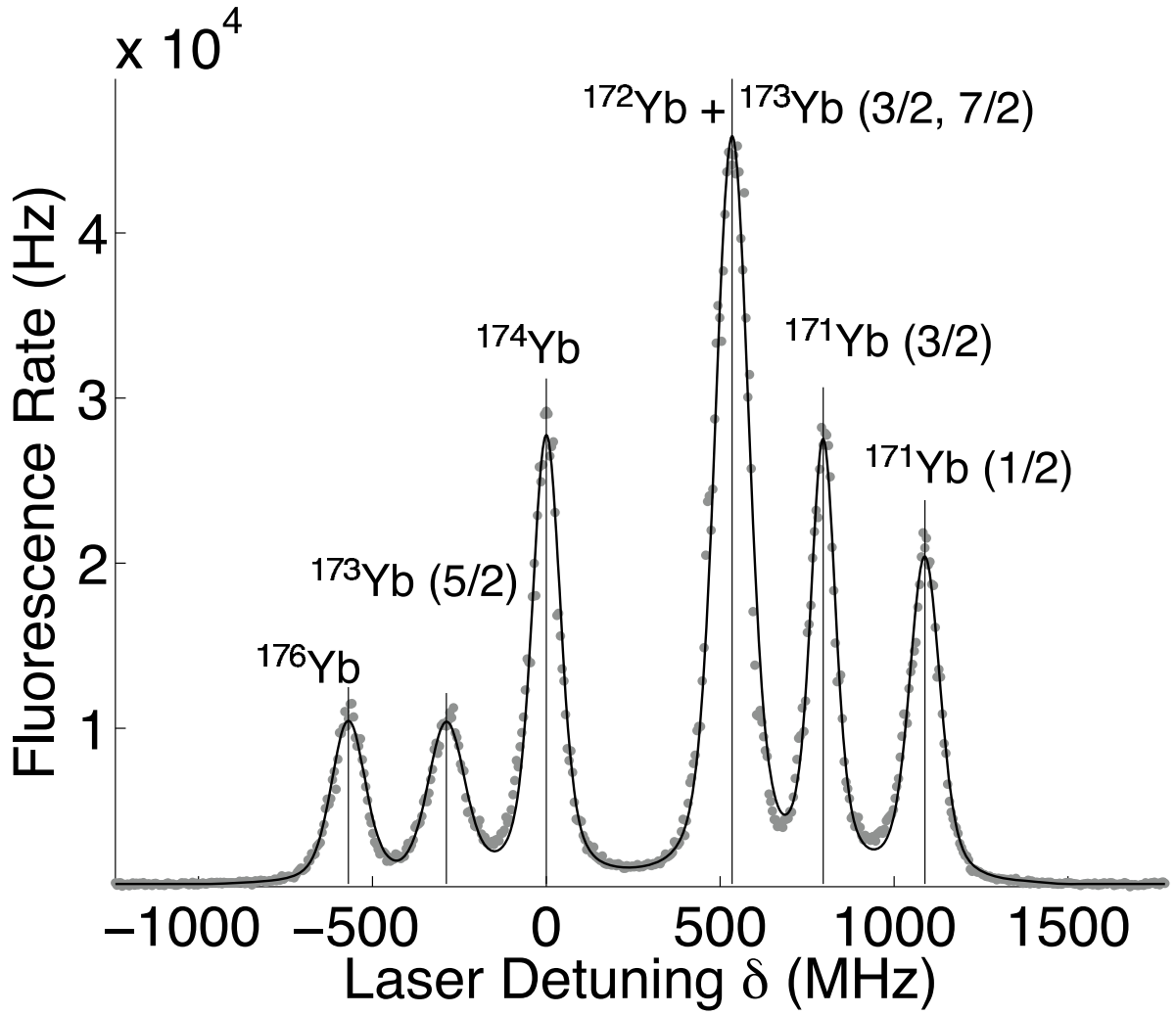

Figure 4.8: Doppler-free atomic excitation spectrum.

In the end the Doppler broadening could be avoided to a large part by aligning the laser beam to form an angle of close to 90° with the oven. Figure 4.8 clearly shows six well-resolved resonance peaks. Comparison with the literature allowed for the determination of the different isotopes as indicated in the graph [Banerjee et al., 2003]. The data was numerically fitted to a sum of six Voigt-profiles. The Lorentzian line-width was determined to 80 MHz (one parameter for all six isotopes), the Gaussian line-width varied between 53 MHz and 87 MHz (six free parameters). No clear dependence between the Gaussian line-width and the isotope number was observed. Furthermore, some of the values for the amplitude deviate from the values expected from the natural isotopes distribution. The calculated values are 3.05%, 16.12%, 31.8%, 54.14%, 14.3% and 17.35%, going from left

to right in Figure 4.8, and using the natural abundance distribution from Appendix C. Normalizing the amplitudes from the fitted spectrum to the largest peak the measured values are 13.7%, 13.3%, 34.2%, 54.1%, 33.6% and 26.1%. Here, a possible difference in oscillator strength on the ground-state transition is neglected, as well as the small difference in the velocity distribution created by the different masses. The origin of the deviation remains puzzling, but for the three middle peaks comprising the main isotopes ^{172}Yb, ^{173}Yb and ^{174}Yb the agreement is satisfactory.

Table 4.1 lists the different isotopes shifts derived from this data in comparison to the data presented by *Banerjee* et al. [Banerjee et al., 2003]. The accuracy of our measurement is limited by the accuracy of the lambda-meter. The starting point and the end point of the scan are determined to within ±95 MHz on a scan range of approximately 3 GHz. This yields an uncertainty almost two orders of magnitude higher than published by Banerjee et al. As the main focus of our work is on the ionic state of ytterbium this accuracy is well enough. Within the error ranges the data agree well.

Isotope	this work (MHz)	Banerjee (MHz)
176	-554 ± 35	-509.98 ± 0.75
173 (5/2)	-262 ± 16	-254.67 ± 0.63
174	0	0
172	534 ± 33	533.90 ± 0.70
171 (3/2)	822 ± 51	833.24 ± 0.75
171 (1/2)	1104 ± 69	1152.86 ± 0.60

Table 4.1: Comparison of isotopes shifts in the atomic excitation spectrum of the $^1S_0 \rightarrow {}^1P_1$ transition in Yb I gained in this work with a measurement by Banerjee et al. [Banerjee et al., 2003].

Isotope selectivity

The isotope selectivity is an interesting aspect of the photo-ionization scheme as it eliminates the need for isotope enriched material and allows to ionize even the isotopes with lowest abundance. In a similar experiment with neutral ytterbium, for example, a cloud of ^{168}Yb I was optically trapped in a magneto-optical trap in the presence of all other isotopes [Rapol et al., 2004]. For ion traps the isotope-selectivity of photo-ionization of rare isotopes has been demonstrated by trapping isotope-pure $^{43}Ca^+$ crystals [Lucas et al., 2004]. Several different ideas were pursued to verify the isotope-selectivity in our lab, which are presented in the following.

As a first qualitative test small clouds of $^{172}Yb^{+}$ ions were trapped from the natural abundance oven. This posed no problem as long as the wave-length of the ionization laser was set to approximately the right wave-length. A detuning of the ionization laser on the order of the smallest isotope shift (255 MHz) is large enough to severely reduce the loading rate such that no small ion clouds were detected anymore.

The direct proof of isotope selective ionization would be the trapping of an isotope pure string of ions for different isotopes. We were not able to identify the experimental parameters - mainly laser wave-lengths - for the other isotopes, as no reference for the isotopes shift of the $D_{3/2} \rightarrow [3/2]_{1/2}$ transition at 935 nm exists. Nonetheless a quantitative

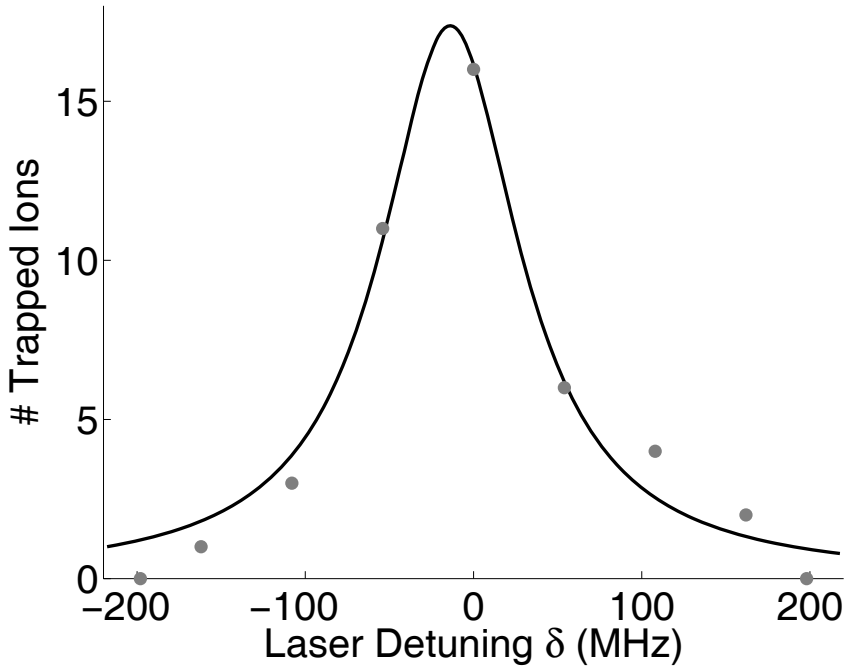

Figure 4.9: Ionization spectrum for different detunings of the ionization laser. The experimental data (asterisks) is numerically fitted to a Lorentzian line-shape (solid line). The full width at half-maximum is 100 MHz. Already at a detuning of 200 MHz no ions are trapped anymore, underlining the isotope selectivity of this process. The data is taken from [Paape, 2004].

analysis was carried out in the ring trap present in our lab [Paape, 2004]. No oven with natural ytterbium was present in the ring trap. Using one-color ionization the wave-length of the ionization laser at 398 nm was detuned and an ionization profile derived from the number of trapped ^{172}Yb ions for a given interaction time. For this experiment, the trap was emptied for each run and the cooling lasers were blocked. The isotope-pure ^{172}Yb oven was in equilibrium at a high oven current. The ionization laser alone shone into the trap

for a interaction time of $\tau = 30\,\mathrm{s}$. The ionization laser was blocked and the cooling laser at 369 nm and the repump laser at 935 nm were unblocked to cool the trapped ions. For the small number of ions trapped during this period the exact number could be determined from the fluorescence level. This process was repeated for several detunings of the ionization laser. Figure 4.9 shows the data together with a numerical fit of a Lorentzian profile. The line-width of the profile is 100 MHz (= FWHM), which is below the lowest isotope shift of 255 MHz (see Table 4.1). More importantly, at a detuning of the ionization laser of± 200 MHz no ions were trapped anymore.

4.3 Deterministic number loading of ions

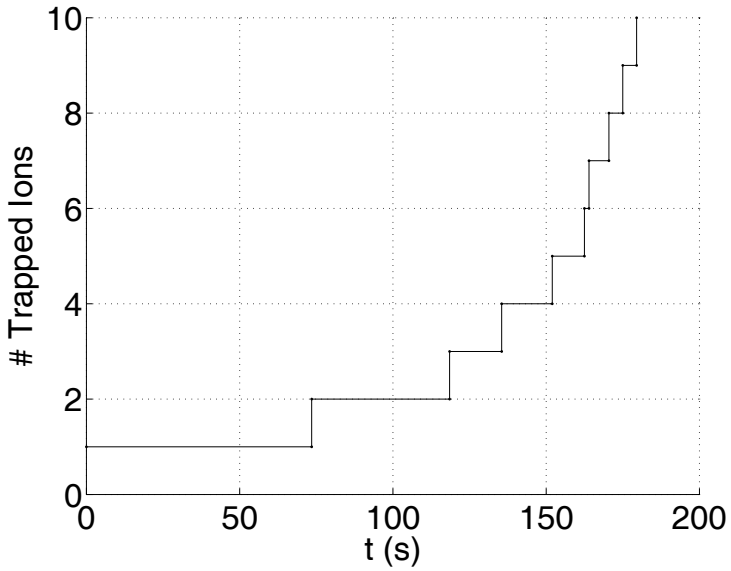

Figure 4.10: Deterministic loading of a certain number of ions. The oven is heating. The number of ions is determined by simply counting them in the CCD-image.

For electron impact ionization, the oven typically has to heat for some 10 minutes for an adequate atom flux. At such a steady atom flux there always remains the chance of trapping two ions at the same time. Through the high efficiency of the photo-ionization process an almost deterministic loading of a desired number of ions is feasible. The following procedure has been established to load a low number of ions into the trap. This process is depicted in Figure 4.10. Starting from a cold oven the heating current is applied (in our case 6 A), and the ionization laser at 399 nm is directed into the trap in addition to the already present cooling laser at 369 nm and 935 nm. When the ionization laser is near

resonance it takes about a minute before the first ions is ionized. The ion is immediately laser cooled, and becomes localized and visible. As the oven is still heating the chance to load a second ion is quite small. If just a single ion is desired, the ionization laser is blocked and the oven current turned off. For higher ion numbers the ionization process continues. The graph clearly shows the increasing probability to load an ion due to the increased atom flux. Nonetheless, on the time-scale given it is easy to simply stop at the desired number of ions by blocking the ionization laser.

5

Addressing single Yb^+ ions

This chapter presents the main experimental results of this thesis. A RF-optical double-resonance spectroscopy was set up to manipulate and probe the state of the ion in the $D_{3/2}$ level. It facilitates the experimental characterization of the four Zeeman sub-levels of the $D_{3/2}$ state, and serves as a tool to measure the effect a magnetic gradient field has on this level-structure for different ions. Sec. 5.1 details the experimental technique itself. With it, both the static magnetic fields that define the quantization axis, and the dynamic magnetic fields manipulating the ions state are characterized in Sec. 5.2 and Sec. 5.3, respectively. The latter is accompanied by a set of numerical simulations of the interaction dynamics, based on the analytical representation of the four-level Bloch equations derived in the theoretical part. Finally, Sec. 5.4 presents the simulations and measurements pertaining to the setup and operation of the magnetic gradient field. There, the addressing of single ytterbium ions within an ion crystal is demonstrated.

5.1 RF-optical double-resonance spectroscopy of a Yb^+ ion

In this section the magnetic dipole transition between the Zeeman levels of the $D_{3/2}$ state of $^{172}Yb^+$ is characterized. The ion is continuously irradiated with both RF-radiation and laser light at 935 nm and at 369 nm. Tuning the radio-frequency leads to fluorescence spectra with a Lorentz-profile as explained in Sec. 2.3.3. Figure 5.1 briefly recapitulates the energy levels relevant for this section. The $D_{3/2}$ level is populated by spontaneous

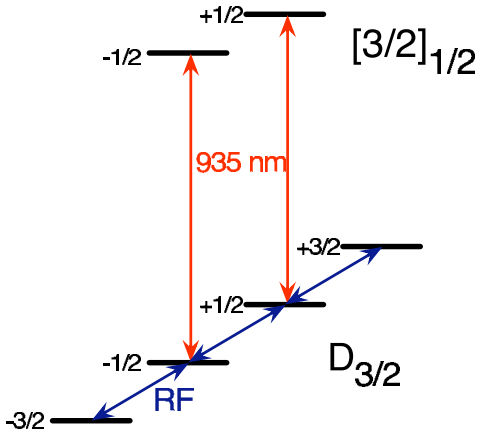

Figure 5.1: Relevant energy levels for the incoherent spectra to characterize the $D_{3/2}, \Delta m_j = 1$ transitions. The RF-radiation couples the different Zeeman sub-levels of the $D_{3/2}$ by M1-transitions. Additionally, the $m_j = \pm 1/2$ levels of the $D_{3/2}$ are coupled to the $[3/2]_{1/2}$ level by the laser light field at 935 nm.

emission from the $P_{1/2}$ level. The laser near 935 nm with π-polarization selectively couples only the $|D_{3/2}, m_j = \pm 1/2\rangle$ levels back to the cooling cycle via the $[3/2]_{1/2}$ level, which rapidly decays back into the ground state $S_{1/2}$. The $|D_{3/2}, m_j = \pm 3/2\rangle$ levels are coupled to the $|D_{3/2}, m_j = \pm 1/2\rangle$ by the RF-field with a Rabi-frequency $\Omega_{\mathrm{rf}} = \vec{\mu} \cdot \vec{B}_{\mathrm{rf}}$.

The parameters of a Lorentz-profile are the amplitude, line-width and center frequency. The center frequency is equal to the Larmor-frequency of the M1-transition, and as such determined by the Zeeman-splitting of the $D_{3/2}$ for a given magnetic field. The static magnetic fields are treated in Sec. 5.2 by measurement of the Larmor-frequency. Here, the variation of the line-width (Sec. 5.1.1) and the amplitude (Sec. 5.1.2) of the spectra with respect to the power of the RF-radiation P_{rf} and the power of the laser light field at 935 nm P_{935} is examined.

5.1.1 Line-width

Without using a RF-field the Zeeman sub-levels of the $D_{3/2}$ level are left uncoupled amongst themselves. The spontaneous transition rate between the levels with different m_j is negligible, and accordingly the life-time of the levels is very high. The $D_{3/2}$ level of course has a life-time of 52.2 ms and a line-width of 3 Hz [Balzer, 2003] with regard to the ground state $S_{1/2}$. This life-time is so long in comparison to the relevant time-scale of the $\Delta m_j = \pm 1$ transitions ($\approx 50\,\mu s$) that its influence can be neglected for the observations in this section. The line-width induced by these transitions has been calculated in Sec. 2.3.3 to be $\sqrt{7}\Omega_{rf}$ (see Eq. 2.57).

If we were looking exclusively at the M1 transition the line-width would be completely determined by this relation. As it is, the $|D_{3/2}, m_j = \pm 1/2\rangle$ levels are selectively coupled to the $[3/2]_{1/2}$ level by the laser light field at 935 nm. The depopulation of these levels by the repump laser can be regarded as a spontaneous decay, with the life-time of the decay on the order of the inverse optical Rabi-frequency Ω_{935}. This process leads to broadening of the line-width of the M1-transition, just like a 'normal' spontaneous decay would. Both types of line-width broadening were examined in the course of this thesis, and the experimental results are presented in the following paragraphs.

Line-width broadening due to the repump laser

For the experiments concerning the line-width broadening due to the laser power all experimental parameters except the laser power were kept constant. The RF-power P_{rf} driving the RF-coil (see Sec. 3.4.2) was set to a constant 31 dBm by amplifying the -9 dBm output signal of a *Rhode&Schwarz* frequency generator with a *Kalmus* 110C RF-amplifier, creating a RF-field with constant magnetic amplitude $\vec{B}_{rf}$. The power of the repump laser at 935 nm, P_{935}, is varied by a combination of a retardation plate ($\lambda/2$ plate) and a polarizing beam splitter (PBS). The PBS determines the polarization going into the trap (see also Sec. 3.2.4), and the retardation plate is turned such that the desired power is transmitted by the PBS. The laser power P_{935} was varied between 10 µW and 500 µW (measured behind the overlay unit and in front of the lens focusing the laser light into the trap), and the resulting graphs are shown in Figure 5.2. Two different regimes are shown. In part (a) of that figure the differences are high, varying between 30 µW, 100 µW and 500 µW. In part (b) of the figure the laser power varies only at low values between 10 µW and 50 µW. This distinction was made to demonstrate that for high powers the line-width is distinctly influenced, whereas below a certain value of the laser power the line-width is nearly independent of the laser power. This is important for practical purposes when striking a

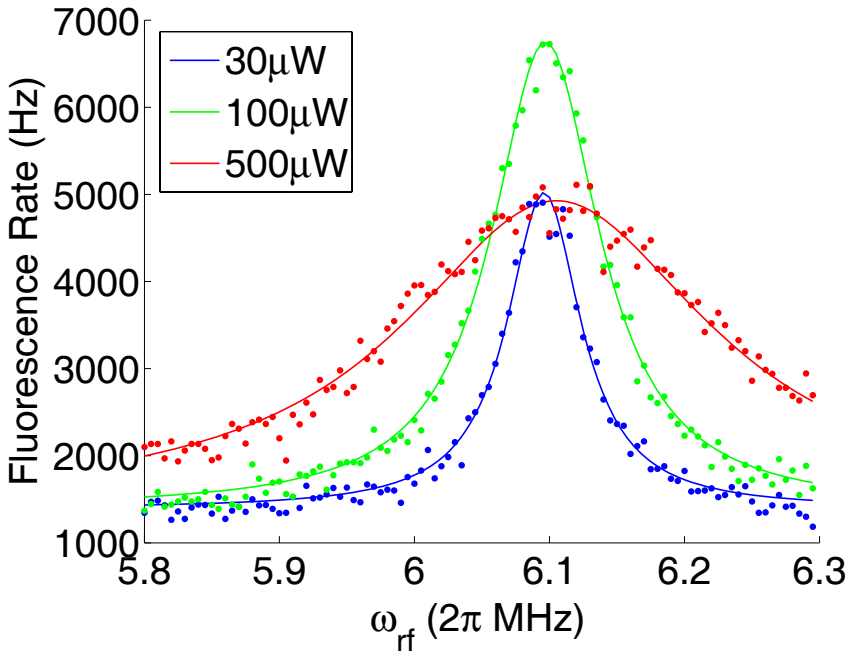

(a) Variation of profile line-width at high power P_{935}, ranging between 30 µW, 100 µW and 500 µW.

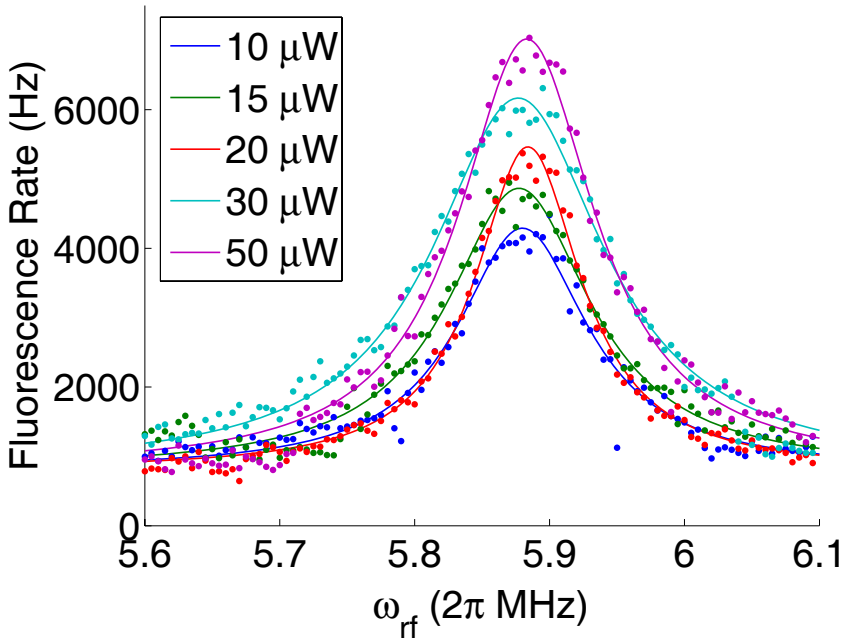

(b) Variation of profile line-width at low power P_{935}, ranging between 10 µW and 50 µW.

Figure 5.2: Line-width broadening of the $D_{3/2}, \Delta m_j = 1$ transitions induced by the laser power P_{935} of the repump laser at 935 nm. For large differences in power (a) the line-width decreases distinctly with power, at lower powers (b) the variation of the laser power does not significantly influence the line-width.

compromise between enough signal and small line-width for high resolution.

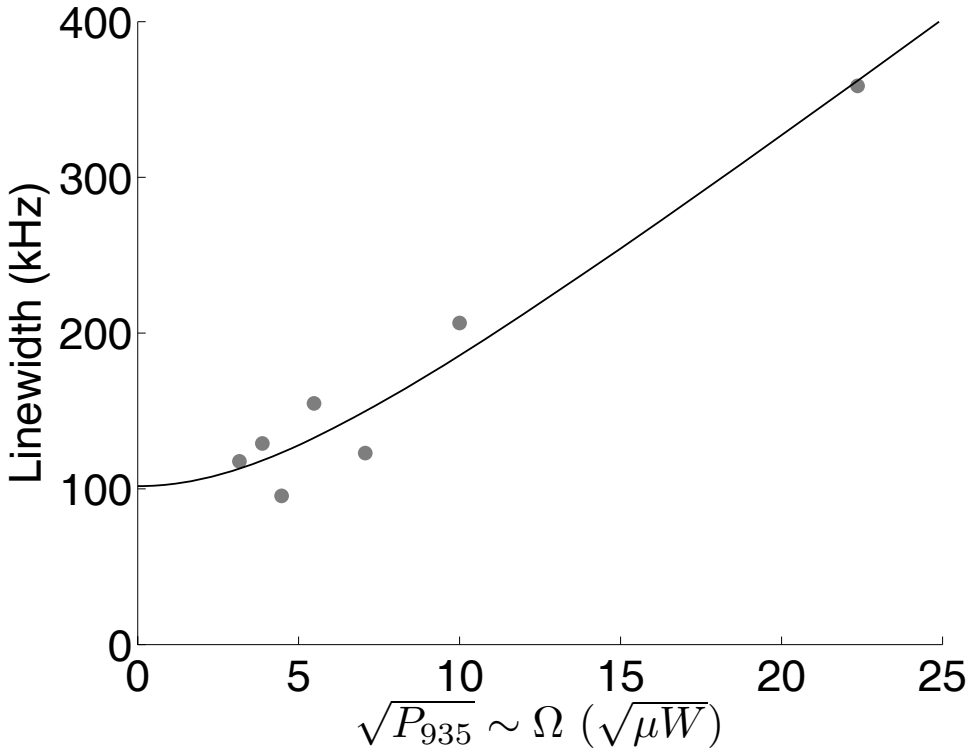

Figure 5.3: The variation of the line-width as extracted from Figure 5.2 above, plotted against the square-root of the laser power P_{935}. The measured data (gray dots) is numerically fitted to Eq. 2.59 (solid line). The ordinate of the fit yields the line-width induced by the RF-radiation, which is 102 kHz.

The line-widths Λ (full width at half maximum, FWHM) of the data for Figure 5.2 are extracted from the numerical fit of the Lorentz-profiles and plotted in Figure 5.3. For large values of Ω_{935} the line-width tends to a linear dependence. This is why the data in Figure 5.3 is plotted against the square-root of the laser power, bearing in mind that

$$\Omega_{935} \sim E \sim \sqrt{I} \sim \sqrt{P_{935}}. \tag{5.1}$$

A numerical fit of the data to Eq. 2.59 yields an ordinate value of 102 kHz, which is equivalent to the line-width caused by the RF-transition. The graph agrees satisfactorily with the theoretical prediction. The fluctuations at low powers are due mainly to the experimental procedure. For every scan a new ion is trapped, with accompanying heating of the oven. Due to collision with background atoms the experiment time is limited, and the apparatus does not have the time to reach thermal equilibrium. As a result, the

ions position will shift from run to run in a non-deterministic manner, and especially the relative position of the ion to the laser focus. This problem will be addressed in future measurements. Consequently, the real laser power and a sensible error estimate are not possible for this graph. As an important qualitative result we note that the line-width broadening due to the laser power is reduced significantly in comparison to the line-width induced by the rf-radiation.

Variation of RF-power

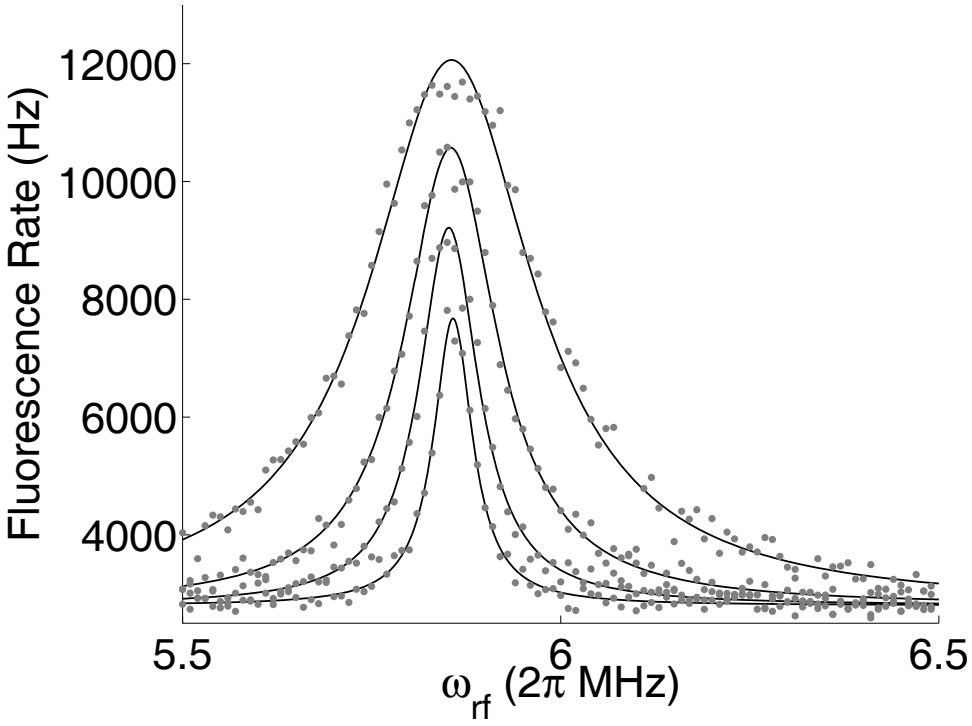

Figure 5.4: Frequency scans for different RF-power levels, implying different amplitudes $\vec{B}_{\mathrm{rf}}$ of the magnetic component of the RF-field. For the scans shown the RF-power is varied from 25 dBm (lowest amplitude) to 37 dBm (highest amplitude) in steps of 4 dB. The power of the repump laser at 935 nm is low ($P_{935} = 50$ µW).

Figure 5.4 shows the different profiles obtained under variation of the RF-power P_{rf}. The power of the repump laser was set to $P_{935} = 50$ µW. For clarity only four of the nine spectra taken are displayed exemplary. All experimental parameters were kept constant except P_{rf}. The output level of the frequency generator (R&S SMG) is varied between -1 dBm and -19 dBm in steps of 2 dB. The amplifier (Kalmus 110C) has a gain of 40 dBm and

a maximum power of 10 W. All profiles are clearly Lorentzian, and again the parameters for each profile are extracted by numerically fitting the data.

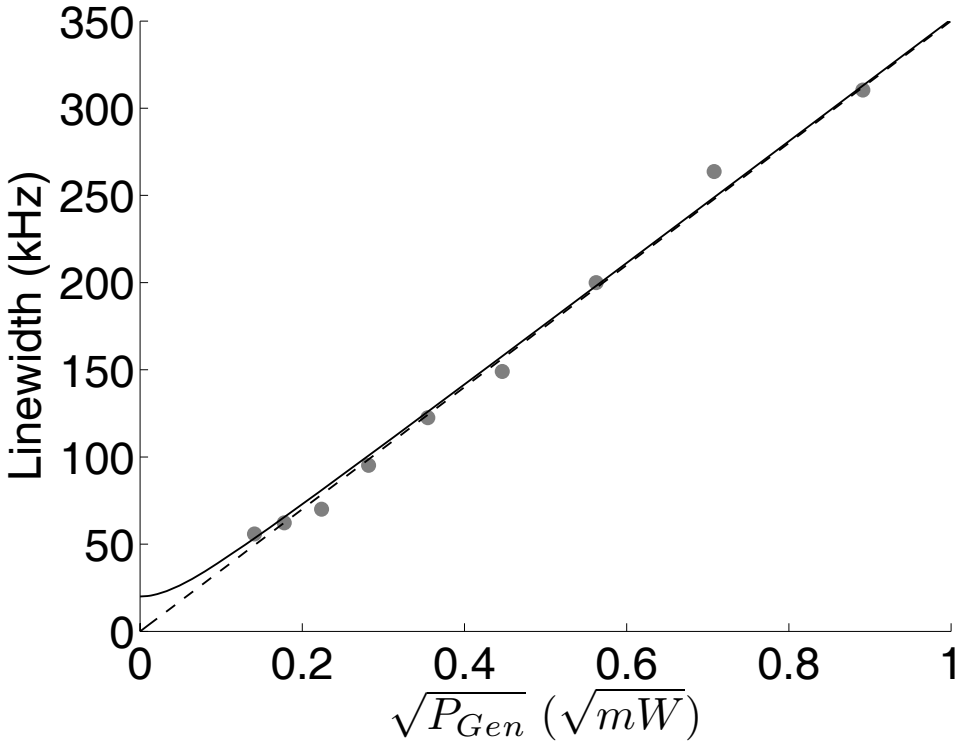

Figure 5.5: The variation of the line-width as extracted from Figure 5.4 above. The line-width Λ (FWHM) is plotted against the square-root of the RF-power. The measured data (gray dots) is numerically fitted to a linear dependence (dashed line) and manually fitted (see text) to Eq. 2.59 (solid line). The manual fit can be regarded as an approximate upper bound on the line-width broadening caused by the repump laser, P_{935} (see text).

Figure 5.5 depicts the extracted line-widths Λ (FWHM) plotted against the square-root of P_{rf}. The line-width is expected to also obey Eq. 2.59. The measured data in gray dots is shown together with both a fit to Eq. 2.59 (solid line) and a linear fit (dashed line). The solid line is a semi-numerical fit of Eq. 2.59, with a fixed value of 20 kHz for the optical Rabi-frequency Ω_{935}. With the optical Rabi-frequency as a free parameter the fit yielded a value for it that is practically zero (< 1 mHz), which is physically not sensible. The 20 kHz used for the graph shown is an eye-estimate where the function still agrees reasonably to the measured data. Any value between 0 and 20 kHz gives a graph that is a reasonable representation of the measured data. As a conclusion we derive from this graph that the line-width broadening induced by the repump laser is quite small, with an estimated upper bound of 20 kHz.

The Rabi-frequency Ω_{rf} is estimated using Eq. 2.59. If the optical depopulation of the $m_j = \pm 1/2$ levels is neglected for a moment, the relation between the line-width and the Rabi-frequency is simply given by a constant factor $2\sqrt{7}$. For the highest line-width of $2\pi \cdot 310\,\mathrm{kHz}$ this results in $\Omega_{\mathrm{rf}} = 2\pi \cdot 59\,\mathrm{kHz}$. Assuming the maximal line-width broadening of $2\pi \cdot 20\,\mathrm{kHz}$ due to the repump laser the value decreases to $2\pi \cdot 57\,\mathrm{kHz}$. This is on the same order of magnitude as the calculated value for this setup, which is 41 kHz (cf. Eq. 3.11). These values confirm that the line-width of the Lorentz-profile is not directly given by the Rabi-frequency Ω_{rf}, but that effects rising from the four-level dynamics have to be considered. The discrepancy between the two values shows that the simplifying assumptions made in Sec. 2.3.3 tend into the right direction but fall short of the exact solution.

5.1.2 Amplitude

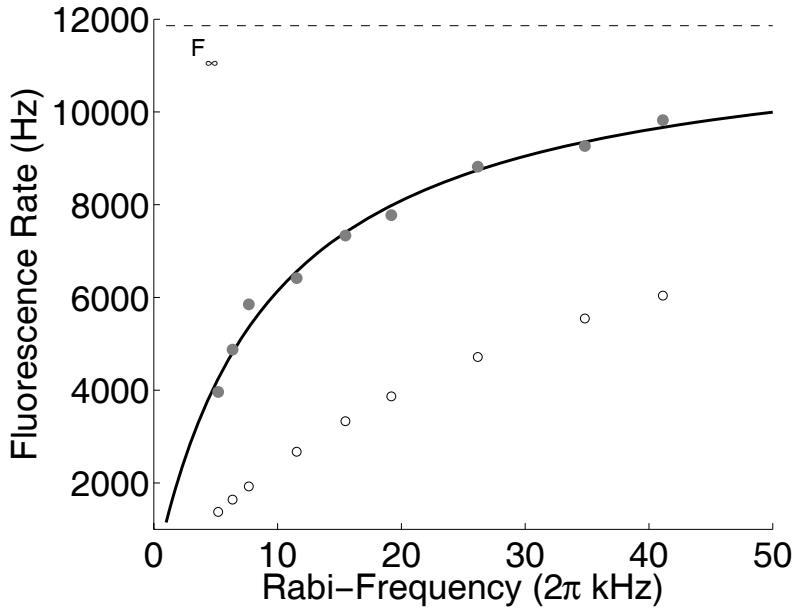

Figure 5.6: Variation of the amplitude of the Lorentz-profiles with regard to the Rabi-frequency of the RF-radiation (gray dots). Here, the Rabi-frequency is derived from the measured line-width shown in Figure 5.5. The solid line graph represents a fit of Eq. B.13 from the rate equation model to the data. The circles are values derived by directly inserting the Rabi-frequencies as transition rates (cf. Eq. 2.57) into the rate equation model.

The amplitude varies with the applied RF-power as well. This relation is depicted by the gray dots in Figure 5.6. The amplitude values are found by fitting and subtracting

the background level in Figure 5.4, and are directly given as a fluorescence rate in Hertz. They are plotted against a Rabi-frequency that is calculated from the line-width derived in Figure 5.5. The solid black line in Figure 5.6 shows a numerical fit of the data to Eq. B.13, where both the maximum fluorescence rate $\mathcal{F}_\infty$ and the saturation parameter b' were fit parameters. The resulting maximal fluorescence rate is indicated by the dashed line. Furthermore, the transition rate - linked to the Rabi-frequency by Eq. 2.57 - is directly inserted into the rate equation model presented in Appendix B. This calculated fluorescence rate is also shown in Figure 5.6 as open circles, normalized to $\mathcal{F}_\infty$.

It is apparent that the simple heuristic model developed in Sec. 2.3.3 does not accurately describe the experimental values. Apparently, the transition rate is distinctly higher than calculated with the simple model. To quantitatively describe the process involves solving the optical Bloch-equations for a 10-level system with two laser light fields and one rf-radiation field. As the model was not developed further in the course of this thesis it is necessary to admit that a thorough understanding of this complex is left to be desired for future work.

5.2 Static magnetic fields

This section details the experimental results characterizing the static external magnetic field present at the site of the ions. Although the magnetic gradient field is a static magnetic field too, it will be treated separately in Sec. 5.4. Here, the spatial orientation and strength of the magnetic field created by the set of field coils and the already present earth field are determined by RF-spectroscopy. For clarity we will separate the different magnetic

Symbol	Name	Source	Typical value
$\vec{B}_0$	residual field	earth-field, ion-getter pump	2.6 G
$\vec{B}_{\text{coils}}$	static (magnetic) field	magnetic field coils	0-30 G
$\vec{B}_{\text{grad}}$	(magnetic) gradient field	permanent magnets (anti-Helmholtz)	0-2 T/m
$\vec{B}$	resulting (magnetic) field	$\vec{B}_0$, $\vec{B}_{\text{coils}}$ [, $\vec{B}_{\text{grad}}$]	variable (see text)
$\vec{B}_{\text{rf}}$	RF-field	RF-coil	50 mG

Table 5.1: Nomenclature for the different magnetic fields used in this chapter.

fields into four expressions. The magnetic field present at the site of the ions without any other magnetic field created experimentally is called the residual field $\vec{B}_0$. The major component of $\vec{B}_0$ stems from the magnet of the ion getter pump. The static magnetic field created by the 'coil-cage' presented in Sec. 3.4.1 is termed $\vec{B}_{\text{coils}}$. The magnetic gradient

field created by the permanent magnets in anti-Helmholtz configuration is called $\vec{B}_{\text{grad}}$. The resulting magnetic field $\vec{B}$ is a sum of the above components. For the measurements presented in this section the gradient field was not set up, and hence the resulting field is $\vec{B} = \vec{B}_0 + \vec{B}_{\text{coils}}$. Finally, the magnetic component of the RF-radiation field is $\vec{B}_{\text{rf}}$. This is not a static magnetic field, and $\vec{B}_{\text{rf}}$ will be characterized in Sec. 5.3. For reference the nomenclature is summarized in Table 5.1, together with typical values of the absolute value of the fields.

Sec. 2.2.2 explains how the $\vec{E}$ vector of the light field needs to be parallel to the resulting $\vec{B}$ to optically pump the ion into the $|D_{3/2}, m_j = \pm 3/2\rangle$ levels. This is a preliminary for the RF-spectroscopy experiments performed in this work, and it nicely allows for the complete characterization of the $\vec{B}$-field. As a first step the earth field $\vec{B}_0$ is determined. By using the three pairs of coils presented in Sec. 3.4 an additional field $\vec{B}_{\text{coils}}$ is created to set the desired resulting magnetic field for the experiment. The resulting field is accurately measured with the RF-spectroscopy method. A numerical simulation of the magnetic field and a comparison between the simulation and the measurement conclude the section.

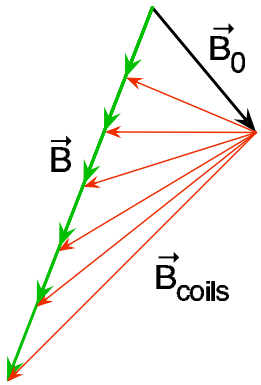

Figure 5.7: Scheme for the determination of $\vec{B}$. By variation of $\vec{B}_{\text{coils}}$ the length of the resulting $\vec{B} = \vec{B}_0 + \vec{B}_{\text{coils}}$ is varied, leading to different Zeeman-splittings and hence Larmor-frequencies of the RF-transition. For the resulting magnetic field $\vec{B} || \vec{E}_{935}$.

In Sec. 5.1 the magnetic field was kept constant and the different parameters for the RF-spectroscopy were varied. In this section the roles are reversed: the parameters for the RF-spectroscopy are kept constant and the magnetic field $\vec{B}$ is varied by changing the current flowing through the magnetic field coils. Figure 5.7 shows the principle idea. It is important not to forget that the orientation of $\vec{B}$ is determined in space by the polarization of the laser light field at 935 nm. To ensure optical pumping it is necessary that $\vec{E}_{935} || \vec{B}$. The residual field $\vec{B}_0$ therefore needs to add with the $\vec{B}_{\text{coils}}$ generated by the field coils to

a $\vec{B}$ that is parallel to $\vec{E}_{935}$. The polarization of the light field was not changed for this measurement series, and thus all resulting $\vec{B}$s need to be parallel to each other.

A series of Lorentz-spectra with ten different magnetic fields forms the experimental basis. The spectra were taken with a single ion each. Figure 5.8 exemplary depicts five of the ten scans for different magnetic fields in one figure. The data (gray dots) together with the numerical fit to the data of a Lorentz profile (solid line) is shown. The center frequencies are determined by the fit. The experimental procedure went as following.

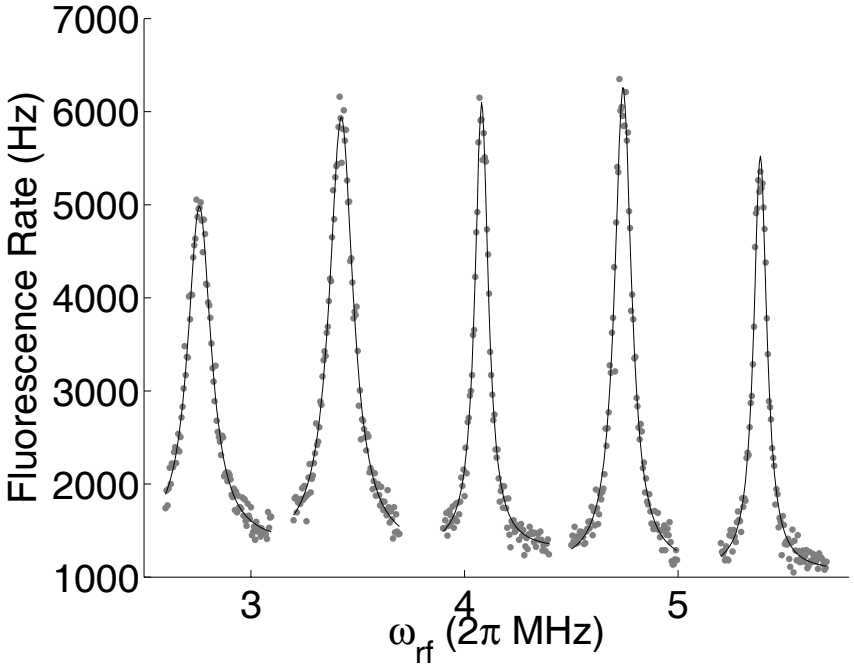

Figure 5.8: Five (of ten) exemplary RF-spectra to determine the magnetic fields at the site of the ion. The measurement data (gray dots) is fitted to a Lorentzian profiles (solid lines).

Choosing the x-axis as principal (perpendicular to the trap axis, pointing upwards to the ceiling of the laboratory) the current I_x through the coil-pair was varied in 100 mA steps from -700 mA ... +200 mA, corresponding to steps of approximately 1 G (see calibration data in Sec. 3.4.1). The current I_x was set to the desired value, and the RF-radiation turned off. With a small string of ions (5-10 ions) and using the photo-multiplier detection optical pumping was restored by adjusting I_y and I_z until the fluorescence signal vanished. The resulting magnetic field $\vec{B}$ is now re-aligned with the polarization of the light field of the repump laser. The large number of ions ensures that a small amount of rest excitation by misalignment of $\vec{B}$ and $\vec{E}_{935}$ is still detected. The trap is emptied and a single ion is trapped for the actual measurement.

As a result four parameters are derived from each scan: I_x, I_y, I_z and ω_{rf}. The magnetic field at the site of the ions can be determined in two ways from this data. For one, the Larmor-frequency ω_{rf} is given by

$$\hbar\omega_{\mathrm{rf}} = g_j \mu_{\mathrm{B}} |\vec{B}|. \tag{5.2}$$

Assuming a known g_j the absolute value of $\vec{B}$ is immediately derived. Secondly, the static magnetic field $\vec{B}_{\mathrm{coils}}$ can be calculated from the coil-currents. Sec. 3.4.1 on p. 78 presents the calibration of the field coils and shows excellent agreement between measured data and simulation. Now only $\vec{B}_0$ needs to be determined to be able to calculate $\vec{B}$ from the coil-currents. Both procedures are presented in the following. First, the residual field $\vec{B}_0$ is determined. Using the value and direction of $\vec{B}_0$ the absolute value of $\vec{B}$ is determined, comparing the two methods of determination. Finally, the complete characterization of $\vec{B}$ with all three components is shown.

Determining $\vec{B}_0$

The resulting magnetic field $\vec{B}$ comprises two components as shown in Figure 5.7. The static field $\vec{B}_{\mathrm{coils}}$ can be calculated directly from the currents, but the residual field $\vec{B}_0$ needs to be determined differently. One way not used in our lab to measure $\vec{B}_0$ directly is a form of electro-magnetically induced transparency, or EIT. When the Zeeman-splitting tends to zero the sub-levels of the $D_{3/2}$ state interfere destructively. The atom becomes 'transparent' for laser light coupling to the state and does not absorb photons from the light field. Accordingly, the resonance fluorescence vanishes. Scanning the magnetic field through zero a dip in the resonance fluorescence of Lorentzian shape appears. With this method it is possible to determine the absolute value of $\vec{B}$ to within several µT (see [Roberts, 1996]).

Here, we use a simpler approach relying on the good calibration result of the field coils. The magnetic field on-axis of a coil is proportional to the current going through the coil (cf. Eq. 3.8, p. 80). As the Larmor-frequency of the Zeeman-splitting ω_{rf} itself is linearly dependent upon $\vec{B}$ (Eq. 2.53) it is also linearly dependent on the three currents I_x, I_y and I_z. Figure 5.9 depicts the variation of the three coil-currents in dependence of the Larmor-frequency ω_{rf}. The measured data (dots) is shown together with linear numerical fits to the data. By extrapolating each graph to zero the currents I_x^0, I_y^0 and I_z^0 are found that exactly compensate the residual field $\vec{B}_0$:

$$I_0 = \begin{pmatrix} I_x^0 \\ I_y^0 \\ I_z^0 \end{pmatrix} = \begin{pmatrix} 426 \\ 110 \\ 118 \end{pmatrix} \mathrm{mA}. \tag{5.3}$$

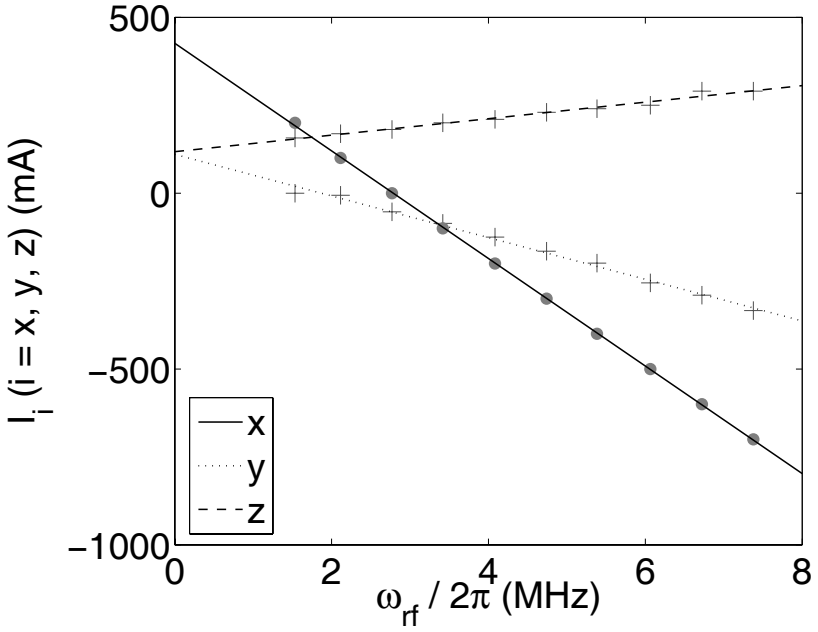

Figure 5.9: Determination of the residual field $\vec{B}_0$ by extrapolation of the measured currents flowing through the magnetic field coils. The legend indicates the coordinate of the current.

Inserting these values into the simulation program and negating the data yields

$$\vec{B}_0 = \begin{pmatrix} B_x \\ B_y \\ B_z \end{pmatrix} = \begin{pmatrix} 2460 \\ 575 \\ 615 \end{pmatrix} \text{mG} = \begin{pmatrix} 246 \\ 57.5 \\ 61.5 \end{pmatrix} \mu\text{T}. \tag{5.4}$$

The absolute value is

$$|\vec{B}_0| = \sqrt{B_x^2 + B_y^2 + B_z^2} = 2.6\,\text{G} = 260\,\mu\text{T}. \tag{5.5}$$

The general direction (downward to the floor of the lab, tilted slightly sideways) is in accordance with the expected magnetic field of the earth at the Institut für Laser-Physik in Hamburg, which is 53° 33′ N. The absolute value though seems too high for an earth field alone, which is expected to be on the order of 400-600 mG[www.magnetfeld.de]. The data sheet for the vacuum pump (Varian VacIon Plus 20) supplies the explanation: the magnetic stray field from the pump at the position of the ions is on the order of 2 G, pointing downwards, adding constructively to the earths magnetic field.

Determining $|\vec{B}|$: measurement of g_j

The absolute value $|\vec{B}|$ alone defines the Zeeman-splitting and hence the value of ω_{rf}. Figure 5.10 shows two graphs of $|\vec{B}|$: one is directly calculated from Eq. 2.53 with $g_j =$

0.802. The other is based on the numerical (Matlab) simulation mentioned before, where the magnetic field is calculated from the measured currents flowing through the magnetic field coils. These two graphs should be the same, but apparently are not. So far it is not clear why the simulation does not match the empirical result, especially as the error ranges on both graphs are distinctly smaller than the difference between the two. The main error

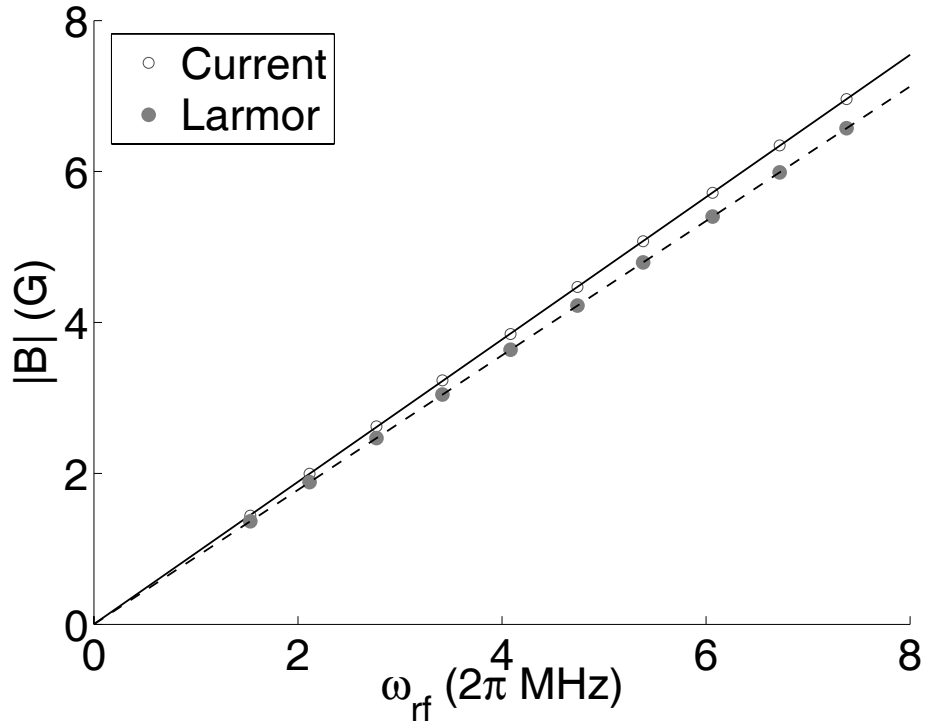

Figure 5.10: $|B|$ in dependence of the Larmor-frequency. 'Current' denotes the data calculated from the measured current flowing through the magnetic field coils, 'Larmor' indicates the calculation from the Larmor-frequency itself.

for the Larmor-frequency is the inaccuracy of the numerical fit of the Lorentz-profile to the data, which is $\pm$ 2 kHz. That error is smaller than the dots representing the data. The main error of the simulation is given by the calibration data in Sec. 3.4.1, which is 0.5%. This evaluates to $\pm$35 mG for the highest magnetic field. This is also smaller than the circles indicating the data for the simulation. This good accuracy is to be expected, for the magnetic field of a simple wire-loop is given analytically and the distances involved are known to construction accuracy (below $\pm$0.1 mm).

Several possible error sources were examined. The repump laser at 935 nm induces a slight light shift when drifting off-resonance over the course of a measurement. The light shift is dependent upon the detuning of the laser light field, and not upon the Zeeman

splitting of the $D_{3/2}$ state. For every measurement a new ion was trapped, and the laser frequencies were optimized by a standard procedure, leading to the same initial laser frequency. Therefore, a constant offset would be expected, or a random fluctuation pointing in the direction of the laser frequency drift. The graphs differ in slope though. This argument excludes another source. If the measurement of the residual field $\vec{B}_0$ includes an error this would also lead to a constant offset. Furthermore, as both graphs pass through the origin the residual field has apparently been well determined.

The position of the ions in the trap and hence in the coil-cage producing the static magnetic fields changes the slope of the graph. Due to experimental constraints every measurement was taken on a different ion, with different oven heating history, leading to a slight displacement of the ion. Numerical simulations though show that a displacement of $\pm 2\,\mathrm{mm}$ - which is much larger than the actual ion displacement - yields an error below 1%. At such a large offset the ion would not be visible in the laser focus anymore, a circumstance never observed. The small deviation of the value of the magnetic field stems from the construction of the coil-cage with an according homogeneity of the static magnetic field.

Last but not least the calibration procedure for the magnetic field coils was examined for errors. An unknown magnetic field present at the site of the calibration would again lead to a constant offset of the calibration data. Furthermore, the Hall-detector operated for the calibration allows for a null-calibration before a measurement, compensating for stray magnetic fields. The sensor of the Hall-detector was fixed on-axis at a distance of 6.5 mm, equivalent to the thickness of the former plus the radius of the wire. An erroneous positioning of the sensor would lead to a wrong calibration slope. The calibration factors determined in Sec. 3.4.1 were recalculated with the on-axis distance of the sensor varying by $\pm 1\,\mathrm{mm}$, which is the upper limit on the positioning error. For $d = 7.5\,\mathrm{mm}$ the calibration factor becomes 1.0217 (1.0117) for the small (large) coil, resulting in a stronger mean deviation (7.07% instead of 6.11%) of the two graphs in Figure 5.10. For $d = 5.5\,\mathrm{mm}$, the calibration factors are 0.9969 (0.9921), yielding a lesser mean deviation of 5.22%. Nonetheless, even for apparently wrong assumption of $d = 0$ the graphs still differ with a mean deviation of 1.93%, indicating that this approach also does not explain the difference between the two measurements.

Finally, the g_j factor of the $D_{3/2}$ level itself was examined. Using LS-coupling it is theoretically evaluated to [Haken & Wolf, 2004]

$$g_j = 1 + \frac{j(j+1) + s(s+1) - l(l+1)}{2j(j+1)} = 4/5, \tag{5.6}$$

inserting $j = 3/2$, $s = 1/2$ and $l = 2$. The tabulated measurement datum deviates strongly from this value with $g_j = 1.802$ [Fawcett & Wilson, 1991], but a footnote in that publication indicates a possible and likely typo in the original publication of the measurement [Meggers, 1967]. The value is currently assumed to be $g_j = 0.802$, and the graph in Figure 5.10 is calculated with $g_j = 0.802$. If the g_j factor were a free parameter a value of $g_j = 0.76$ would bring the numerical simulation and the calculation from the Larmor-frequency to excellent agreement. Considering that the measurements of g_j factors is a well-established art we do not want to call into the question the older value, and it seems necessary to admit that an error is present in the simulation, which has not been found so far. Nonetheless, as an important result these measurements confirm - to our knowledge for the first time since the original measurements of Meggers - that the value of $g_j = 1.802$ cannot be correct, and that the value is very close to the theoretical value of the LS-coupling.

Determining $\vec{B}$

Using $\vec{B}_0$ as determined above it is now possible to visualize and to calculate the resulting magnetic field $\vec{B}$ at the location of the ion. Figure 5.11 depicts the projection of $\vec{B}$ onto three planes: as seen from above (yz) (a), from the side (zx) (b), and watching along the trap axis (yx) (c). The inset illustrates the orientation of the linear trap in relation to the magnetic fields. The black vector marks $\vec{B}_0$. The red vectors display the static field $\vec{B}_{\text{coils}}$ for the different settings of the coil currents. Note that these are measurement values derived by calculation with Matlab from the measured currents (see Sec. 3.4.1, p. 80). The head of each red vector is emphasized with a small black dot. The long green vector is the resulting $\vec{B}$ for the highest magnetic field. Clearly, the vectors $\vec{B}_0$ and $\vec{B}_{\text{coils}}$ always add up to a resulting $\vec{B}$ parallel to the green vector as expected from Figure 5.7. The orientation in space agrees with the expectations from the polarization of the laser light field of the repump laser at 935 nm. This series of graphs illustrates that the magnetic field at the site of the ions has been completely determined by RF-optical double-resonance spectroscopy.

5.3 Dynamic magnetic fields

After the characterization of the static magnetic fields present at the site of the ion we now turn to the dynamic magnetic fields. The dynamic field is created by the RF-coil (see Sec. 3.4.2) to induce magnetic dipole transitions between different Zeeman sub-levels of the $D_{3/2}$ state. The tool of coherent spectroscopy in the form of Rabi-oscillations in

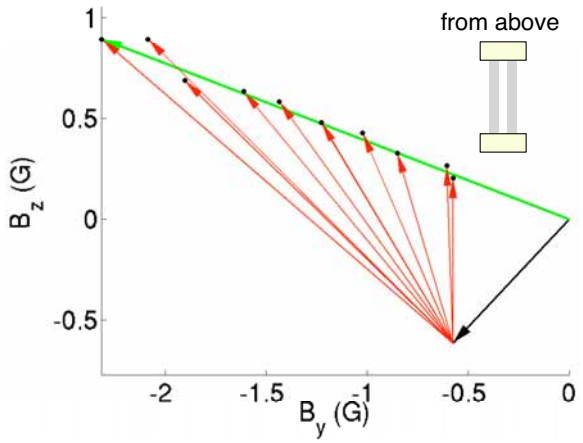

(a) View yz (above)

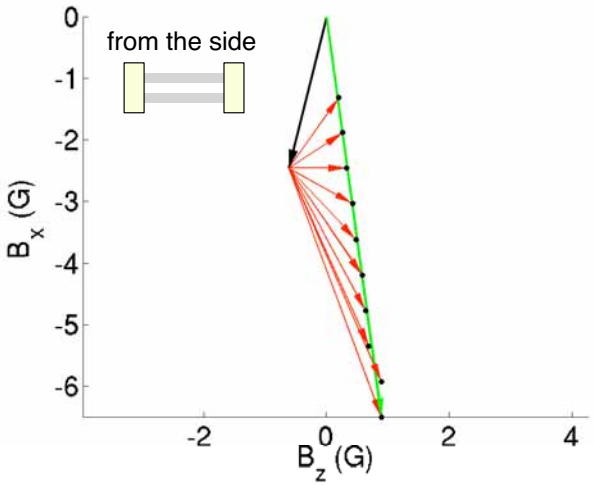

(b) View zx (sideways)

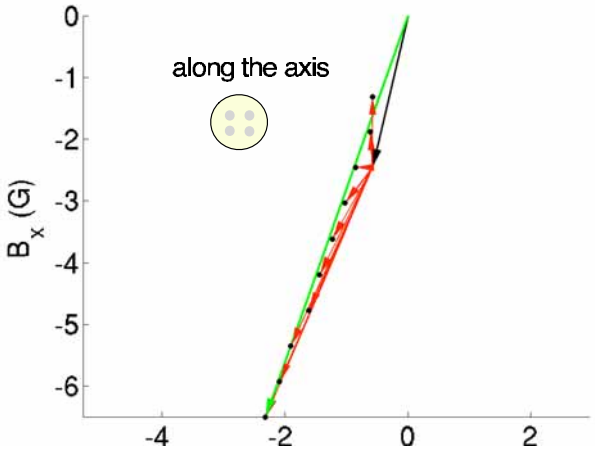

(c) View yx (axial)

Figure 5.11: Visualization of $\vec{B}$

the time domain allows for the precise determination of the amplitude of the magnetic component of the RF-field. As explained in Sec. 2.3.2 the magnetic dipole moment $\vec{\mu}$ of the ion rotates around the effective magnetic field comprising the static and the dynamic magnetic fields present at the site of the ion. Classically, the magnetic dipole precesses at the Rabi-frequency defined by $\hbar\Omega = \vec{\mu} \cdot \vec{B}_{\mathrm{rf}}$. Quantum mechanically, the dipole moment $\vec{\mu}$ is proportional to the angular momentum j of the ion, and the precession of $\vec{\mu}$ accords to transitions between sub-levels with different magnetic quantum numbers m_j. For a two-level system (e.g. $j = 1/2$) the population oscillates between the two possible states as $\sin^2(\frac{\Omega}{2}t)$. For arbitrary j the transient behavior of the level populations is more complex, but one thing remains: the dipole precesses at Ω, and hence returns to the original state after $t = 2\pi/\Omega$.

A Rabi-oscillation measurement in the time domain always follows the sequence 'preparation - manipulation - detection'. The ion (or atom) is prepared in a certain state. In our case, these are the $m_j = \pm 3/2$ Zeeman sub-levels of the $D_{3/2}$ state. A RF-pulse irradiates the ion for a certain time τ, possibly inducing a change of the ions state into other Zeeman sub-levels. The resulting state may well be a super-position of the participating energy levels. The ions state is detected by a projective measurement, yielding the m_j state the ion was projected into as a measurement value. This cycle of preparation, manipulation and detection is repeated many times, giving an approximate distribution of the level populations for that pulse length τ. When the ion is irradiated for a different time τ the final state of the ion is different, and again many repetitions of the measurement cycle are necessary to determine the resulting state. By systematically varying τ, e.g. from short to long pulse lengths, the evolution of the ions state is measured. Plotting the level population - usually as a probability that the ion was found in a certain state - over τ the Rabi-oscillations (in the time domain) are retrieved.

Figure 5.12 depicts the three steps used in this work. The ion is prepared in the $m_j = \pm 3/2$ Zeeman sub-levels of the $D_{3/2}$ state using optical pumping, see part (a) of that figure. The $D_{3/2}$ state is populated by spontaneous emission from the $P_{1/2}$ state, with a branching ratio for this transition of $Q_{P\to D} = 0.00483$. The probability to end up in a given m_j sub-level of the $D_{3/2}$ state is determined by the Clebsch-Gordan coefficients calculated in Sec. 2.2.2. When the ion decays into a $m_j = \pm 3/2$ level it remains there, uncoupled by the π-polarized repump laser at 935 nm.

The light fields are turned off, and the ion is manipulated by a RF-pulse with varying duration and frequency, see part (b). The energy difference between the four levels is equal, as no hyper-fine structure induces a quadratic Zeeman-shift. The resulting (possible) super-position of the four levels is projected into a particular m_j state by the spontaneous

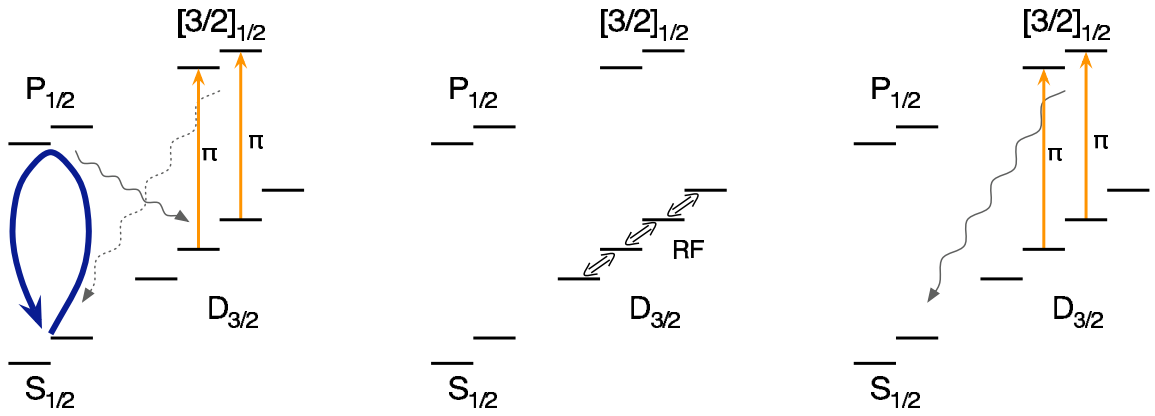

(a) Preparation (and detection)

(b) Manipulation

(c) Projection

Figure 5.12: Scheme for the coherent measurements of the Rabi-oscillations, comprising preparation by optical pumping (a), manipulation with RF-radiation (b) and state projection (c). The projection stage is illustrated as a separate step to clarify the point where the wave-function is reduced. In the experiment this step is incorporated in (a). Furthermore, the preparation of iteration $n+1$ is the detection of iteration n (see text).

emission from the $[3/2]_{1/2}$ level (see (c)), occuring after the repump laser selectively couples the $m_j = \pm 1/2$ states back to the $[3/2]_{1/2}$ level. The probability to return to the ground-state $S_{1/2}$ is very high with a theoretical branching ratio of 0.981 (see [Roberts, 1996] and the discussion therein).

The preparation of the $n+1$ iteration of the measurement cycle is the detection for nth iteration. When the ion was in the $m_j = \pm 1/2$ states after the nth manipulation the ion returns to the ground state, and cooling fluorescence is observable while the ion is optically pumped during the $n+1$ preparation stage. When the ion was in the $m_j = \pm 3/2$ states it simply remains there, and no resonance fluorescence signal is observable during the next preparation stage. The 'qubit' state is therefore detectable by the presence or absence of resonance fluorescence on the 369 nm cooling transition.

This section presents the actual measurements of Rabi-oscillations between the four Zeeman sub-levels performed during the course of this thesis. These measurements are vital for quantum information processing, as coherent manipulation of atomic states is at the very heart of a quantum computer. Due to the four-level structure used instead of a qubit and, accordingly, the more complex evolution of the ions states a limited set of numerical simulations of the Bloch-equations for four-levels were calculated. The results

are presented in Sec. 5.3.1. The actual measurement data is discussed in Sec. 5.3.2. These measurements finally characterize the dynamic magnetic field created by the RF-coil.

5.3.1 Simulation

Figure 5.13 depicts the simulation results, performed with Mathematica. The simulations were run with realistic parameters. The Rabi-frequency was held constant at $2\pi \cdot 30\,\mathrm{kHz}$ for all graphs shown. The detuning varies between 0 kHz and 100 kHz. The simulations were calculated up to a Rabi pulse length of 150 µs. The initial state for all simulations is $m_j = -3/2$. Many variations of these parameters are imaginable, but were not pursued further within the scope of this thesis.

Every graph plots a level population (given as probability) against the length of the Rabi-pulse in µs. In the left column (i.e. parts (a), (c), (e), (g) and (i)) the combined population of the $m_j = \pm 1/2$ levels is displayed as $P_{|1\rangle}$, and in the right column the $m_j = \pm 3/2$ levels as $P_{|0\rangle}$. Therefore, in every graph the main plot - the bold set solid line - is the combined probability of two levels. Every row shows the simulation results for a different detuning of the RF-radiation field from the Larmor-frequency of the Zeeman splitting of the $D_{3/2}$ level.

The individual contributions are also shown. For brevity the sub-levels were renumbered from 1 to 4, indicating $m_j = -3/2$ to $m_j = +3/2$, respectively. In the left column, the dashed line always represents the probability of the sub-level 2 ($m_j = -1/2$), in the right column the dashed line represents the sub-level 1 ($m_j = -3/2$). Accordingly, the light set line represents the respective other contributions. It is important to note that the actual measurement result of the experiment is the combined probability $P_{|1\rangle}$ of the two levels $m_j = \pm 1/2$. The two contributions can not be distinguished experimentally.

For $\Delta = 0\,\mathrm{kHz}$, the first observation is the $\sin^2$ form of $P_{|1\rangle}$ and $P_{|0\rangle}$ at double the frequency of a two-level system, shown in part (a) and (b) of Figure 5.13. It is interesting to note that the individual contributions always add to $\sin^2$ even though the amount of the contributions changes from period to period. This behavior exhibits an envelope on a longer time scale that was not examined further and consequently is not shown. The double frequency stems from the arrangement of the four levels. At half the period of the turning magnetic dipole the whole population is transferred from, e.g., the $m_j = -3/2$ level to the $m_j = +3/2$. Therefore, in one period of the turning dipole the $m_j = \pm 1/2$ levels are completely depopulated twice, instead of only once as in a two-level system. Furthermore, the maximal combined population of the $m_j = \pm 1/2$ levels is 0.8, i.e. these states can not be completely populated. This clearly shows that the four-level dynamics can not

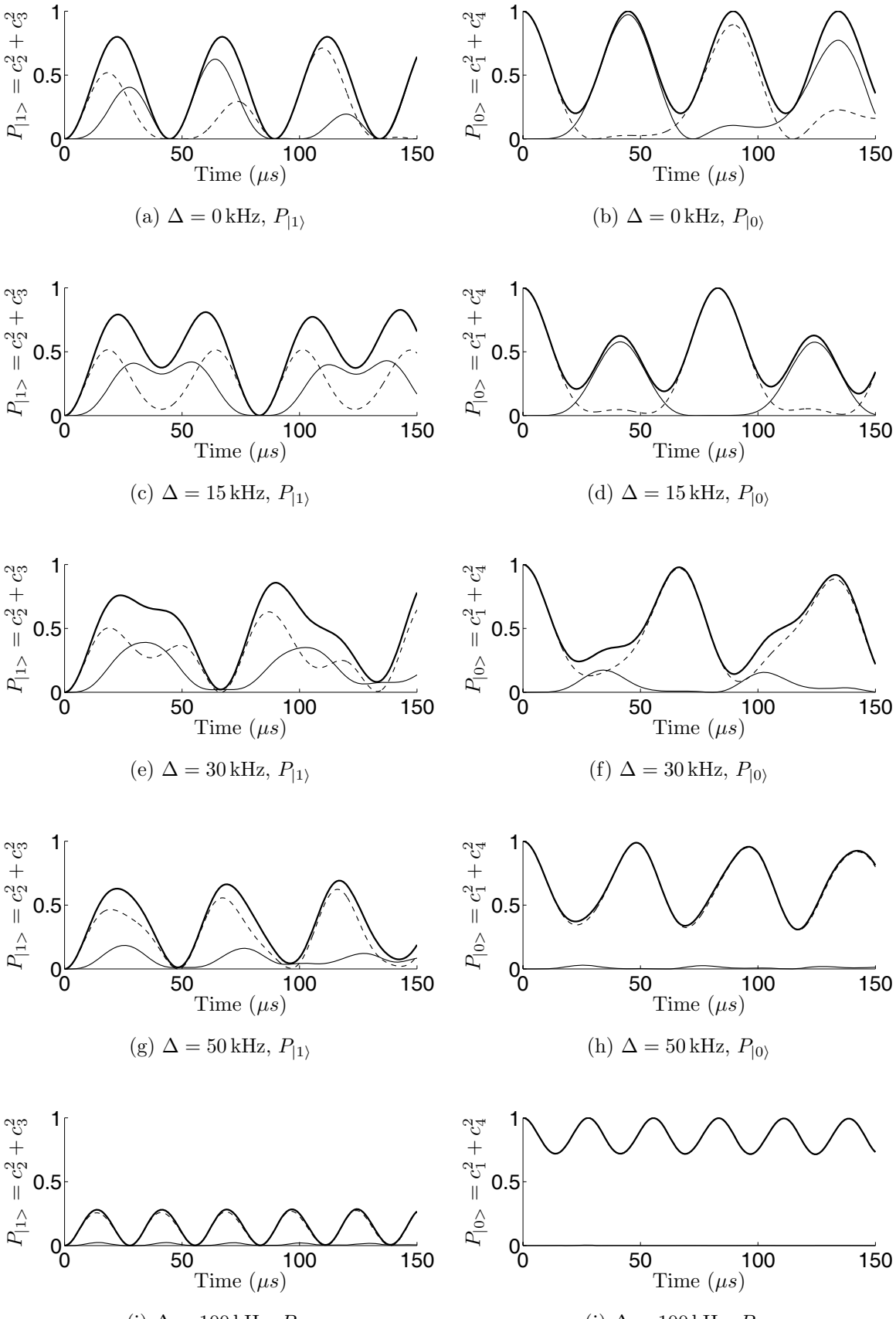

(a) $\Delta = 0\,\text{kHz}$, $P_{|1\rangle}$

(b) $\Delta = 0\,\text{kHz}$, $P_{|0\rangle}$

(c) $\Delta = 15\,\text{kHz}$, $P_{|1\rangle}$

(d) $\Delta = 15\,\text{kHz}$, $P_{|0\rangle}$

(e) $\Delta = 30\,\text{kHz}$, $P_{|1\rangle}$

(f) $\Delta = 30\,\text{kHz}$, $P_{|0\rangle}$

(g) $\Delta = 50\,\text{kHz}$, $P_{|1\rangle}$

(h) $\Delta = 50\,\text{kHz}$, $P_{|0\rangle}$

(i) $\Delta = 100\,\text{kHz}$, $P_{|1\rangle}$

(j) $\Delta = 100\,\text{kHz}$, $P_{|0\rangle}$

Figure 5.13: Numerical simulation of the 4-level Bloch equations for different detunings of the RF-radiation field from the Larmor-frequency.

accurately simulate two-level qubit dynamics, and that in fact this system is not suitable for standard quantum computing. Nonetheless, the aim of this work is to demonstrate a new addressing scheme for quantum computing, which remains feasible with the four-level structure.

Applying a detuning to the RF-radiation field this double-frequency feature is first reduced to a local minimum (sequence (a), (c), (e)), and finally is not discernible as a separate minimum anymore (sequency (g) and (i)). Regarding the graphs column-wise two effects are mainly notable. First, the population transfer from the $m_j = -3/2$ to the $m_j = +3/2$ becomes incomplete, implying a rest population in the $m_j = \pm 1/2$ levels, and the maximal amplitude decreases. The first minimum in part (a) is elevated, and the real period of the turning magnetic dipole appears. Secondly, this 'real' period decreases with increasing detuning. As we will see in the following experiments this accords to an effective Rabi-frequency known from the two-level system.

Going to larger detunings the four-level dynamics are more and more resembling those of a two-level system, and are finally (again) well described by the $\sin^2$ dependence of the two-level system, this time both in amplitude and in frequency. Graphically speaking, the population is 'stuck' in only two levels, the $m_j = -3/2$ and the $m_j = -1/2$ (again without loss of generality). The chance of the small population in the $m_j = -1/2$ to be transferred to the $m_j = +1/2$ becomes negligible, such that an effective two-level system arises.

5.3.2 Rabi oscillations

The main experimental difference between the incoherent spectroscopy presented in Sec. 5.1 and the coherent spectroscopy presented in this section is the switching of the laser light fields during the interaction of the ion with the RF-radiation. Figure 5.14 depicts the experimental timing cycle used for the coherent Rabi-type experiments. The overall measurement cycle is a repetition of synchronization, cooling and measuring. This cycle is repeated approximately $N = 50$ - 100 times, as indicated at the repetition bars, and depending on the selected time resolution. As the first step, the frequency generator VFG-150 and the DSP-system synchronize to each other to verify experimental timing on the timescale of the DSP (25 ns, cf. Sec. 3.5). As the second step, the cooling part with length τ_{cool} ensures the good localization of the ion. During cooling both the cooling laser at 369 nm and the repump laser at 935 nm as well as the RF-field irradiate the ion. The power of the repump laser and the RF-radiation are set to maximum, indicated by the height of the gray boxes. The frequency ν_{cool} of the RF-field is set on resonance to achieve maximal fluorescence rate, and hence good cooling of the ion. The resulting fluorescence signal is

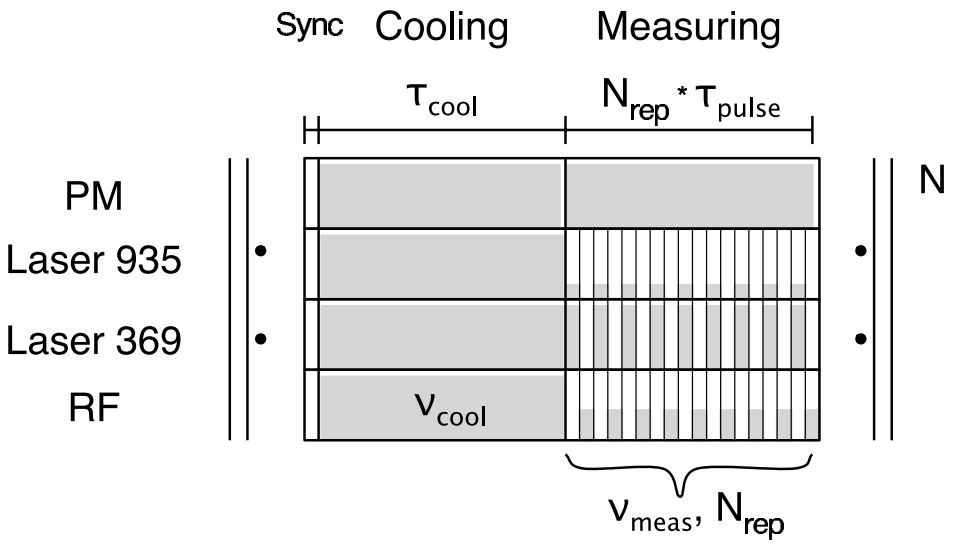

Figure 5.14: Experimental timing cycle for time-resolved Rabi measurements of the coherent interaction.

integrated for τ_{cool} by the photo-multiplier.

The measurement part comprises an alternating sequence of state preparation and detection on the one hand, and coherent manipulation with the RF-radiation on the other. Experimentally this is realized by exclusively irradiating the ion with either both light fields or with the RF-radiation field. This is indicated by the alternating gray boxes in the measuring part of Figure 5.14. During measurement the rf-radiation is set to the measurement frequency ν_{meas}. The alternating sequence is repeated N_{rep} times. The length of the measurement part thus becomes $N_{\text{rep}} \cdot \tau_{\text{pulse}}$, as indicated in the figure. The photo-multiplier signal is integrated for this period, which changes with increasing pulse length τ_{pulse}. This increasing integration time will be treated in the data preparation part below. The aforementioned division into three elements 'preparation - manipulation - detection' is thus implemented in two steps only, as preparation and detection coincide. The repump laser is set to low power at 30 µW - indicated by the lower height of the gray boxes - to minimize residual (σ) excitations from the $m_j = \pm 3/2$ levels. Due to imperfect polarization there always remains a certain error excitation.

Detection efficiency and time requirements

An important question for the detection is how many photons can be detected per iteration, such that the two different state ensembles are clearly distinguishable. Unfortunately it turns out that this value is very low. The number of photons scattered per detection stage

is determined by the branching ratio $Q_{P\to D}$. After $N_{\text{pump}} = 1/0.00483 = 207$ photons on average the ion decays into the $D_{3/2}$ state. This takes $N_{\text{pump}} \cdot \tau_{p_{1/2}} = 1.68\,\mu\text{s}$, with $\tau_{p_{1/2}} = 8.1\,\text{ns}$ (see Appendix C). These values have to be weighted by the ratio of the Clebsch-Gordon coefficients to account for the chance that the ion decays into the $m_j = \pm 1/2$ level of the $D_{3/2}$ state, which remains coupled to the cooling cycle by the π-polarized repump laser at 935 nm. In that case a second cooling and hence detection cycle occurs, doubling the number of photons. Table 2.1 on page 26 lists the Clebsch-Gordon coefficients for the transition from the $P_{1/2}$ into the $D_{3/2}$ state. Their square values give the probability that the transition occurs. Summing the square of the coefficients column-wise it is apparent that the chances for the four different levels are equally probable. The chance for another cooling cycle to happen therefore is 0.5. Of course, after that cooling cycle there is yet another chance for another cooling cycle without optical pumping into the $m_j = \pm 3/2$ levels, and thus the average number of photons scattered per optical pumping period becomes

$$P = N_{\text{pump}} \left[1 + \sum_{n=1}^{\infty} \left(\frac{1}{2} \right)^n \right] = 3 \cdot N_{\text{pump}} = 621\,. \tag{5.7}$$

The average pumping time increases to $(3 \cdot 1.68 = 5.03)\,\mu\text{s}$.

The absolute detection efficiency of the whole photo-multiplier detection path (cf. Figure 3.17) is estimated by the rate equation model presented in Appendix B to $5 \cdot 10^{-4}$ (cf. also Sec. 3.3). Taking this into account the absolute number of detected photons per preparation stage becomes $N_{\text{prep}} = 5 \cdot 10^{-4} \cdot 621 = 0.31$. This value is apparently too low to detect the state of the ion based on a single measurement. Accordingly, the signal is integrated over many repetitions N_{rep} of this manipulation-detection cycle. Going back to Figure 5.14, the photo-multiplier signal is integrated during the whole time that this alternating sequence of laser-light and RF-radiation is running. N_{rep} thus needs to be selected quite high to achieve a good signal, and it ranges on the order of 5000-10000. For $N_{\text{rep}} = 5000$ the total number of photons scattered during the measurement part is $N_{\text{rep}} \cdot P = 3105000$, of which $5 \cdot 10^{-4}$ or 1552 photons can maximally be detected. When optimizing the experiment this number can be reduced, but for these first measurements an ample signal-to-noise ratio was aimed for.

Fortunately, the individual iterations are quite short. The pulse length τ_{pulse} depends on the Rabi-frequency and is selected on the order of $2\pi/\Omega \approx$ 30-50 µs. The pumping time is on the order of 5 µs (see above), and an empirical waiting time of 1 µs is added as well to the sequence to let the laser-switching AOMs settle after switching on or off. The overall repetition rate thus ranges on the order of a few tens of kilohertz, and a sequence of $N_{\text{rep}} = 5000$ iterations is executed in less than one second. A typical measurement of a

Rabi-oscillation with $\Omega = 2\pi \cdot 30\,\mathrm{kHz}$ and a variation of τ_{pulse} between $1\,\mu\mathrm{s}$ and $40\,\mu\mathrm{s}$ thus takes about half a minute.

Data preparation

In quantum computing the computing result is formed by the states of the output qubits, given by the measured square of the state amplitudes, i.e. the probability distribution. The raw data of the measurements presented in this work needs to be calibrated to yield the probability distribution. This data preparation includes two steps. First, the stray-light incidents are eliminated from the photon count rate. This is displayed in Figure 5.15. In a second step, the measurement amplitude is normalized using the level of the cooling fluorescence signal, which is depicted in Figure 5.16.

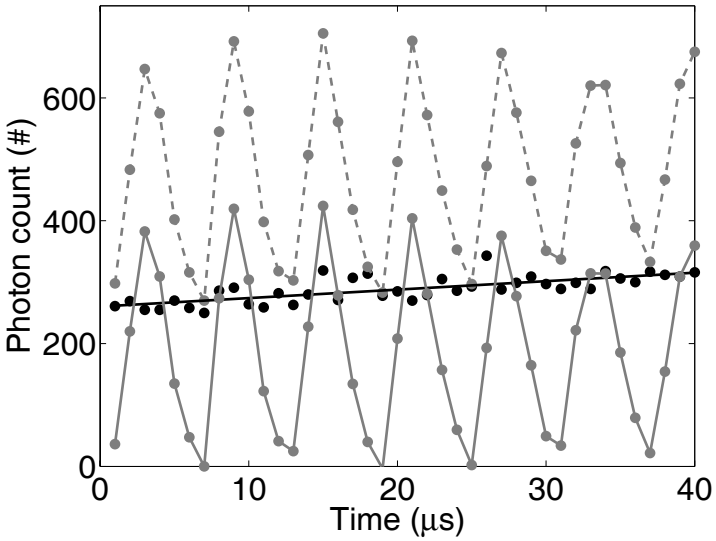

Figure 5.15: An example of the data preparation. The raw measurement data is connected by a line to guide the eye (dashed gray line with dots) . A null measurement without ions (black dots, black line is linear fit) indicates the stray-light level. The resulting data (solid gray line with dots) is the difference between the raw data and the null measurement.

The exposure time of the photo-multiplier is linearly increasing with the length τ_{pulse} of the RF-pulse (see Figure 5.14). Due to the fixed number of iterations N_{rep} the product $T_{\mathrm{exp}} = N_{\mathrm{rep}} \cdot \tau_{\mathrm{pulse}}$ defines the exposure time. A null measurement without ions calibrates the stray-light level (black dots in Figure 5.15) created by the cooling laser at 369 nm. It is linearly fitted (solid black line) to avoid the statistical fluctuations of the stray-light level. The linear fit is subtracted from the raw data, which represents the actual ionic fluorescence signal (solid gray line).

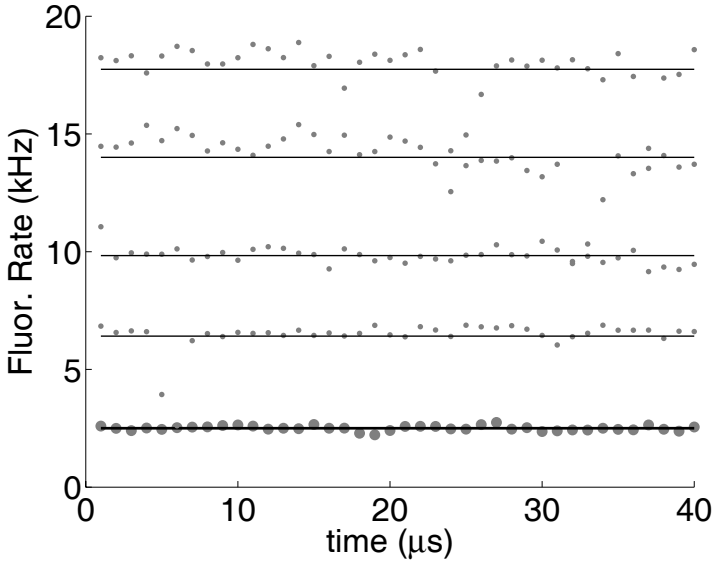

Figure 5.16: Cooling fluorescence collected during the cooling phase of the measurement. The bold-set line-series is a null measurement used for calibration, indicating the stray-light level. The amplitude of the measurement signal is normalized with the average value of the cooling fluorescence (solid lines) to make the measurement amplitudes resulting from different ion numbers comparable.

The measurements were taken with different numbers of ions. This clearly is not the preferred choice to perform these measurements, but the high background pressure in the vacuum chamber made this the only practical method. Collisions of the ions with the background atoms possibly induce transitions from the $D_{3/2}$ level into the $D_{5/2}$ level, from where the ion may decay into the extremely long-lived $F_{7/2}$ level. This is a dark state, and the fluorescence from the ion vanishes. The collision rate was so high that a single ion practically remains fluorescent for only one measurement scan, which implies a trap reload for every scan. Thus several ions were used to minimize the number of reloads. The amplitude of the integrated fluorescence signal can be normalized by the cooling fluorescence. Figure 5.16 shows the cooling fluorescence for up to four ions (gray dotted line-series). The bold-set line-series indicates the null measurement without ions. The solid lines represent the mean value for each series. The amplitude of the fluorescence signal now is the difference of the mean value of the null measurement and the according mean value of the cooling fluorescence. For every spectrum the background-free data from Figure 5.15 is divided by this amplitude and multiplied with the average fluorescence level of a single ion to yield the measurement data presented in Figure 5.17.

Measurements

Figure 5.17 shows the Rabi-oscillations in the time domain for nine different frequencies of the exciting RF-radiation. The gray dots represent the measurement data. The solid lines are numerical fits of a $\sin^2(\frac{\Omega}{2}t)$ function to derive the Rabi-frequency. The reason for this will become apparent below. The amplitude is scaled as described above in 'Data preparation'. The time resolution is 1 µs, starting at 0.5 µs, and going to 39.5 µs in thirty-nine steps. Unfortunately the measurement range could not be prolonged to higher pulse lengths as the duration of a single scan would then be longer than the average time for a background collision to occur, with subsequent transition to the $F_{7/2}$ level. Thus only the first oscillation period is recorded for scan (e) close to resonance, but the minimum is clearly resolved. As expected from the simulations above, the Rabi-frequency Ω increases with the detuning of the radiation frequency from the resonance frequency, while at the same time the amplitude decreases. This behavior is similar to a two-level system. The resonance frequency has been determined in different ways, and the detunings given beneath the images are taken as the difference from 7.3236 MHz.

The simulations show that the four-level system behaves more and more like a two-level system for larger detunings from resonance. This is clearly observable in the measurement data in Figure 5.17. In part (e) of that figure, the $\sin^2$ fit deviates strongly from the measurement data. The slope of the data at the beginning and the end of the oscillation period is higher than that of the sinusoidal fit. This agrees with Eq. 2.49 and Eq. 2.51 (on page 35), where the Rabi-frequencies for the transitions from the outer $m_j = \pm 3/2$ to the inner $m_j = \pm 1/2$ are higher by a factor of $\sqrt{3}$. The broad plateau in (e) stems from the interaction between the inner m_j levels. Graphically speaking, there is more ground to cover before the dipole has turned completely from, e.g., $m_j = -3/2$ to $m_j = +3/2$. Going to larger detunings the deviation from the $\sin^2$ form becomes less and less prominent, in accordance with the numerical simulation. In part (c) and (h) the measurement data is already described well by the function originally describing the two-level system.

Even though qualitatively the Rabi-spectrum of the four-level system is not adequately described by the $\sin^2$ function, the numerical fits shown in Figure 5.17 nonetheless allow for a quantitative analysis of the effective Rabi-frequency Ω_{eff}, defined by

$$\Omega_{\text{eff}} = \sqrt{\Omega_0^2 + \Delta^2}, \tag{5.8}$$

where Δ is the detuning from resonance, and Ω_0 is the Rabi-frequency on resonance. The reason for this is that the system can be treated as a turning magnetic dipole, as explained in Sec. 2.3.2. The individual level populations deviate from the $\sin^2$ form, but the overall

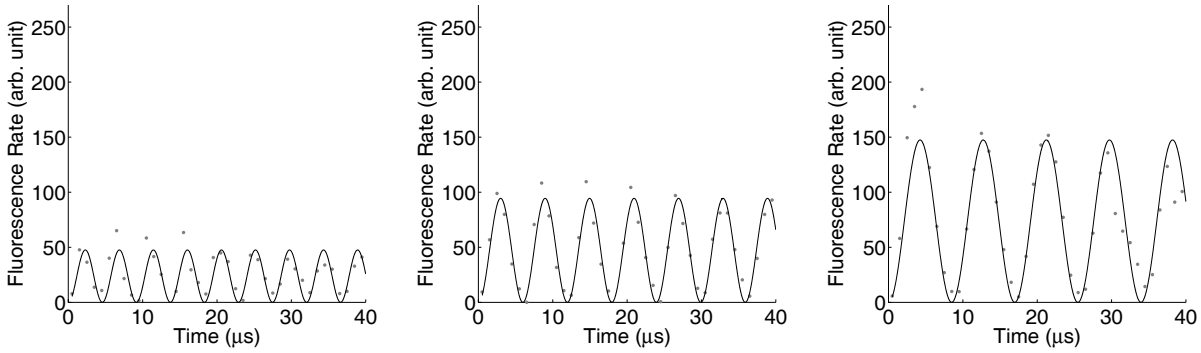

(a) 7.11 MHz ($\Delta = -214$ kHz) (b) 7.16 MHz ($\Delta = -164$ kHz) (c) 7.21 MHz ($\Delta = -114$ kHz)

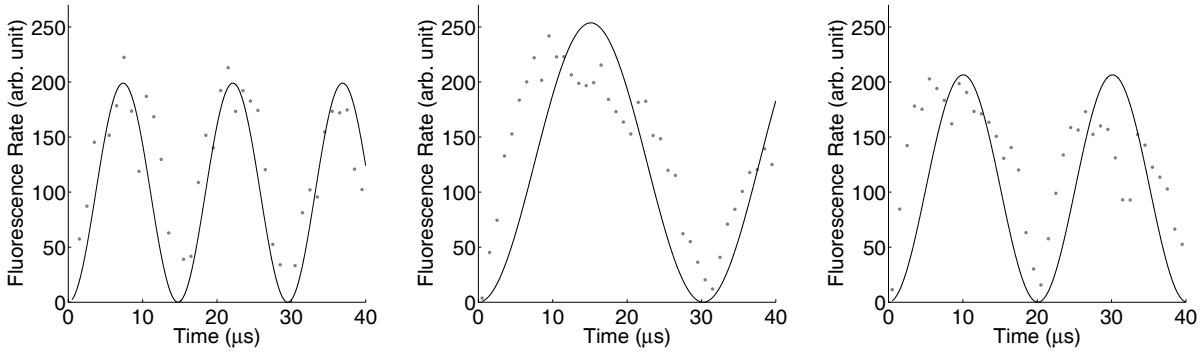

(d) 7.26 MHz ($\Delta = -64$ kHz) (e) 7.31 MHz ($\Delta = -14$ kHz) (f) 7.36 MHz ($\Delta = 36$ kHz)

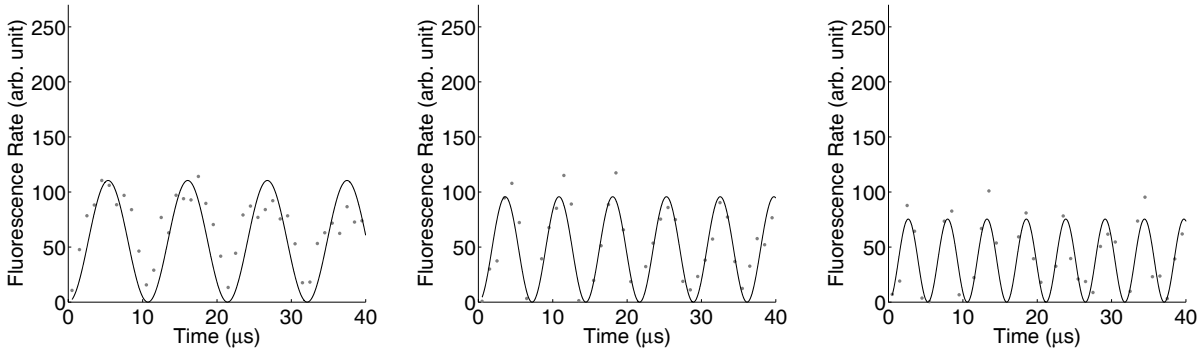

(g) 7.41 MHz ($\Delta = 86$ kHz) (h) 7.46 MHz ($\Delta = 136$ kHz) (i) 7.51 MHz ($\Delta = 186$ kHz)

Figure 5.17: Coherent Rabi-oscillations. The frequency of the RF-radiation is given below each graph. The detuning indicated is taken as the difference to 7.324 MHz, the value derived from Figure 5.18.

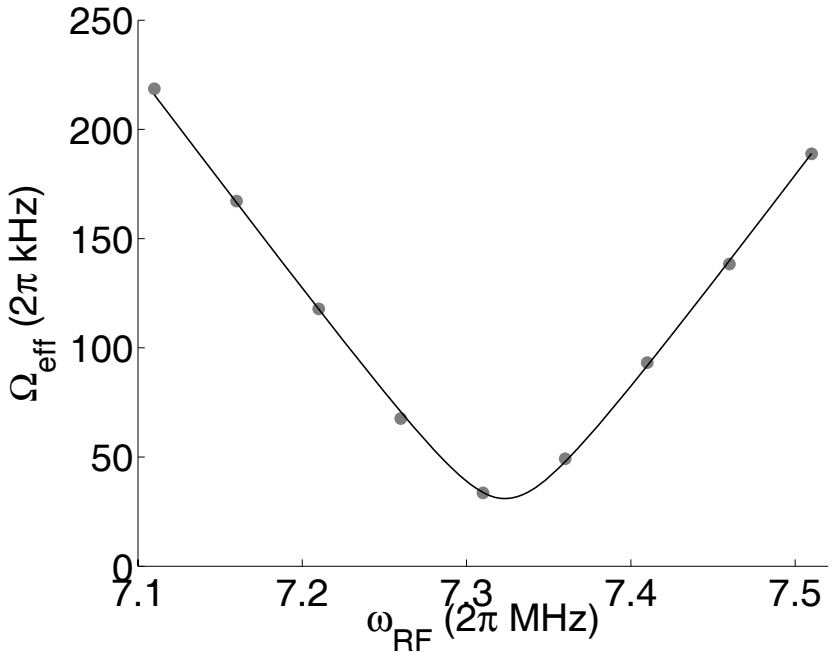

Figure 5.18: Generalized Rabi-frequency Ω_{eff} in dependence of the detuning Δ from resonance as extracted from Figure 5.17.

precession frequency is given by Ω_0. This is in fact independent of the number of Zeeman sub-levels [Koerber, 2003].

In Figure 5.18 the generalized Rabi-frequency Ω_{eff} - as determined by the $\sin^2$ fits - is plotted against the frequency of the RF-radiation, shown as gray dots. The solid line represents the numerical fit of Eq. 5.8 to this data with two free parameters. First, the resonance frequency ω_0 (thus determining Δ), and second the Rabi-frequency on resonance Ω_0. The data and the calculation agree well, with $\omega_0 = 2\pi \cdot 7.3236\,\text{MHz}$, and $\Omega_0 = 2\pi \cdot 30.9\,\text{kHz}$. This accordance is further proof that it makes sense to define *the* Rabi-frequency as the frequency at which the magnetic dipole is turning.

Of further interest is the dependence of the amplitude of the Rabi-oscillations on the detuning of the RF-frequency. In the two-level case this should be a Lorentzian form with a line-width (FWHM) of $2 \cdot \Omega_0$. For the four-level case the exact line-width is not apparent - as discussed for the series of incoherent spectra in Sec. 5.1.1 - but the Lorentzian form is also expected, again due to the picture of a turning magnetic dipole. This is confirmed in Figure 5.19, where the fitted amplitudes from Figure 5.17 are plotted against the frequency of the RF-radiation as gray dots. The solid line is a numerical fit of a Lorentzian profile with the amplitude, the line-width and the resonance frequency as free parameters. The

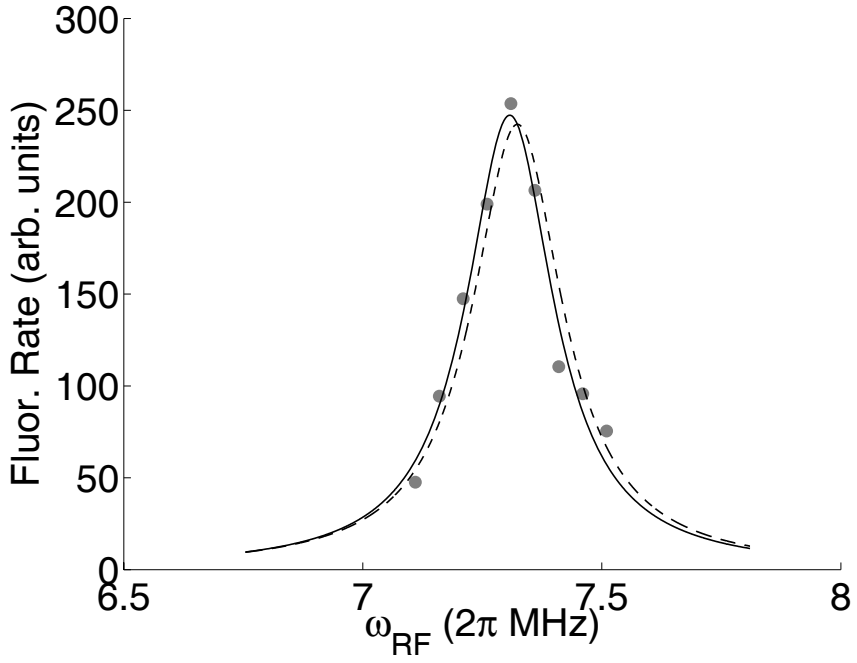

Figure 5.19: Fit of a Lorentzian profile to the fitted amplitudes from Figure 5.17. The solid line is a fit with the central frequency as a free parameter, the dashed line represents a fit where the central frequency has been fixed at 7.3236 MHz, the value derived from Figure 5.18.

resonance frequency is 7.3075 MHz, with a line-width (FWHM) of 222 kHz. The dashed line is another fit where the resonance frequency has been fixed at the value derived in Figure 5.18, 7.3236 MHz. The line-width (FWHM) has been determined to 230 kHz.

Assuming again that this profile is described by Eq. 2.59 (and neglecting the influence of the repump laser, i.e. $\Omega_{935} = 0$) the factor of $2\sqrt{7}$ scales the measured line-widths to Rabi-frequencies of $2\pi \cdot 42.0$ kHz and $2\pi \cdot 43.5$ kHz, respectively. As the exact Rabi-frequency has been determined above to $2\pi \cdot 30.9$ kHz the discrepancy mentioned in Sec. 5.1.1 between the simple line-width model yielding Eq. 2.59 and the measurements appears here also. The erroneous factor is almost equal for the two cases. In Sec. 5.1.1, the Rabi-frequency was a factor of $59/41 = 1.44$ too high, whereas in this section the factor evaluates to $43.5/30.9 = 1.41$. This is a first indication for a systematic difference, which could not be finally resolved in the frame of this thesis.

5.4 Magnetic gradient field

Finally, the following section presents the measurements performed with the magnetic gradient field in place. A simulation in Sec. 5.4.1 explains the general features of the setup, and the choice of the working range. The alignment of said range is detailed in Sec. 5.4.2. Closing this section and the experimental chapter of this thesis Sec. 5.4.3 presents the actual addressing measurements.

5.4.1 Simulation

Simulations of the magnetic fields were calculated in order to estimate the value of the magnetic gradient realizable with two permanent magnets. Whereas the field of the magnetic field coils is simulated by a home-made Matlab-script, a commercial program called Biot-Savart is used to calculate the magnetic field of two permanent magnets in quadrupole configuration (this is also named anti-Helmholtz-like configuration in reference to the quadrupole setup with actual coils). The derived values agree well with numerical simulations published online by the manufacturer of the permanent magnets [www.ibs-magnet.de] for the on-axis magnetic field of a single magnet. Both the absolute value $|B|$ and its derivative $\partial_z|B|$ are shown in Figure 5.20 over the full range of the 'coil-cage', the set of three pairs of coils producing the static magnetic field. The distance from the coil-windings to the trap center is 63.5 mm. In this simulation the permanent magnets are placed with a distance of 35 mm between the trap center and the front facette of the magnet. For Figure 5.20 both magnets are placed symmetrically on the trap axis. Figure 5.20 clearly shows that the magnets are too far apart for an effective large gradient at the trap center. In real anti-Helmholtz configuration the two maxima of the gradient graph (shown in green) would approach each other so much that the discontinuity at the trap center would jump from approximately -60 T/m to 60 T/m. Due to construction constraints the 35 mm used for the simulation is the minimal distance that can be realized experimentally.

The region of interest for the ions is not the full coil-cage but a small region on the order of several millimeters in the center of the trap. Figure 5.21 therefore pictures the excerpt indicated by the small black rectangle in Figure 5.20. In part (a) of Figure 5.21 the absolute value of B is plotted against the distance on-axis from the trap center, while part (b) shows the gradient calculated from the same data. Four graphs are shown that differ in the position of one of the permanent magnets. The first graph shows perfect alignment, where both permanent magnets have the same distance axially and radially from the trap center. For the second graph, one magnet is moved from this position 1 mm off-axis in

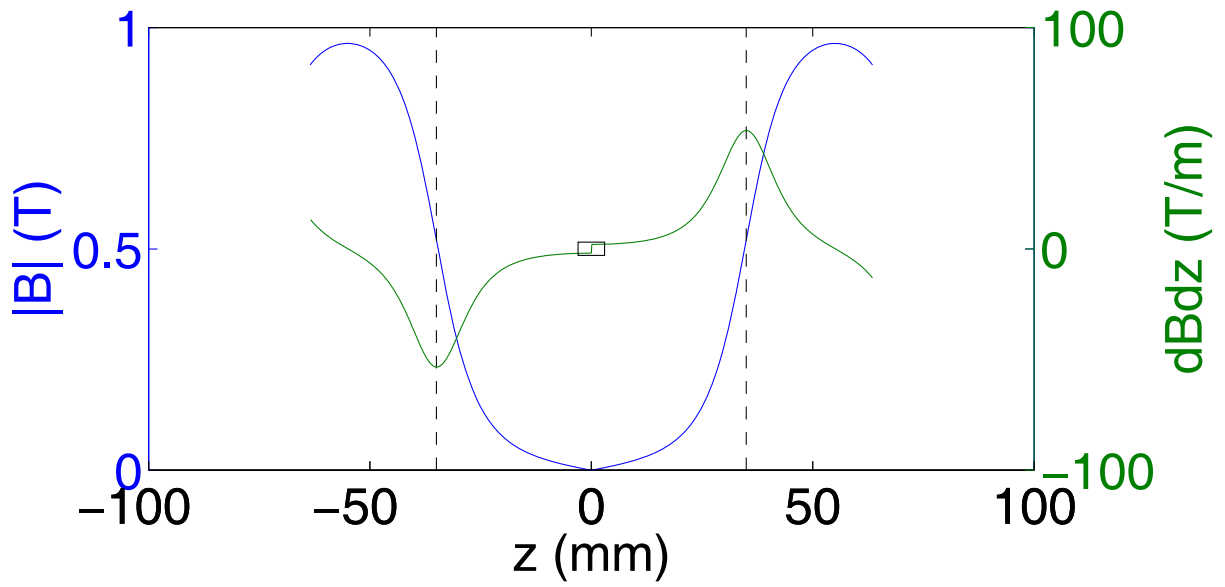

Figure 5.20: Full range simulation of $|B|$ (blue) and $\partial_z|B|$ (green). The range is the inside of the coil-cage. The two dashed lines indicate the position of the front facette of the permanent magnets. The small rectangle defines the window used for Figure 5.21 (b).

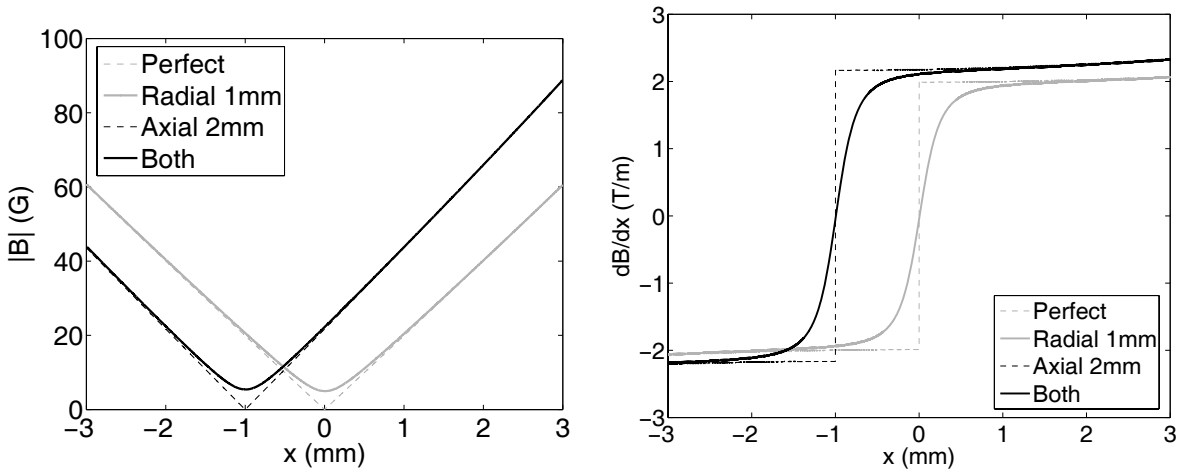

(a) $|B|$ (b) $\partial_z|B|$

Figure 5.21: Simulation of the magnetic field (a) and the resulting gradient (b) produced by two permanent magnets with four different positions (see text). The ions are situated at the center $z = 0\,\mathrm{mm}$.

radial direction. For the the third graph the magnet remains on-axis, but is moved 2 mm closer to the trap center. Graph 4 combines these two misalignments, i.e. one magnet is placed 1 mm off-axis radially, and 2 mm closer to the trap center.

A striking feature of perfect alignment is the discontinuity of the absolute value of B at the trap center. This holds true for both graphs one and three, as unsurprisingly the repositioning on-axis only leads to a different center position between the two permanent magnets. If that perfect alignment were realized, then the ion chain would only have to lie completely to one side of the center to experience the almost maximal gradient achievable within 3 mm of the trap center. This alignment was aimed for in the beginning of the addressing measurements. It soon became clear though that the rest uncertainty of alignment softened the discontinuity to a zero-crossing of the gradient at the trap center. This softening is clearly visible in the graphs two and four. The width of the region where the gradient almost vanishes is on the order of the radial displacement. Based on these results another approach to maximizing the gradient was developed.

5.4.2 Gradient alignment

In the following, an addition to the magnetic nomenclature introduced in Sec. 5.2 (see Table 5.1) is in order to distinguish the resulting magnetic field in the two cases where the gradient field is present or not. In this section, $\vec{B}_{\text{fix}}$ denotes the case without the gradient field, i.e. just the contributions from the residual field $\vec{B}_0$ and the static magnetic field $\vec{B}_{\text{coils}}$. The resulting magnetic field $\vec{B}$ (also given as B_{result} in the following figures) is the sum of all three components, including the magnetic gradient field $\vec{B}_{\text{grad}}$.

As the simulation shows the gradient is quite sensitive to misalignment, leading to a zero crossing of the gradient value near the middle of the permanent magnets and hence near the ions. The maximum gradient obtainable would be realized with a single magnet alone. But a single permanent magnet alone would create a large field $\vec{B}_{\text{grad}}$ at the position of the ions, pointing roughly - assuming an acceptable alignment - in the direction of the trap axis, as indicated in Figure 5.22 (a). This $\vec{B}_{\text{grad}}$ would then turn the overall $\vec{B}$ out of the prerequisite alignment with the electric component of the light field, impeding π-polarization and thus optical pumping. This $\vec{B}_{\text{grad}}$ is so large that it can not be compensated for by the current experimental setup, i.e. the $\vec{B}_{\text{coils}}$ created by the magnetic field coils (see Sec. 3.4.1). Accordingly, both magnets are used, with one magnet as close to the trap as possible and the other with a slightly higher distance, as seen in Figure 5.22 (b). This smaller $\vec{B}_{\text{grad}}$ can be compensated for by an additional current through the magnetic field coils producing the axial component of $\vec{B}_{\text{coils}}$, and hence $\vec{B}_{\text{fix}}$. The maximum distance Δz

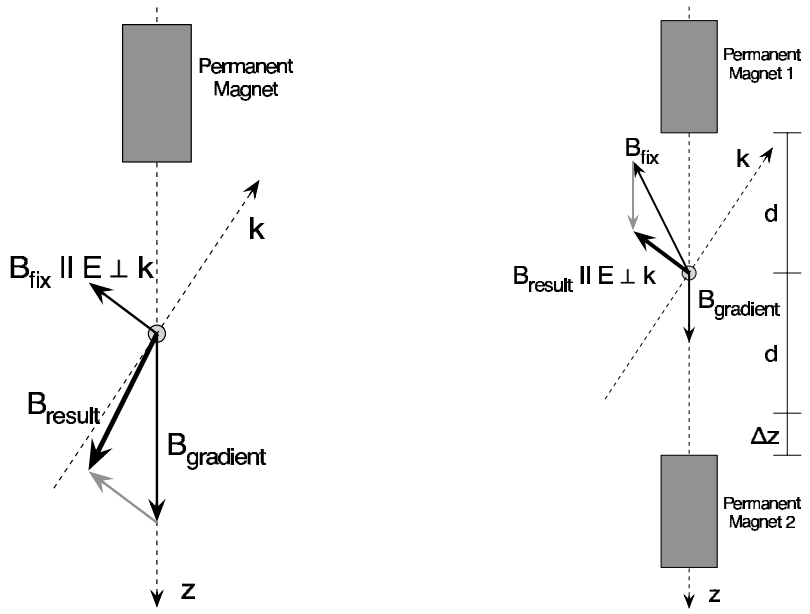

(a) One permanent magnet (b) Two permanent magnets

Figure 5.22: Illustrating the alignment needed to retain π-polarization and optical pumping. One permanent magnet (a) would maximize the gradient, but the extra B_{gradient} can not be compensated for. With two permanent magnets (b) the extra field B_{gradient} is adjustable, and hence limited.

is determined by the maximum compensating $\vec{B}_{\text{fix}}$ currently attainable (and sustainable) with the magnetic field coils. At that point, we achieve a profile of the magnetic gradient that is similar to the graph marked 'both' in Figure 5.21 (b).

Starting the alignment, the permanent magnets are moved to positions such that $\vec{B}_{\text{grad}}$ becomes zero. For this, $\vec{B}_{\text{fix}}$ (without the gradient magnets) is characterized by incoherent Lorentz-spectroscopy. The Larmor-frequency determines the absolute value of the resulting $\vec{B}$, and the polarization of the light field yields the spatial orientation. The 'alignment towers' for the permanent gradient magnets are aligned by eye-sight to be co-linear with the ion traps axis, and the magnets are mounted. An equidistant alignment of the permanent magnets to the trap center is aimed for. Nonetheless, this alignment is an estimate - especially for the axial distance - and an extra $\vec{B}_{\text{grad}}$ results at the position of the ions. This interrupts the optical pumping with a noticeable σ-component of the light field, and the ion(s) remain visible even when the rf-radiation is turned off. The permanent magnets are aligned to restore optical pumping by moving one magnet until the resonance

fluorescence vanishes. The $\vec{B}_{\text{grad}}$ from the permanent magnets now points in the direction of $\vec{B}_{\text{fix}}$. A measurement of the Larmor-frequency determines a remaining discrepancy, and the direction of $\vec{B}_{\text{grad}}$, which can then be aligned again by moving both magnets together. Both permanent magnets have now the exact same distance to the trap center, defined by the ion positions.

Starting from this zero position, the current through the magnetic field coil for the axial magnetic component is inversed and set to its maximum value, and optical pumping is interrupted. One permanent magnet is translated along the trap axis, from the trap center away, until the resulting $\vec{B}_{\text{grad}}$ from the permanent magnets compensates the axial field component and optical pumping is restored. The value of the magnetic field gradient at the trap center is now maximal. In theoretically perfect alignment (in radial direction) the displacement distance would be infinitesimal (implying at least the length of the ion string), in practice this ranges on the order of one to a few millimeters.

5.4.3 Ion addressing

Ion addressing is the first step in the magnetic gradient scheme, and it is the first that has been experimentally examined. Both detection systems - the photo-multiplier and the intensified CCD-camera - were employed for the addressing measurements. The photo-multiplier is more sensitive to smaller signals due to the integrated nature of the signal. This allowed for smaller radio-frequency power and smaller integration times. With the CCD-camera on the other hand it is possible to regard the frequency dependence of every ion separately by integrating over only a small part of the whole image, belonging to, e.g., only one ion.

Scalar measurements

The first measurements with the static magnetic gradient field were incoherent radio-frequency spectra. The fluorescence signal was detected with the photo-multiplier without spatial information, hence scalar measurements. Figure 5.23 shows the experimental data. In part (a) of that figure, the fluorescence signal of two ions in dependence of the radio-frequency is plotted together with a numerical fit of two Lorentz-profiles. The data is the average of four individual scans taken right after each other. The scan ranges from 6.9 MHz to 7.6 MHz in 120 steps. At each frequency step, the photo-multiplier count was integrated for 100 ms. For the numerical fit the sum of the two profiles is drawn in bold black, the individual profiles are represented by the dashed lines. The free parameters were the two

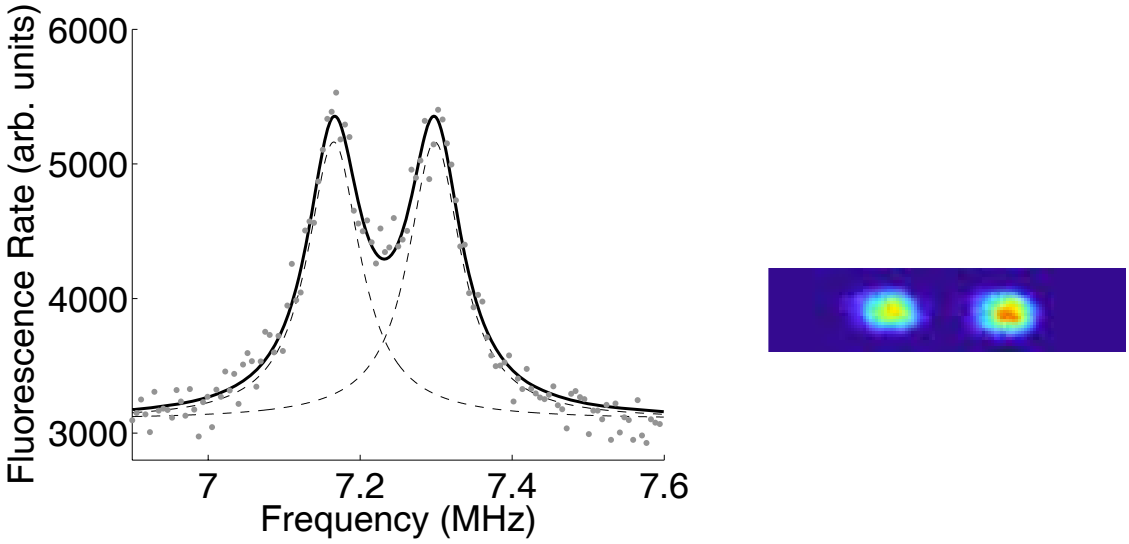

(a) RF-Scan (b) Averaged image

Figure 5.23: Adressing two ions with different Zeeman-splitting in a magnetic gradient field.

center frequencies, a common amplitude and a common line-width for both profiles. The background was determined from the average of the outermost data points of the scan.

The two ions are clearly resolved, indicating the presence of the magnetic field gradient. The frequency difference is determined from the fit of the two Lorentz-profiles to 133(2) kHz. The error is given by the numerical fit. To obtain the value of the gradient a calibration image was taken and is shown in (b) of Figure 5.23. The image is an average of a 100 frames with 200 ms exposure time each. During that scan the radio-frequency was varied manually back and forth over a range of 300 kHz, with a step size of 10 kHz. The center of the ions is determined both manually and with the numerical fit of an Airy aperture function, yielding a distance of the two centers of 39 px. The error for both procedures is ± 1 px, which is below the error inherent to the spatial calibration of the CCD-camera (see Sec. 3.3). Using the calibration scale of 0.65(5) µm/px this evaluates to a distance of 25(2) µm. With the usual $\hbar\omega = g_j \mu_\mathrm{B} |B|$ the gradient is thus determined to

$$\frac{\partial}{\partial z}|B| = \frac{h}{g_j \mu_\mathrm{B}} \cdot \frac{133}{25} \frac{\mathrm{kHz}}{\mu\mathrm{m}} = 0.47(4)\,\mathrm{T/m}. \tag{5.9}$$

Spatially resolved measurements

After the initial success with the scalar measurements the image-intensified CCD-camera was employed to verify the relation between spatial position and frequency of the exciting radiation. The measurement timing is depicted in Figure 5.24. A sequence of cooling

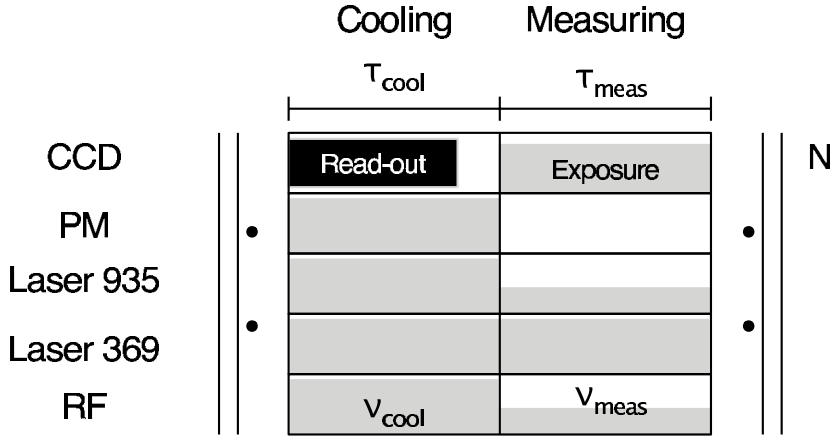

Figure 5.24: Experimental timing cycle of the spatially resolved RF-scans for addressing experiments.

and measuring cycle with lengths τ_{cool} and τ_{meas} alternates N times, as indicated by the repetition bars. During cooling, the frequency ν_{cool} of the rf-radiation and the power of the repump laser at 935 nm P_{cool} are set such that the maximum resonance fluorescence and thus maximum cooling rate is realized. During the cooling part, the fluorescence signal is monitored with the photo-multiplier (indicated by the gray box).

During measurement the image-intensifier is activated for τ_{meas}, defining the exposure time of the image. The radiation frequency ν_{meas} is fixed for one measurement part, and is scanned through the desired frequency range during the series of N steps. The power of the rf-radiation is set to the measurement power level, which is usually lower than during the cooling part to avoid power-broadening (indicated by the lower gray box). The power of the repump laser P_{meas} is set to a minimum to reduce the power-broadening of the transitions line-width as well. The image is read-out by the camera PC during the cooling part of the cycle (indicated by the black box). Care has to be taken that τ_{cool} is long enough to accommodate for the read-out time.

The measurement data is presented in Figure 5.25. Four scans for two (a), three (b), five (c) and 16 ions (d) are shown. For every scan $N = 100$, i.e. a hundred frames per scan. Both the frequency range and the spatial extent vary. The cooling and the measuring time were equal at $\tau_{\text{cool}} = \tau_{\text{meas}} = 200$ ms. Each of the four parts comprises two images. The

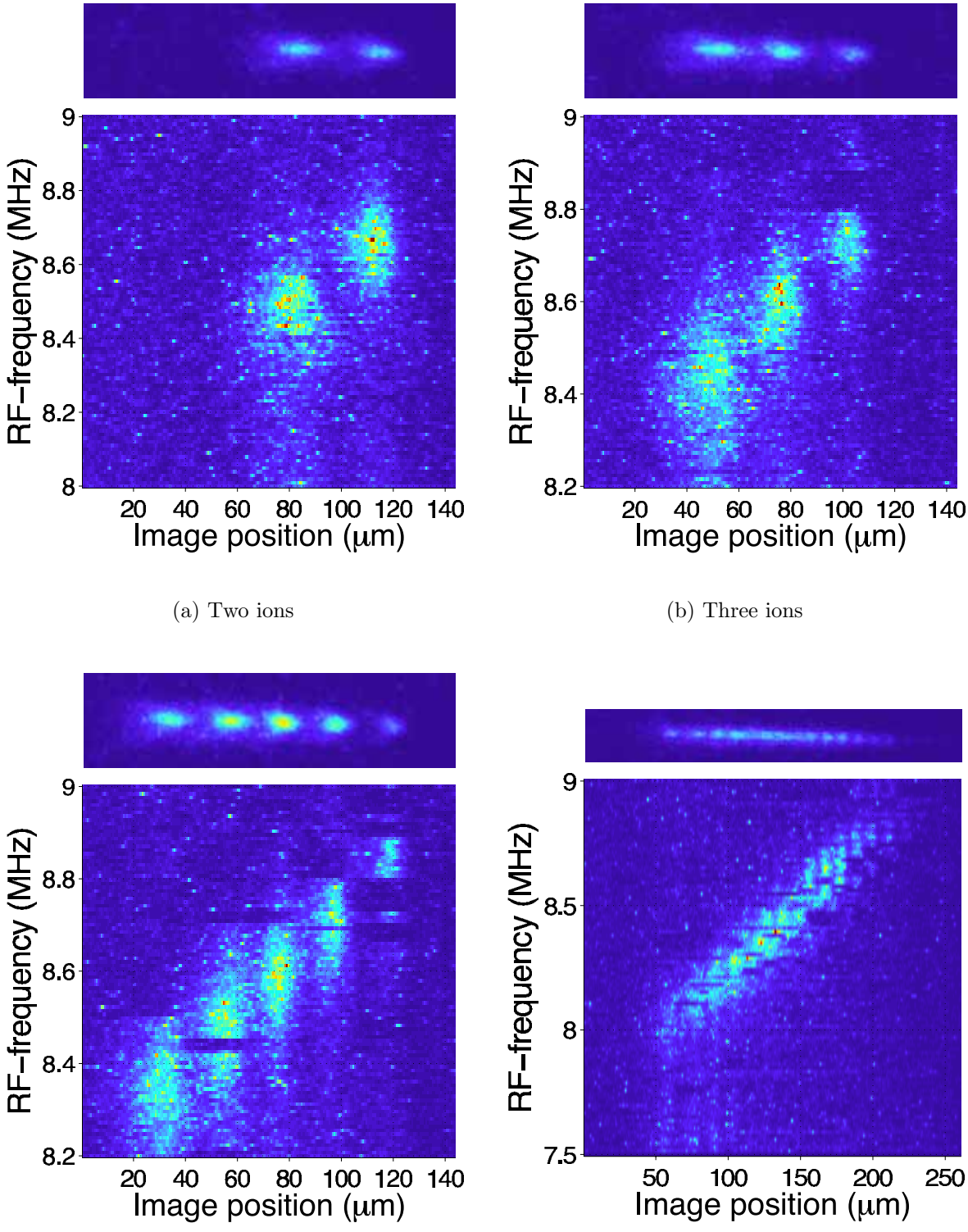

(a) Two ions

(b) Three ions

(c) Five ions

(d) 16 ions

Figure 5.25: Ion addressing in a static magnetic gradient field with spatial resolution for two (a), three (b), five (c) and many (16) (d) ions.

upper image is the average over all frames, giving an impression of the ions position and state. For all four averaged images the same color-table is applied, and the amplitudes may directly be compared. The lower image is a collection of all hundred frames, rearranged to illustrate the relation between spatial position and radiation frequency. For it, every frame is integrated over its height, yielding a one-dimensional fluorescence distribution. The N profiles are then arranged in scan order, corresponding to the frequency scan. The resulting array is false-color coded to retain the impression of the CCD-image. Each color-coding is scaled to the maximum of the according scan, and the fluorescence values between the four scans can not be compared directly. For all images, the spatial axes are scaled with the calibration data.

The effect of the magnetic gradient is clearly visible. Every ion trace exhibits a distinct maximum whose center frequency depends on the ion position. In some scans the resonance fluorescence is interrupted for brief intervals, a good example is the five-ion scan in part (c). The ion briefly jumps into the dark state $F_{7/2}$, from where it is shortly afterwards brought back into the cooling cycle by either a collision with a background atom or by the repump laser at 638 nm. The ion does not leave the trap, as otherwise the position of all other ions would shift, which would clearly be visible in the scans.

A striking feature of the averaged images is the spatial spread of the ions, especially for part (a) and (b), indicating insufficient cooling. This insufficient cooling is furthermore demonstrated by the resonance fluorescence collected during the cooling part of the scan cycle. The fluorescence signal - collected with the photo-multiplier - is shown in Figure 5.26, for three (a) and five (b) ions. For three ions, the signal continuously deteriorates while the scan proceeds. Apparently, the heating produced during the measurement part of the scan-cycle is higher than can be countered during the cooling part. For five ions this is not as clear. Here the scan shows a series of steps rather than a continuous decrease of the fluorescence signal. These steps are caused by the ions jumping into the $F_{7/2}$ dark state. Judging by the averaged image the cooling has been more effective for this scan, as the ions are better localized and have a higher resonance fluorescence. It is clear from this data that the experimental timing has to be revised to increase the cooling efficiency, e.g., by cutting the measurement part into smaller time slices.

The value of the gradient is determined by two methods. The first is illustrated by Figure 5.27. The scan-profiles - comparable to Figure 5.23 - are extracted by integration for every frame over the rectangular area indicated in the lower image of Figure 5.27. The upper part depicts the profiles thus derived, by plotting the integration value against the frequency of the rf-radiation. The background level of the CCD-image has been determined from the averaged image by taking the mean value of the upper 10 image rows. The

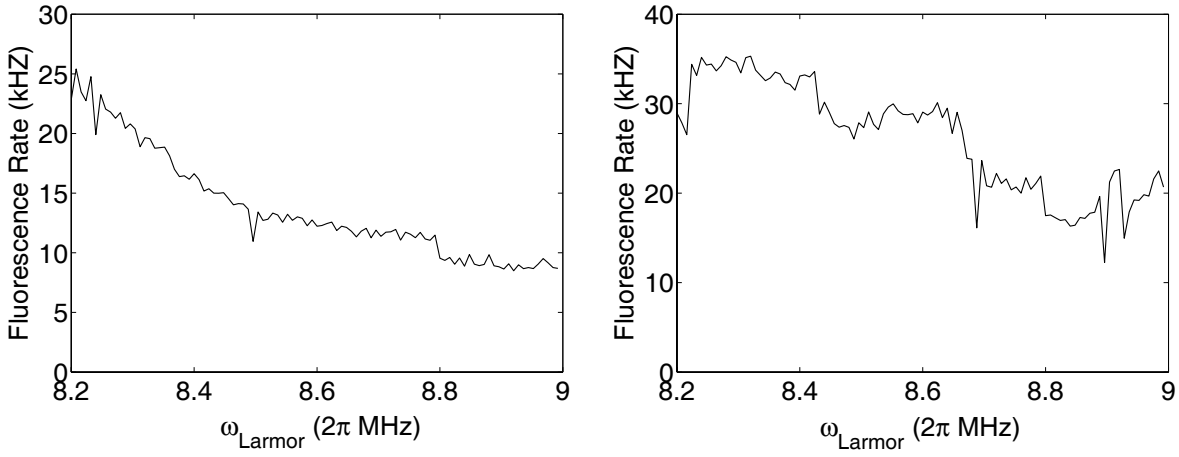

(a) Three ions

(b) Five ions

Figure 5.26: Fluorescence signal collected by the photo-multiplier during cooling for the addressing measurements. The graphs directly relate to Figure 5.25 (b) for three ions and (c) for five ions. The diminishing fluorescence signal in part (a) indicates insufficient cooling over the course of a measurement. In part (b) the cooling signal remains stable between quantum jumps to dark states, visible by the plateau-like structure of the signal.

background of the rectangular integration area is already subtracted in the profile plot. The data (marked by asterisks) is numerically fitted with a Lorentz-profile (solid lines).

Two differences to Figure 5.23 are immediately apparent. First, the line-width of the two profiles is larger, especially so for the left ion (black graph). They were independently fitted to 208 kHz (black graph) and 204 kHz (blue graph). A fit mask ignored the lower-frequency flank of the first ion as, secondly, the fluorescence data for the left ion exhibits a strong deviation from the fit profile. The large line-width stems from two facts. First, the rf-power used for the spatially resolved scans was set higher by a factor of 14 dB in comparison to the scalar measurements presented in Figure 5.23. Figure 5.5 predicts an increase of approximately 4.5 in line-width for such a power difference. The second effect predominantly affects the left ion. From the spatial image it is apparent that the ions are insufficiently cooled, the ions are stretched in the horizontal direction (i.e., along the trap axis) in comparison to, e.g., Figure 5.23 (b). Without gradient this should only minimally affect the line-width of the transition. In the magnetic field gradient the resonance frequency is position dependent, and thus a spatial spread leads to an increase of the transition line-width.

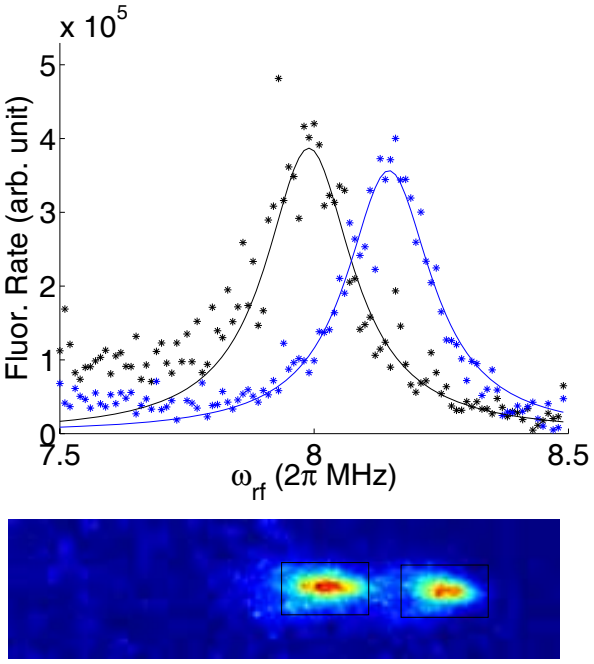

Figure 5.27: Extraction of the excitation profiles from the image data by integration over the indicated area.

Finally, the deviation of the scan-profile from the Lorentzian form is also explained by the spatial spread of the ion. Figure 5.25 (a), and (b) as well, illustrate the cause. When the scan starts, the radio-frequency is set off-resonant below the resonance frequency. At this point the ions are not cooled efficiently during the measurement phase (see Figure 5.24), which for these measurements has been as long as the cooling phase. The ions heat up, and the spatial spread increases. As soon as the frequency is increased and the cooling becomes more effective, the line-width decreases again. This effect is only prominent for the first ion, the other ions are sympathetically cooled by the first - now cold - ion. In the images the decrease of the spatial spread can clearly be inferred for the first (left-most) ion of each scan. This behavior explains why in Figure 5.27 the lower-frequency flank of the left ion (black graphs) deviates from the fit profile, whereas the higher-frequency flank agrees well. The second (right) ion does not exhibit this behavior.

The frequency difference of the two fit functions is 157(2) kHz, and the spatial distance was determined to $47\,\mathrm{px} \cdot 0.65\ \mu\mathrm{m/px} = 31(2)\ \mu\mathrm{m}$, yielding a gradient value of

$$\frac{\partial}{\partial z}|B| = \frac{h}{g_j \mu_\mathrm{B}} \cdot \frac{157}{31} \frac{\mathrm{kHz}}{\mu\mathrm{m}} = 0.45(4)\,\mathrm{T/m}. \tag{5.10}$$

The second method to find the gradient is by simple drawing a line through the centers of the ions traces, as depicted in Figure 5.28. The line is drawn manually, and the error

estimated by drawing lines that clearly deviate from the ion centers. This works especially well for the long string of ions in part (d) of Figure 5.25. The frequency difference is determined to 1020(30) kHz, and the spatial distance to 179(2) µm. The error range is reduced due to the larger lever. The gradient derived is

$$\frac{\partial}{\partial z}|B| = \frac{h}{g_j \mu_B} \cdot \frac{1020}{179} \frac{\text{kHz}}{\text{µm}} = 0.51(2)\,\text{T/m}. \tag{5.11}$$

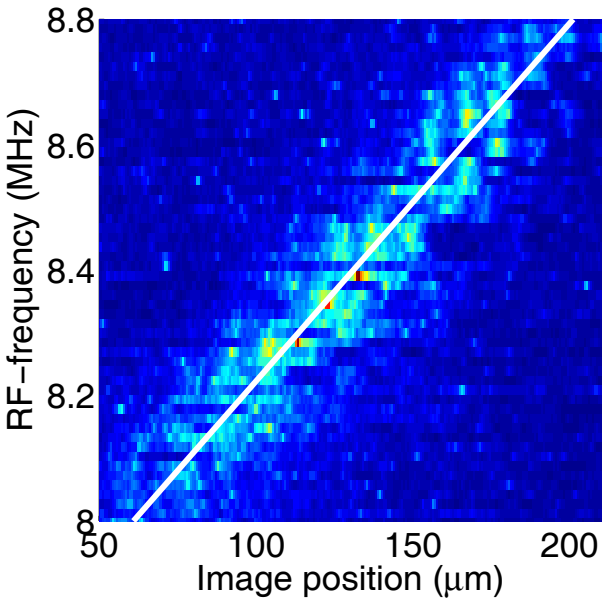

Figure 5.28: Deriving the gradient value by manually fitting a line to the ions maxima.

Gradient alignment revisited

The experimental prerequisite of optical pumping allows for the alignment of the magnetic fields in both magnitude and direction, as the resulting magnetic field needs to be parallel to the polarization of the light field at 935 nm. This has been illustrated in Figure 5.22. Another aspect neglected so far is the length of the ion chain. Due to the magnetic gradient the resulting magnetic field apparently changes over the length of the ion chain (which is the whole aim of the gradient). It is not evident that this change should leave the resulting magnetic field in parallel to the light field polarization. Figure 5.29 demonstrates on a ion crystal comprising 16 ions that indeed the resulting magnetic field is tilted away from the polarization direction.

Starting at an axial position of approximately 130 µm and going to the right the ions are never optically pumped and remain fluorescent, i.e. visible. The ions traces exhibit no

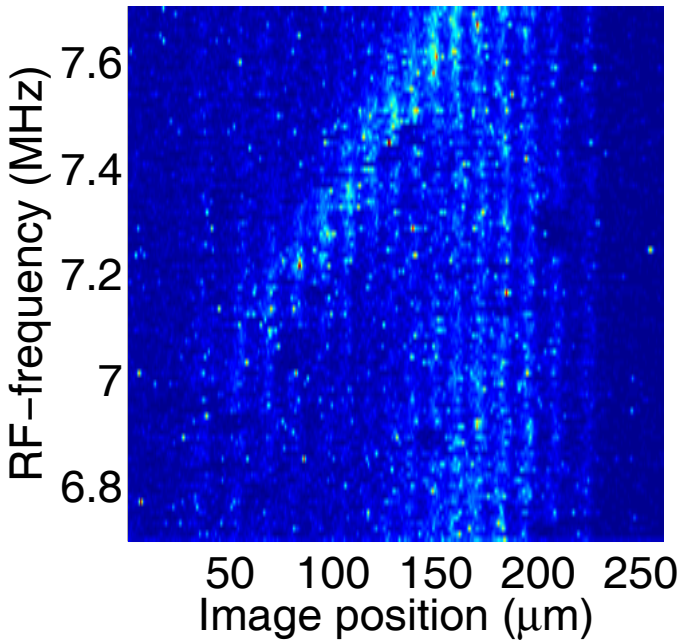

Figure 5.29: Influence of the magnetic gradient on the direction of the $\vec{B}$-field visible by incomplete optical pumping on a crystal of 16 ions.

maximum of the fluorescence signal, but are straight lines over the full frequency range. At this point the added magnetic field from the magnetic gradient has turned the resulting magnetic field so far out of parallelism with the light field polarization that σ-components in the excitation spectrum appear and optical pumping is incomplete (cf. Sec. 2.4). For the ions to the left the added magnetic field from the gradient is compensated well enough to retain optical pumping. These ion traces show the fluorescence signal maximum typical for the addressing scheme.

It is in principle possible to account for the extra magnetic field from the gradient by aligning the polarization, the static magnetic field and the gradient magnetic field such that the added gradient field always points in the direction of the polarization. Then only the absolute value of the resulting magnetic field would change - which is the desired effect from the gradient - without changing its direction. For our experimental setup this would require to turn either the light field or the magnetic gradient field by approximately forty-five degrees. Unfortunately, the current construction does not allow for such a change of the experiment. So far, the gradient needs to be aligned such that the error is distributed over the length of the ion chain, as for example in Figure 5.25 (d). Furthermore, it should be noted that this problem disappears with the original aim of using ^{171}Yb isotope. There, the

polarization of the light field near 935 nm plays no significant role for the qubit transition and manipulation, and hence only the absolute value of the magnetic field is relevant.

Effective Lamb-Dicke-parameter η_{eff}

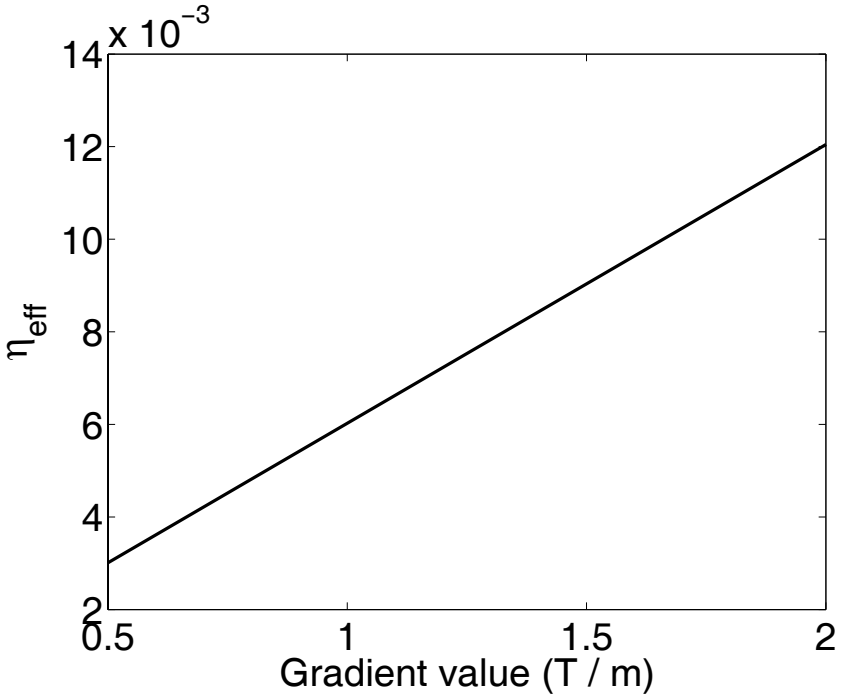

Figure 5.30: Calculation of the effective LDP η_{eff} for the current experimental setup, under the assumption that the value of the magnetic gradient can be maximized to 2 T/m. The axial secular frequency ω_z is fixed at 37 kHz, the value derived from Figure 5.27.

The question arises if the effective LDP η_{eff} is observable with the value of the magnetic gradient achieved in the previous measurements. The calculation of η_{eff} for this experimental situation is depicted in Figure 5.30. The graph shows η_{eff} under variation of the value of the magnetic field gradient. η_{eff} is calculated using Eq. 2.73, as explained in Sec. 2.4.2. The axial secular frequency is assumed to be 37 kHz, which is calculated from the distance of 30.6 µm between the two ions of Figure 5.27 above. For the experimentally realized gradient of 0.51 T/m (see Eq. 5.10) the effective LDP is evaluated to

$$\eta_{\text{eff}} = 3.2 \cdot 10^{-3}. \tag{5.12}$$

In a first, rough estimate this yields a fluorescence rate for the side-bands on the order of $\eta_{\text{eff}} \cdot \mathcal{F} \approx 10$ Hz, where the amplitude of 2200 Hz from Figure 5.23 has been taken as a reference

value for the fluorescence rate $\mathcal{F}$. With the given experimental situation this side-band is not observable. Mainly, the measurement time required for the averaging of the spectra to resolve this small amplitude can not be realized under the present vacuum conditions, as explained before. Furthermore, the power of the rf-radiation can not simply be increased to increase the signal, as the line-width then becomes larger than the axial secular frequency. In other words, the prerequisite of the strong trapping regime is not met anymore, and the side-bands vanish in the profile of the carrier transition. And increasing the axial secular frequency ω_z decreases the effective LDP as explained in Sec. 2.4.2. Nonetheless, as Figure 5.30 shows, the value of η_{eff} can be increased by a factor of four when the value of the magnetic field gradient is maximized to the calculated 2 T/m. Experiments have been envisaged to detect the $\eta_{\text{eff}} = 1.2 \cdot 10^{-2}$ and are currently being prepared in the lab.

Addressing error

What is the error quantity ϵ_{err} defined by Eq. 2.63 (p. 40) for the achieved gradient values? For this discussion the data from the scalar measurements (see Figure 5.23 and Eq. 5.9) is taken as reference, as these measurements were performed with the lowest rf-power and the most averaging. The line-width (FWHM) of the profiles is 85 kHz. If the Rabi-frequency is estimated based on the simple model presented in Sec. 2.3.3 (see Eq. 2.59) we obtain $\Omega = 2\pi \cdot 16\,\text{kHz}$, and hence Eq. 2.63 yields $\epsilon_{\text{err}} = 1.4\,\%$. On the one hand, this appears too optimistic, as the line-width itself is larger than the Rabi-frequency, as discussed before. Using the full line-width, if we simply take the fit value of the resonance fluorescence of one ion at the center frequency of the other ion we obtain $\epsilon_{\text{err}} = 9.2\,\%$. On the other hand, both the numerical simulation and the experiments of the coherent interaction (see Sec. 5.3.1 and Sec. 5.3.2) demonstrate how the four-level system behaves more and more like a two-level system for larger detunings. The frequency difference of 133 kHz clearly is a large detuning in comparison to the Rabi-frequency of 16 kHz. Therefore, the lower ϵ_{err} does not seem unjustified. In any event these values necessarily remain an estimate until the actual experiments with coherent Rabi-spectra on both ions can be performed with a true two-level system like $^{171}\text{Yb}^+$. Nonetheless, under the only assumption of a maximized gradient value of 2 T/m the frequency difference is quadrupled, yielding an error ϵ_{err} distinctly below 1% for both calculations. These values are within experimental reach. It is clear from these estimates that the addressing performance of the gradient scheme is a viable alternative to the addressing scheme by exclusive illumination of the desired ion by a tight laser focus.

6 Conclusion

This work presents the first experimental steps taken to demonstrate a new scheme for quantum information processing in linear ion traps. The scheme employs a static magnetic gradient field to simplify both the addressing of individual ions, and the interaction between them. A long-term goal reserved for high field gradients is the combination of current NMR techniques for quantum information processing with the advantages of an ion trap quantum computer. During the course of this thesis the addressing of individual ions in a linear ion crystal has been successfully implemented by RF-optical double-resonance spectroscopy.

The existing spherical Paul trap ('ring trap') did not allow for the testing of the gradient scheme. A new, linear trap has been put in operation for the first time in our group. Accordingly, a large part of the experimental work - and hence of the whole thesis - was devoted to practical problems of largely technical nature to get acquainted with the peculiarities of this trap. Two new techniques were developed for the characterization of the ovens properties that in the future will aid in the construction and setup of the next-generation of ion traps. First, the imaging of the Planck-spectrum from the heating ovens with an IR-sensitive camera proved to be very resourceful. Second, the atomic beam could be detected by the new ionization laser, resonant to the atomic ground-state transition $^1S_0 \rightarrow {}^1P_1$. The resonance fluorescence from the atom beam is *the* tool in testing the ovens, as it unambiguously detects the presence of ytterbium atoms in the trap center.

The two methods together relieve the experimenter of a large error source while setting up a new trap.

Already for the first loading of the new trap the photo-ionization scheme had to be in place, as the employed electron gun interacted too strongly with the trap potential and thus prevented trapping of ions. The new photo-ionization technique is now firmly established as the first choice for ionization. Only one extra diode laser at a readily available wave-length of 399 nm is required, rendering it both comparatively cheap and easy to implement. From the $^1P_1$ level in Yb I a second photon with a wave-length < 394 nm ionizes the atom. This second light field is supplied by the ionic cooling laser at 369 nm. To our surprise it turned out that the ionization laser at 399 nm alone is enough to ionize the atoms. Examination of this phenomenon showed that the ionization threshold is lowered by the large electric field amplitude of the trapping potential.

The new ionization scheme is so effective that the quasi-deterministic loading of a desired number of ions became feasible. Instead of pre-heating the oven for several minutes it is now possible to ionize atoms and trap ions during the heating period of the oven. The atom flux and hence the loading rate is so low that the ions become countable on the CCD-images or the photo-multiplier signal during loading. To obtain a certain number of trapped ions is now simply a matter of blocking the ionization laser at the right time. Last but not least, the new ionization laser permitted to build and use a new oven with natural abundance isotope distribution of Yb I. Inserting the oven into the trap setup such that it forms an angle of approximately 90° with the ionization laser beam allowed for Doppler-free spectra of the atomic resonance fluorescence. These spectra clearly resolve the different isotopes of Yb I. In a first measurement series the resonant enhancement of isotope selective trapping has been demonstrated.

Ultimately, using the ground-state hyper-fine structure of the $^{171}Yb^+$ ion as a qubit is aimed for. The $^{171}Yb^+$ ion has - in comparison to the $^{172}Yb^+$ ion - higher experimental demands though. First, due to the smaller line-width of the main cooling transition at 369 nm it has a lower cooling rate, and the small line-width implies a more stringent demand on the frequency control of the cooling laser. Second, the mandatory use of micro-wave radiation to avoid optical pumping adds to the complexity of the cooling procedure. Therefore, the trapping and cooling of the ^{171}Yb isotope is an added experimental challenge that is retained for future experiments.

In this work, the Zeeman sub-levels of the $D_{3/2}$ state of $^{172}Yb^+$ are utilized as a magnetically sensitive level-structure. Irradiating the ion with π-polarized light at 935 nm - which couples the $D_{3/2}$ state to the $[3/2]_{1/2}$ state - the $m_j = \pm 3/2$ levels are optically pumped, and the resonance fluorescence is interrupted. RF-radiation at the Larmor-frequency of the

Zeeman splitting induces transitions between the different m_j energy levels. The resulting state of the ion is probed by the π-polarized light field at 935 nm. If a transition occured from the $m_j = \pm 3/2$ levels to the $m_j = \pm 1/2$ levels, the ion is coupled back to the cooling cycle via the $[3/2]_{1/2}$ level, and the resulting resonance fluorescence can be detected. If, on the other hand, the ion remains in the $m_j = \pm 3/2$ state, the ion is left uncoupled from the cooling cycle, and no resonance fluorescence occurs.

This installation of a RF-optical double-resonance spectroscopy now facilitates the characterization of both the static and the dynamic magnetic fields present at the site of the ions. When the RF-radiation and the light fields interact simultaneously with the ions the cooling cycle is permanently closed, but its efficiency depends on the frequency of the RF-radiation. Scanning the RF-radiation through the resonance of the $D_{3/2}$ level splitting a Lorentz-profile of the cooling fluorescence at 369 nm is obtained. The center frequency of this profile determines the absolute value of the static magnetic fields, as $\hbar\omega = \vec{\mu} \cdot \vec{B}$. Irradiating the ion instead with alternating pulses of RF- and optical radiation renders possible the coherent spectroscopy of the Zeeman level-structure. The result are a Rabi-oscillation measurements. These characterize the dynamic magnetic fields and their interaction with the ion.

A set of three pairs of solenoids around the center of the trap creates a static magnetic field with arbitrary orientation, producing the desired Zeeman splitting of the $D_{3/2}$ state. These magnetic fields were measured in a first step with the RF-optical double-resonance spectroscopy, thereby establishing the method as well. The RF-radiation is created by a simple RF-coil, oriented such that the resulting dynamic magnetic field is perpendicular to the static magnetic field. The magnitude of the static magnetic field was varied systematically, shifting the resonance frequency of the resulting Lorentz-profiles. The exact value of the magnetic field was extracted from numerical fits of the fluorescence profiles. The direction of the linear polarization of the laser light field at 935 nm defines the spatial orientation of the field. For the experimental prerequisite of π-polarization the electric component of the light field needs to be parallel to the resulting static field. Thus the magnetic field could be thoroughly characterized.

As a second step the dynamic magnetic fields created by the RF-coil were examined with coherent spectroscopy. The light fields at 369 nm and 935 nm were switched on and off, alternating with RF-radiation pulses of variable length. The resulting Rabi-oscillation spectra determine the amplitude of the magnetic component of the RF-radiation. The main aspect worth stressing again, though, is the easy implementation of the coherent spectroscopy. Instead of a high-profile laser system with state-of-the-art frequency and intensity stabilization a simple RF-coil suffices for the coherent manipulation of the Zee-

man sub-level structure. The maximal Rabi-frequency obtained with the present setup is $2\pi \cdot 31\,\mathrm{kHz}$, well in agreement with numerical simulations. The absolute value is easily extensible. Replacing the current broad-band RF-coil with a resonance circuit the magnetic amplitude of the RF-field may be distinctly increased. Basically, a limit for the increase in amplitude is given by the necessary band-width needed to address a string of ions, as the quality factor of the resonant circuit determines both the amplitude multiplication factor as well as the band-width of the circuit. The higher the gain in amplitude, the lower the band-width, and vice versa. For every given problem these parameters therefore need to be weighed against each other. Nonetheless, Rabi-frequencies in the hundreds of kilohertz pose no intricate technical problems.

Finally, a static magnetic gradient field was set up with two permanent magnets facing each other in quadrupole configuration. Numerical simulations of the resulting magnetic field estimated the value of the gradient to be on the order of $2\,\mathrm{T/m}$. The subsequent measurements revealed that the resonance frequency of the ions did indeed split depending on their position. The realized maximal gradient was determined to $0.51(2)\,\mathrm{T/m}$, corresponding to a frequency splitting between two ions on the order of 160 kHz, for a rather large distance of 30 µm. The axial secular frequency was selected so low to render the visualization of the splitting more accessible. The remaining erroneous excitation of neighboring ions is on the order of 10%. This large value is due mainly to the broad line-width of the transition. First, it stems partly from the four-level dynamics of the interaction of the RF-radiation with the $D_{3/2}$ state. But second, for these first experiments the amplitude of the RF-field was set quite high for a good signal-to-noise ratio. Assuming that the measurement had been performed with two $^{171}Yb^{+}$ ions at a Rabi-frequency of 10 kHz the error value would decrease to below 0.4%. All of this is not even taking into account the possibilities for error reduction offered by pulse shaping techniques or pulse sequences known from NMR experiments.

The reason for the lower value of the gradient is imperfect alignment of the permanent magnets, and due partly also to the limitations of the coil-cage. The maximum gradient experienced by the ions is found to the left or right (on the trap axis) of the gradients geometrical center. Only in the exact center of the two permanent magnets do the magnetic fields cancel, off-center an additional magnetic component arises that needs to be compensated for. Due to the high magnetization of the permanent magnets ($B_{\mathrm{rem}} = 1.08\,\mathrm{T}$) this extra field quickly becomes very large. The currents needed to compensate this field are larger than the coils were constructed for. Nonetheless, assuming optimal alignment of the permanent magnets it should be possible to distinctly increase the value of the magnetic field gradient to $2\,\mathrm{T/m}$ with the current setup.

Outlook

The first step for the gradient scheme has been taken in this thesis, but many more await. The obvious next step is the direct proof of a coupling between internal and external degrees of freedom of the ions, allowing for conditional quantum gates with RF-radiation. For this, the gradient has to be maximized, a goal that is already being worked on. Also, new micro-traps are in preparation that will allow for much larger gradients to be incorporated into the trap setup, with gradient values ranging in the hundreds of T/m. Another important goal will then be to utilize the odd isotope ^{171}Yb with its two-level hyper-fine structure, a true qubit. Adding pulse sequence techniques that have been developed in the last couple of months in the lab will then facilitate the formation of a ion-spin molecules, where the advantages of ion trap and NMR quantum computing may be combined.

A

Solution of the four level Bloch-equations

This appendix details the explicit calculation of the Hamiltonian of the four-level system in the interaction picture. The Hamilton operator in rotating-wave approximation is transformed into a reference frame co-rotating with the exciting RF-radiation by a unitary transformation given below. Inserting the resulting Hamiltonian $\hat{H}$ into the von-Neumann equation a set of sixteen coupled linear differential equations emerge. The literature used for this section is the same as in Sec. 2.3.2.

Interaction picture

The atomic Hamilton operator reads

$$H_0 = \hbar\omega \begin{pmatrix} -3/2 & 0 & 0 & 0 \\ 0 & -1/2 & 0 & 0 \\ 0 & 0 & +1/2 & 0 \\ 0 & 0 & 0 & +3/2 \end{pmatrix}. \tag{A.1}$$

The Hamiltonian describing the interaction of a four-level atom with a RF-radiation field in the laboratory frame is given by

$$H_{\text{int}} = \frac{\hbar}{2}\begin{pmatrix} 0 & \Omega_{12}e^{i\omega_{\text{rf}}t} & 0 & 0 \\ \Omega_{21}e^{-i\omega_{\text{rf}}t} & 0 & \Omega_{23}e^{i\omega_{\text{rf}}t} & 0 \\ 0 & \Omega_{32}e^{-i\omega_{\text{rf}}t} & 0 & \Omega_{34}e^{i\omega_{\text{rf}}t} \\ 0 & 0 & \Omega_{43}e^{-i\omega_{\text{rf}}t} & 0 \end{pmatrix}. \tag{A.2}$$

To change the basis of the problem to the reference frame co-rotating with ω a unitary transformation is applied. The mathematical basis of quantum mechanics tells us that

$$\hat{\rho} = U\rho U^{\dagger}, \tag{A.3}$$

and

$$\hat{H} = UHU^{\dagger} - i\hbar U\frac{dU^{\dagger}}{dt}. \tag{A.4}$$

The unitary transformation that eliminates the time-dependence for our problem reads

$$U = \begin{pmatrix} e^{-i\frac{3}{2}\omega_L t} & 0 & 0 & 0 \\ 0 & e^{-i\frac{1}{2}\omega_L t} & 0 & 0 \\ 0 & 0 & e^{i\frac{1}{2}\omega_L t} & 0 \\ 0 & 0 & 0 & e^{i\frac{3}{2}\omega_L t} \end{pmatrix}. \tag{A.5}$$

For the atomic Hamiltonian H_0

$$UH_0U^{\dagger} = H_0, \tag{A.6}$$

and for the interaction Hamiltonian

$$UH_{\text{int}}U^{\dagger} = \frac{\hbar}{2}\begin{pmatrix} 0 & \Omega_{12} & 0 & 0 \\ \Omega_{21} & 0 & \Omega_{23} & 0 \\ 0 & \Omega_{32} & 0 & \Omega_{34} \\ 0 & 0 & \Omega_{43} & 0 \end{pmatrix}. \tag{A.7}$$

The last term is of Eq. A.4 given by

$$i\hbar U\frac{\mathrm{d}}{\mathrm{d}t}U^{\dagger} = -\hbar\begin{pmatrix} \frac{3}{2}\omega_L & 0 & 0 & 0 \\ 0 & \frac{1}{2}\omega_L & 0 & 0 \\ 0 & 0 & -\frac{1}{2}\omega_L & 0 \\ 0 & 0 & 0 & -\frac{3}{2}\omega_L \end{pmatrix}. \tag{A.8}$$

Inserting Eq. A.6 - Eq. A.8 into Eq. A.4 yields

$$\begin{aligned}\hat{H} &= H_0 + U H_{\text{int}} U^\dagger - i\hbar U \frac{\mathrm{d}U^\dagger}{\mathrm{d}t} \\ &= \hbar\omega_0 \begin{pmatrix} -\frac{3}{2} & 0 & 0 & 0 \\ 0 & -\frac{1}{2} & 0 & 0 \\ 0 & 0 & \frac{1}{2} & 0 \\ 0 & 0 & 0 & \frac{3}{2} \end{pmatrix} + \frac{\hbar}{2} \begin{pmatrix} 0 & \Omega_{12} & 0 & 0 \\ \Omega_{21} & 0 & \Omega_{23} & 0 \\ 0 & \Omega_{32} & 0 & \Omega_{34} \\ 0 & 0 & \Omega_{43} & 0 \end{pmatrix} + \hbar\omega_L \begin{pmatrix} \frac{3}{2} & 0 & 0 & 0 \\ 0 & \frac{1}{2} & 0 & 0 \\ 0 & 0 & -\frac{1}{2} & 0 \\ 0 & 0 & 0 & -\frac{3}{2} \end{pmatrix} \\ &= \frac{\hbar}{2} \begin{pmatrix} -3\delta & \Omega_{12} & 0 & 0 \\ \Omega_{21} & -\delta & \Omega_{23} & 0 \\ 0 & \Omega_{32} & +\delta & \Omega_{34} \\ 0 & 0 & \Omega_{43} & +3\delta \end{pmatrix},\end{aligned} \tag{A.9}$$

where

$$\delta = \omega_0 - \omega_L. \tag{A.10}$$

Solution

Equipped with this Hamilton operator we can now retrieve the actual equations that define the time evolution of the individual components of ρ:

$$i\hbar\dot{\rho} = [\hat{H}, \rho] = \hat{H}\rho - \rho\hat{H}. \tag{A.11}$$

This solution is given explicitly in the following:

$$\dot{\rho}_{11} = \frac{\hbar}{2}[\Omega_{12}(\rho_{21} - \rho_{12})] \tag{A.12}$$

$$\dot{\rho}_{12} = \frac{\hbar}{2}[-2\delta\rho_{12} + \Omega_{12}(\rho_{22} - \rho_{11}) \; - \; \Omega_{23}\rho_{13}] \tag{A.13}$$

$$\dot{\rho}_{13} = \frac{\hbar}{2}[-4\delta\rho_{13} + \Omega_{12}\rho_{23} - \Omega_{23}\rho_{12} - \Omega_{34}\rho_{14}] \tag{A.14}$$

$$\dot{\rho}_{14} = \frac{\hbar}{2}[-6\delta\rho_{14} + \Omega_{12}\rho_{24} - \Omega_{34}\rho_{13}] \tag{A.15}$$

$$\dot{\rho}_{21} = \frac{\hbar}{2}[+2\delta\rho_{21} + \Omega_{12}(\rho_{22} - \rho_{11}) + \Omega_{23}\rho_{31}] \tag{A.16}$$

$$\dot{\rho}_{22} = \frac{\hbar}{2}[\Omega_{21}(\rho_{12} - \rho_{21}) + \Omega_{23}(\rho_{32} - \rho_{23})] \tag{A.17}$$

$$\dot{\rho}_{23} = \frac{\hbar}{2}[-2\delta\rho_{23} + \Omega_{12}\rho_{13} - \Omega_{23}(\rho_{33} - \rho_{22}) - \Omega_{34}\rho_{24}] \tag{A.18}$$

$$\dot{\rho}_{24} = \frac{\hbar}{2}[-4\delta\rho_{24} + \Omega_{12}\rho_{14} + \Omega_{23}\rho_{34} - \Omega_{34}\rho_{23}] \tag{A.19}$$

$$\dot{\rho}_{31} = \frac{\hbar}{2}[4\delta\rho_{31} - \Omega_{12}\rho_{32} + \Omega_{23}\rho_{21} + \Omega_{34}\rho_{31}] \tag{A.20}$$

$$\dot{\rho}_{32} = \frac{\hbar}{2}[2\delta\rho_{32} - \Omega_{12}\rho_{31} + \Omega_{23}(\rho_{22} - \rho_{33}) + \Omega_{34}\rho_{42}] \tag{A.21}$$

$$\dot{\rho}_{33} = \frac{\hbar}{2}[\Omega_{23}(\rho_{23} - \rho_{32}) + \Omega_{34}(\rho_{43} - \rho_{34})] \tag{A.22}$$

$$\dot{\rho}_{34} = \frac{\hbar}{2}[-2\delta\rho_{34} + \Omega_{23}\rho_{24} + \Omega_{34}(\rho_{44} - \rho_{33})] \tag{A.23}$$

$$\dot{\rho}_{41} = \frac{\hbar}{2}[6\delta\rho_{41} - \Omega_{12}\rho_{42} + \Omega_{34}\rho_{31}] \tag{A.24}$$

$$\dot{\rho}_{42} = \frac{\hbar}{2}[4\delta\rho_{42} - \Omega_{12}\rho 41 - \Omega_{23}\rho_{43} + \Omega_{34}\rho_{32}] \tag{A.25}$$

$$\dot{\rho}_{43} = \frac{\hbar}{2}[2\delta\rho_{43} - \Omega_{23}\rho_{42} + \Omega_{34}(\rho_{33} - \rho_{44})] \tag{A.26}$$

$$\dot{\rho}_{44} = \frac{\hbar}{2}\Omega_{34}(\rho_{34} - \rho_{43}) \tag{A.27}$$

B

Fluorescence rate: a simple rate equation model

In the following, an elementary rate equation analysis is developed to obtain the fluorescence rate more accurately. This analysis is similar to the one described by Matthew Roberts in his PhD thesis [Roberts, 1996] for the ^{172}Yb system. Figure B.1 shows the energy levels and the transitions involved here. Linearly polarized light at 935 nm is assumed, optically pumping the $m_j = \pm 3/2$ Zeeman sub-levels of the $D_{3/2}$ state. The $D_{3/2}$ state is split into two levels, the uncoupled state (i.e. the $m_j = \pm 3/2$ levels) called D^{u} and the coupled state called D^{c}, which is the level coupled by the light field at 935 nm to the $[3/2]_{1/2}$ level (i.e. the $m_j = \pm 1/2$ levels). This is possible as the level structure is completely symmetric with regard to Clebsch-Gordan coefficients for the transition from the $P_{1/2}$ and to the $[3/2]_{1/2}$ level. A quadratic Zeeman-shift is not present as the ^{172}Yb isotope has no nuclear spin I. The radio-frequency transition takes place between these two levels.

The population of five levels are to be determined then, requiring five dependencies or equations to mathematically solve this system. The first is simply the completeness of the populations:

$$P_S + P_P + P_{D^u} + P_{D^c} + P_{[3/2]} = 1 \tag{B.1}$$

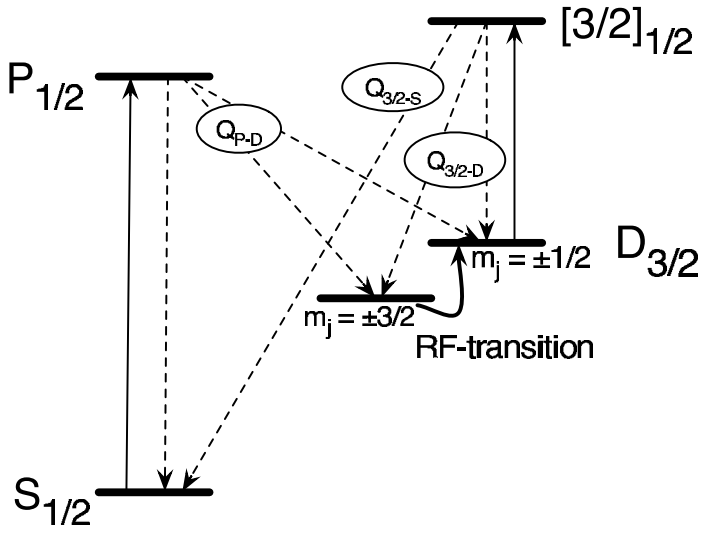

Figure B.1: Energy levels and transitions used for the rate equation analysis

The second and third dependency are based on the assumption that both laser light fields at 369 nm and 935 nm are in saturation, which means that the population of the coupled levels are equal:

$$P_S = P_P, \tag{B.2}$$

and

$$P_{[3/2]} = P_{D^c}. \tag{B.3}$$

The final two equations are obtained by looking at the transition rates. Certainly for every transition from the left to the right branch of the cycle a transition back needs to occur, i.e. these rates need to be equal:

$$P_P\,\gamma_P\,Q_{P\to D} = P_{[3/2]}\,\gamma_{[3/2]}\,Q_{[3/2]\to S}, \tag{B.4}$$

where $\gamma_x = 1/\tau_x$ is the decay rate of the according level in s^{-1} ($\Gamma = \gamma/2\pi$), and Q_x is the branching ratio for that transition. Lastly, the population and depopulation rates of the dark state level D^u need to equal, too. The level is populated by decay from either the $\mathrm{P}_{1/2}$ or the $[3/2]_{1/2}$ state. These rates need to be corrected for by the Clebsch-Gordon coefficients of the transitions. The depopulation takes places only through a RF-transition into the D^c level. This is treated as a 'decay' with a decay rate of γ_{D^u}, such that

$$P_P\,\gamma_P\,Q_{P\to D}\,C_{P\to D^u} + P_{[3/2]}\,\gamma_{[3/2]}\,Q_{[3/2]\to D}\,C_{[3/2]\to D^u} = P_{D^u}\,\gamma_{D^u} \tag{B.5}$$

This set of five equations is now solved to give P_P, as the population of the $\mathrm{P}_{1/2}$ state directly yields the resulting fluorescence rate via $\mathcal{F} = P_P\gamma_P$. First, equations B.2 and B.3

are inserted into Eq. B.1:

$$1 = 2P_P + 2P_{[3/2]} + P_{D^u}. \tag{B.6}$$

Next, both $P_{[3/2]}$ and P_{D^u} are expressed in dependence of P_P. Eq. B.4 determines $P_{[3/2]}$:

$$P_{[3/2]} = P_P \frac{\gamma_P \, Q_{P\to D}}{\gamma_{[3/2]} \, Q_{[3/2]\to S}}, \tag{B.7}$$

with together with Eq. B.5 yields

$$\begin{aligned} P_{D^u} &= \frac{1}{\gamma_{D^u}} \left[P_P \, \gamma_P \, Q_{P\to D} \, C_{P\to D^u} + P_{[3/2]} \, \gamma_{[3/2]} \, Q_{[3/2]\to D} \, C_{[3/2]\to D^u} \right] & \text{(B.8)} \\ &= \frac{1}{\gamma_{D^u}} \left[P_P \, \gamma_P \, Q_{P\to D} \, C_{P\to D^u} + P_P \frac{\gamma_P \, Q_{P\to D}}{\gamma_{[3/2]} \, Q_{[3/2]\to S}} \gamma_{[3/2]} \, Q_{[3/2]\to D} \, C_{[3/2]\to D^u} \right]. & \text{(B.9)} \end{aligned}$$

Putting everything together Eq. B.6 becomes:

$$P_P = \left[2 + 2\frac{\gamma_P \, Q_{P\to D}}{\gamma_{[3/2]} \, Q_{[3/2]\to S}} + \frac{\gamma_P \, Q_{P\to D}}{\gamma_{D^u}} \left(C_{P\to D^u} + C_{[3/2]\to D^u} \frac{Q_{[3/2]\to D}}{Q_{[3/2]\to S}} \right) \right]^{-1} \tag{B.10}$$

Here, P_P is expressed solely in terms of known constants and the transition rate γ_{D^u}. The values for these constants are taken from Appendix C and Table 2.1 (p. 26). The branching ratio from the $[3/2]_{1/2}$ level to the $D_{3/2}$ level is assumed to be $1 - Q_{[3/2]\to S}$. Figure B.2 shows a simulation of the fluorescence rate $\mathcal{F} = P_P \gamma_P$ for different transition rates.

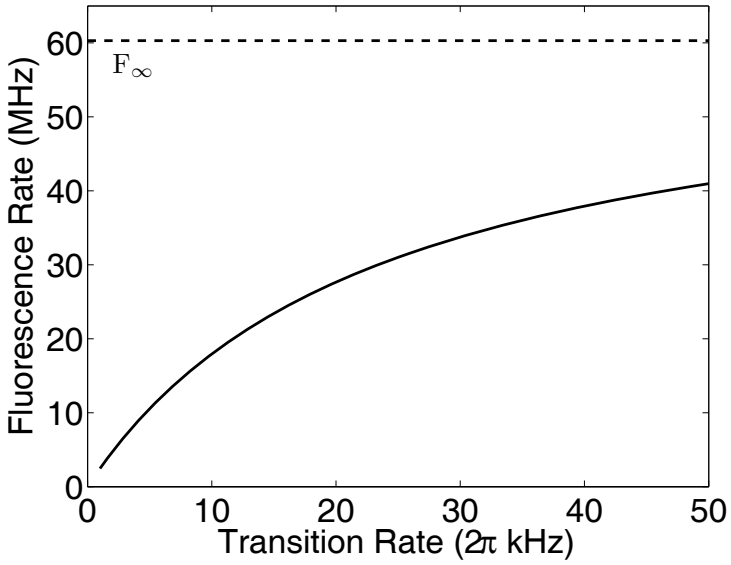

Figure B.2: Simulated fluorescence rate in dependence of transition rate.

Using the abbreviations

$$a = \frac{\gamma_P \, Q_{P\to D}}{\gamma_{[3/2]} \, Q_{[3/2]\to S}} \tag{B.11}$$

$$b = \gamma_P \, Q_{P\to D} \left(C_{P\to D^u} + C_{[3/2]\to D^u} \frac{Q_{[3/2]\to D}}{Q_{[3/2]\to S}} \right) \tag{B.12}$$

the fluorescence rate and the unwieldy term Eq. B.10 can be written as

$$\mathcal{F} = \frac{\gamma_P}{2 + 2a + \frac{b}{\gamma_{D^u}}} = \frac{\mathcal{F}_\infty}{1 + \frac{b'}{\gamma_{D^u}}}. \tag{B.13}$$

$\mathcal{F}_\infty$ and b' follow. Thus abbreviated the saturation characteristic of this relation becomes evident. The maximum fluorescence rate

$$\mathcal{F}_\infty = \frac{\gamma_P}{2 + 2a} = 60.3\,\mathrm{MHz} \tag{B.14}$$

is just the maximum fluorescence rate derived by Matthew Roberts [Roberts, 1996]. a, b and b' are convenient abbreviations comprising only atomic constants. a and b are numerically evaluated to $a = 0.0229$ and $b = 2\pi \cdot 48.4\,\mathrm{kHz}$, such that

$$b' = \frac{b}{a + 2a} = 2\pi \cdot 23.7\,\mathrm{kHz}. \tag{B.15}$$

This figure is interesting for the characterization of the saturation: at a transition rate $\gamma_{D^u} = b'$ the resulting fluorescence rate is just half of $\mathcal{F}_\infty$.

Using these results we estimate the overall detection efficiency of the photo-multiplier setup. The maximal photon counting rate achieved was 30 kHz. This value needs interpretation, though, to render it applicable in a given situation. The 30 kHz were realized without the RF-spectroscopy in place, with both the cooling laser at 369 nm and the repump laser at 935 nm well in saturation and set for maximum fluorescence rate. Furthermore, the aperture to filter stray-light (see Figure 3.17, p. 72) later was closed further to reduce the stray-light signal. This reduced the fluorescence signal to 27 kHz. Last but not least, several measurements presented in this thesis were performed without micro-motion compensation, yielding a distinctly lower value for the maximally attainable fluorescence rate. But even for the best compensation the remaining modulation index of 0.7 implies a photon signal that is approximately 11% lower than $\mathcal{F}_\infty$. Therefore, the 27 kHz increase back to 30 kHz as the maximal detected photon count rate. Taken together, the overall detection efficiency is estimated to be

$$\frac{30\,\mathrm{kHz}}{60.3\,\mathrm{MHz}} = 5 \cdot 10^{-4}. \tag{B.16}$$

C Ytterbium

Ytterbium derives its name from the Swedish village of *Ytterby*. The swiss chemist *Jean Charles Galissard de Marignac* discovered in 1878 a new component which he called Ytterbia. This was in fact ytterbium-oxide, contaminated with Lutetium-oxide. In 1907 the french chemist *Georges Urbain* - and independently *Auer von Welsbach* - separated the components and named the two components Ytterbium and Lutetium. Ytterbium is a rare-earth metal of the Lanthanide series with atomic number 70. It has seven naturally occuring stable isotopes. The atomic mass is given as 173.04 a.u. The distribution of the relative abundance of the different isotopes is given in Table C.1 [Meggers & Tech, 1978].

Neutral ytterbium has an electron structure similar to an alkaline-earth metal, with singlet and triplet states. Its structure is briefly presented in Sec. 4.1 about photo-ionization. Singly ionized ytterbium - with which we are mainly concerned in this work - has a single valence electron and hence an alkaline-like energy level structure. A closed shell in Xenon-configuration with angular momentum and spin zero is complemented by this electron, which accordingly determines the energetic spectrum. The odd isotopes $^{171}Yb^+$ and $^{173}Yb^+$ have a nuclear momentum of $I = 1/2\hbar$ and $I = 5/2\hbar$, respectively, creating a hyper-fine splitting of the energy levels. For ion trap purposes the isotopes 171, 172 and 174 are known to have been used. Due to its relevance for optical clocks the ytterbium ion is a relatively well researched element, both experi-

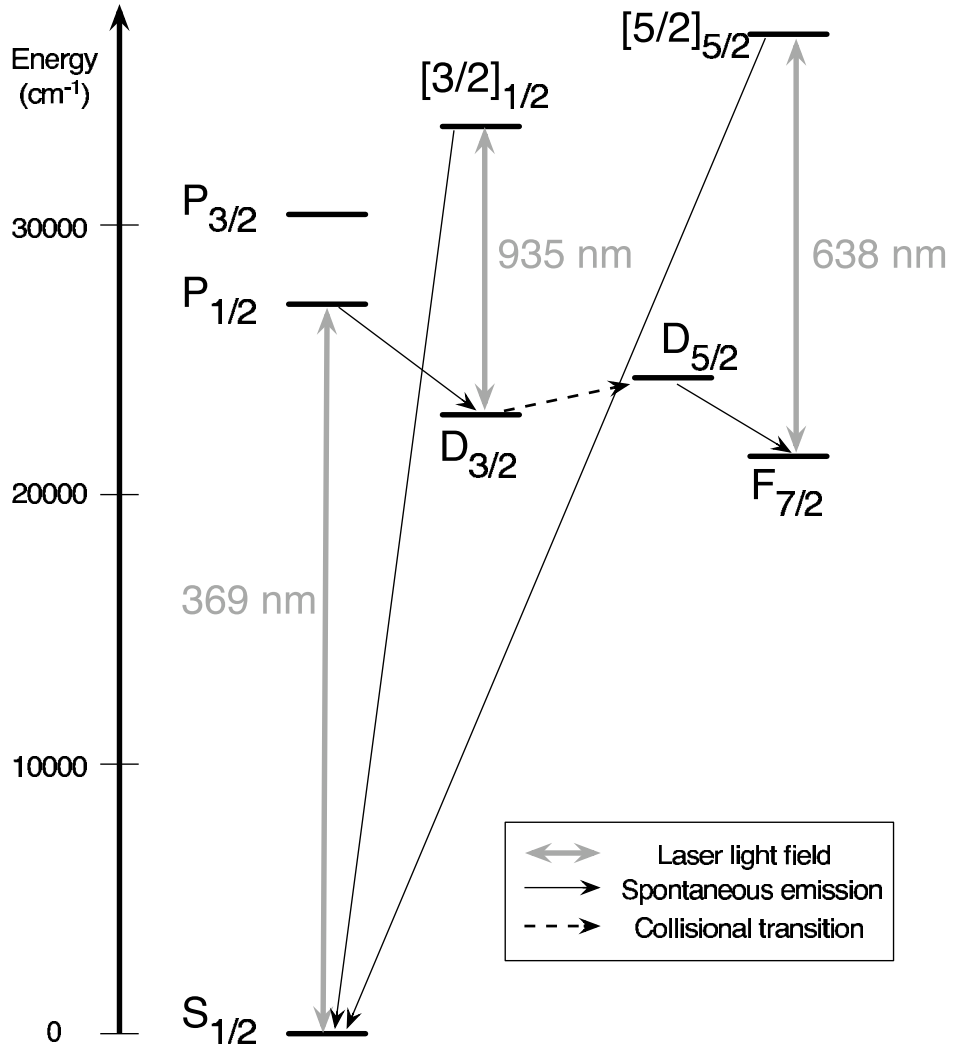

Figure C.1: Relevant excerpt of the ^{172}Yb II energy level diagram. The energy values are to scale.

Isotope	rel. abundance (%)	Nuclear momentum ($\hbar$)
168	0.13	0
170	3.05	0
171	14.3	1/2
172	21.9	0
173	16.12	5/2
174	31.8	0
176	12.7	0

Table C.1: Natural abundance distribution of the different ytterbium isotopes.

mentally and with numerical simulations [Meggers, 1941a, Meggers, 1941b, Meggers, 1967, Meggers & Tech, 1978, Fawcett & Wilson, 1991]. In the following, the discussion and the data restricts itself to the ^{172}Yb isotope.

Term	Configuration	Energy (cm^{-1})	Life-time	Ref.
$^2P_{1/2}$	$4f^{14}6p$	27062	8.07 ± 0.09 ns	[Pinnington et al., 1997]
$^2P_{3/2}$	$4f^{14}6p$	30392	6.15 ± 0.09 ns	[Pinnington et al., 1997]
$^2D_{3/2}$	$4f^{14}5d$	22961	52.7 ± 2.4 ms	[Yu & Maleki, 2000]
$^2D_{5/2}$	$4f^{14}5d$	24333	7.0 ± 0.4 ms	[Yu & Maleki, 2000]
$^2F_{7/2}$	$4f^{13}6s^2$	21419	10^{+7}_{-4} a	[Roberts et al., 1997]
$^3[3/2]_{1/2}$	$4f^{13}5d6s$	33654	37.7 ± 0.5 ns	[Berends et al., 1993]
$^3[5/2]_{5/2}$	$4f^{13}5d6s$	37078	< 50 ms	[Roberts et al., 1997]

Table C.2: Energy and life-time of the relevant energy levels of $^{172}Yb^+$

Table Table C.2 list the energy levels of $^{172}Yb^+$ relevant for this work. These levels are also depicted (to scale) in Figure C.1. Furthermore, Table C.3 lists the transitions used for laser cooling in this work, as well as those pertaining to optical clock research. The ground state of Yb^+ is the $4f^{14}6s$ level, $^2S_{1/2}$. The main transition used for laser (Doppler) cooling is the $^2S_{1/2} \leftrightarrow ^2P_{1/2}$ transition with a line-width of 19.8 MHz, implying an ample scattering rate. From the $P_{1/2}$ level the ion can decay into the meta-stable $D_{3/2}$ state, with a branching ratio of 0.483% [Yu & Maleki, 2000]. Owing to the long life-time of the $D_{3/2}$ level of 52.7 ms the cooling fluorescence is interrupted. The 'usual' way for Doppler cooling in ion traps would be to couple the $D_{3/2}$ level back to the cooling cycle via the $P_{1/2}$ level. In ytterbium this corresponds to a laser wave-length of 2.438 µm, which is experimentally cumbersome. In [Bell et al., 1991] a four-level excitation scheme has been proposed and

Transition	Line-width	ΔE (cm^{-1})	Wave-Length (nm)	Reference
$^2S_{1/2} \leftrightarrow ^2P_{1/2}$	19.8 MHz	27062	369.4	[Berends et al., 1993]
$^2D_{3/2} \leftrightarrow ^3[3/2]_{1/2}$	< 2.7 MHz	10693	934.9	[Berends et al., 1993]
$^2F_{7/2} \leftrightarrow ^3[5/2]_{5/2}$	> 3 Hz	15659	638.4	[Roberts et al., 1997]
$^2S_{1/2} \leftrightarrow ^2D_{3/2}$	3 Hz	22961	435	[Yu & Maleki, 2000]
$^2S_{1/2} \leftrightarrow ^2D_{5/2}$	22.7 Hz	24333	411	[Yu & Maleki, 2000]
$^2S_{1/2} \leftrightarrow ^2F_{7/2}$	$5 \cdot 10^{-10}$ Hz	21419	467	[Roberts et al., 1997]

Table C.3: Relevant transitions driven by laser light fields in $^{172}Yb^+$. The upper part presents the transitions used in this work, the lower part shows the proposed (and measured) clock transitions.

implemented that utilizes an excited state. The $4f^{13}5d6s$ level ($[3/2]_{1/2}$) is described by jK-coupling, where a hole in the f-shell couples with the LS-coupled outer two electrons. This process is described in detail in [Balzer, 2003]. The transition between the $D_{3/2}$ and the $[3/2]_{1/2}$ level has a wave-length of 935 nm, which is readily accessible with diode lasers. The $[3/2]_{1/2}$ level quickly decays mainly back into the ground state $S_{1/2}$, with a calculated branching ratio of 0.981 [Fawcett & Wilson, 1991] (see also discussion in [Roberts, 1996]). Taken together the two transitions at 369 nm and 935 nm form a closed four-level optical-excitation scheme for laser cooling that has proven itself. A rate-equation analysis (see Appendix B) estimates the overall fluorescence rate to 60.3 MHz. The ion thus spends only about 3% in the $D_{3/2}$ level.

The ytterbium ion features a special level worth mentioning, the $F_{7/2}$ or $4f^{13}6s^2$. The transition from the ground-state $S_{1/2}$ to this level is the only known (optical) electric octupole transition, with a measured life-time of 10 years (!) [Roberts, 1996]. Due to its incomparably small line-width of $5 \cdot 10^{-10}$ Hz this transition is the prime candidate for an optical frequency reference [Roberts et al., 1999, Stenger et al., 2001]. For the experiments performed in this thesis though this long-lived state poses a certain problem. A decay channel into the $F_{7/2}$ exists based on a collisional transition between the two $5d$-levels. From the ${}^2D_{5/2}$ level the ion decays into the $F_{7/2}$ level with a branching ratio of 0.83 [Taylor et al., 1997]. Thus a collision of the ion with a background atom can cause a trapping of the population in the $F_{7/2}$ state, interrupting the cooling fluorescence. Another laser light field depletes this population by coupling the $F_{7/2}$ level to another jK-coupled level, the ${}^3[5/2]_{5/2}$ level. From this upper level the ion decays back into the ground-state. This transition has a wave-length of 638 nm, which is also accessible with a diode laser.

Bibliography

[Appasamy, 1997] Appasamy, B. (1997). *Über die Bewegungszustände eines einzelnen harmonisch gespeicherten Ba^+-Ions*. PhD thesis, Universität Hamburg.

[Balzer, 2003] Balzer, C. (2003). *Zur Dynamik eines beobachteten einzelnen Quantensystems*. PhD thesis, Universität Hamburg.

[Balzer et al., 2006] Balzer, C., Braun, A., Hannemann, T., Paape, C., Ettler, M., Neuhauser, W., & Wunderlich, C. Electrodynamically trapped Yb^+ ions for quantum information processing. *Physical Review A*, **73**, 041407 (R) (2006).

[Balzer & Wunderlich, 2003] Balzer, C. & Wunderlich, C. Quantum measurements and new concepts for experiments with trapped ions. *Adv. At. Mol. Opt. Phys.*, **49**, 293 (2003).

[Banerjee et al., 2003] Banerjee, A., Rapol, U. D., Das, D., Krishna, A., & Natarajan, V. Precise measurements of UV atomic lines: Hyperfine structure and isotope shifts in the 398.8nm line of Yb. *Europhysics Letters*, **63**, 340–346 (2003).

[Barrett et al., 2004] Barrett, M. D., Chiaverini, J., Schaetz, T., Britton, J., Itano, W. M., Jost, J. D., Knill, E., Langer, C., Leibfried, D., Ozeri, R., & Wineland, D. J. Deterministic quantum teleportation of atomic qubits. *Nature*, **429**(6993), 737–739 (2004).

[Bell et al., 1991] Bell, A. S., Gill, P., Klein, H. A., Levick, A. P., Tamm, C., & Schnier, D. Laser cooling of trapped ytterbium ions using a four-level optical-excitation scheme. *Physical Review A*, **44**, 20–23 (1991).

[Berends et al., 1993] Berends, R. W., Pinnington, E. H., Guo, B., & Ji, Q. Beam-laser lifetime measurements for four resonance levels of Yb II. *Journal of Physics: B*, **26**(20), L701–L704 (1993).

[Borisov et al., 1998] Borisov, S. K., Kuzmina, M. A., & Mishin, V. A. Selective photoionisation of ^{168}Yb in an extended optically dense medium. *Quantum Electronics*, **28**, 169–172 (1998).

[Camus et al., 1980] Camus, P., Debarre, A., & Morillon, C. Highly excited levels of neutral ytterbium I. Two-photon and two-step spectroscopy of even spectra. *Journal of Physics: B*, **13**, 1073–1087 (1980).

[Cermaka, 2005] Cermaka, I. Compact radio-frequency power supply for ion and particle guides and traps. *Rev. Sci. Instrum.*, **76**, 063302 (2005).

[Chiaverini et al., 2004] Chiaverini, J., Leibfried, D., Schaetz, T., Barrett, M. D., Blakestad, R. B., Britton, J., Itano, W. M., Jost, J. D., Knill, E., Langer, C., Ozeri, R., & Wineland, D. J. Realization of quantum error correction. *Nature*, **432**(7017), 602–605 (2004).

[Choet et al., 1995] Choet, A. S., Rheet, Y., Leet, J., Kuzmina, M. A., & Mishint, V. A. Selective photoionization of ^{168}Yb in a three-level atomic medium by the collinear propagation of laser pulses. *Journal of Physics: B*, **28**, 3805–3820 (1995).

[Chuang, 2003] Chuang, I. (2003). Principles of Quantum Computation. In D. Esteve, J.-M. Raimond, & J. Dalibard (Eds.), *Quantum Entanglement and Information Processing, Session LXXIX*: Elsevier.

[Cirac & Zoller, 1995] Cirac, J. I. & Zoller, P. Quantum Computations with Cold Trapped Ions. *Physical Review Letters*, **74**, 4091–4094 (1995).

[Cohen-Tannoudji et al., 1999a] Cohen-Tannoudji, C., Diu, B., & Laloë, F. (1999a). *Quantenmechanik (Band 1)*, volume 1. Walter de Gruyter.

[Cohen-Tannoudji et al., 1999b] Cohen-Tannoudji, C., Diu, B., & Laloë, F. (1999b). *Quantenmechanik (Band 2)*, volume 2. Walter de Gruyter.

[Cohen-Tannoudji et al., 1998] Cohen-Tannoudji, C., Dupont-Roc, J., & Grynberg, G. (1998). *Atom-Photon interactions*. Wiley-Interscience.

[Demtröder, 2003] Demtröder, W. (2003). *Laser spectroscopy*. Springer Verlag.

[Deutsch, 1985] Deutsch, D. Quantum theory, the Church-Turing principle and the universal quantum computer. *Proc. R. Soc. Lond. A*, **400**, 97–117 (1985).

[Deutsch & Jozsa, 1992] Deutsch, D. & Jozsa, R. Rapid solution of problems by quantum computation. *Proc. R. Soc. Lond. A*, **439**, 553–558 (1992).

[Devoret & Martinis, 2003] Devoret, M. H. & Martinis, J. M. (2003). Superconducting Qubits. In D. Esteve, J.-M. Raimond, & J. Dalibard (Eds.), *Quantum Entanglement and Information Processing, Session LXXIX*: Elsevier.

[Einstein, 1905] Einstein, A. Über einen die Erzeugung und Verwandlung des Lichtes betreffenden heuristischen Gesichtspunkt. *Annalen der Physik*, **17**, 132–148 (1905).

[Ettler, 2004] Ettler, M. (2004). Präparation einzelner $^{171}Yb^{+}$-Ionen in den Zustand $^{2}S_{1/2}, F = 0$. Master's thesis, Universität Hamburg.

[Fawcett & Wilson, 1991] Fawcett, B. C. & Wilson, M. *At. Data Nuc. Data Tables*, **47**, 241–317 (1991).

[Feynman, 1982] Feynman, R. P. (1982). Simulating Physics with Computers. In *International Journal of Theoretical Physics*, volume 21 (pp. 467–488).

[Fröhlich et al., 2004] Fröhlich, U., Roth, B., Antonini, P., Lämmerzahl, C., Wicht, A., & Schiller, S. Ultracold Trapped Molecules: Novel Systems for Tests of the Time-Independence of the Electron-to-Proton Mass Ratio. *Lect. Notes Phys.*, **648**, 297–307 (2004).

[Garca-Ripoll et al., 2003] Garca-Ripoll, J. J., Zoller, P., & Cirac, J. I. Speed Optimized Two-Qubit Gates with Laser Coherent Control Techniques for Ion Trap Quantum Computing. *Physical Review Letters*, **91**(15), 157901 (2003).

[Ghosh, 1995] Ghosh, P. K. (1995). *Ion traps*. International series of monographs on physics. Oxford Science Publications.

[Gulde, 2003] Gulde, S. (2003). *Experimental Realization of Quantum Gates and the Deutsch-Josza Algorithm with Trapped $^{40}Ca^{+}$ Ions*. PhD thesis, Universität Innsbruck.

[Gulde et al., 2003] Gulde, S., Riebe, M., Lancaster, G. P. T., Becher, C., Eschner, J., Haffner, H., Schmidt-Kaler, F., Chuang, I. L., & Blatt, R. Implementation of the Deutsch-Jozsa algorithm on an ion-trap quantum computer. *Nature*, **421**(6918), 48–50 (2003).

[Gulde et al., 2001] Gulde, S., Rotter, D., Barton, P., Schmidt-Kaler, F., Blatt, R., & Hogervorst, W. Simple and efficient photo-ionization loading of ions for precision ion-trapping experiments. *Applied Physics B*, **73**, 861–863 (2001).

[Haffner et al., 2005] Haffner, H., Hansel, W., Roos, C. F., Benhelm, J., Chek-al kar, D., Chwalla, M., Korber, T., Rapol, U. D., Riebe, M., Schmidt, P. O., Becher, C., Guhne, O., Dur, W., & Blatt, R. Scalable multiparticle entanglement of trapped ions. *Nature*, **438**(7068), 643–646 (2005).

[Haken & Wolf, 2004] Haken, H. & Wolf, H. C. (2004). *Atom- und Quantenphysik*. Springer-Verlag Berlin Heidelberg New York.

[Hallwachs, 1888] Hallwachs, W. Über den Einfluß des Lichtes auf electrostatisch geladene Körper. *Annalen der Physik*, **33**, 301–311 (1888).

[Hannemann, 2002] Hannemann, T. (2002). *Schätzung von Quantenzuständen und Charakterisierung von Quantenkanälen*. PhD thesis, Universität Hamburg.

[Hannemann et al., 2002] Hannemann, T., Reiss, D., Balzer, C., Neuhauser, W., Toschek, P. E., & Wunderlich, C. Self-learning estimation of quantum states. *Physical Review A*, **65**, 050303 (2002).

[Hänsch & Schawlow, 1975] Hänsch, T. W. & Schawlow, A. L. Cooling of gases by laser radiation. *Optics Communication*, **13**, 69–69 (1975).

[Hansen, 2006] Hansen, D. (2006). *Meta-stable Calcium*. PhD thesis, Universität Hamburg.

[Heisenberg, 1990] Heisenberg, W. (1990). *Physik und Philosophie*. S. Hirzel Stuttgart, 5. edition.

[James, 1998] James, D. Quantum dynamics of cold trapped ions with application to quantum computation. *Applied Physics B*, **66**, 181–190 (1998).

[Jones & Mosca, 1998] Jones, J. A. & Mosca, M. Implementation of a Quantum Algorithm on a Nuclear Magnetic Resonance Quantum Computer. *J. Chem. Phys.*, **109**, 1648–1653 (1998).

[Jones & Anderson, 2000] Jones, R. M. & Anderson, S. L. Simplified radio-frequency generator for driving ion guides, traps, and other capacitive loads. *Rev. Sci. Instrum.*, **71**, 4335 (2000).

[Jones et al., 1997] Jones, R. M., Gerlich, D., & Anderson, S. L. Simple radio-frequency power source for ion guides and ion traps. *Rev. Sci. Instrum.*, **68**, 3357 (1997).

[Kielpinski et al., 2002] Kielpinski, D., Monroe, C., & Wineland, D. J. Architecture for a large-scale ion-trap quantum computer. *Nature*, **417**(6890), 709–711 (2002).

[Kjrgaard et al., 2000] Kjrgaard, N., Hornekr, L., Thommesen, A., Videsen, Z., & Drewsen, M. Isotope selective loading of an ion trap using resonance-enhanced two-photon ionization. *Applied Physics B*, **71**, 207–210 (2000).

[Kobzar et al., 2003] Kobzar, K., Skinnern, T., N.Khaneja, Glaser, S., & Luy, B. *J. Mag. Res.*, **170**, 8 (2003).

[Koerber, 2003] Koerber, T. W. (2003). *Measurement of light shift ratios with a single trapped $^{138}Ba^{+}$ ion, and prospects for a parity violation experiment.* PhD thesis, University of Washington.

[Leibfried et al., 2003] Leibfried, D., DeMarco, B., Meyer, V., Lucas, D., Barrett, M., Britton, J., Itano, W. M., Jelenkovic, B., Langer, C., Rosenband, T., & Wineland, D. J. Experimental demonstration of a robust, high-fidelity geometric two ion-qubit phase gate. *Nature*, **422**(6930), 412–415 (2003).

[Lucas et al., 2003] Lucas, D. M., Donald, C. J. S., Home, J. P., McDonnell, M. J., Ramos, A., Stacey, D. N., Stacey, J.-P., Steane, A. M., & Webster, S. C. Oxford ion-trap quantum computing project. *Phil. Trans. R. Soc. Lond. A*, (pp. 10.1098/rsta.2003.1209). (2003).

[Lucas et al., 2004] Lucas, D. M., Ramos, A., Home, J. P., McDonnell, M. J., Nakayama, S., Stacey, J.-P., Webster, S. C., Stacey, D. N., , & Steane, A. M. Isotope-selective photoionization for calcium ion trapping. *Physical Review A*, **69**, 012711 (2004).

[Meggers, 1967] Meggers, W. The second spectrum of Ytterbium (Yb II). *Journal of Research of the National Bureau of Standards*, **71A**, 396–544 (1967).

[Meggers & Tech, 1978] Meggers, W. & Tech, J. *Journal of Research of the National Bureau of Standars*, **83** (1978).

[Meggers, 1941a] Meggers, W. F. Emission Spectra of the Rare Earth Elements. *Journal of the Optical Society of America*, **31**, 157–159 (1941a).

[Meggers, 1941b] Meggers, W. F. The Strongest Lines of Singly Ionized Atoms. *Journal of the Optical Society of America*, **31**, 605–611 (1941b).

[Meyer et al., 2001] Meyer, V., Rowe, M. A., Kielpinski, D., Sackett, C. A., Itano, W. M., Monroe, C., & Wineland, D. J. Experimental demonstration of entanglement-enhanced rotation angle estimation using trapped ions. *Physical Review Letters*, **86**(26), 5870–5873 (2001).

[Mintert & Wunderlich, 2001] Mintert, F. & Wunderlich, C. Ion-Trap Quantum Logic Using Long-Wavelength Radiation. *Physical Review Letters*, **87**(25), 257904 (2001).

[Molhave, 2000] Molhave, K. (2000). Construction of and Experiments with a Linear Paul Trap. Master's thesis, University of Aarhus.

[Monroe et al., 1995] Monroe, C., Meekhof, D. M., King, B. E., Itano, W. M., & Wineland, D. J. Demonstration of a Fundamental Quantum Logic Gate. *Physical Review Letters*, **75**, 4714–4717 (1995).

[Nägerl et al., 1998] Nägerl, H., Leibfried, D., Schmidt-Kaler, F., Eschner, J., & Blatt, R. Coherent excitation of normal modes in a string of Ca^+ ions. *Optics Express*, **3**, 89–96 (1998).

[Nägerl et al., 1998] Nägerl, H. C., Bechter, W., Eschner, J., Schmidt-Kaler, F., & Blatt, R. Ion strings for quantum gates. *Applied Physics B*, **66**, 603–608 (1998).

[Neuhauser et al., 1978] Neuhauser, W., Hohenstatt, M., Toschek, P., & Dehmelt, H. Optical-Sideband Cooling of Visible Atom Cloud Confined in Parabolic Well. *Physical Review Letters*, **41**(4), 233–236 (1978).

[Neuhauser et al., 1980] Neuhauser, W., Hohenstatt, M., Toschek, P. E., & Dehmelt, H. Localized visible Ba^+ mono-ion oscillator. *Physical Review A*, **22**(3), 1137–1140 (1980).

[Oskay et al., 2006] Oskay, W. H., Diddams, S. A., Donley, E. A., Fortier, T. M., Heavner, T. P., Hollberg, L., Itano, W. M., Jefferts, S. R., Delaney, M. J., Kim, K., Levi, F., Parker, T. E., & Bergquist, J. C. Single-Atom Optical Clock with High Accuracy. *Physical Review Letters*, **97**(2), 020801–4 (2006).

[Paape, 2004] Paape, C. (2004). Isotopenselektive Photoionisation von Ytterbium zur Speicherung einzelner Ionen in einer Ionenfalle. Master's thesis, Universität Hamburg.

[Paul et al., 1958] Paul, W., Osberghaus, O., & Fischer, E. (1958). *Ein Ionenkäfig*. Technical report, Wirtschafts- und Verkehrsministerium Nordrhein-Westfalen. Westdeutscher Verlag Köln-Opladen.

[Pinnington et al., 1997] Pinnington, E. H., Rieger, G., & Kernahan, J. A. Beam-laser measurements of the lifetimes of the 6p levels in Yb II. *Physical Review A*, **56**, 2421–2423 (1997).

[Prestage et al., 1989] Prestage, J., Dick, G. J., & Maleki, L. New ion trap for frequency standard applications. *Journal of Applied Physics*, **66**, 1013–1017 (1989).

[Raizen et al., 1992] Raizen, M. G., Gilligan, J. M., Berquist, J. C., Itano, W. M., & Wineland, D. J. Ionic crystals in a linear Paul trap. *Physical Review A*, **45**, 6493–6501 (1992).

[Rapol et al., 2004] Rapol, U., Krishna, A., Wasan, A., & Natarajan, V. Laser cooling and trapping of Yb from a thermal source. *The European Physical Journal D*, **29**, 409–414 (2004).

[Riebe et al., 2004] Riebe, M., Haffner, H., Roos, C. F., Hansel, W., Benhelm, J., Lancaster, G. P. T., Korber, T. W., Becher, C., Schmidt-Kaler, F., James, D. F. V., & Blatt, R. Deterministic quantum teleportation with atoms. *Nature*, **429**(6993), 734–737 (2004).

[Rivest et al., 1978] Rivest, R., Shamir, A., & Adleman, L. A Method for Obtaining Digital Signatures and Public-Key Cryptosystems. *Communications of the ACM*, **21**, 2 (1978).

[Roberts, 1996] Roberts, M. (1996). *Spectroscopy of a Single Ytterbium Ion*. PhD thesis, Imperial College, University of London.

[Roberts et al., 1997] Roberts, M., Taylor, P., Barwood, G. P., Gill, P., Klein, H. A., & Rowley, W. R. C. Observation of an Electric Octupole Transition in a Single Ion. *Physical Review Letters*, **78**, 1876–1879 (1997).

[Roberts et al., 1999] Roberts, M., Taylor, P., Gateva-Kostova, S. V., Clarke, R. B. M., Rowley, W. R. C., & Gill, P. Measurement of the $^2S_{1/2} -^2 D_{5/2}$ clock transition in a single $^{171}Yb^+$ ion. *Physical Review A*, **60**, 2867–2872 (1999).

[Rohde, 2001] Rohde, B. (2001). *Experimente zur Quanteninformationsverarbeitung in einer linearen Ionenfalle*. PhD thesis, Universtiät Innsbruck.

[Rohde et al., 2001] Rohde, H., Gulde, S. T., Roos, C. F., Barton, P. A., Leibfried, D., Eschner, J., Schmidt-Kaler, F., & Blatt, R. Sympathetic ground-state cooling and coherent manipulation with two-ion crystals. *Journal of Optics B*, **3**, S34–S41 (2001).

[Roos, 2000] Roos, C. (2000). *Controlling the quantum state of trapped ions*. PhD thesis, Universtiät Innsbruck.

[Roos et al., 1999] Roos, C., Zeiger, T., Rohde, H., Nägerl, H. C., Eschner, J., Leibfried, D., Schmidt-Kaler, F., & Blatt, R. Quantum State Engineering on an Optical Transition and Decoherence in a Paul Trap. *Physical Review Letters*, **83**, 4713–4716 (1999).

[Rotter, 2003] Rotter, D. (2003). Photoionisation von Kalzium. Master's thesis, Universität Innsbruck.

[Rowe et al., 2001] Rowe, M. A., Kielpinski, D., Meyer, V., Sackett, C. A., Itano, W. M., Monroe, C., & Wineland, D. J. Experimental violation of a Bell's inequality with efficient detection. *Nature*, **409**(6822), 791–794 (2001).

[Sankari & Suryanarayana, 1998] Sankari, M. & Suryanarayana, M. V. Studies on the isotope selective photoionization of the low-abundant ^{168}Yb isotope. *Journal of Physics: B*, **31**, 261–273 (1998).

[Schmidt-Kaler et al., 2003a] Schmidt-Kaler, F., Gulde, S., Riebe, M., Deuschle, T., Kreuter, A., Lancaster, G., Becher, C., Eschner, J., Haffner, H., & Blatt, R. The coherence of qubits based on single Ca+ ions. *JOURNAL OF PHYSICS B-ATOMIC MOLECULAR AND OPTICAL PHYSICS*, **36**(3), 623–636 (2003a).

[Schmidt-Kaler et al., 2003b] Schmidt-Kaler, F., Haffner, H., Riebe, M., Gulde, S., Lancaster, G. P. T., Deuschle, T., Becher, C., Roos, C. F., Eschner, J., & Blatt, R. Realization of the Cirac-Zoller controlled-NOT quantum gate. *NATURE*, **422**(6930), 408–411 (2003b).

[Schneider et al., 2005] Schneider, T., Peik, E., & Tamm, C. Sub-Hertz Optical Frequency Comparisons between Two Trapped $^{171}Yb^{+}$ Ions. *Physical Review Letters*, **94**(23), 230801 (2005).

[Shor, 1994] Shor, P. (1994). Algorithms for Quantum Computation: Discrete Logarithms and Factoring. In *Proceedings of the 35th Annual Symposium on Foundations of Computer Science* (pp. 124–134).: IEEE Computer Society Press.

[Sleator & Weinfurter, 1995] Sleator, T. & Weinfurter, H. Realizable Universal Quantum Logic Gates. *Physical Review Letters*, **74**(20), 4087–4090 (1995).

[Sorensen & Molmer, 2000] Sorensen, A. & Molmer, K. Entanglement and quantum computation with ions in thermal motion. *Physical Review A*, **62**(2), 022311 (2000).

[Staanum, 2004] Staanum, P. (2004). *Quantum Optics with Trapped Calcium Ions*. PhD thesis, University of Aarhus.

[Stacey, 2003] Stacey, J.-P. (2003). *Stabilization and Control In a Linear Ion Trap*. PhD thesis, Oxford University.

[Stenger et al., 2001] Stenger, J., Tamm, C., Haverkamp, N., Weyers, S., & Telle, H. R. Absolute frequency measurement of the 435.5-nm 171Yb+-clock transition with a Kerr-lens mode-locked femtosecond laser. *Optics Letters*, **26**, 1589–1591 (2001).

[Taylor et al., 1998] Taylor, P., Roberts, M., Barwood, G. P., & Gill, P. Combined optical-infrared single-ion frequency standard. *Optics Letters*, **23**, 298–300 (1998).

[Taylor et al., 1997] Taylor, P., Roberts, M., Gateva-Kostova, S. V., Clarke, R. B. M., P.Barwood, G., Rowley, W. R. C., & Gill, P. Investigation of the $^2S_{1/2}$ - $^2D_{5/2}$ clock transition in a single ytterbium ion. *Physical Review A*, **56**, 2699–2704 (1997).

[Tkachev & Yakovlenko, 1996] Tkachev, A. & Yakovlenko, S. Multistage photoionisation of ytterbium. *Quantum Electronics*, **26**, 839–843 (1996).

[Vandersypen, 2001] Vandersypen, L. M. K. (2001). *Experimental Quantum Computation with Nuclear Spins in Liquid Solution*. PhD thesis, Stanford University.

[von Weizsäcker, 1990] von Weizsäcker, C. F. (1990). *Zum Weltbild der Physik*, chapter Komplementarität und Logik, (pp. 281–331). S. Hirzel Stuttgart, 13. edition.

[Webster, 2005] Webster, S. (2005). *Raman Sideband Cooling and Coherent Manipulation of Trapped Ions*. PhD thesis, Oxford University.

[Weisgerber, 2003] Weisgerber, I. (2003). Aufbau eines Magnetfeldsystems, eines Helixresonators und eines optischen Strahlenganges. Master's thesis, Universitt Hamburg.

[Wineland & Dehmelt, 1975] Wineland, D. J. & Dehmelt, H. G. Proposed $10^{14}\nu/\Delta\nu$ laser fluorescence spectroscopy on Tl^+ monoion oscillator. *Bull. Am. Phys. Soc.*, **20**, 637 (1975).

[Wineland et al., 1978] Wineland, D. J., Drullinger, R. E., & Walls, F. L. Radiation-pressure cooling of bound resonant absorbers. *Physical Review Letters*, **40**, 1639 (1978).

[Wineland et al., 1973] Wineland, D. J., Ekstrom, P., & Dehmelt, H. Monoelectron oscillator. *Physical Review Letters*, **31**, 1279 (1973).

[Wunderlich, 2001] Wunderlich, C. (2001). Conditional spin resonance with trapped ions. In *Laser Physics at the Limit*. Springer Verlag, Heidelberg-Berlin-New York.

[Wunderlich et al., 2006] Wunderlich, C., Hannemann, T., Körber, T., Häffner, H., Roos, C., Hänsel, W., Blatt, R., & Schmidt-Kaler, F. Robust state preparation of a single trapped ion by adiabatic passage. *Journal of Modern Optics*, (pp. 0–9). (2006).

[Wunderlich et al., 2005] Wunderlich, C., Morigi, G., & Reiss, D. Simultaneous cooling of axial vibrational modes in a linear ion trap. *Physical Review A*, **72**(2), 023421 (2005).

[Xu et al., 1994] Xu, C., Xu, X., Huang, W., Xue, M., & Chen, D. Rydberg and autoionizing states of neutral ytterbium. *Journal of Physics: B*, **27**, 3905–3913 (1994).

[Yu & Maleki, 2000] Yu, N. & Maleki, L. Lifetime measurements of the $4f^{14}5d$ metastable states in single ytterbium ions. *Physical Review A*, **61**, 022507 (2000).

Danksagung

Ich danke Prof. Dr. Werner Neuhauser und Prof. Dr. Christof Wunderlich für die Betreuung dieser Doktorarbeit. Prof. Wunderlich danke ich insbesondere für die physikalischen Ideen und Anregungen, die als zentrale Aspekte in diese Arbeit eingeflossen sind. Prof. Neuhauser danke ich für die Motivation während der täglichen Tücken des Ionen-Fangens. Seine stete Ruhe und Gelassenheit gepaart mit kritischer Distanz haben mir ein großes Durchhalte-Vermögen vermittelt.

Ohne die Einarbeitung, Hilfe und Geduld von Vorgängern und Kollegen in der Arbeitsgruppe kann eine solche Arbeit nicht gelingen. Daher gilt mein Dank (in ungefähr chronologischer Reihenfolge) Dr. Andreas Keil, Dipl.-Phys. Klaus Abich, Dr. Thilo Hannemann, und Dr. Christoph Balzer, die mich in oft nächtelanger Arbeit in die Kunst des Ionen-Fangens - mit den Nebenschauplätzen Laser-Bau, Laser-Justage und Am-Laser-Verzweifeln - eingewiesen haben.

Danken möchte ich auch den ehemals Cand.-Phys., nun Dipl.-Phys. Manuel Ettler und Christian Paape. Zum einen haben Ihre Beiträge das Experiment 'wie die Hulle' vorangebracht, zum anderen war die nicht immer ausschließlich fachliche Konversation mindestens sehr erheiternd, wenn nicht sogar freundschaftlich!

Mittlerweile in Siegen sind B.A. Nuala Timoney und Dr. Michael Johanning. Ihnen danke ich für die gute Atmosphäre beim gemeinschaftlichen Arbeiten in Hamburg, und ich wünsche Ihnen viel Erfolg bei den zukünftigen Experimenten!

Als vorbildlich möchte ich die Zusammenarbeit mit der elektronischen und der mechanischen Werkstatt des Instituts für Laser-Physik in Hamburg nennen. Stellvertretend seien deren Leiter Reinhard Mielck, Frank Jonas und Stephan Fleig genannt, die mit Geduld meine sehr einfachen Zeichnungen hinnahmen und in Bauteile für das Experiment verwandelten. Auch Dieter Barlösius möchte ich für seine Glasbläser-Kunst und den neuen Vakuum-Rezipienten danken.

Großer Dank gebührt auch meiner Familie, die mich immer mit Anteilnahme unterstützt hat, selbst wenn die Materie fern ihres Alltags liegt, und sie ihren Bekannten nicht immer erklären konnten, was ihr Sohn denn nun macht.

Am meisten Dank gebührt meiner Freundin Anne-Kathrin. Mit größter Geduld hat sie mich die vielen Jahre unterstützt, die es letztendlich doch geworden sind, und gemeinsam mit mir die oft schwierigen Phasen überstanden.